Artificial Gauge Fields in Driven Optical Lattices

From Frustrated XY Models to Ising Ferromagnetism

Dissertation
zur Erlangung des Doktorgrades
des Departments Physik
der Universität Hamburg

vorgelegt von
Julian Struck
aus Hamburg

Hamburg
2013

Gutachter der Dissertation:	Prof. Dr. Klaus Sengstock Prof. Dr. Andreas Hemmerich Prof. Dr. Ian B. Spielman
Gutachter der Disputation:	Prof. Dr. Klaus Sengstock Prof. Dr. Henning Moritz
Datum der Disputation:	29. Juli 2013
Vorsitzender des Prüfungsausschusses:	Prof. Dr. Ludwig Mathey
Vorsitzender des Promotionsausschusses:	Prof. Dr. Peter Hauschildt
Dekan der Fakultät für Mathematik, Informatik und Naturwissenschaften:	Prof. Dr. Heinrich Graener

Zweifle an allem wenigstens einmal, und wäre es auch der Satz: zweimal zwei ist vier.

Georg Christoph Lichtenberg
(1 July 1742 – 24 February 1799)

Abstract

Since the beginning of this century quantum degenerate gases in optical lattices have developed from proof-of-principle experiments into quantum emulators with a continuously increasing number of tools for manipulation and probing. They provide a clean, controllable and isolated environment for the investigation of model Hamiltonians, especially of those eluding thorough analytical and numerical treatment. In recent years, major efforts have been undertaken to mimic the presence of gauge fields in these systems.

In this thesis time-periodic driving of bosons in optical lattices is systematically utilized to engineer tunneling matrix elements. In particular, sinusoidal driving is employed to change the sign and magnitude of J, thereby emulating ferro- or antiferromagnetic coupling schemes. The conventional tuning method for tunneling, which is based on proper lattice depth adjustment, restricts the values of the tunneling parameter J to the set of positive real numbers. Moreover, for the first time complex valued tunneling matrix elements are synthesized by breaking time-reversal symmetry. Within the framework of the Peierls substitution, this corresponds to the creation of artificial vector gauge potentials for neutral atoms confined in optical lattices.

The first part of this work is focusing on the simulation of a classical XY model on the triangular lattice, which is the simplest lattice structure featuring geometrical frustration for antiferromagnetic coupling. The phases of the coherent local wavefunctions are mapped onto continuous two-dimensional vector-spins. Spin-spin interactions are mediated by tunneling processes, where the sign of J determines the nature of this coupling. A whole variety of different spin configurations and phase transitions could be studied via the adjustable anisotropy of the tunneling. Measured spin-configurations are finally mapped into a comprehensive phase diagram. Due to the strong frustration certain phases exhibit a ground state degeneracy of two. The spontaneous symmetry breaking induced by a macroscopic occupation of one of the ground states is statistically analyzed.

The second part of this thesis is devoted to the creation of synthetic gauge potentials and the emulation of strong magnetic fields for neutral atoms. In a proof-of-principle experiment the feasibility of the creation of tunable gauge potentials via periodic forcing, which breaks time-reversal symmetry, is demonstrated. Furthermore, on the triangular lattice, gauge-invariant staggered fields are engineered, which correspond to artificial magnetic fluxes. The resulting deformations of the dispersion relation are inferred from the measured momentum distributions of the atoms.

The underlying Hamiltonian exhibits a discrete Ising-type $\mathbb{Z}_2$ symmetry for maximum flux strength of π. A thermal phase transition from a ferromagnetic phase with spontaneously broken $\mathbb{Z}_2$ symmetry to a paramagnetic phase is observed. The corresponding order parameter of the system, the so called magnetization, can be identified with long-range ordered chiral mass currents. In addition, by lowering the gauge field strength, the $\mathbb{Z}_2$ symmetry can be broken on purpose. Furthermore, the long-range coherence is qualitatively measured, revealing a close relationship to the magnetization order parameter.

In the final part of this work, a scheme for the creation of synthetic spin-orbit coupling in a tight-binding lattice is derived and discussed. It is based on the idea of spin-dependent lattice forcing via an oscillating magnetic field gradient. The resulting band structure is comprised of two spin dependent dispersion relations, which are coupled via radio frequency fields.

Zusammenfassung

Seit Beginn dieses Jahrhunderts hat sich das Feld der quantenentarteten Gase in optischen Gittern kontinuierlich weiterentwickelt. Die Zahl der Manipulations- und Detektionsmethoden hat stetig zugenommen. Dabei stellt die Reinheit und Kontrollierbarkeit dieser Systeme eine ideale Umgebung für die Untersuchung einfacher, aber trotzdem nicht vollständig verstandener Festkörpermodelle dar.

Im Rahmen der vorliegenden Arbeit wurden zeitperiodisch getriebene, ultrakalte, bosonische Gase in optischen Gittern untersucht. In der Zeitmittelung über eine Periode führt der Antrieb effektiv zur Renormalisierung der Tunnelmatrixelemente im Gitter. Die konventionelle Methode zur Modifikation des Tunnels beruht auf der Anpassung der Gittertiefe und lässt nur Werte des Tunnelparameter J zu, die positiv reell sind. In dieser Arbeit wurde eine sinusförmig oszillierende Kraft verwendet, um das Vorzeichen von J zu invertieren und damit, neben ferromagnetischen, auch antiferromagnetische Kopplungsschemata zu realisieren. Darüber hinaus konnte zum ersten Mal demonstriert werden, dass ein zeitperiodischer Antrieb, der die Zeitumkehrinvarianz verletzt, zu komplexwertigen effektiven Tunnelmatrixelementen führen kann.

Der erste Teil dieser Arbeit beschäftigt sich mit der Simulation eines klassischen XY-Modells auf einem Dreiecksgitter. Im Falle bestimmter antiferromagnetischer Kopplungsschemata ist dieses Gitter geometrisch frustriert. Die Phasen der lokalen Wellenfunktionen eines jeden Gitterplatzes lassen sich als kontinuierliche, vektorielle Spins interpretieren. Die Wechselwirkung zwischen benachbarten Spins ist durch das Vorzeichen des Tunnelmatrixelements bestimmt. Mit Hilfe einer einstellbaren Anisotropie des Tunnelns konnten verschiedene Spin-Ordnungen und Phasenübergänge realisiert und studiert werden. So gelang es das entsprechende Phasendiagramm dieses Systems zu charakterisieren. Spezielle Bereiche des Phasendiagramms weisen eine, durch die geometrische Frustration bedingte, zweifache Entartung des Grundzustandes auf. Die entsprechende Symmetriebrechung, die durch die einzelne Besetzung eines dieser beiden Zustände auftritt, wurde statistisch analysiert.

Der zweite Teil der vorliegenden Arbeit beschäftigt sich mit der Erzeugung künstlicher Eichfelder und der Simulation magnetischer Flüsse für neutrale Atome. Es konnte experimentell gezeigt werden, dass es möglich ist, mit einem zeitperiodisch getriebenen Gittersystem Eichfelder für neutrale Atome zu simulieren. Im Dreiecksgitter gelang es synthetische, alternierende Magnetfelder zu erzeugen. Die daraus resultierende Deformation der Dispersionsrelation wurde anhand der Impulsverteilung der im Gitter gefangenen Atome vermessen. Im Falle maximaler magnetischer Flussstärke π weist der Hamiltonoperator eine $\mathbb{Z}_2$ Symmetrie auf. Für diesen Fall konnte ein thermisch getriebener Phasenübergang von einer ferromagnetischen zu einer paramagnetischen Phase beobachtet werden. Der entsprechende Ordnungsparameter des Systems, der die $\mathbb{Z}_2$ Symmetriebrechung beschreibt, ist die Magnetisierung. Diese wird über die langreichweitige Ordnung der lokalen Masseströme definiert. Für magnetische Flussstärken abweichend von π ist die $\mathbb{Z}_2$ Symmetrie des Hamiltonoperators gebrochen und eine bestimme Magnetisierung des Systems energetisch bevorzugt. Darüber hinaus ist das an die Magnetisierung gekoppelte Verhalten der Kohärenz der lokalen Phasen untersucht worden.

Im letzten Teil dieser Arbeit wird die Erzeugung einer künstlichen Spin-Bahn Kopplung in einem Gitter diskutiert. Das grundlegende Konzept basiert dabei auf einem spinabhängigem, zeitperiodischen Antrieb. Eine Rabi-Kopplung beider Spin-Zustände führt zu einer Hybridisierung der spinabhängigen Dispersionsrelationen.

Publikationen

Im Rahmen dieser Arbeit sind die folgenden Veröffentlichungen entstanden.

Publications

The following articles have been published in the course of this thesis.

- P. Soltan-Panahi, J. Struck, P. Hauke, A. Bick, W. Plenkers, G. Meineke, C. Becker, P. Windpassinger, M. Lewenstein and K. Sengstock
  Multi-component quantum gases in spin-dependent hexagonal lattices
  Nature Physics **7**, 434 – 440 (2011)

- J. Struck, C. Ölschläger, R. Le Targat, P. Soltan-Panahi, A. Eckardt, M. Lewenstein, P. Windpassinger and K. Sengstock
  Quantum Simulation of Frustrated Classical Magnetism in Triangular Optical Lattices
  Science **333**, 996 – 999 (2011)

- P. Soltan-Panahi, D.-S. Lühmann, J. Struck, P. Windpassinger and K. Sengstock
  Quantum phase transition to unconventional multi-orbital superfluidity in optical lattices
  Nature Physics **8**, 71 – 75 (2012)

- J. Struck, C. Ölschläger, M. Weinberg, P. Hauke, J. Simonet, A. Eckardt, M. Lewenstein, K. Sengstock and P. Windpassinger
  Tunable Gauge Potential for Neutral and Spinless Particles in Driven Optical Lattices
  Phys. Rev. Lett. **108**, 225304 (2012)

- P. Hauke, O. Tieleman, A. Celi, C. Ölschläger, J. Simonet, J. Struck, M. Weinberg, P. Windpassinger, K. Sengstock, M. Lewenstein and A. Eckardt
  Non-Abelian Gauge Fields and Topological Insulators in Shaken Optical Lattices
  Phys. Rev. Lett. **109**, 145301 (2012)

- J. Struck, M. Weinberg, C. Ölschläger, P. Windpassinger, J. Simonet, K. Sengstock, R. Höppner, P. Hauke, A. Eckardt, M. Lewenstein and L. Mathey
  Engineering Ising-XY spin-models in a triangular lattice using tunable artificial gauge fields
  Nature Physics **9**, 738 – 743 (2013)

Contents

Chapter 1

Introduction

Over the past three decades the field of cold dilute atomic gases has undergone a vast evolution. What started with the development of new trapping and cooling techniques [1–5] for thermal clouds of atoms – rewarded by the noble prize in 1997 for Chu, Phillips and Tannoudji [6–8] – changed into the comprehensive field of quantum many-body physics, bridging the gap between AMO (atomic, molecular, optical) and condensed matter physics. The experimental milestone, opening this era of interdisciplinary research, was without a doubt the condensation of bosonic gases in 1995 [9–11]. This and the first fundamental studies of collective excitations [12, 13], atom lasing [14], coherence properties [15] and vortices [16], lead to the Nobel prize of 2001 for Cornell, Wieman and Ketterle [17, 18]. Subsequent achievement of quantum degeneracy in fermionic vapours [19] and novel manipulation techniques, such as the control over atomic interactions via Feshbach resonances [20, 21], initiated research towards, e.g. the thorough exploration of the continuous BEC (Bose-Einstein condensate) to BCS (Bardeen-Cooper-Schrieffer) crossover and the unitary limit [22, 23].

Current fields of research include ultracold gases with long-range interactions [24–28], ultracold chemistry [29] and the study of the equation of state in Fermi and Bose gases [30–35], to name only a few.

At the beginning of the 1990's, in parallel to the attempts to achieve BEC in dilute gases, several groups started to work on optical lattices [36–39]. Such artificial crystals of light, created by the interference pattern of overlapping laser beams, were used to trap, cool and manipulate thermal atoms. For these, the regime of many body physics was out of reach as densities were to small for any considerable interactions among the atoms. This situation dramatically changed with the availability of quantum gases.

In 2001, Greiner *et al.* [40] measured the transition of a superfluid (SF) to Mott insulating (MI) state of bosons in an optical lattice, following the seminal proposal by Jaksch and Zoller [41]. A quantum phase transition that had been predicted over twenty years ago by Fisher *et al.* [42] in the framework of the Bose-Hubbard model. This marked the step from the weakly-interacting to strongly correlated regime for ultracold bosons and triggered a huge amount of theoretical and experimental interest in, e.g. many-body entanglement [43–45], the realization of the SF to MI transition in reduced dimensions [46–49] and the short range coherence of Mott insulators [50–52]. After the first trapping of fermions in three dimensional lattices and the observation of Fermi surfaces [53], subsequently anti-bunching [54] and the phase transition to a fermionic Mott insulator was measured [55, 56]. Recent developments include, e.g. single-site resolved detection

and manipulation of atoms in lattices with quantum gas microscopes [57–59] and the realization of unconventional superfluids involving excited bands [60–62]. Moreover, a variety of non-cubic lattice geometries has lately been created: honeycomb [63, 64], triangular [65] and kagome lattices [66]. Hence, future perspectives include, e.g. the study of nonlinear Dirac equations [67, 68] and highly frustrated spin-liquid phases [69, 70]. In general, quantum degenerate gases in optical lattices have proven their capabilities to serve as tunable and well controlled quantum simulators for solid state models [71, 72].

One of the most important manipulation techniques for ultracold atoms in optical lattices is the time periodic modulation of either the potential depth or position by control over the intensity or phase of the lattice beams. Amplitude modulation has been widely explored as a probe for the excitation spectrum of the system [46, 73, 74] but can as well be used for, e.g. pump probe experiments [75, 76], algorithmic cooling [77], photon assisted tunneling [78] or probing of nearest-neighbor correlations [79]. In principle, phase modulation can be used for the same purposes [80] but has been especially utilized for coherent band structure engineering, where bands with opposite curvature hybridize due to the strong coupling [81, 82].

Furthermore, lattice potentials can be easily accelerated by phase modulation, creating inertial forces for the atoms in the co-moving reference frame. As shown by Eckardt *et al.* [83] the effect of an oscillating force on a Bose Hubbard model can be captured in a time-averaged picture with renormalized tunneling matrix elements. The renormalization can modify the tunneling parameter in magnitude and sign independently of the lattice depth. Pioneering experimental work on this topic has been performed by the group of Arimondo, including the direct measurement of tunneling suppression with a BEC [84] and the periodically driven SF to MI transition [85]. Driving induced modification of the tunneling for single particle quantum systems has been explored earlier, both theoretically [86–90] and experimentally [91].

As the recurrent theme of this thesis, tunneling renormalization via time periodic lattice driving is utilized to emulate and tune various different model Hamiltonians. In this way, unconventional superfluid phases are created, characterized by exotic properties, e.g. finite quasimomentum, spontaneously broken discrete symmetry, metastability and chiral mass currents.

The two main topics of this thesis are detailed in the following:

Frustrated magnetism in a triangular optical lattice

The simulation of magnetic model Hamiltonians has emerged as one of the driving forces for the quantum gas community [23, 92]. Recently, a variety of magnetic phenomena have been investigated with quantum gases, including superexchange interactions [93–95], Ising phase transitions [96], spin fluctuations [97] and short-range magnetic correlations [98]. Current interest aims at, e.g. the realization of antiferromagnetic order in optical lattices, itinerant ferromagnetism [99–102] and frustrated magnetism [70].

Frustrated spin models are among the most challenging open problems of magnetism and condensed matter. One of the simplest lattices that features geometrical frustration is the triangular lattice with antiferromagnetic nearest-neighbor spin-interactions [103]: The spins cannot minimize the interaction energy pairwise but have to find a compromise that minimizes the total energy of the system (see Fig. 1.1). This is typically accompanied by degenerate ground states and residual low temperature entropy. In

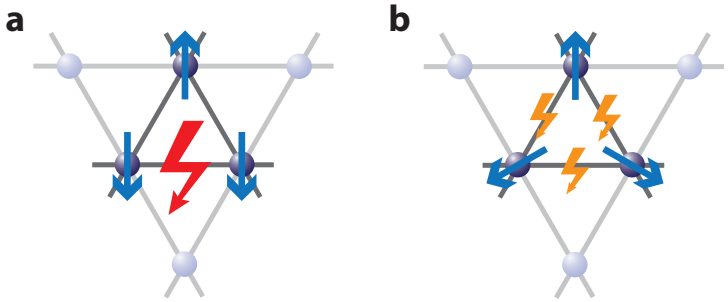

Figure 1.1: Classical spins on the antiferromagnetic triangular lattice. **a** Two pairs of spins are aligned antiparallel, thus minimizing the energy. However, the third spin pair has to align in parallel. This maximizes the spin-spin interactions for the bond. **b** The 120°-configuration is the ground state of the system.

quantum spin-models, frustration can give rise to exotic phases like valence bond states or spin liquids [69, 71, 104]. Classical models are as well strongly influenced by geometrical frustration, resulting in, e.g. macroscopically degenerate ground states [105, 106] and emergent quasiparticles, that behave like deconfined magnetic monopoles [107–110]. The experimental realization and investigation of frustrated phases in solid-state materials is extremely difficult as it is almost impossible to realize pure exchange models. Ground state degeneracies are often lifted by perturbations such as Dzyaloshinskii-Moriya couplings or other spin-orbit interactions. In this context, ultracold atoms in optical lattices offer unique possibilities for the experimental realization of pure spin models without defects and additional interactions.

In this thesis, we report on the experimental realization of a frustrated classical XY model on a two-dimensional triangular lattice. The phases of the local wavefunctions can be identified with classical vector-spins. Spin-spin interactions are mediated by the tunneling matrix elements. Positive values of these elements describe ferromagnetic and negative values antiferromagnetic interactions. Thus, the type of interaction between the spins can be controlled by the periodic driving of the lattice. An important feature of this system is the adjustable anisotropy of the spin-spin interactions, which allows for the realization of several different spin configurations. Furthermore, symmetry breaking has been observed in a part of the phase diagram where two degenerate ground states exist.

Gauge fields for neutral particles

Gauge fields play an important role in the theoretical description of many branches of physics, ranging form the standard model of particle physics to the general theory of relativity. A gauge field is characterized by the type of local gauge transformation that leaves the relevant physical quantities of the system invariant. This concept was first introduced in the context of classical electrodynamics, where electric and magnetic fields can be described by gauge dependent scalar and vector potentials. In recent years the interest to emulate gauge theories with ultracold atoms has significantly raised [71, 111]. In particular, the generation of artificial magnetic fields for neutral atoms is crucial for the quantum simulation of exotic condensed matter phenomena like the integer and fractional quantum hall effect [112–115], the Hofstadter butterfly [116, 117]

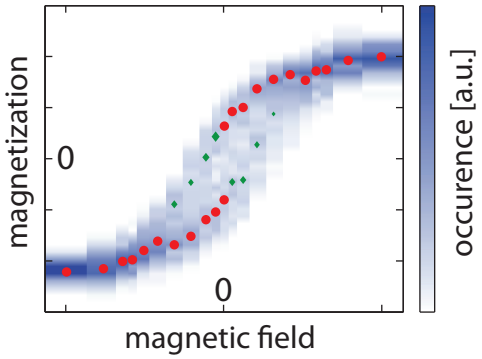

Figure 1.2: Magnetization behavior of a ferromagnetic state in a triangular lattice: Emulated with spinless, neutral bosons exposed to an artificial magnetic field. The plot consist of more than 4000 single experiments. The color code indicates the occurrence of each value of the magnetization. The red circles indicate the global and green diamonds the local maxima of the magnetization. The data curve strongly resembles the hysteresis curve, which is known from the classical Ising model.

or more generally the study of topological insulators [118, 119].

Neutral atoms do not respond to magnetic or electric fields like charged particles do. Therefore one has to engineer the corresponding effects artificially. The first approaches to this problem exploited the similarity of the Coriolis force and Lorentz force by rapidly rotating ultracold gases [120–126]. However, this technique is limited by the centrifugal forces which drag the atoms out of the trap for high rotation frequencies. More recently, several theoretical proposals [127–133] and experiments concentrated on Raman laser based approaches to this issue. In this way, the creation of synthetic vector gauge potentials $\mathbf{A}(\mathbf{r}, t)$ for either bulk systems [134–136] or optical lattices [137, 138] was successfully demonstrated. These schemes rely on the spatially and/or momentum dependent coupling of internal states by the Raman laser beams. Even spin-orbit coupling – belonging to the class of non-abelian gauge potentials – could lately be realized by exploiting spin-dependent Raman process [139, 140] opening the route towards highly interesting phenomena, such as the spin Hall effect [141].

The influence of the potential $\mathbf{A}(\mathbf{r}, t)$ on a charged particle in a lattice is captured within the framework of the Peierls substitution [142, 143]: Tunneling matrix elements acquire a complex phase, called the Peierls phase, which is given by the line integral over $\mathbf{A}(\mathbf{r}, t)$ along a lattice bond. A gauge-invariant quantity is given by the sum of the Peierls phases around an elementary plaquette of the lattice. This quantity corresponds to the magnetic flux through the plaquette. In solid state materials it is notoriously hard to reach the strong-field limit, where the flux strength is on the order of an elementary flux quantum. This has been realized only very recently with homogenous fields in Moiré superlattices of graphene [144–146].

In the context of this thesis a novel universal applicable method for the generation of artificial gauge potentials for neutral atoms has been developed. The required complex valued tunneling matrix elements are engineered via lattice driving, which breaks time-reversal symmetry. This technique represents an easy to implement, tunable and spontaneous-scattering-free alternative for the emulation of synthetic gauge fields compared to Raman coupling schemes. In the triangular lattice, staggered magnetic fluxes in the strong-field limit have been created. The corresponding deformation of the dis-

persion relation was investigated according to the momentum distribution of the atoms. For a flux strength around π the system features an interesting interplay between discrete and continuous degrees of freedom, resembling Ising-like phase transitions and magnetization behavior (see Fig. 1.2).

Structure of the thesis

The chapters two and three provide the basic information on the experimental setup and the theory of periodically driven lattices. Chapters 4, 5 and 6 represent the main results of this work. Chapter 7 introduces an idea for the extension of the lattice driving technique towards non-Abelian gauge potentials. Chapters 4 and 5 can be read independently, while chapters 6 and 7 partly rely on the results of chapter 5.

In the following the content of each chapter is summarized:

Ch. 2 – Ultracold Bosons in Optical Potentials
This chapter briefly explains the experimental setup as well as the concept of optical potentials arising from atom-light interactions. The dipole trap and different kinds of lattice potentials are introduced. Special emphasis is placed on the generation of optical lattices with hexagonal symmetry by a three beam laser configuration. The last part of the chapter is devoted to single-particle and many-body lattice Hamiltonians and the measurement of the momentum distribution of atoms confined in a lattice.

Ch. 3 – Description of Periodically Driven Lattices
A theoretical framework for the treatment of time periodic systems is described. The focus lies on the renormalization of the tunneling matrix elements in a periodically accelerated lattice. We discuss how the momentum distribution of the system is connected to the effective model and experimentally demonstrate the simple case of monochromatic shaking in a one-dimensional lattice.

Ch. 4 – Simulation of a Frustrated XY Model on a Triangular Lattice
This chapter introduces a versatile simulator approach for the classical XY model on a triangular lattice. First, the mapping of the ultracold bosonic gas onto the spin-model is described. Then, a diversity of spin-configurations and phase transitions is introduced together with the corresponding experimental signatures. The measured spin-configurations are compared to the corresponding zero temperature phase diagram. Particular attention is paid on the behavior of phases with degenerate ground states, arising due to the presence of strong frustration. In this context spontaneous symmetry breaking is observed.

Ch. 5 – Tunable Gauge Potentials for Neutral Particles in Driven Lattices
Basic concepts of lattice gauge theory are discussed for the case of classical electrodynamics. Time-asymmetric lattice shaking is introduced as a method for the creation of complex valued tunneling matrix elements, mimicking the presence of a vector gauge potential for neutral particles in an optical lattice. As a proof-of-principle experiment, the emulation of a tunable gauge potential for ultracold bosons in a one-dimensional lattice is demonstrated. The dynamical response of the atoms to changes of the gauge potential is investigated. The last part of this

chapter is devoted to the realization of gauge-independent staggered fluxes in a two-dimensional triangular lattice by means of time-asymmetric lattice shaking.

Ch. 6 – Engineering Ising-XY Spin Models in a Triangular Lattice
A spin-model exhibiting a combined discrete $\mathbb{Z}_2$ (Ising) and continuous $U(1)$ symmetry is engineered in a triangular lattice. Full control over the $\mathbb{Z}_2$ symmetry is obtained by applying strong staggered gauge fluxes to the lattice. We define two distinct order parameters, the magnetization and the coherence, which are connected to the two symmetries of the system. The behavior of those order parameters is studied in dependence of the initial entropy and the gauge flux strength.

Ch. 7 – Towards Spin-Orbit Coupling in Driven Lattices
We discuss a scheme for the realization of a spin-orbit coupled tight-binding lattice system. The atoms are subjected to a spin-dependent periodic forcing, which is realized by an oscillating magnetic field gradient. This results in a spin selective renormalization of the tunneling matrix elements. In consequence, the dispersion relations for two spin states with inverse magnetic moments are shifted in opposite directions. Additional radio frequency coupling between the internal spin states of the atoms leads to a hybridization of the two spin bands. This resembles the effect of spin-orbit coupling.

Chapter 2

Ultracold Bosons in Optical Potentials

This chapter briefly explains the experimental setup as well as the concept of optical potentials arising from atom-light interactions. The dipole trap and different kinds of lattice potentials are introduced. Special emphasis is placed on the generation of optical lattices with hexagonal symmetry by a three beam laser configuration. The last part of the chapter is devoted to single-particle and many-body lattice Hamiltonians and the measurement of the momentum distribution of atoms confined in a lattice.

2.1 Preparing Ensembles of Quantum Degenerate Bosons

The starting point for all experiments described in this thesis is a BEC of ^{87}Rb atoms. This section briefly describes the apparatus and the experimental procedures used to cool the atoms to quantum degeneracy. The apparatus was initially designed and constructed by M. Erhard [147] and H. Schmaljohann [148]. Modifications and further improvements were implemented in the course of the theses of J. Kronjäger, C. Becker and P. Soltan-Panahi [63, 149, 150]. The vacuum system consists of two glass cells, which are connected via a differential pumping stage. In the upper cell, dispensers create a constant background pressure of rubidium atoms. A part of these atoms is captured in a two-dimensional magneto-optical trap (2D-MOT). A nearly resonant pushing beam continuously transfers the precooled atoms from the 2D-MOT through the pumping stage into the second glass cell, where the atoms are recaptured in a 3D-MOT. The pressure in the 3D-MOT cell is 10^{-11}mbar and approximately two orders of magnitude lower than in the 2D-MOT cell. The loading procedure of the MOT usually takes between 12 and 15 seconds, depending on the final atom numbers. In the following step the ensemble is Sisyphus cooled [3–5] in an optical molasses. The atoms are then optically pumped from the F=2 hyperfine manifold into the ground state manifold F=1. Subsequently, the particles are loaded into a 8-Dee magnetic trap [151] and radio frequency induced forced evaporation is performed for 16-22 seconds. At this stage the ensemble is close to the critical temperature but not yet condensed. For the final cooling step the atoms are loaded from the magnetic trap into an optical dipole trap. Further evaporation is performed by slowly lowering the dipole trap power until a BEC with no discernable thermal fraction is produced. The number of the condensed atoms

usually lies between $5 \cdot 10^4$ and $3 \cdot 10^5$. Two different dipole trap setups have been used throughout the experiments presented in this thesis. Both setups will be introduced in section 2.3. The whole experimental cycle, including the production of a BEC and the measurements, lasts typically 40 seconds.

2.2 Atom-Light Interaction

The relevant light matter interactions for the manipulation of ultracold neutral atoms are electric dipole interactions. They arise from the interplay between the induced dipole moment of the atom and the electromagnetic wave. The interaction leads to new eigenstates which are energetically shifted with respect to the uncoupled atomic states [152]. This energy shift is called the AC-Stark shift. It is proportional to the intensity of the light field and allows to trap atoms on length scales determined by the wavelength of the light. For far-off-resonant light, where the scattering rate is small compared to the detuning, the atoms experience an almost purely conservative force. The proper design of the intensity profile of laser beams allows to directly engineer a potential landscape for the atoms. For an extensive review on this topic in the context of optical traps see Ref. [153]. As we will see in section 2.4 the interference pattern of laser beams acts as a periodic potential for atoms.

In order to create strong AC-Stark shifts we mainly couple the $5^2S_{1/2}$ ground state of ^{87}Rb to the $5^2P_{1/2}$ (D_1 line) and $5^2P_{3/2}$ state (D_2 line). The resulting potential for the atoms reads [63, 150, 153]:

$$\begin{aligned} V_{\mathrm{dip}}(\mathbf{r}) = &-\frac{1}{18\epsilon_0\hbar c} \mid \langle L=0||e\mathbf{r}||L^{'}=1\rangle \mid^2 I(\mathbf{r}) \\ &\left\{ \left(\frac{1}{\omega_{\mathrm{D}_1}-\omega}+\frac{1}{\omega_{\mathrm{D}_1}+\omega}\right) + 2\left(\frac{1}{\omega_{\mathrm{D}_2}-\omega}+\frac{1}{\omega_{\mathrm{D}_2}+\omega}\right) \right. \\ &\left. -\mathcal{P}(\mathbf{r}) g_F m_F \left[\left(\frac{1}{\omega_{\mathrm{D}_1}-\omega}+\frac{1}{\omega_{\mathrm{D}_1}+\omega}\right) - \left(\frac{1}{\omega_{\mathrm{D}_2}-\omega}+\frac{1}{\omega_{\mathrm{D}_2}+\omega}\right)\right] \right\}, \end{aligned} \tag{2.1}$$

where ϵ_0 is the absolute permittivity, $\hbar$ the reduced Planck constant, c the speed of light, g_F is the Landé factor of the hyperfine state and m_F is the Zeeman quantum number. The indices D1 and D2 describe the two relevant transition lines which have a wavelength of 780.24nm and 794.98nm. $I(\mathbf{r})$ is the intensity, ω the frequency of the laser and

$$\mathcal{P}(\mathbf{r}) = \frac{I_{\sigma^+}(\mathbf{r}) - I_{\sigma^-}(\mathbf{r})}{I(\mathbf{r})} \tag{2.2}$$

is the polarization of the light field. In the case of π polarized light $\mathcal{P}(\mathbf{r})$ is zero. The value for the reduced dipole matrix element $\mid \langle L=0||e\mathbf{r}||L^{'}=1\rangle \mid$ can be obtained from Ref. [154]. In our case we cannot employ the commonly used rotating wave approximation as the counter-rotating terms are non-negligible. The potential Eq.(2.1) can be split into a spin-independent and a spin-dependent part

$$V_{\mathrm{dip}}(\mathbf{r}) \equiv V_{\mathrm{SI}}(\mathbf{r}) + g_F m_F \mu_{\mathrm{B}} B_{\mathrm{eff}}, \tag{2.3}$$

where we have introduced an effective magnetic field $B_{\mathrm{eff}} = -\alpha V_{\mathrm{SI}}(\mathbf{r})\mathcal{P}(\mathbf{r})/\mu_{\mathrm{B}}$. This field describes the effect of the spin-dependent potential in analogy to the linear Zeeman

effect in a magnetic field. The factor α quantifies the ratio between both parts of the potential. As we can infer from Eq. (2.1) the spin-dependent part vanishes for very large detuning where the difference between the D_1 and the D_2 line is not resolved anymore. For our lattice we use a wavelength of 830nm resulting in $\alpha = 0.13$, while for our dipole trap the wavelength is 1064nm resulting in $\alpha = 0.02$. In section 2.4 we will see how one can engineer light fields which feature a spatially varying polarization resulting in state-dependent lattices.

For convenience in later calculations we introduce the following abbreviated version of the spin-independent potential

$$V_{\mathrm{SI}}(\mathbf{r}) \equiv -\tilde{u}(\omega) I(\mathbf{r}), \tag{2.4}$$

with $\tilde{u}(\omega)$ as a conversion factor for a given wavelength between the intensity and the resulting light shift on the atoms. The conversion factor for our lattice wavelength (830nm) is $\tilde{u}(\omega_{\mathrm{L}}) = 9.38 \cdot 10^{-36}\mathrm{m}^2\mathrm{s}$ and for the dipole trap wavelength (1064nm) $\tilde{u}(\omega_{\mathrm{DT}}) = 2.11 \cdot 10^{-36}\mathrm{m}^2\mathrm{s}$.

2.3 Dipole Trap

The dipole trap serves as a spin-independent for the atoms. Thus, it provides the necessary basis for experiments involving several spin-components which cannot be performed in magnetic traps confining only low field seeking spin states. The intensity profile of a single, radial symmetric gaussian laser beam is given by

$$I(\rho, z) = \frac{2P}{\pi w(z)^2} \exp\left(\frac{-2\rho}{w(z)^2}\right), \tag{2.5}$$

where P is the power of the beam, $w(z) = w_0\sqrt{1 + (z/z_R)^2}$ is the beam waist with minimal waist w_0 and $z_R = \pi w_0^2/\lambda$ is the Rayleigh length. Single beam traps result in very asymmetric trap configurations with a comparably weak confinement along the axial direction of the beam which is determined by the Rayleigh length. In order to create a more symmetric trapping geometry we use a crossed dipole trap consisting of two laser beams which intersect under an angle of 90° in the horizontal plane. The dipole trap setup has been changed in the course of this thesis. Parts of the experiments described in this work have been performed with the *circular* trap and parts with the *elliptical* trap.

2.3.1 *Circular* Crossed Dipole Trap

This dipole trap is formed by two radially symmetric gaussian laser beams, resulting in an intensity profile

$$I(\mathbf{r}) = \frac{2P}{\pi w_0^2} \mathrm{e}^{-2y^2/w_0^2} \left(\mathrm{e}^{-2x^2/w_0^2} + \mathrm{e}^{-2z^2/w_0^2}\right), \tag{2.6}$$

where we neglected the weak confinement along the axial directions of the beams. The y-axis is defined as the vertical axis. The minimal waists of the laser beams are $w_0 \approx 37\mu\mathrm{m}$, resulting in trapping frequencies of approximately $\omega_{\mathrm{Horizontal}} = 2\pi \cdot 88\mathrm{Hz}$ and $\omega_{\mathrm{Vertical}} = 2\pi \cdot 72\mathrm{Hz}$ as the smallest possible values before the atoms fall out of the

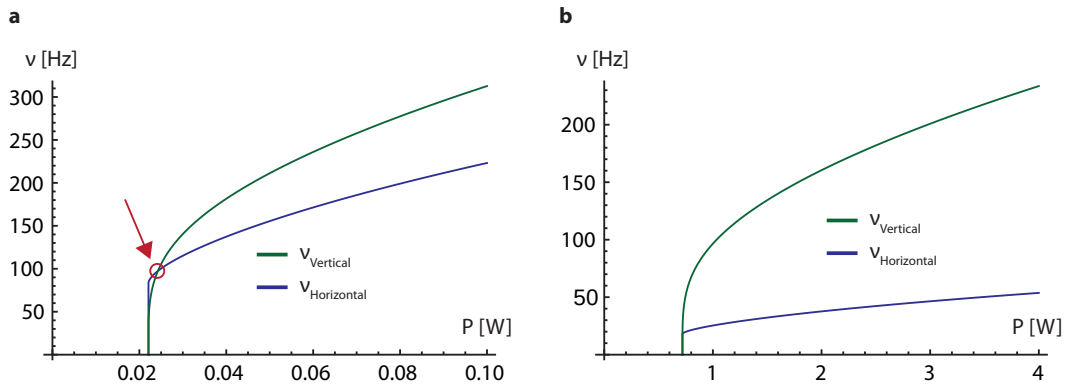

Figure 2.1: Numerically calculated trapping frequencies including the influence of the gravitational sag. **a** Trapping frequencies for the circular dipole trap. The red circle indicates the isotropic point, where the trapping frequencies in all directions are equal ≈ 97Hz. **b** Trapping frequencies for the elliptical dipole trap. Note the difference in the scale of the beam power. The trapping frequency in the horizontal directions are always smaller than the vertical frequency.

trap. It is possible to work at laser powers where the trap is almost perfectly isotropic (see Fig. 2.1) [150]. The shift in vertical direction due to the influence of gravity can be large if the intensity of the laser beams is lowered. The maximal gravitational sag, before the atoms fall out of the trap, is given by the half the waist size ($-w_0/2$). This yields a minimal holding power of

$$P_{\mathrm{Min}} = \frac{\pi}{8\tilde{u}(\omega_{\mathrm{DT}})} m g w_0^3 \mathrm{e}^{1/2} \sim w_0^3. \tag{2.7}$$

The holding power scales as the minimal waist size cubed. Therefore P_{Min} strongly for larger waist sizes. This sets a lower bound on the achievable trapping frequencies for this kind of dipole trap. The calculated trapping frequencies, including the influence of the gravitational sag, are shown in Fig. 2.1a.

2.3.2 *Elliptical* Crossed Dipole Trap

For experiments in optical lattices it is usually desirable to achieve densities corresponding on average to one or two atoms per lattice site. In order to reach these filling factors it is either possible to reduce the total atom number or to lower the harmonic trapping frequencies. With the *circular* setup, where the mean trapping frequencies are on the order of 100Hz, very small atom numbers are required. However, this approach poses two new problems: For small atom numbers the signal to noise ratio is decreased and the lattice size is strongly reduced.

To overcome the aforementioned limitations, a new trap setup with strongly reduced mean trapping frequencies has been implemented at the experiment. This dipole trap is formed by two elliptically shaped gaussian laser beams: The aspect ratio of the beam waist in the vertical direction ($w_{0,\mathrm{v}} \approx 82\mu$m) with respect to the horizontal direction ($w_{0,\mathrm{h}} \approx 245\mu$m) is 1:3. This allows for very low mean trapping frequency at holding powers in the range of 0.5W per beam. In figure 2.1b the numerically calculated trapping frequencies for the elliptical dipole trap are shown. Typical final trapping frequencies after evaporation in the dipole trap are shown in figure 2.2 and amount to $\omega_{\mathrm{Horizontal}} = 2\pi \cdot 19$Hz and $\omega_{\mathrm{Vertical}} = 2\pi \cdot 48$Hz. The discrepancy between the

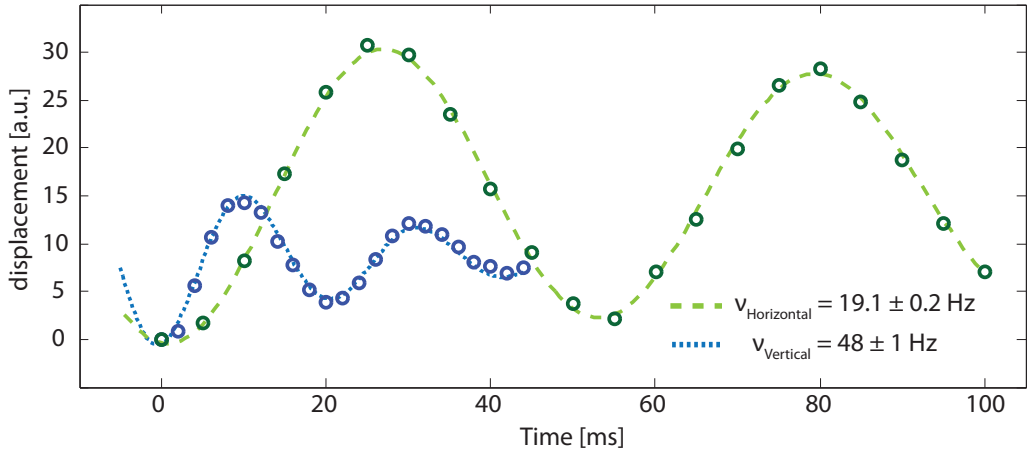

Figure 2.2: Measurement of typical trapping frequencies for the shallow elliptical dipole trap. The power in the dipole trap beams is approximately 550mW, which is below the theoretically expected minimal holding power. The frequencies are determined by measuring the center of mass oscillations of a BEC in the trap. The oscillations are induced by applying a strong magnetic field gradient.

measured and the theoretically expected trapping frequencies probably stems from the systematical errors in the calibration of the beam power due to, e.g. the partial reflectivity of the glass cell. The intensity distribution for the crossed elliptical dipole trap is

$$I(\mathbf{r}) = \frac{2P}{\pi w_{0,\mathrm{h}} w_{0,\mathrm{v}}} \mathrm{e}^{-2y^2/w_{0,\mathrm{v}}^2} \left(\mathrm{e}^{-2x^2/w_{0,\mathrm{h}}^2} + \mathrm{e}^{-2z^2/w_{0,\mathrm{h}}^2} \right). \tag{2.8}$$

The maximal gravitational sag is determined by the waist size in the vertical direction and amounts to $-w_{0,\mathrm{v}}/2$. The minimal holding power against gravity is given by

$$P_{\mathrm{Min}} = \frac{\pi}{8\tilde{u}(\omega_{\mathrm{DT}})} mg \; w_{0,\mathrm{v}}^2 \; w_{0,\mathrm{h}} \; \mathrm{e}^{1/2} \sim w_{0,\mathrm{v}}^2 \; w_{0,\mathrm{h}}. \tag{2.9}$$

This means by choosing a strong confinement along the vertical direction and a weak confinement along the horizontal directions the gravitational sag and the minimal holding power can be reduced. Thus, the trapping frequencies in the horizontal directions can become very small and the atomic densities are reduced.

2.4 Periodic Potentials

2.4.1 Three Beam Lattice Setup

The three beam lattice consist of three interfering, running waves, which pairwise intersect under angle of 120° within the xy-plane (see Fig. 2.3 **a**)[37, 65]. The orientations of the laser beams are characterized by the wave vectors

$$\mathbf{k}_1 = k_{\mathrm{L}} \begin{pmatrix} 0 \\ 1 \\ 0 \end{pmatrix}, \quad \mathbf{k}_2 = \frac{k_{\mathrm{L}}}{2} \begin{pmatrix} \sqrt{3} \\ -1 \\ 0 \end{pmatrix}, \quad \mathbf{k}_3 = \frac{k_{\mathrm{L}}}{2} \begin{pmatrix} -\sqrt{3} \\ -1 \\ 0 \end{pmatrix}, \tag{2.10}$$

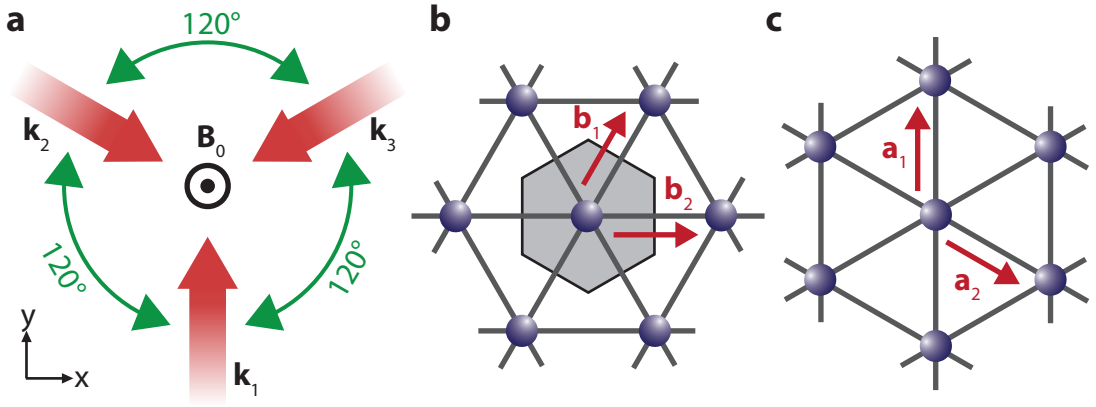

Figure 2.3: Three beam lattice. **a** Three running waves intersect in the xy-plane under an angle of 120° respectively. The quantization axis – a homogenous magnetic field – is oriented perpendicular to the lattice plane. **b** The reciprocal lattice of the three beam lattice has a hexagonal symmetry. Indicated in red are the primitive reciprocal vectors. The first Brillouin zone is highlighted by the grey shaded region. **c** The real space Bravais lattice is as well hexagonal but turned by 90° with respect to the reciprocal lattice. The primitive lattice vectors are shown as the red arrows.

---

with $k_\mathrm{L} = 2\pi/\lambda_\mathrm{L}$ as the wavenumber and $\lambda_\mathrm{L} = 830\mathrm{nm}$ as the lattice laser wavelength. In close vicinity to the waists of the laser beams the electric fields can be approximated by plane waves and the total electric field reads

$$\mathbf{E}_\mathrm{Lat}(\mathbf{r},t) = \mathrm{Re}\left[\tilde{\mathbf{E}}_\mathrm{Lat}(\mathbf{r},t)\right] = E_0\,\mathrm{Re}\left[\sum_{i=1}^{3}\boldsymbol{\varepsilon}_i\ \mathrm{e}^{\mathrm{i}(\mathbf{k}_i\mathbf{r}-\omega_L t+\phi_i)}\right]. \tag{2.11}$$

Here, we assumed an equal, real valued amplitude E_0 for all beams. $\boldsymbol{\varepsilon}_i$ is the polarization vector of the respective laser beam, $\omega_L = ck_\mathrm{L}$ and the ϕ_i's correspond to the phases of each beam. The intensity distribution $I(\mathbf{r},t) = \epsilon_0 c|\tilde{\mathbf{E}}_\mathrm{Lat}(\mathbf{r},t)|^2/2$ is readily obtained by using the complex electric fields.

The reciprocal lattice (see Fig. 2.3 b) is given by the momentum transfer, resulting from the absorption of a photon from one beam and the stimulated emission into another beam. We define the two primitive reciprocal lattice vectors as

$$\mathbf{b}_1 = \mathbf{k}_1 - \mathbf{k}_3 = \frac{b}{2}\begin{pmatrix}1\\\sqrt{3}\\0\end{pmatrix}, \quad \mathbf{b}_2 = \mathbf{k}_2 - \mathbf{k}_3 = b\begin{pmatrix}1\\0\\0\end{pmatrix}, \tag{2.12}$$

with $b = \sqrt{3}k_L$. The primitive lattice vectors of the real space Bravais lattice (see Fig. 2.3 c) can be obtained by using the well-known relation $\mathbf{a}_i \cdot \mathbf{b}_j = 2\pi\delta_{ij}$:

$$\mathbf{a}_1 = d\begin{pmatrix}0\\1\\0\end{pmatrix}, \quad \mathbf{a}_2 = \frac{d}{2}\begin{pmatrix}\sqrt{3}\\-1\\0\end{pmatrix}, \tag{2.13}$$

with $d_\mathrm{2D} = \lambda_\mathrm{L}2/3 = 4\pi/(b\sqrt{3}) \approx 553\mathrm{nm}$ as the lattice constant. Both the Bravais lattice and the reciprocal lattice are of hexagonal shape but rotated by 90° with respect to each other.

The topography of the three beam lattice is insensitive to fluctuations and drifts of the phases ϕ_i, as the lattice is build up by the minimum number of lattice beams: A d-dimensional lattice requires a minimum number of $d+1$ beams [37]. Even though the phases have no influence on the lattice structure, they do have strong influence on the absolute position of the lattice. Fluctuations of the phases directly lead to a randomly moving lattice, which in turn can lead to undesired heating of the atoms confined in the lattice. In order to avoid this heating, the phases of the lattice beams are actively stabilized to a reference value [150]. The phase stabilization can in fact be used to translate and accelerate the lattice in a controlled fashion (see appendix B).

The polarization of the lattice beams $\boldsymbol{\varepsilon}_i$ plays an important role for the final potential experienced by the atoms. A natural basis for the decomposition of the polarization into circular and linear polarized parts is determined by the quantization axis of the atoms. In the experiment, a homogenous magnetic field along the z-axis (see Fig. 2.3) defines the quantization axis. If the polarization vector $\boldsymbol{\varepsilon}_i$ is parallel to the quantization axis the light is purely π-polarized for the atoms. For a polarization vector perpendicular to the quantization axis the laser beam consists in equal parts of σ^+ and σ^- polarized light.

In the z-direction the atoms are only weakly confined by the external harmonic potential, that arises due to the dipole trap and the gaussian profiles of the lattice laser beams. The three beam lattice only generates a periodic potential in the xy-plane, resulting in a periodic array of tubes usually filled with up to hundreds of atoms. To create a three dimensional lattice potential, an additional periodic confinement along the z-direction is needed. For example, a retro-reflected laser beam, which is far detuned with respect to the other beams, can be used to create an independent standing wave. This leads to layers of the three beam lattice potential along the z-direction.

The experimental setup exhibits deviations from the ideal three beam lattice as the beams are not perfectly aligned with an angle of 120°. The angle deviations have been determined in the course of C. Ölschläger's diploma thesis [155] and the most important results are summarized in appendix A. These corrections have minor influence on the results and their interpretation. It will be mentioned where the corrected angle values have been used for the data analysis.

Triangular Lattice

The realization of the triangular lattice requires that the polarization vectors of all three beams are aligned parallel to the quantization axis (see Fig. 2.4)

$$\boldsymbol{\varepsilon}_1 = \boldsymbol{\varepsilon}_2 = \boldsymbol{\varepsilon}_3 = \hat{\mathbf{e}}_\mathrm{z}. \tag{2.14}$$

This results in an optical potential

$$V_\triangle(\mathbf{r}) = -V_0 \left[\frac{3}{4} + \frac{1}{2}(\cos[(\mathbf{b}_1 - \mathbf{b}_2)\mathbf{r} - \phi_2] + \cos[\mathbf{b}_1\mathbf{r} - \phi_3] + \cos[\mathbf{b}_2\mathbf{r} + \phi_2 - \phi_3])\right], \tag{2.15}$$

which is purely spin-independent as the polarization is everywhere π. Here, $V_0 = 4\tilde{u}(\omega_\mathrm{L})I_0$ is the lattice depth with $I_0 = \epsilon_0 c E_0^2/2$ and we have set the phase of the first beam to zero without loss of generality. Figure 2.4 shows the potential of the triangular lattice. The lattice depth is commonly expressed in units of recoil energy $E_\mathrm{rec} = \hbar^2 k_L^2/2m$. The coordination number of the lattice, quantifying the number of

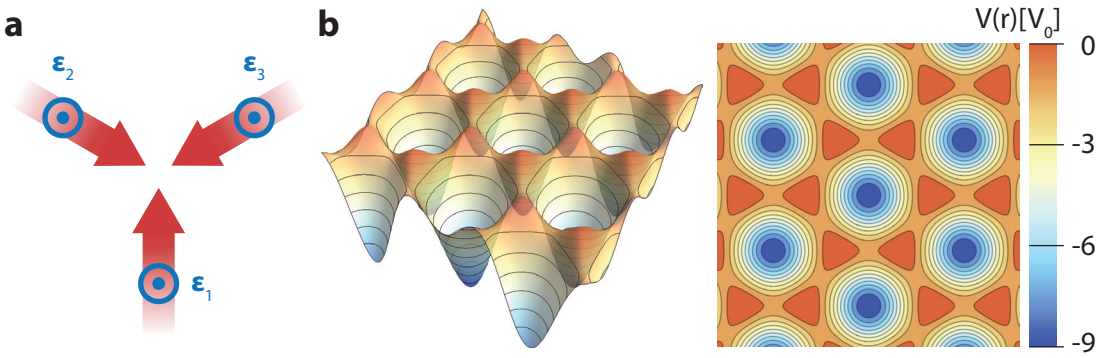

Figure 2.4: Triangular optical lattice. **a** The orientation of the polarization vectors and **b** the resulting optical potential.

the nearest-neighbors, is six. Compared to cubic lattice the confinement in a lattice well is very strong and the tunneling rates decrease much faster with respect to the lattice depth [156].

Spin-Dependent Honeycomb Lattice

For the honeycomb lattice the polarization vectors are aligned parallel to the xy-plane (see Fig. 2.5 a)

$$\varepsilon_1 = \begin{pmatrix} 1 \\ 0 \\ 0 \end{pmatrix}, \quad \varepsilon_2 = \frac{1}{2}\begin{pmatrix} -1 \\ \sqrt{3} \\ 0 \end{pmatrix}, \quad \varepsilon_3 = \frac{1}{2}\begin{pmatrix} -1 \\ -\sqrt{3} \\ 0 \end{pmatrix}. \tag{2.16}$$

In contrast to the triangular lattice, the resulting potential is spin-dependent. This can be seen by decomposing the electric fields into circular polarization components. The quantization axis pointing along $\hat{\mathbf{e}}_z$ defines the basis states for the polarization as $\varepsilon_{\sigma^\pm} = (1, \mp \mathrm{i}, 0)^{\mathrm{T}}/\sqrt{2}$. By recalling expression (2.3) we separate the potential into a spin-independent part and a spin-dependent part. The spin-independent potential has the following form [63]

$$V_{\mathrm{HC}}(\mathbf{r}) = -V_{0,\mathrm{HC}}\left[6 - 2(\cos[(\mathbf{b}_1 - \mathbf{b}_2)\mathbf{r} - \phi_2] + \cos[\mathbf{b}_1\mathbf{r} - \phi_3] + \cos[\mathbf{b}_2\mathbf{r} + \phi_2 - \phi_3])\right], \tag{2.17}$$

resulting in a potential where the minima form a honeycomb lattice. The spin-independent potential is basically the inverted version of the triangular lattice potential, featuring large potential hills in the center of a hexagon (see Fig. 2.5 a). The atoms move along the channels between the potential hills. Compared to the triangular lattice, the actual confinement of the atoms in the wells is very small. This is reflected in the definition of the lattice depth for the honeycomb lattice which is $V_{0,\mathrm{HC}} = V_0/8$.
The light field projected onto the basis defined by the quantization axis is purely σ-polarized and results in the following expression for the polarization (see Eq. (2.2))

$$\mathcal{P}(\mathbf{r}) = \frac{\sqrt{3}\left(\sin[(\mathbf{b}_1 - \mathbf{b}_2)\mathbf{r}] - \sin[\mathbf{b}_1\mathbf{r}] + \sin[\mathbf{b}_2\mathbf{r}]\right)}{3 - \left(\cos[(\mathbf{b}_1 - \mathbf{b}_2)\mathbf{r}] + \cos[\mathbf{b}_1\mathbf{r}] + \cos[\mathbf{b}_2\mathbf{r}]\right)}. \tag{2.18}$$

At the position of the lattice minima the polarization is either σ^+ or σ^-, creating an alternating pattern between neighboring lattice sites (see Fig. 2.5 b). This leads to a

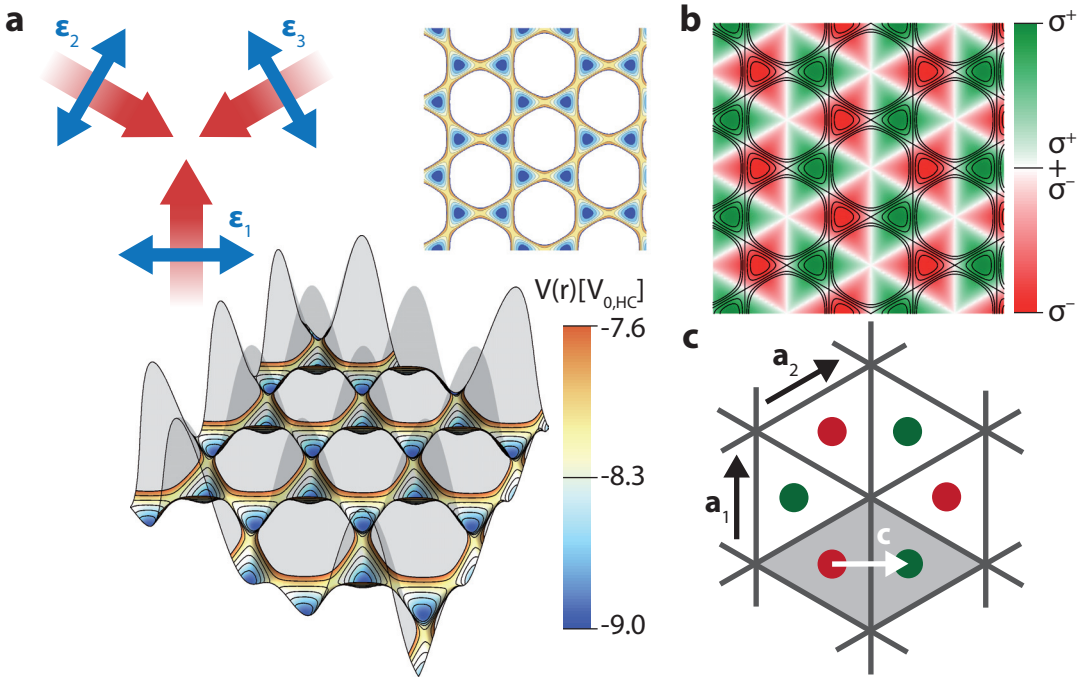

Figure 2.5: Spin-dependent honeycomb lattice. **a** The polarization vectors are aligned parallel to the lattice plane, resulting in a potential where the minima are located on a honeycomb lattice. The spin-independent part of the potential features large potential hills, which are shown grayed out. **b** The polarization structure of the lattice with the contour lines of the spin-independent part of the potential. The polarization alternates between σ^+ and σ^- from one lattice site to the neighboring. **c** The honeycomb lattice consist of a hexagonal Bravais lattice with a two-atomic basis. The color of the basis indicates the different polarizations on the lattice sites. The primitive unit cell is shaded grey.

spin-dependent part of the potential, which lifts the degeneracy between neighboring lattice sites for atoms with non-zero magnetic moment. The effective magnetic field describing the spin-dependent potential (see Eq. (2.3)) is given by [63]

$$\mu_B B_{\text{eff}} = 2\sqrt{3}\,\alpha V_{0,\text{HC}} \left(\sin[(\mathbf{b}_1 - \mathbf{b}_2)\mathbf{r}] - \sin[\mathbf{b}_1\mathbf{r}] + \sin[\mathbf{b}_2\mathbf{r}]\right). \tag{2.19}$$

The honeycomb lattice features two lattice sites per elementary unit cell corresponding to a two-atomic basis in the language of solid state physics. We can define a basis vector (see Fig. 2.5 c)

$$\mathbf{c} = \frac{d}{\sqrt{3}} \begin{pmatrix} 1 \\ 0 \\ 0 \end{pmatrix}, \tag{2.20}$$

which connects the two lattice sites within the same elementary unit cell. The degeneracy of the two-atomic basis is strongly influenced by the spin-dependent potential. Furthermore, the honeycomb lattice is the 2D lattice with smallest possible coordination number, namely three.

In the course of this thesis the first realization of an ultracold quantum gas in a spin-dependent honeycomb lattice has been achieved [157]. In this lattice potential different spin-states experience different lattice geometries and depths. For a spin-component

with vanishing magnetic moment the lattice geometry is a perfect honeycomb structure. In contrast, for spin-components with non-zero magnetic moment the symmetry of the two lattice sites in a unit cell is broken: The atoms predominantly occupy a triangular-shaped sublattice. Thus, a forced antiferromagnetic order can be realized for spins with opposite magnetic moments.

Of particular interest is the rich interplay between the spin-dependent lattice potential and the interactions of different constituents of a multi-component quantum gas. In this way it is possible to study, e.g. mixtures of weakly interacting superfluid and strongly-correlated Mott-insulating spin-components. For a mixture of two spin-components, which occupy different sublattices (antiferromagnetic order), we have observed a tunneling blockade effect in the strongly correlated regime: The tunneling between different sites of a given sublattices is suppressed by the presence of the other spin-component. The repulsive interactions between the components induce a blockade of the tunneling. Thus, the corresponding superfluid to Mott-insulator transition occurs at a much smaller lattice depth than compared to a single-component system.

Interestingly, even in the weakly-interacting regime the interplay of the potential and the inter-component interactions reveals exotic and unexpected phenomena. In a binary spin-mixture we have observed a quantum phase transition from a conventional to a twisted superfluid phase, where the phase of the local order parameter continuously twists between neighboring lattice sites [61].

As an additional feature, these effects can be studied by a novel state- and sublattice resolved microwave spectroscopy. With this technique, information about the band structure as well as the density distribution of the atoms can be obtained.

A detailed presentation and discussion of the above-mentioned experiments and future perspectives can be found in the PhD thesis of P. Soltan-Panahi [63] and is not repeated in this work.

2.4.2 Running Wave 1D Lattice

In order to create a one-dimensional lattice with the full control over the relative phase between the interfering beams, we use two beams of the three beam lattice (see Fig. 2.6a). Thus, the lattice structure as a whole can be moved. The completely spin-independent potential reads

$$V_{\mathrm{RW}}(x) = -\frac{V_0}{2}\left[1+\cos(\mathbf{b}_2\mathbf{r}-\phi_2)\right] = -\frac{V_0}{2}\left[1+\cos(bx-\phi_2)\right], \tag{2.21}$$

where we have set the phase ϕ_3 to zero without loss of generality. The lattice spacing is given by

$$d_{\mathrm{RW}}(\beta) = \frac{2\pi}{b(\beta)} = \frac{\lambda}{2\sin(\beta/2)}. \tag{2.22}$$

The lattice constant has the smallest possible value for $\beta = 180^\circ$ and diverges as $\beta \to 0$. For the case of $\lambda = 830$ and $\beta = 120^\circ$ the value is $d_{\mathrm{RW}}(120^\circ) = 479\mathrm{nm}$ but due to the alignment deviations from the perfect three beam lattice, the lattice constant for the 1D running wave lattice shows a slight deviation from this value (see appendix A). The atoms are only weakly confined in the y- and z-direction effectively forming an array of 2D pancakes along the lattice axis.

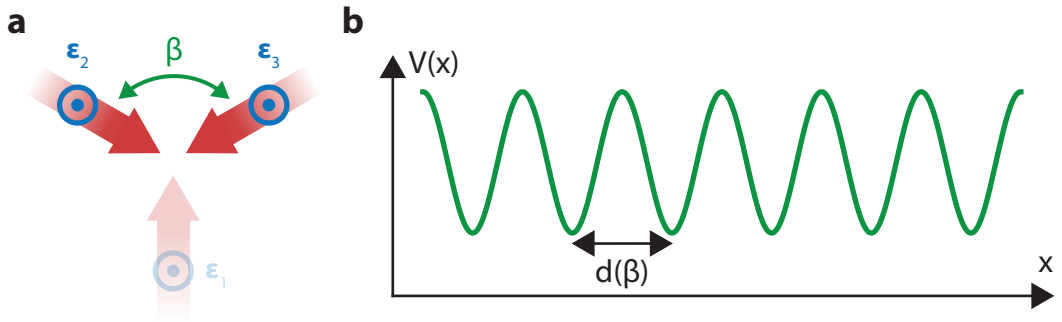

Figure 2.6: Running wave 1D lattice. **a** The 1D lattice is created by using only two beams from three beam lattice. In the ideal case, the angle α between the beams is 120°. The polarization of the beams is parallel to the quantization axis. **b** The resulting lattice potential has a sinusoidal shape and the lattice spacing is given by the angle between the beams.

2.4.3 Non-Interacting Atoms in Optical Lattices

It is a well-known fact that the single particle spectrum for a periodic potential is separated in energy bands by finite band gaps. The eigenstates of the Schrödinger equation for a particle in a spatially periodic potential

$$h_{\mathrm{Lat}}\phi^n_{\mathbf{q}}(\mathbf{r}) = \left[\frac{\hat{\mathbf{p}}^2}{2m} + V_{\mathrm{Lat}}(\mathbf{r})\right]\phi^n_{\mathbf{q}}(\mathbf{r}) = E^n_{\mathbf{q}}\ \phi^n_{\mathbf{q}}(\mathbf{r}), \tag{2.23}$$

are given by Bloch functions $\phi^n_{\mathbf{q}}(\mathbf{r})$ [158, 159], where n is the band index and $\mathbf{q}$ is called the quasimomentum. The energy spectrum and Bloch functions are periodic with respect to the quasimomentum $E^n_{\mathbf{q}} = E^n_{\mathbf{q}+\mathbf{G}}$ and $\phi^n_{\mathbf{q}}(\mathbf{r}) = \phi^n_{\mathbf{q}+\mathbf{G}}(\mathbf{r})$, where $\mathbf{G}$ is a reciprocal lattice vector. A non-interacting atom in an optical lattice obeys the same Schrödinger equation with a minor difference: The additional slowly varying potential due to the gaussian intensity profile of the dipole trap and the lattice beams. This potential is very well approximated with a parabolic (harmonic) potential V_{Harm}. It acts as a perturbation term in the single particle Hamiltonian leading to a weak coupling of the Bloch states and small corrections of the band structure. A particle occupying a single Bloch state is completely delocalized in real space. A complete set of localized states is provided by Wannier functions [160, 161]. Wannier functions are connected to Bloch functions in the following way:

$$w_n(\mathbf{r} - \mathbf{R}_i) = \frac{1}{\sqrt{M}}\sum_{\mathbf{q}} \mathrm{e}^{-\mathrm{i}\mathbf{q}\mathbf{R}_i}\phi^n_{\mathbf{q}}(\mathbf{r}), \tag{2.24}$$

where $w_n(\mathbf{r} - \mathbf{R}_i)$ is the Wannier function of the n-th band localized around the site i with the lattice vector $\mathbf{R}_i$ and the normalization constant M. In the case of a mono-atomic basis this constant corresponds to the number of lattice sites. Wannier functions with different band or lattice site index are orthogonal to each other. From now on we will use the abbreviated notation $w_n(\mathbf{r} - \mathbf{R}_i) \equiv w_{n,i}(\mathbf{r})$. The inverse of the transformation given by Eq. (2.24) allows for the following formal identification: The occupation of single finite quasimomentum Bloch state corresponds to a state where the local wavefunctions acquire a complex phase

$$\varphi_i = \mathbf{q} \cdot \mathbf{R}_i. \tag{2.25}$$

2.4.4 Many-Body Hamiltonian

For the experiments considered in this thesis, the relevant interactions between the ultracold atoms arise from low energy, isotropic, two-particle, s-wave scattering. The interaction potential between two atoms (in the spin states σ and σ') can in this case be modelled by contact interactions $V_{\mathrm{Int}}^{\sigma,\sigma'} = g_{\sigma,\sigma'} \cdot \delta(\mathbf{r}-\mathbf{r}')$ [162], with $g_{\sigma,\sigma'} = 4\pi\hbar^2 a_s^{\sigma,\sigma'}/m$. The s-wave scattering length $a_s^{\sigma,\sigma'}$ completely describes the interactions between the particles, independent from microscopic details of the interatomic potential. However, one should keep in mind that this only works for short-ranged interatomic potentials.

The second quantized many-body Hamiltonian for bosons with contact interactions trapped in an optical lattice V_{Lat} with an additional overall harmonic confinement V_{Harm} is given by

$$\begin{aligned} H(t) = &\sum_{\sigma} \int \mathrm{d}\mathbf{r}\ \hat{\psi}_\sigma^+(\mathbf{r},t) \left[-\frac{\hbar^2}{2m}\nabla^2 + V_{\mathrm{Lat}}(\mathbf{r},t) + V_{\mathrm{Harm}}(\mathbf{r},t) \right] \hat{\psi}_\sigma(\mathbf{r},t) \\ &+ \sum_{\sigma,\sigma'} \frac{g_{\sigma\sigma'}}{2} \int \mathrm{d}\mathbf{r}\ \hat{\psi}_\sigma^+(\mathbf{r},t)\hat{\psi}_{\sigma'}^+(\mathbf{r},t)\hat{\psi}_{\sigma'}(\mathbf{r},t)\hat{\psi}_\sigma(\mathbf{r},t), \end{aligned} \tag{2.26}$$

with the bosonic field operators $\hat{\psi}_\sigma(\mathbf{r},t)$ and $\hat{\psi}_\sigma^+(\mathbf{r},t)$ annihilating and creating a boson at position $\mathbf{r}$. The harmonic confinement approximates the trapping potential of the dipole trap and the slowly varying potential of the lattice laser beams arising from their gaussian intensity profile. The field operators have to fulfill the bosonic commutation relation

$$\left[\hat{\psi}_\sigma(\mathbf{r},t), \hat{\psi}_{\sigma'}^+(\mathbf{r}',t) \right] = \delta_{\sigma\sigma'}\ \delta(\mathbf{r}-\mathbf{r}'). \tag{2.27}$$

Starting from the many-body Hamiltonian (Eq. (2.26)) we will introduce two Hamiltonians: The first one is the Bose-Hubbard Hamiltonian [163] which is particular suited to study strongly correlated physics and the second one being the energy functional for weakly interacting condensates arranged in periodic arrays of pancakes (1D lattice) or tubes (2D lattice). For simplicity we will consider in the rest of this section only single component systems dropping the index σ.

Bose-Hubbard Model

Expanding the bosonic field operators of the many-body Hamiltonian (Eq. (2.26)) in the lowest band[1] Wannier basis

$$\hat{\psi}(\mathbf{r}) = \sum_i \hat{a}_i\ w_i(\mathbf{r}), \tag{2.28}$$

leads to the Bose-Hubbard Hamiltonian first introduced by Gersch and Knollman [163]

$$H_{\mathrm{BH}} = -J \sum_{\langle ij \rangle} \hat{a}_i^+ \hat{a}_j + \frac{U}{2} \sum_i \hat{n}_i(\hat{n}_i - 1) + \sum_i \epsilon_i \hat{n}_i. \tag{2.29}$$

with the annihilation, creation and particle number operators $\hat{a}_i$, $\hat{a}_j^+$ and $\hat{n}_i = \hat{a}_i^+ \hat{a}_i$ respectively for a particle on lattice site i. Angle brackets in the first sum denote that

[1] From now on we will omit the band index as only the lowest band is considered.

the sum extends over all sites i and their respective nearest-neighbors. A quantum degenerate gas of atoms, adiabatically loaded into a deep lattice, usually only occupies the lowest band. The energy scale associated to the temperature of the ensemble is significantly smaller than the energy gap to the next band. Moreover, the single band approximation only holds provided that the interactions are not to strong[2]. The operators $\hat{a}_j^+$ and $\hat{a}_i$ obey the bosonic commutation relation $[\hat{a}_i, \hat{a}_j^+]=\delta_{ij}$.

The first term of the Hamiltonian (2.29) corresponds the kinetic part and describes the tunneling between neighboring lattice sites. The tunneling parameter between site i and j is defined as

$$J_{ij} = -\int \mathrm{d}\mathbf{r}\; w_i(\mathbf{r}) \left[-\frac{\hbar^2}{2m}\nabla^2 + V_{\mathrm{Lat}}(\mathbf{r},t)\right] w_j(\mathbf{r}), \tag{2.30}$$

where in the Bose-Hubbard Hamiltonian only nearest-neighbor tunneling is considered. This tight-binding approximation is fulfilled for sufficiently deep lattices. For conventional optical lattices the tunneling parameter J_{ij} is positive real valued. In Eq. (2.29) we assumed isotropic tunneling in all lattice directions.

The second part of the Hamiltonian describes the interactions between the particles under the assumption that only on-site interactions contribute. This means that interactions between particles, residing on different lattice sites, are neglected. The on-site interaction parameter is defined via the expression

$$U = g \int \mathrm{d}\mathbf{r}\, |w_i(\mathbf{r})|^4 . \tag{2.31}$$

And the last term of the Hamiltonian gives account to the additional parabolic confinement introducing a site-dependent energy offset

$$\epsilon_i = \int \mathrm{d}\mathbf{r} |w_i(\mathbf{r})|^2 V_{\mathrm{Harm}}(\mathbf{r}) \approx V_{\mathrm{Harm}}(\mathbf{R}_i), \tag{2.32}$$

where $V_{\mathrm{Harm}} = m(\omega_{\mathrm{H},x}^2\, x^2 + \omega_{\mathrm{H},y}^2\, y^2 + \omega_{\mathrm{H},z}^2\, z^2)/2$ and $\omega_{\mathrm{H},i}$ is the trapping frequency in direction i.

One should keep in mind that the Wannier functions are single particle functions. In principle, the shape of the localized wavefunctions depends on the finite interactions between the particles. Therefore, the Bose-Hubbard parameters are, strictly speaking, density dependent [165–169].

The $T = 0$ phase diagram of the Bose-Hubbard Hamiltonian was first thoroughly studied by Fisher et al. [42]. They found a quantum phase transition from a delocalized superfluid to localized Mott-insulating (MI) state for commensurate filling factors while increasing the ratio U/J. The extreme cases of the corresponding phases read [170]

$$|\psi_{\mathrm{SF}}\rangle_{\mathbf{q}=0}\,(U=0) \propto \left(\sum_i^M \hat{a}_i^+\right)^N |0\rangle \quad \overset{U/J}{\rightarrow} \quad |\psi_{\mathrm{MI}}\rangle_{n\epsilon\mathbb{Z}}\,(J=0) \propto \prod_i^M \left(\hat{a}_i^+\right)^n |0\rangle\,, \tag{2.33}$$

where N is the total number of atoms, M the number of lattice sites and $n = N/M$ the filling factor. The bosonic vacuum state is denoted by $|0\rangle$. For typical particle numbers

[2]For typical optical lattice experiments, the interactions are not strong enough but the use of, e.g. Feshbach resonances [164] can lead to a break down of this assumption.

in optical lattice experiments, the superfluid state is well approximated by a product of local coherent states with well defined phases and long-range coherence[3]. The $J = 0$ MI phase consist of a product of local Fock states and shows no phase coherence.

Optical lattices are particularly suited to study this quantum phase transition as initially proposed by Jaksch et al. [41] and subsequently demonstrated in the experiment of Greiner et al. [40]. Via the lattice beam intensity, the potential depth of the lattice can be strongly modified. Thus, the ratio U/J can be tuned over many orders of magnitude.

Weakly Interacting Regime in Low-Dimensional Lattices

For one and two dimensional lattices the field operators can be expanded like

$$\hat{\psi}(\mathbf{r}) = \sum_i \; w_i(\mathbf{r}_\parallel) \; \hat{d}_i(\mathbf{r}_\perp), \tag{2.34}$$

where the operator $\hat{d}_i(\mathbf{r}_\perp)$ annihilates a particle in lattice site i at position $\mathbf{r}_\perp$ perpendicular to the lattice. In the following we use the notation $\mathbf{r}_\parallel$ to describe the coordinates along the lattice and $\mathbf{r}_\perp$ as the coordinates perpendicular to the lattice ($\mathbf{r}_\parallel \cdot \mathbf{r}_\perp = 0$). Insertion of the field operators from Eq. (2.34) into the many-body Hamiltonian (Eq. (2.26)) leads to

$$\begin{aligned} H = \int \mathrm{d}\mathbf{r}_\perp \Bigg(& - J \sum_{\langle ij \rangle} \hat{d}_i^+(\mathbf{r}_\perp) \hat{d}_j(\mathbf{r}_\perp) \\ & + \sum_i \hat{d}_i^+(\mathbf{r}_\perp) \left[-\frac{\hbar^2 \nabla_\perp^2}{2m} + V_{\mathrm{Harm}}(\mathbf{r}_\perp) + V_{\mathrm{Harm}}(\mathbf{R}_i) + \frac{\tilde{g}}{2} \hat{d}_i^+(\mathbf{r}_\perp) \hat{d}_i(\mathbf{r}_\perp) \right] \hat{d}_i(\mathbf{r}_\perp) \Bigg), \end{aligned} \tag{2.35}$$

where only on-site interactions and nearest-neighbor tunneling are considered. The discrete position of site i is given by the lattice vector $\mathbf{R}_i$. Tunneling events between neighboring lattice wells are described by the parameter

$$J_{ij} = - \int \mathrm{d}\mathbf{r}_\parallel \; w_i(\mathbf{r}_\parallel) \left[-\frac{\hbar^2}{2m} \nabla_\parallel^2 + V_{\mathrm{Lat}}(\mathbf{r}_\parallel, t) \right] w_j(\mathbf{r}_\parallel), \tag{2.36}$$

and interactions by the renormalized scattering parameter

$$\tilde{g} = g \int \mathrm{d}\mathbf{r}_\parallel \left| w_i(\mathbf{r}_\parallel) \right|^4 . \tag{2.37}$$

For one- and two-dimensional lattices with high filling factors the strongly correlated regime is experimentally out of reach and, at zero temperature, the condensate fraction is large. Therefore, one can replace the creation and annihilation operators $\hat{d}_i(\mathbf{r}_\perp)$ with complex numbers

$$\hat{d}_i(\mathbf{r}_\perp) \to \sqrt{n_i} \; |\chi_i(\mathbf{r}_\perp)| \mathrm{e}^{\mathrm{i}\varphi_i}, \tag{2.38}$$

where the χ_i are normalized interaction broadened wavefunctions with fixed phase φ_i along the non-lattice axes $\mathbf{r}_\perp$. In this approximation, possible phase twists or fluctuations along the tubes are neglected. By integrating out the non-lattice directions $\mathbf{r}_\perp$ we

[3] In three dimensional systems the onset of superfluidity and BEC, i.e. long-range order are linked [171].

arrive at following expression for the energy

$$E(\{\varphi_i, n_i\}) = -J \sum_{\langle ij \rangle} \sqrt{n_i n_j}\ \mathrm{e}^{\mathrm{i}(\varphi_j - \varphi_i)} + \frac{U}{2} \sum_i n_i^2 + \sum_i \epsilon_i n_i, \tag{2.39}$$

where the kinetic energy of the particles along the interaction broadened wavefunctions has been completely neglected (Thomas-Fermi approximation). The on-site interaction parameter is given by

$$U = \tilde{g} \int \mathrm{d}\mathbf{r}_\perp \, |\chi_i(\mathbf{r}_\perp)|^4 \,. \tag{2.40}$$

U is explicitly calculated for 1D and 2D lattices in appendix C. The external harmonic confinement gives rise to a site dependent energy offset

$$\epsilon_i \approx V_{\mathrm{Harm}}(\mathbf{R}_i) + \int \mathrm{d}\mathbf{r}_\perp |\chi_i(\mathbf{r}_\perp)|^2 V_{\mathrm{Harm}}(\mathbf{r}_\perp). \tag{2.41}$$

For our experimental parameters interactions dominate the energy expressed by Eq. (2.39). Therefore, density is directly adapting to the external harmonic confinement independent of the tunneling values J_{ij} and the local phases φ_i. Nevertheless, tunneling can strongly influence the phase configuration φ_i for negative or even complex values of J_{ij} as will be shown in the following chapters. It can be intuitive to recast the kinetic part of expression (2.39) in terms of vector spins $\mathbf{S}_i \equiv \{\cos\varphi_i, \sin\varphi_i, 0\}$. We will use vector spin representations in order to illustrate certain local phase arrangements of superfluid states.

2.4.5 Momentum Distribution: Time-of-Flight Measurement

The most common observable extracted from ultracold gas experiments is related to the in trap momentum distribution of the ensemble of atoms. For an optical lattice, this observable is given by [23]

$$\tilde{n}(\mathbf{k}) = \tilde{\psi}^+(\mathbf{k})\tilde{\psi}(\mathbf{k}) = |\tilde{w}(\mathbf{k})|^2 \sum_{i,j} \mathrm{e}^{\mathbf{i}\mathbf{k}(\mathbf{R_i}-\mathbf{R_j})} a_i^+ a_j, \tag{2.42}$$

where we have introduced the Fourier transform of the field operator

$$\tilde{\psi}(\mathbf{k}) = \left(\frac{1}{2\pi}\right)^{3/2} \int \mathrm{d}\mathbf{r}\ \mathrm{e}^{\mathbf{i}\mathbf{k}\mathbf{r}} \hat{\psi}(\mathbf{r}), \tag{2.43}$$

and the Fourier transform of the Wannier function

$$\tilde{w}(\mathbf{k}) = \left(\frac{1}{2\pi}\right)^{3/2} \int \mathrm{d}\mathbf{r}\ \mathrm{e}^{\mathbf{i}\mathbf{k}\mathbf{r}} w(\mathbf{r}). \tag{2.44}$$

With the momentum distribution it is possible to obtain information about the first order correlation function $\langle a_i^+ a_j \rangle$ of the respective state in the lattice. The extension of $\langle \tilde{n}(\mathbf{k}) \rangle$ in the reciprocal space is determined by the width of $|\tilde{w}(\mathbf{k})|^2$. The Fourier transformed Wannier function grows if the real space Wannier function shrinks, which usually happens if the lattice depth is increased. However, one should keep in mind, that the coherence properties and therefore the first order correlation function are also altered when changing the lattice depth. For a MI state (Eq. (2.33)), the non diagonal

elements of the first order correlation function rapidly decay, resulting in an almost featureless momentum distribution. For increasing correlation length the non-diagonal elements of $\langle a_i^+ a_j \rangle$ start to contribute and the momentum distribution develops a peak structure. In a superfluid state with local phases φ_i (see Eq. (2.25)) the correlation function reads $\langle a_i^+ a_j \rangle = \sqrt{n_i n_j}\exp[\mathrm{i}(\varphi_j - \varphi_i)]$ and the momentum distribution features narrow peaks centered at quasimomentum $\mathbf{q}$.

It has been controversially debated wether sharp momentum peaks are a clear signature for a finite superfluid fraction or already states without long-range order, e.g. a normal fluid can posses narrow momentum structures [51, 172–177]. A recent thorough comparison of experiment and quantum-monte carlo simulations has shown that the identification of the superfluid to normal fluid transition according to the measured momentum distribution is possible [178], even tough one has to be careful as broad momentum peaks can arise in a pure normal fluid or Mott-insulating state [51, 173, 177].

The standard way of measuring the momentum distribution is based on a sudden release of the atomic ensemble by abruptly switching off all confining potentials. The cloud of atoms expands, while falling under the influence of gravity, according to the in-trap momentum distribution. After a certain *time-of-flight* (TOF) t_{TOF}, a resonant imaging beam illuminates the atomic cloud. Due to the scattering of the light by the atoms the beam gets attenuated and a shadow image of the density distribution can be cast on a CCD camera. The density distribution after TOF approximately corresponds to the in-trap momentum distribution [23]

$$\langle \hat{n}(\mathbf{r}) \rangle_{\mathrm{TOF}} \approx \left(\frac{m}{\hbar t_{\mathrm{TOF}}} \right)^3 \langle \tilde{n}(\mathbf{k}) \rangle_{\mathrm{Trap}} \,, \tag{2.45}$$

with the coordinate relation $\mathbf{r} = \hbar \mathbf{k} t_{\mathrm{TOF}}/m$ between real and momentum space. The shadow image on the CCD camera reflects the column integrated density profile

$$\hat{n}(x,y)_{\perp} = \int \mathrm{d}z \; \hat{n}(\mathbf{r})_{\mathrm{TOF}}, \tag{2.46}$$

where the z-axes is parallel to the absorption beam. Repetition of the same experiment and subsequent averaging of the obtained images leads to the expectation value $\langle \hat{n}(x,y)_{\perp} \rangle$.

The main deviation between the momentum distribution and the density distribution – neglected in Eq. (2.45) – arises from the finite TOF realized in the experiment. For a finite amount of t_{TOF} one has to consider the in-trap size of the atomic cloud. As shown by Gerbier et al. [176], this problem is analogous to Fresnel-diffraction occurring in the near-field regime. As a result of the near-field diffraction, sharp momentum peaks are broadened in the density distribution after TOF. A characteristic timescale t_{FF} to reach the far-field regime is given by [176]

$$t_{\mathrm{FF}} \approx \frac{m l_{\mathrm{c}} R_0}{\hbar}, \tag{2.47}$$

where l_{c} is the coherence length of the state in the lattice and R_0 the radius of the cloud. Assuming a coherent superfluid state we obtain for our parameters ($l_{\mathrm{c}} \approx R_0 \approx 15\mu$m) a value $t_{\mathrm{FF}} \approx 300$ms which is 10 times longer then the TOF's used in our experiments. We thus expect that the width of the momentum peaks obtained for a superfluid state is strongly dominated by the finite extend of the cloud in the trap.

Chapter 3

Description of Periodically Driven Lattices

A theoretical framework for the treatment of time periodic systems is described. The focus lies on the renormalization of the tunneling matrix elements in a periodically accelerated lattice. We discuss how the momentum distribution of the system is connected to the effective model and experimentally demonstrate the simple case of monochromatic shaking in a one-dimensional lattice.

In recent years, the time-periodic driving of quantum gases in optical lattices has developed into a reliable technique for the coherent manipulation of the motional degrees of freedom [81, 83, 179–181]. Far-off-resonant driving – compared to the band gap, the kinetic and the interaction energy scales – has been used as a highly versatile method for the engineering of tunneling matrix elements. This was demonstrated for weakly interacting BECs in optical lattices in the Arimondo group [84, 182] and has been extended into the strongly correlated regime [78, 85, 94]. Throughout this thesis, periodic driving is systematically utilized to manipulate the tunneling between adjacent lattice sites.

In this chapter, we describe how to realize the driving force for the atoms in a lattice and introduce the basic theory for the description of time-periodic Hamiltonians. Furthermore, it is explained under which constraints the system can be described by an effective time-averaged Hamiltonian and how this gives rise to renormalized tunneling matrix elements in the effective description of the driven Bose-Hubbard Hamiltonian.

3.1 Inertial Forces Induced by Lattice Acceleration

This section describes a convenient method for the generation of a spatially homogeneous, time-dependent force across an optical lattice. This is the prerequisite for the majority of experiments presented in this thesis. A simple way to create inertial forces in the co-moving reference frame is to accelerate an optical lattice. In our case, we shift the lattice potential via the control over the phases of the lattice beams. We consider the corresponding single-particle Hamiltonian in the reference frame of the laboratory

$$h_{\mathrm{Lab}} = \frac{\hat{\mathbf{p}}^2}{2m} + V_{\mathrm{Lat}}(\mathbf{r} - \mathbf{R}_0(t)) + V_{\mathrm{Harm}}(\mathbf{r}), \tag{3.1}$$

where V_{Lat} is the lattice potential, $V_{\mathrm{Harm}}(\mathbf{r})$ an overall harmonic confinement and the function $\mathbf{R}_0(t)$ describes the trajectory of the moving lattice. As shown in Refs. [181, 183] the unitary operator $U_{\mathrm{T}} = U_3U_2U_1$ transforms the Hamiltonian h_{Lab} into the lattice frame,

$$\begin{aligned} h_{\mathrm{LF}} &= U_{\mathrm{T}} h_{\mathrm{Lab}} U_{\mathrm{T}}^{+} - \mathrm{i}\hbar U_{\mathrm{T}} \frac{\partial U_{\mathrm{T}}^{+}}{\partial t} \\ &= \frac{\hat{\mathbf{p}}^2}{2m} + V_{\mathrm{Lat}}(\mathbf{r}) - \mathbf{F}(t)\mathbf{r} + V_{\mathrm{Harm}}(\mathbf{r} + \mathbf{R}_0(t)), \end{aligned} \tag{3.2}$$

with the inertial force $\mathbf{F}(t) = -m\ddot{\mathbf{R}}_0(t)$, the translation operator

$$U_1 = \exp\left(\frac{\mathrm{i}}{\hbar}\mathbf{R}_0(t)\hat{\mathbf{p}}\right), \tag{3.3}$$

the momentum shift operator

$$U_2 = \exp\left(-\frac{\mathrm{i}}{\hbar}m\dot{\mathbf{R}}_0(t)\mathbf{r}\right), \tag{3.4}$$

and an operator

$$U_3 = \exp\left(-\frac{\mathrm{i}}{\hbar}\frac{m}{2}\int_0^t \mathrm{d}t'\,\dot{\mathbf{R}}_0(t')^2\right), \tag{3.5}$$

that removes the kinetic energy term $m\dot{\mathbf{R}}_0(t)^2/2$ from the Hamiltonian.

In the following, we always assume time-periodic forces $F(t+T) = F(t)$ that exhibit a zero time-average $\langle F(t)\rangle_T = 0$. Here, we have introduced the notation $\langle\cdots\rangle_T = \frac{1}{T}\int_0^T \cdots \mathrm{d}t$ for the time-average. The expression for the corresponding momentum shift of the atoms is

$$\Delta\mathbf{p}(t) = \int_{-\infty}^{t} \mathrm{d}t'\mathbf{F}(t'), \tag{3.6}$$

which can be simplified under the assumption that the lattice was at rest prior to the acceleration ($\dot{\mathbf{R}}_0(t \to -\infty) = 0$),

$$\Delta\mathbf{p}(t) = \int_{t_0}^{t} \mathrm{d}t'\mathbf{F}(t') - \left\langle \int_{t_0}^{t} \mathrm{d}t'\mathbf{F}(t') \right\rangle_T = -m\dot{\mathbf{R}}_0(t). \tag{3.7}$$

Note that expression (3.7) is invariant under changes of the initial time t_0. Furthermore, the trajectory is time-periodic[1] ($\mathbf{R}_0(t) = \mathbf{R}_0(t+T)$) and the time-average of the momentum shift vanishes ($\langle\Delta\mathbf{p}\rangle_T = 0$).

In the lattice frame, the harmonic trapping potential is time-dependent, giving rise to a time-dependent restoring force. The harmonic potential can be decomposed into three terms,

$$V_{\mathrm{Harm}}(\mathbf{r} + \mathbf{R}_0(t)) = \sum_{i=1}^{3}\Bigg(\underbrace{\frac{1}{2}m\omega_{\mathrm{H},i}^2 r_i^2}_{V_{\mathrm{Harm}}^i(r_i)} + \underbrace{m\omega_{\mathrm{H},i}^2 r_i R_{0,i}(t)}_{F_{\mathrm{H}}^i(t)r_i} + \frac{1}{2}m\omega_{\mathrm{H},i}^2 R_{0,i}^2(t)\Bigg), \tag{3.8}$$

where $\omega_{\mathrm{H},i}$ is the harmonic trapping frequency along the axis i, r_i the respective coordinate and $F_{\mathrm{H}}^i(t) = m\omega_{\mathrm{H},i}^2 R_{0,i}(t)$ the restoring force of the harmonic trap. The last term

[1] For a finite initial velocity the trajectory is not time-periodic even though the forcing function is.

of Eq. (3.8) only represents a time-dependent global energy offset in the Hamiltonian and will be omitted in the following. An estimate for the influence of the restoring force can be given in comparison to the inertial force,

$$\frac{F^i_{\mathrm{H}}(t)}{F^i(t)} = \frac{\omega^2_{\mathrm{H},i} R_{0,i}(t)}{\ddot{R}_{0,i}(t)} \overset{\text{Amplitudes}}{\propto} \frac{\omega^2_{\mathrm{H},i}}{\Omega^2}, \tag{3.9}$$

where we employed a Fourier expansion of $R_{0,i}(t) = R_{0,i}(t+T)$ in harmonics of $\Omega{=}2\pi/T$, in order to determine the scaling of the amplitude of $\ddot{R}_{0,i}(t)$. In the experiments presented in this thesis the shaking frequency Ω is at least ten times larger than the harmonic trapping frequencies, resulting in $\omega^2_{\mathrm{H},i} \ll \Omega^2$. In this limit we can neglect the effect of the restoring force and approximate the lattice frame Hamiltonian by

$$h_{\mathrm{LF}} \approx \frac{\hat{\mathbf{p}}^2}{2m} + V_{\mathrm{Lat}}(\mathbf{r}) - \mathbf{F}(t)\mathbf{r} + V_{\mathrm{Harm}}(\mathbf{r}). \tag{3.10}$$

This approximation only holds provided that the time-average of the momentum shift vanishes $\langle \Delta\mathbf{p}(t)\rangle_T = 0$. Otherwise the restoring force increases with time until it is not negligible anymore.

As interactions between the particles are not modified by the transformation into the lattice frame, it is straightforward to write down the corresponding many-body Hamilton operator in second quantization. Expansion of the field operators in Wannier functions finally leads to a Bose-Hubbard Hamiltonian with an additional driving term.

3.2 Intuitive Picture of the Tunneling Renormalization

In this section, we introduce the concept of tunneling matrix renormalization via periodic lattice forcing in a semiclassical single-particle model. This approach is not rigourous and does not describe the conditions imposed on the forcing of the lattice, but it gives an intuitive picture of the underlying physics. The single particle Hamiltonian of the system is given by the lattice Hamiltonian introduced in Eq. (2.23) with an additional term describing the influence of an external force

$$h(x,t) = h_{\mathrm{Lat}}(x) - F(t)x. \tag{3.11}$$

As already discussed, eigenstates of $h_{\mathrm{Lat}}(x)$ are Bloch functions with well defined quasimomentum q. In the presence of an external force (Eq. (3.11)) the solutions to the Schrödinger equation are Houston states [184, 185] with a time-dependent quasimomentum $q_k(t)$. For the sake of simplicity, we restrict the system to one dimension, but the calculation can easily be extended to higher dimensions. In the semiclassical approximation the quasimomentum of the state changes according to the equation [158, 159]

$$\hbar \frac{\mathrm{d}}{\mathrm{d}t} q_k(t) = F(t). \tag{3.12}$$

Let us first consider the case of a monochromatic forcing function

$$F(t){=}F_0 \sin(\Omega t), \tag{3.13}$$

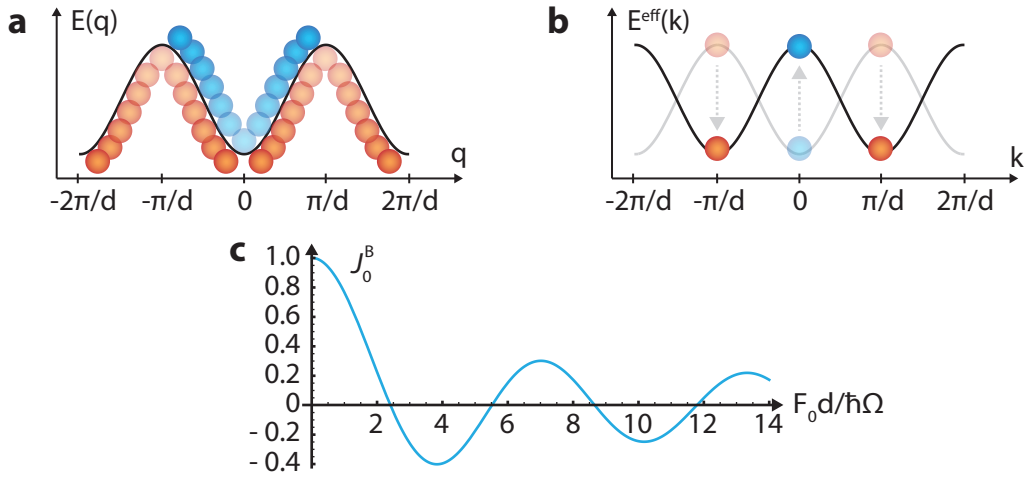

Figure 3.1: Tunnel matrix renormalization for monochromatic forcing. **a** Time-dependent momentum shift of the particle in the reciprocal space. The blue circles indicate oscillations around $q = 0$ and the red circles indicate oscillations at the edges of the Brillouin zone at $q = \pm\pi/d$. **b** Effective dispersion relation experienced by the particles with different k-oscillations. The time-averaged energy is lowered for particles oscillating around $q = \pm\pi/d$ (red circles) while it is increased for particles oscillating around $q = 0$ (blue circles). The black line shows the effective dispersion relation, which arises from averaging around each k-value in the first Brillouin zone. **c** Renormalization of the tunneling matrix elements. The effective tunneling parameter, depending on the amplitude of the forcing (F_0), follows a zeroth order Bessel function of the first kind. For negative values, the dispersion relation is inverted, as shown in **b**.

resulting in a time-dependent shift of the quasimomentum

$$q_k(t) = k - F_0 \cos(\Omega t)/(\hbar\Omega). \tag{3.14}$$

We can insert this expression into the tight-binding dispersion relation of the lowest band given by

$$E(q_k(t)) = -2J \cos(dq_k(t)), \tag{3.15}$$

where the energy varies due to the motion of the particle in the reciprocal space (see Fig. 3.1). In the so called high frequency limit, when $\hbar\Omega$ ($\Omega = 2\pi/T$) is large compared to the energy scales of the system (in this case large against the tunneling element) one can approximate the energy of the oscillating particle with its time-average over one cycle

$$E^{\text{eff}}(k) = \langle E(q_k(t))\rangle_T = -2J^{\text{eff}} \cos(dk) \quad \text{with} \quad J^{\text{eff}} = J \cdot J_0^{\text{B}}(F_0 d/\hbar\Omega). \tag{3.16}$$

Here, J_0^{B} denotes the zeroth order Bessel function of the first kind (see Fig. 3.1). The effective dispersion relation has the same shape as the unforced one but shows a renormalized width of $|J^{\text{eff}}|$. As the Bessel function can become negative, the sign of the tunneling matrix element can be inverted by the shaking. Adjusting the magnitude of the forcing amplitude F_0 allows to tune the tunneling matrix element according to the Bessel function.

More generally, it can be shown that for any time-periodic force, with zero time-average, the effective band structure can be expressed as

$$E^{\text{eff}}(k) = -2|J|^{\text{eff}} \cos(dk - \theta). \tag{3.17}$$

Hence, indicating that it is possible to induce a continuous shift of the dispersion relation given by θ/d. This resembles the effect of a complex valued tunneling matrix element. The general expression for J^{eff} and θ read

$$|J|^{\text{eff}} = J\sqrt{\langle \sin\left[d\Delta p(t)\right]\rangle_T^2 + \langle \cos\left[d\Delta p(t)\right]\rangle_T^2}\,, \tag{3.18}$$

$$\tan(\theta) = \frac{\langle \sin\left[d\Delta p(t)\right]\rangle_T}{\langle \cos\left[d\Delta p(t)\right]\rangle_T}, \tag{3.19}$$

where $\Delta p(t)$ is the momentum shift of the atoms, which can be obtained by formal integration of Eq. (3.12)

$$q_k(t) = k - \frac{1}{\hbar}\int_{-\infty}^{t} \mathrm{d}t' F(t') = k - \frac{1}{\hbar}\Delta p(t). \tag{3.20}$$

The challenge is to find an appropriate forcing function that renormalizes the tunneling matrix elements in the desired way.

3.3 Floquet Theory

This section reviews the basic concepts of Floquet theory, which provides an appropriate theoretical framework for the full quantum-mechanical treatment of the periodically driven many-body system. As the main advantage, this approach results in a time-independent eigenvalue problem, which bears strong resemblance to the stationary Schrödinger equation. This simplification of the time-periodic problem comes at the expense of an infinitely extended, periodic Hilbert space.

In particular, Floquet theory allows for a rigorous derivation of the tunneling renormalization, going beyond the semiclassical single-particle treatment of the last section. For comprehensive reviews on Floquet theory the reader is referred to the Refs. [186, 187]. Assuming a Schrödinger equation

$$\mathrm{i}\hbar\frac{\partial}{\partial t}\left|\psi(t)\right\rangle = H(t)\left|\psi(t)\right\rangle, \tag{3.21}$$

with a time-periodic Hamiltonian ($H(t)$=$H(t+T)$), one can use Floquet's theorem [188, 189] to prove the existence of solutions for Eq. (3.21) that have the form

$$\left|\psi_\alpha(t)\right\rangle = \mathrm{e}^{-\mathrm{i}\varepsilon_\alpha t/\hbar}\left|\phi_\alpha(t)\right\rangle. \tag{3.22}$$

These solutions are called Floquet-states. They are analogous to the well-known Bloch-states arising for spatially periodic Hamiltonians[2]. ε_α is the quasienergy of the system and the $|\phi_\alpha(t)\rangle$ are called Floquet modes. They are time-periodic $|\phi_\alpha(t)\rangle = |\phi_\alpha(t+T)\rangle$. Inserting Eq. (3.22) into Eq. (3.21) results in an eigenvalue problem for the Floquet modes [190]

$$H_{\mathcal{F}}\left|\phi_\alpha(t)\right\rangle = \varepsilon_\alpha\left|\phi_\alpha(t)\right\rangle, \tag{3.23}$$

with the Floquet Hamiltonian $H_{\mathcal{F}} = H(t) - \mathrm{i}\hbar\frac{\partial}{\partial t}$. This equation is similar to the stationary Schrödinger equation and we will see in the following that they share many properties.

[2]Actually the Floquet-Theorem can be applied to any kind of linear periodic differential equation. Therefore, the same kind of states appear for spatially periodic Hamiltonians.

If one obtains a single solution for Eq. (3.23), it is possible to construct infinitely many new solutions by adding a phase term

$$|\phi_{\alpha'}(t)\rangle = \exp(\mathrm{i}n\Omega t)\,|\phi_\alpha(t)\rangle = |\phi_{\alpha n}(t)\rangle\,, \tag{3.24}$$

where $\Omega = 2\pi/T$. Due to the constraint that the Floquet modes are time-periodic, n needs to be an integer number. This results in a periodic energy spectrum for the quasienergies with Floquet bands separated by $\hbar\Omega$,

$$\varepsilon_{\alpha n} = \varepsilon_\alpha + n\hbar\Omega. \tag{3.25}$$

The quasienergies can be projected into a first Brillouin zone which is defined by $\varepsilon \,\epsilon\, [-\hbar\Omega/2, \hbar\Omega/2]$. The name Brillouin zone stems from the similarity of the quasienergy spectrum to the periodicity of the quasimomenta in a spatially periodic solid. This redundancy of the Floquet modes is removed in the Floquet states, being the solutions to Eq. (3.21)

$$|\psi_{\alpha n}(t)\rangle = \exp(-\mathrm{i}\varepsilon_{\alpha n}t/\hbar)\,|\phi_{\alpha n}(t)\rangle = \exp(-\mathrm{i}\varepsilon_\alpha t/\hbar)\,|\phi_\alpha(t)\rangle = |\psi_\alpha(t)\rangle\,. \tag{3.26}$$

Using Eq. (3.23), it is convenient to work in a composite Hilbert space $\mathcal{H}\otimes\mathcal{H}_T$, where $\mathcal{H}$ is the Hilbert space of the states from Eq. (3.21) and $\mathcal{H}_T$ the Hilbert space of T-periodic complex functions. The Floquet modes belong to this Hilbert space. A scalar product for this composite space fulfilling the conditions for an inner product of a Hilbert space can be defined as [190]

$$\langle\langle\varphi(t)|\gamma(t)\rangle\rangle_T = \frac{1}{T}\int_0^T \mathrm{d}t\,\langle\varphi(t)|\gamma(t)\rangle\,. \tag{3.27}$$

The Floquet Hamiltonian $H_\mathcal{F}$ is a hermitian operator in the composite Hilbert space [190], meaning that

$$\langle\langle\varphi(t)|H_\mathcal{F}|\gamma(t)\rangle\rangle_T = \langle\langle\gamma(t)|H_\mathcal{F}|\varphi(t)\rangle\rangle_T^*\,, \tag{3.28}$$

for any states $|\gamma\rangle\,, |\varphi\rangle$ from $\mathcal{H}\otimes\mathcal{H}_T$. Thus, Floquet modes with different quasienergies are orthogonal to each other

$$\langle\langle\phi_{\alpha n}(t)|\phi_{\beta m}(t)\rangle\rangle_T = \delta_{\alpha\beta}\delta_{nm}. \tag{3.29}$$

Here, we assumed an appropriate normalization of the Floquet modes. The Floquet modes form a complete set of basis states in the composite Hilbert space

$$\sum_{\alpha,n} |\phi_{\alpha n}(t)\rangle\,\langle\phi_{\alpha n}(t')| = \mathbb{1}_\mathcal{H}\otimes\delta(\{t-t'\}\mathrm{mod}\,T), \tag{3.30}$$

which, by using Eq. (3.24), reduces to a complete set in $\mathcal{H}$ for $t = t'\mathrm{mod}(T)$

$$\sum_{\alpha} |\phi_\alpha(t)\rangle\,\langle\phi_\alpha(t')| = \mathbb{1}_\mathcal{H}. \tag{3.31}$$

Therefore it is possible to expand non-time-periodic states in terms of Floquet states.

The instantaneous energy of a Floquet-state is not constant and will rapidly change on a timescale given by T. However, the time-averaged energy $\overline{E}_\alpha$ is directly related to the quasienergy of the state [191]

$$\overline{E}_\alpha = \langle\langle \psi_\alpha(t)|H(t)|\psi_\alpha(t)\rangle\rangle_T = \varepsilon_\alpha + \mathrm{i}\hbar \left\langle \left\langle \phi_\alpha(t) \left| \frac{\partial}{\partial t} \right| \phi_\alpha(t) \right\rangle \right\rangle_T . \tag{3.32}$$

A Fourier expansion of the Floquet modes into the basis

$$|n, k(t)\rangle = |n\rangle \exp(\mathrm{i}k\Omega t), \tag{3.33}$$

where the $|n\rangle$ form an arbitrary stationary basis in the Hilbert space $\mathcal{H}$ and k is an integer number, leads to the following expression for the time-averaged energy [191]

$$\overline{E}_\alpha = \varepsilon_\alpha + \hbar\Omega \sum_{n,k} |c_{nk}|^2 k = \varepsilon_\alpha + \hbar\Omega \sum_k |c_k|^2 k. \tag{3.34}$$

The series coefficients are defined as $c_{nk} = \langle\langle n, k(t)|\phi_\alpha(t)\rangle\rangle_T$. In the last step of Eq. (3.34) we used the relation

$$\sum_n |c_{nk}|^2 = \frac{1}{T^2} \int_0^T \mathrm{d}t \; \mathrm{d}t' \, \langle \phi_\alpha(t')|\phi_\alpha(t)\rangle \, \mathrm{e}^{\mathrm{i}k\Omega(t-t')} = |c_k|^2. \tag{3.35}$$

Therefore, a Floquet state has a time-averaged energy, which is determined by its quasienergy and the occupation of the Floquet bands.

3.4 Time-Averaged Effective Hamiltonian

This section introduces the concept of an effective Hamiltonian, approximating a part of the quasienergy spectrum of a Floquet Hamiltonian. As shown by Hemmerich [180], one can define a unitary operator $U_{Q,m}(t) = \exp(-\mathrm{i}Q(t) + \mathrm{i}m\Omega t)$ with a hermitian time-periodic operator $Q(t) = Q(t+T)$ and integer m, which transforms an arbitrary stationary orthonormal basis $|n\rangle$ of $\mathcal{H}$ into an orthonormal basis of the composite Hilbert space $\mathcal{H} \otimes \mathcal{H}_T$

$$|n(t), m\rangle = U_{Q,m}(t) \, |n\rangle \, . \tag{3.36}$$

The matrix elements of the Floquet Hamiltonian in this basis are given by

$$\langle\langle n(t), m|H_\mathcal{F}|s(t), p\rangle\rangle_T = \langle\langle n|U_Q^+(t)H_\mathcal{F}U_Q(t)|s\rangle \, \mathrm{e}^{\mathrm{i}(p-m)\Omega t} \, \rangle_T + p\hbar\Omega\delta_{pm}\delta_{ns}, \tag{3.37}$$

with $U_Q \equiv U_{Q,0}$. The matrix elements can be decomposed into diagonal blocks ($m = p$) and elements coupling different Floquet bands ($m \neq p$)

$$\langle\langle n(t), m|H_\mathcal{F}|s(t), p\rangle\rangle_T = \delta_{pm} \left(\langle n|H_\mathrm{eff}|s\rangle + p\hbar\Omega\delta_{ns} \right) + (1 - \delta_{pm}) \, \langle n|V_{p,m}|s\rangle \, . \tag{3.38}$$

Here, the effective Hamiltonian is defined as [180]

$$H_\mathrm{eff} = \langle U_Q^+(t)H_\mathcal{F}U_Q(t)\rangle_T \tag{3.39}$$

and the perturbation term as

$$V_{p,m} = \langle \, \mathrm{e}^{\mathrm{i}(p-m)\Omega t} U_Q^+(t)H_\mathcal{F}U_Q(t)\rangle_T \, . \tag{3.40}$$

We are interested in the conditions under which a single Brillouin zone of the quasienergy spectrum of $H_{\mathcal{F}}$ can be approximated by the energy spectrum of H_{eff}. First, we diagonalize each block of the Floquet Hamiltonian, which corresponds to the diagonalization of the effective Hamiltonian

$$\langle n|D^{+}H_{\text{eff}}D|s\rangle = \langle\tilde{n}|H_{\text{eff}}|\tilde{s}\rangle = E^{\text{eff}}_{\tilde{n}}\delta_{\tilde{n}\tilde{s}}, \tag{3.41}$$

with D as the unitary diagonalization operator and the eigenstates $|\tilde{s}\rangle = D\,|s\rangle$ of H_{eff}. The influence of the perturbation term on the quasienergy spectrum can be determined by using perturbation theory. The first order energy correction vanishes, while the second order yields the result

$$E^{(2)}_{\tilde{n},m} = \sum_{\tilde{s}}\sum_{p\neq m}\frac{|\langle\tilde{n}|V_{p,m}|\tilde{s}\rangle|^2}{E^{\text{eff}}_{\tilde{n}} - E^{\text{eff}}_{\tilde{s}} + (m-p)\hbar\Omega}. \tag{3.42}$$

If the splitting of the Floquet bands is large compared to all eigenvalues of the effective Hamiltonian

$$\left|E^{\text{eff}}_{\tilde{n}}\right| \ll \hbar\Omega, \tag{3.43}$$

as well as to all off-diagonal coupling terms

$$|\langle\tilde{n}|V_{p,m}|\tilde{s}\rangle| \ll \hbar\Omega, \tag{3.44}$$

$E^{(2)}_{\tilde{n},m}$ is small. Hence, the perturbation term $V_{p,m}$ and the overlap between different Floquet bands can be safely neglected. In this high-frequency approximation, the spectrum of the Floquet Hamiltonian is well approximated by the spectrum of H_{eff} modulo $\hbar\Omega$ and the states $|\tilde{n}(t), m\rangle = U_{Q,m}D\,|n\rangle$ behave like Floquet modes. For the first Brillouin zone of the quasienergy spectrum we obtain

$$\begin{aligned}\langle\langle\tilde{n}(t),0|H_{\mathcal{F}}|\tilde{s}(t),0\rangle\rangle_T &\approx \langle\tilde{n}|H_{\text{eff}}|\tilde{s}\rangle\,,\\ &\Leftrightarrow \varepsilon_{\tilde{n}} \approx E^{\text{eff}}_{\tilde{n}}.\end{aligned} \tag{3.45}$$

The quasienergies of the first Brillouin zone and the energy eigenvalues of the effective Hamiltonian coincide in the high-frequency approximation. Within this approximation it is possible to relate an arbitrary state $|\psi(t)\rangle$, obeying the Schrödinger (3.21) with the time-dependent Hamiltonian $H(t)$, to the corresponding solution $|\psi_{\text{eff}}(t)\rangle$ of the effective Schrödinger equation with H_{eff}. Following the completeness relation (3.31), we expand $|\psi(t)\rangle$ in terms of the approximate Floquet states,

$$\begin{aligned}|\psi(t)\rangle &\approx \sum_{\tilde{n}} c_{\tilde{n}}\ \mathrm{e}^{-\mathrm{i}\varepsilon_n t/\hbar}\ |\tilde{n}(t),0\rangle\\ &\approx U_Q\sum_{\tilde{n}} c_{\tilde{n}}\ \mathrm{e}^{-\mathrm{i}E^{\text{eff}}_{\tilde{n}}t/\hbar}\,|\tilde{n}\rangle = U_Q\,|\psi_{\text{eff}}(t)\rangle\,,\end{aligned} \tag{3.46}$$

where we have used Eq. (3.45) and the unitary transformation (3.36) in the step from the first to the second line. The series coefficients are defined as $c_{\tilde{n}} = \langle\tilde{n}(t),0|\psi(t)\rangle$.

If the coupling between Floquet bands can be completely neglected, it is worth reconsidering Eq. (3.34). Under this approximation the population of each Floquet band remains fixed and the time-averaged energy only depends on quasienergies up to an unimportant constant.

3.5 Effective Description of a Driven Lattice

We will now use the concept of the effective Hamiltonian to treat a periodically driven optical lattice in the tight binding regime. The particles trapped in the lattice are bosonic and hence, the system is well described by the Bose-Hubbard Hamiltonian with an additional driving term,

$$H(t) = H_{\text{Tunnel}} + H_{\text{OnSite}} + H_{\text{Force}}(t), \tag{3.47}$$

where we seperated Eq. (2.29) into a tunneling term H_{Tunnel} and a term which only includes on site density operators H_{OnSite}. The time-periodic driving term ($H_{\text{Force}}(t) = H_{\text{Force}}(t+T)$) is given by

$$H_{\text{Force}}(t) = \sum_i v_i(t)\hat{n}_i, \tag{3.48}$$

with $v_i(t) = -\mathbf{F}(t)\,\mathbf{R}_i$ and $\mathbf{F}(t)$ as a time-periodic, inertial force (as in Eq. (3.2)) acting on the atoms in the lattice. $\mathbf{R}_i$ is the lattice vector of site i. By choosing the hermitian operator of the unitary transformation (3.36) as

$$Q = \frac{1}{\hbar}\sum_i W_i(t)\hat{n}_i, \tag{3.49}$$

with

$$W_i(t) = \int_{t_0}^{t} \mathrm{d}t' v_i(t') - \left\langle \int_{t_0}^{t} \mathrm{d}t' v_i(t') \right\rangle_T = -\Delta\mathbf{p}(t)\cdot\mathbf{R}_i, \tag{3.50}$$

one obtains an effective Hamiltonian without the driving term (see Eq. (3.39)),

$$H_{\text{eff}} = -\sum_{\langle i,j\rangle} J_{ij}^{\text{eff}} a_i^+ a_j + H_{\text{OnSite}} \tag{3.51}$$

as shown by Eckardt *et al.* [83]. The effective Hamiltonian has exactly the same structure as the undriven Bose-Hubbard Hamiltonian but with renormalized tunneling elements

$$J_{i,j}^{\text{eff}} = J \left\langle\, \mathrm{e}^{\mathrm{i}(W_i(t)-W_j(t))/\hbar} \right\rangle_T . \tag{3.52}$$

With a suitable driving function it is possible to create effective tunneling elements - in contrast to the conventional unrenormalized tunneling parameter - which can be negative or even complexed valued.

For the validation of the effective Hamiltonian approximation it is suitable to work with Floquet-Fock states [83], which can be obtained from the well-known Fock states and Eq. (3.36),

$$|\{n_i\}(t), m\rangle = U_{Q,m}(t)\,|\{n_i\}\rangle = \mathrm{e}^{-\mathrm{i}/\hbar\sum_i W_i n_i + \mathrm{i}m\Omega t}\,|\{n_i\}\rangle . \tag{3.53}$$

In this basis set, transitions between different Floquet bands, which are not captured by the effective Hamiltonian, are only mediated by the tunneling term. The Floquet-Fock states are eigenstates of $H_{\mathcal{F}}$ for $J = 0$,

$$H_{\mathcal{F}}\,|\{n_i\}(t), m\rangle \overset{J=0}{=} \left(\frac{U}{2}\sum_i n_i(n_i-1) + \hbar\Omega m\right)|\{n_i\}(t), m\rangle . \tag{3.54}$$

This means that the Floquet-Fock states only coincide with the true Floquet states of the system for a vanishing tunneling matrix element. The coupling elements between Floquet bands ($m \neq p$) read

$$\langle\{n_i\}|V_{p,m}|\{n_i'\}\rangle = -J\sum_{\langle i,j\rangle}\langle\{n_i\}|a_i^+a_j|\{n_i'\}\rangle\,\langle \mathrm{e}^{\mathrm{i}/\hbar(W_i(t)-W_j(t))+\mathrm{i}(p-m)\Omega t}\rangle_T \tag{3.55}$$

(see Eq.(3.40)). The tunneling matrix elements, involving creation and annihilation operators, roughly scale like the average filling factor $\bar{n}$, whereas the absolute value of the time-averaging integral in Eq. (3.55) lies between zero and unity. Recalling Eq. (3.43), the coupling terms between different Floquet bands can be neglected if $\bar{n}J \ll \hbar\Omega$. In addition to this condition the energy levels of states belonging to different Floquet bands must not overlap (Eq. (3.43)). As the effective Hamiltonian scales with the on-site interaction and the effective tunneling, which is always smaller than the original tunneling parameter, this leads to the additional constraint $\bar{n}(\bar{n}-1)U \ll \hbar\Omega$. Combining these conditions and assuming low average filling factors $\bar{n} \approx 1$, results in the lower bound for the driving frequency [83, 180]

$$\max\{U, J\} \ll \hbar\Omega. \tag{3.56}$$

The validity of Eq. (3.51) under condition (3.56) has been verified in numerical simulations [83, 192, 193].

One should keep in mind that the derivation of the lattice Hamiltonian (2.29) involves a single band approximation. If the driving frequency gets resonant with higher Bloch bands, this approximation lacks justification. In order to avoid band excitations, the driving frequency must differ from the band gap energy E_{Gap},

$$\hbar\Omega \cdot l \not\approx E_{\mathrm{Gap}}, \quad l \in \mathbb{N}^*. \tag{3.57}$$

This expression includes resonant multi-photon transitions to higher bands. Indeed, these transitions do play a role due to the strong forcing of the system. Figure 3.2 shows a typically excitation spectrum obtained by scanning the shaking frequency. The coherence of the system strongly decreases for integer ratios of $E_{\mathrm{Gap}}/(\hbar\Omega)$. These discrete resonances correspond to multi-photon excitations to the higher band. The deviations at low frequencies between the measured and the expected position of the resonances probably stem from systematic errors in the band gap measurement.

3.6 Momentum Distribution of the Effective State in the Laboratory Frame

In section 2.4.5 we derived the momentum distribution for an arbitrary state in an optical lattice. Since we are interested in describing the time-periodic system by an effective Hamiltonian, it is important to find an observable for the *effective* states. In the lattice frame the momentum distribution for a state obeying the time-dependent Schrödinger equation reads (see Eq. (2.42))

$$\begin{aligned}\langle\psi(t)|\hat{n}_{\mathbf{k}}|\psi(t)\rangle &= |\tilde{w}(\mathbf{k})|^2\sum_{i,j}\mathrm{e}^{\mathrm{i}\mathbf{k}(\mathbf{R}_i-\mathbf{R}_j)}\,\langle\psi(t)|a_i^+a_j|\psi(t)\rangle \\ &= |\tilde{w}(\mathbf{k})|^2\sum_{i,j}\mathrm{e}^{\mathrm{i}(\mathbf{k}-\Delta\mathbf{p}(t)/\hbar)[\mathbf{R}_i-\mathbf{R}_j]}\,\langle\psi_{\mathrm{eff}}(t)|a_i^+a_j|\psi_{\mathrm{eff}}(t)\rangle\,,\end{aligned} \tag{3.58}$$

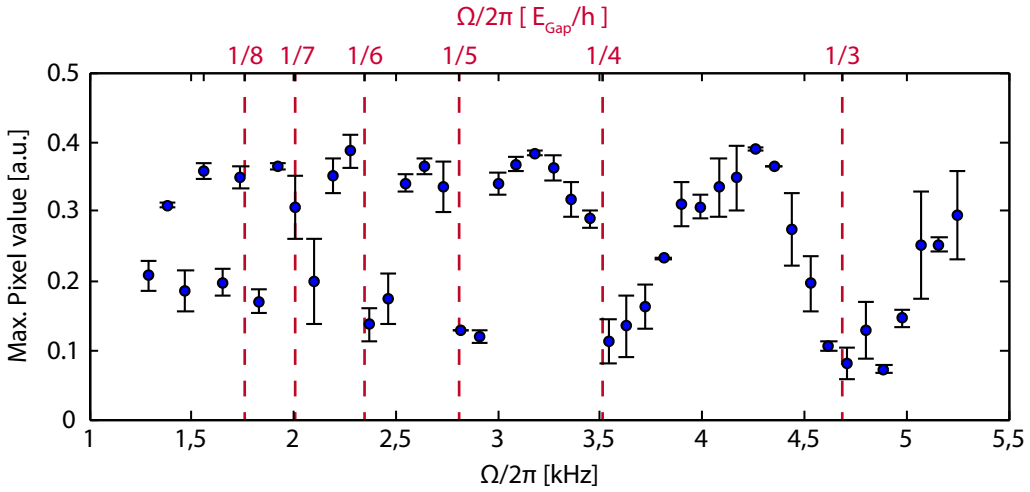

Figure 3.2: Typical excitation spectrum for a periodically driven lattice. The coherence of the system is inferred from the maximum pixel value of the TOF absorption image. A loss of coherence is indicated by smaller pixel values. The frequency is depicted in kHz and units of the band gap energy divided by the Planck constant h. In this case, the spectrum was recorded in a triangular lattice at a depth of $V_0 = 6.1 E_{\mathrm{rec}}$, resulting in a band gap of $E_{\mathrm{Gap}}/h = 14.07$kHz.

where we have made use of Eqs. (3.46) and (3.50) in the second step. In the next step, we need to transform the momentum observable from the co-moving lattice frame into the laboratory frame. The observable transforms according to the unitary operator U_{T} (see Eqs. (3.3), (3.4), (3.5)) as $\hat{n}_{\mathbf{k}}^{\mathrm{Lab}} = U_{\mathrm{T}} \hat{n}_{\mathbf{k}} U_{\mathrm{T}}^{+} = \hat{n}_{\mathbf{k}+\Delta\mathbf{p}(t)/\hbar}$. This results in a momentum distribution in the laboratory frame, which is given by [181]

$$\langle \psi(t) | \hat{n}_{\mathbf{k}}^{\mathrm{Lab}} | \psi(t) \rangle = |\tilde{w}(\mathbf{k} + \Delta\mathbf{p}(t)/\hbar)|^2 \sum_{i,j} \mathrm{e}^{\mathrm{i}\mathbf{k}(\mathbf{R}_i - \mathbf{R}_j)} \langle \psi_{\mathrm{eff}}(t) | a_i^{+} a_j | \psi_{\mathrm{eff}}(t) \rangle \,. \tag{3.59}$$

In the high-frequency limit the momentum distribution of the full solution to the periodically driven Hamiltonian $H(t)$ gives direct access to the correlation function of the effective state $\psi_{\mathrm{eff}}(t)$. As a remnant of the lattice shaking the envelope of the momentum distribution, given by the Fourier transformed Wannier function, oscillates according to the driving function. For a superfluid effective state the positions of the momentum peaks remain fixed, while only the height of the peaks varies according to the moving envelope.

3.7 Benchmark Experiment: Monochromatic Shaking

A paradigm example of tunneling matrix renormalization is given by monochromatic shaking as introduced in section 3.2 (see Eqs. (3.13) and (3.16)). The first experimental realization in the context of quantum degenerated gases was reported by Lignier *et al.* [84], demonstrating the coherent manipulation of the dispersion relation and the dynamical suppression of tunneling between neighboring lattice wells. Similar results have been obtained shortly afterwards with single particles in double well systems [194].

As a benchmark experiment, we employ monochromatic shaking and compare it to the theoretically expected renormalization of J. The atoms are adiabatically loaded into the running wave 1D lattice (see Eq. (2.21)) at a lattice depth of a $V_0 = 8 E_{\mathrm{rec}}$, resulting

in a tunneling value of $J = 0.012E_{\mathrm{rec}}$ and a band gap of $E_{\mathrm{gap}} = 3.6E_{\mathrm{rec}} = h \cdot 12.1\mathrm{kHz}$. Frequency modulation of one beam with

$$\delta\omega_2(t) = -2\pi\nu_0 \cos(\Omega t), \tag{3.60}$$

leads to a time-dependent phase shift

$$\phi_2(t) = -\int_{-\infty}^{t} \mathrm{d}t' \delta\omega_2(t'), \tag{3.61}$$

and an accelerated motion of the lattice, resulting in an inertial force as described in Eq. (3.13) (see appendix B for a derivation of the forcing function). We describe the renormalization of the tunneling matrix elements in terms of the dimensionless forcing parameter

$$A = \frac{d_{\mathrm{RW}} F_0}{\hbar\Omega} = \frac{m {d_{\mathrm{RW}}}^2 \nu_0}{\hbar}, \tag{3.62}$$

as the argument of the Bessel function (see Eq. (3.16)). Here, d_{RW} is the corrected spacing of the running wave lattice (see appendix A). In agreement with the conditions (3.56) and (3.57) we choose $\Omega = 2\pi \cdot 1.5\mathrm{kHz}$ (Shaking energy scale $\hbar\Omega = 0.45E_{\mathrm{rec}}$). At a fixed final lattice depth V_0, the forcing parameter is linearly ramped up by increasing the frequency modulation amplitude $\tilde{\nu}_0(t) = \nu_0 \cdot t/T_{\mathrm{R}}$ over a time of $T_{\mathrm{R}} = 20\mathrm{ms}$. Subsequently, the system is subjected to shaking with a constant forcing amplitude $A(\nu_0)$ for a duration of 40ms, allowing the bosons to relax into the minima of the effective dispersion relation. From TOF measurements we finally infer the momentum distribution and thus the minima of the dispersion relation (see Fig. 3.3). If the sign of effective tunneling matrix element is positive the atoms remain in the center of the first Brillouin zone ($q = 0$), while for negative values they relax to the edges of the first Brillouin zone ($q = \pm\pi/d$). The *contrast* which is defined in Fig. 3.3b quantifies the relative occupation of these two quasimomentum states in a single TOF measurement.

Fig. 3.3c shows the momentum distribution of the atoms as a function of the final forcing amplitude. One can clearly identify distinct values of $A(\nu_0)$ where the momentum peaks get shifted by π/d. The comparison of zero crossings for the measured *contrast* and the calculated Bessel function shows almost perfect agreement (see 3.3d), thus indicating the expected renormalization of the tunneling matrix elements. A remarkable point is the coherence of the sample subjected to very strong forcing. Even for forcing parameters up to ten – corresponding to a real space shaking amplitude of approximately five lattice sites – the system still features sharp momentum peaks.

These measurements confirm that a coherent manipulation via periodic lattice shaking is possible in our system and even very strong forcing does not lead to excessive heating of the atomic sample.

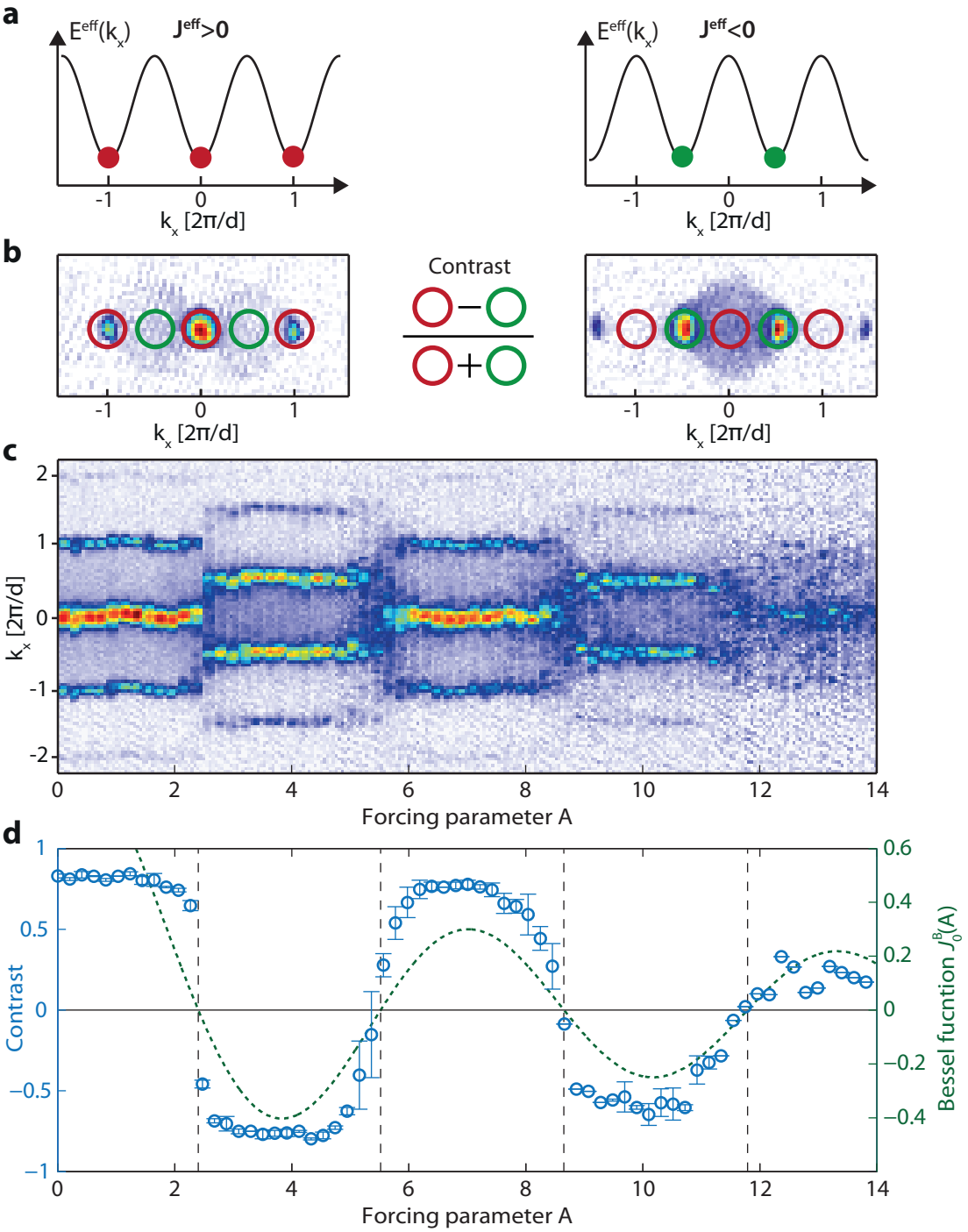

Figure 3.3: Momentum distribution and contrast of the monochromatically shaken one dimensional lattice. **a** Effective dispersion relation for positive and negative tunneling. **b** Measured momentum distribution of the atoms for the dispersion relations shown in **a** and definition of the *contrast*: Particle numbers in the green and red circles are counted, subtracted and finally normalized. **c** Cut of the measured momentum distribution along the x-axis, depending on the forcing parameter A. The blue points indicate the contrast of the momentum distribution (as defined in **b**) for different values of the forcing parameter. The green dashed curved depicts the corresponding renormalization of the tunneling matrix element. Both curves have coinciding zero crossing points.

Chapter 4

Simulation of a Frustrated XY Model on a Triangular Lattice

This chapter introduces a versatile simulator approach for the classical XY model on a triangular lattice. First, the mapping of the ultracold bosonic gas onto the spin-model is described. Then, a diversity of spin-configurations and phase transitions is introduced together with the corresponding experimental signatures. The measured spin-configurations are compared to the corresponding zero temperature phase diagram. Particular attention is paid on the behavior of phases with degenerate ground states, arising due to the presence of strong frustration. In this context spontaneous symmetry breaking is observed.

In general, a system is called frustrated if competing constraints, which are imposed by the underlying Hamiltonian, cannot be fulfilled simultaneously. Frustration in spin models with short range interactions typically arises as a consequence of the lattice geometry. This effect is called geometrical frustration. The total energy of the system cannot be minimized by the preferred, pairwise alignment of the spins.

In this chapter, a versatile simulator approach for a classical XY model on a two-dimensional triangular optical lattice is described. The motional degrees of freedom of bosonic atoms are used to mimic spin-interactions, while the phases of the local coherent wavefunctions are mapped onto vector-spins [70]. The most important control knob in our simulation is the tuning of the nearest-neighbor coupling elements J and J' (Fig. 4.1) resembling the spin-interaction parameters. The sign of these parameters [83, 84] can be inverted. Thus, it is possible to switch between ferromagnetic and antiferromagnetic interactions. This is achieved by a fast periodic translation of the lattice on a closed two-dimensional orbit. In this way, we are able to study a variety of different spin configurations, phase transitions, as well as spontaneous symmetry breaking in presence of degenerate ground states.

Parts of this chapter have been published in Ref. [195] and in the diploma thesis of C. Ölschläger [155], which was co-supervised by the author of this work. The experiments and the data analysis presented in this chapter were performed within the team of: J. Struck, C. Ölschläger, R. Le Targat and P. Soltan-Panahi.

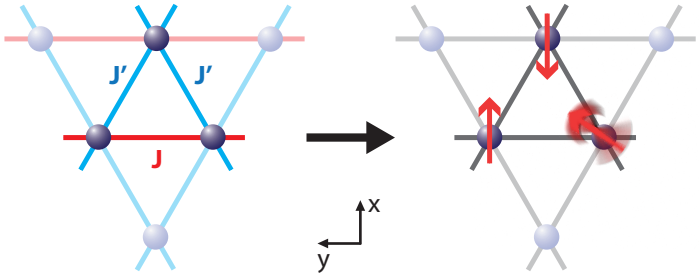

Figure 4.1: Representation of a triangular plaquette as part of a larger lattice. The phases of the local on-site wave functions are mapped on classical two-dimensional vector spins (red arrows). The coupling parameters J (red line) and J' can be tuned independently in magnitude and sign (ferro- or antiferromagnetic).

4.1 Mapping to the Classical XY-Model

In the following, we describe the key ingredients of our quantum gas simulator. Ultracold bosonic atoms are trapped in the minima of a two-dimensional triangular lattice. A weak confinement in the z-direction is provided by the external harmonic trap. Thus, the atoms form a triangular array of elongated tubes with large filling factors in the center of the lattice. We are working in the weakly interacting regime, where local on-site wavefunctions can be described as $\psi_i = \sqrt{n_i}\exp(\mathrm{i}\varphi_i)$ with well defined local phases φ_i. The energy of the system is described by (see Eq. (2.39)),

$$E(\{\varphi_i, n_i\}) = -2\sum_{\overline{\langle ij\rangle}} J_{ij}\sqrt{n_i n_j}\ \cos(\varphi_j - \varphi_i) + \frac{U}{2}\sum_i n_i^2 + \sum_i \epsilon_i n_i, \tag{4.1}$$

where we have introduced the notation $\overline{\langle ij\rangle}$ indicating the sum over all lattice bonds. The tunneling matrix elements of Eq. (4.1) are already the effective tunneling parameters, renormalized by periodic driving as introduced in chapter 3.

A large mean field energy effectively decouples the kinetic part and the interaction part of the energy. On the one hand, the density profile is dominated by the external harmonic trap and the interactions, while the phase distribution has only a negligible influence (Thomas-Fermi regime). On the other hand, the kinetic energy is dominated by the phase distribution, and the density distribution only results in a weighting of the lattice sites, according to the local filling factors. The concept of our spin-simulator is based on the mapping of the phase of the coherent state on each lattice site onto a vector spin $\mathbf{S}_i \equiv \{\cos\varphi_i, \sin\varphi_i, 0\}$. It can point in any direction of the two-dimensional plane and is not quantized. Such a spin is called classical. Furthermore, as a consequence of the large filling factors per tube, the fluctuations of the local phase can be neglected in first approximation. The spin distribution is solely determined by the kinetic part of the Hamiltonian. This results in the classical XY-type model

$$E_{\mathrm{kin}}(\{\varphi_i, n_i\}) = -2\sum_{\overline{\langle ij\rangle}} J_{ij}\sqrt{n_i n_j}\ \cos(\varphi_j - \varphi_i) = -2\sum_{\overline{\langle ij\rangle}} J_{ij}\sqrt{n_i n_j}\ \mathbf{S}_i \cdot \mathbf{S}_j. \tag{4.2}$$

In this model the coupling between the different spins is restricted to nearest-neighbors. Ferromagnetic ordering is realized for parallel alignment of the spins, while the anti-parallel alignment is called antiferromagnetic configuration. The signs of the

tunneling matrix elements J_{ij} determine the energetically preferred spin configuration: If J_{ij} is positive the energy is minimized by parallel alignment of the spins, while for negative J_{ij} the antiparallel orientation leads to the minimal energy of the system. Thus, the parameters J_{ij} characterize the nature of the spin interactions in the lattice system. Positive tunneling matrix elements correspond to ferromagnetic spin interactions, whereas negative ones describe antiferromagnetic couplings between the spins. As the key property of our simulator approach we can independently control the coupling parameters J and J' along two different lattice directions as indicated in Fig. 4.1. This allows for the realization of various different spin-configurations and the investigation of phase transitions connecting them.

Due to the density weighting of the spins as described above, the energy contribution of the spins in the center of the lattice is the highest, while the outlying spins contribute less. This "fading" effect leads to a reduced influence of the lattice boundary on the spin distribution. As a consequence of this effect and the large extend of the lattice we can approximate Eq. 4.1 by its homogenous density counterpart

$$E_{\mathrm{XY}}(\{\varphi_i\}) = -2\bar{n}\sum_{\langle ij\rangle} J_{ij}\ \cos(\varphi_j - \varphi_i) = -2\bar{n}\sum_{\langle ij\rangle} J_{ij}\ \mathbf{S}_i \cdot \mathbf{S}_j, \tag{4.3}$$

where we have introduced the homogenous mean density $\bar{n} = N/M$, with the total number of atoms N and the number of occupied lattice site M.

The energy functions, given in the Eqs. (4.2) and (4.3), obey two fundamental symmetries with respect to spin transformations: First, those expressions are invariant under a global spin rotation, where every spin is rotated by the same angle η

$$\{\varphi_i\} \to \{\varphi_i + \eta\},. \tag{4.4}$$

This is usually referred as rotation symmetry or $U(1)$ symmetry. And second, the energy is unchanged by an inversion transformation of the spins

$$\{\varphi_i\} \to \{-\varphi_i\}, \tag{4.5}$$

which corresponds to a discrete $\mathbb{Z}_2$ symmetry, where every spin is changed into a mirror version.

4.2 Experimental Realization and Parameters

Periodic lattice shaking on an elliptical orbit as proposed by Eckardt *et al.* [70] allows for the creation of effective tunneling matrix elements that can be independently tuned as shown in Fig. 4.1. The forcing function, which was used in the experiments, is given by

$$\mathbf{F}(t) = -F_{0,\mathrm{x}}\cos(\Omega t)\hat{\mathbf{e}}_{\mathrm{x}} - F_{0,\mathrm{y}}\sin(\Omega t)\hat{\mathbf{e}}_{\mathrm{y}}. \tag{4.6}$$

In appendix B the corresponding necessary frequency modulations of the lattice beams are derived, yielding the result

$$\begin{aligned}\delta\omega_2(t) &= 2\pi\left(+\nu_{0,\mathrm{x}}\sin(\Omega t) + \nu_{0,\mathrm{y}}\cos(\Omega t)\right),\\ \delta\omega_3(t) &= 2\pi\left(-\nu_{0,\mathrm{x}}\sin(\Omega t) + \nu_{0,\mathrm{y}}\cos(\Omega t)\right),\end{aligned} \tag{4.7}$$

with the frequency modulation amplitudes $\nu_{0,\mathrm{x}}$ and $\nu_{0,\mathrm{y}}$.

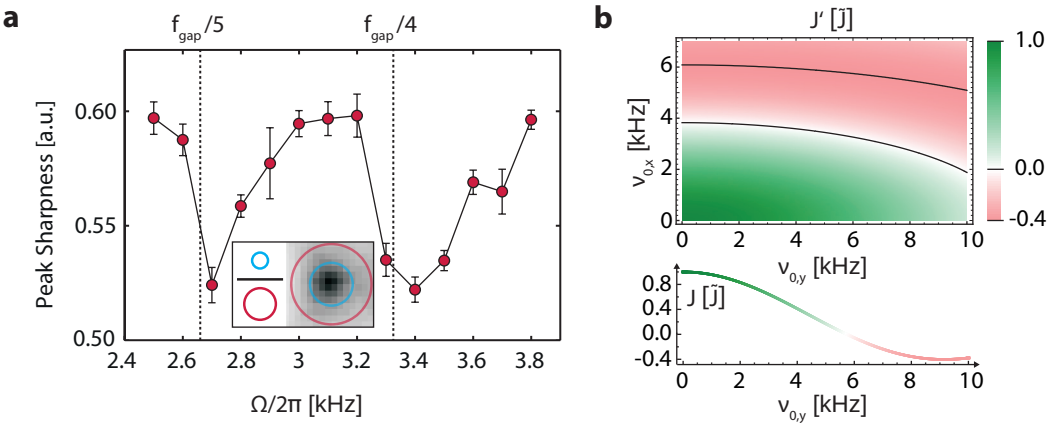

Figure 4.2: Parameters for the elliptical shaking of the triangular lattice. **a** Qualitative peak sharpness extracted via the circle contrast defined in the inset: Atoms in the blue and red circles are counted. If the ratio is one, all atoms are located inside the blue circle. For increasing peak size the ratio drops. **b** Effective tunneling matrix elements J and J' as a function of the frequency modulation amplitudes $\nu_{0,\mathrm{x}}$ and $\nu_{0,\mathrm{y}}$. J' depends on both amplitudes.

The elliptical forcing (Eq. (4.6)) leads to a renormalization of the tunneling matrix elements with zeroth order Bessel functions of the first kind $J_0^{\mathrm{B}}(x)$ (see appendix B.2),

$$J = J_0^{\mathrm{B}}(A) \cdot \tilde{J}, \quad J' = J_0^{\mathrm{B}}(A') \cdot \tilde{J}, \tag{4.8}$$

where the dimensionless forcing parameters are defined as

$$A = \frac{d_{2\mathrm{D}} F_{0,\mathrm{y}}}{\hbar\Omega} = \frac{m d_{2\mathrm{D}}^2 \nu_{0,\mathrm{y}}}{\hbar}, \quad A' = \frac{d_{2\mathrm{D}}}{2\hbar\Omega}\sqrt{3F_{0,\mathrm{x}}^2 + F_{0,\mathrm{y}}^2} = \frac{m d_{2\mathrm{D}}^2}{2\hbar}\sqrt{9\nu_{0,\mathrm{x}}^2 + \nu_{0,\mathrm{y}}^2}. \tag{4.9}$$

To simplify the notation, we have redefined the effective tunneling matrix elements as J and J', while the bare tunneling element is denoted as $\tilde{J}$ for the rest of the chapter.

We load a BEC of about 10^5 Rubidium 87 atoms with no discernable thermal fraction into a static triangular lattice, which results in a maximum filling of around 250 atoms per tube in the center of the lattice and a total occupation of roughly 1000 sites[1]. The lattice depth is $V_0 = 5.6 E_{\mathrm{rec}}$, leading to an on-site interaction energy of $U = 4 \cdot 10^{-3} E_{\mathrm{rec}}$, a bare (unrenormalized) tunneling matrix element of $\tilde{J} = 2 \cdot 10^{-3} E_{\mathrm{rec}}$ and a band gap of $E_{\mathrm{gap}} \approx 4 E_{\mathrm{rec}} \approx h \cdot 13.3\mathrm{kHz}$. In the rest of this chapter the effective tunneling matrix elements will be given in units of $\tilde{J}$. The overall harmonic confinement is nearly isotropic and on the order of $\omega \approx 2\pi \cdot 100\mathrm{Hz}$.

After the final lattice depth is reached, we linearly increase the frequency modulation amplitudes over a time of 25ms to the final values, resulting in the desired effective tunneling elements. As the Bessel function is non-linear, J and J' are generally changed in a non-linear way during the ramp. After the linear increase of the frequency modulation amplitudes the systems is subjected to a forcing with fixed amplitudes for a few milliseconds until the atoms are released from the lattice and imaged after TOF.

The shaking frequency Ω needs to fulfill the conditions (3.56) and (3.57) in order to avoid heating of the ensemble and loss of coherence. A suitable frequency was chosen

[1]The density distribution of the atoms was calculated in the Thomas-Fermi approximation. For further details we refer to appendix C.

by measuring the broadening of the momentum peaks as a function of Ω, yielding information about the coherence across the lattice. Pronounced reduction of the peak sharpness at certain frequencies (Fig. 4.2) is consistent with excitations due to multi-photon transitions to the next band (see Fig. 4.2). For the experiments presented in this chapter the shaking frequency is given by $\Omega = 2\pi \cdot 3.125\text{kHz}$. Fig. 4.2 displays the renormalized tunneling matrix elements as a function of the frequency amplitudes $\nu_{0,\mathrm{x}}$ and $\nu_{0,\mathrm{y}}$ resulting from Eqs. (4.8) and (4.9).

4.3 Zero Temperature Phase Diagram

In a tight-binding approximation the dispersion relation of the driven triangular lattice reads

$$\epsilon(J, J', \mathbf{k}) = -2J\cos(k_\mathrm{y} d_\mathrm{2D}) - 4J'\cos(k_\mathrm{x} d_\mathrm{2D}\sqrt{3}/2)\cos(k_\mathrm{y} d_\mathrm{2D}/2), \tag{4.10}$$

where we have omitted the parabolic dispersion relation term along the tubes perpendicular to the lattice. The spin configuration that minimizes the energy of the system (Eq. (4.2)) is obtained via the relation (see Eq. (2.25))

$$\varphi_i^\mathrm{gs} = \mathbf{q}_\mathrm{gs} \cdot \mathbf{R}_i, \tag{4.11}$$

with the minima of the dispersion relation located at $\mathbf{q}_\mathrm{gs}$. This is a very important point: Each long-range spin configuration is connected to a superfluid state with quasi-momentum $\mathbf{q}_\mathrm{gs}$. According to the dispersion relation (4.10) the minima are given by

$$\mathbf{q}_\mathrm{gs}(J, J') = \begin{cases} (0,0) & \text{for } J' > -2J \text{ and } J' > 0 \text{ (Ferromagnetic)}, \\ \frac{2}{d_\mathrm{2D}}\left(\frac{\pi}{\sqrt{3}}, 0\right) & \text{for } J' < \ \ 2J \text{ and } J' < 0 \text{ (Rhombic)}, \\ \frac{2}{d_\mathrm{2D}}\left(\frac{\pi}{\sqrt{3}}, \pm\arccos\left(\frac{J'}{2J}\right)\right) & \text{for } J' > \ \ 2J \text{ and } J' < 0 \text{ (Spiral 1)}, \\ \frac{2}{d_\mathrm{2D}}\left(0, \pm\arccos\left(-\frac{J'}{2J}\right)\right) & \text{for } J' < -2J \text{ and } J' > 0 \text{ (Spiral 2)}, \end{cases} \tag{4.12}$$

where we introduced names for the spin configurations that arise in different regimes of the coupling parameters J and J'. Equation (4.12) does not include the cases for $J' = 0$ where the system consist of decoupled chains and the dispersion relation becomes degenerate along k_x. The energy of the dispersion relation at the position of the minima is equivalent to the ground state energy of the XY model $E_\mathrm{XY}^\mathrm{gs}(J, J')$ per particle

$$\epsilon(J, J', \mathbf{q}_\mathrm{gs}) = \frac{E_\mathrm{XY}^\mathrm{gs}(J, J')}{N} = \begin{cases} -J - 2|J'| & \text{for } |J'| > -2J \\ J + \frac{J'^2}{2J} & \text{for } |J'| < -2J, \end{cases} \tag{4.13}$$

where N is the total number of particles in the lattice. With Eq. (4.10) one can determine a zero-temperature phase diagram, which is spanned by J and J'. Identifying non-analyticities in the expression for $E_\mathrm{XY}^\mathrm{gs}$ one finds phase boundaries separating three phases. When moving from the ferromagnetic into the rhombic region, one crosses a cusp in the ground state energy, which is accompanied by a discontinuity in the first derivative of $E_\mathrm{XY}^\mathrm{gs}$ with respect to the coupling parameters. This indicates a first order phase transition, which is shown as the thick solid line in Fig. 4.3. A smooth evolution

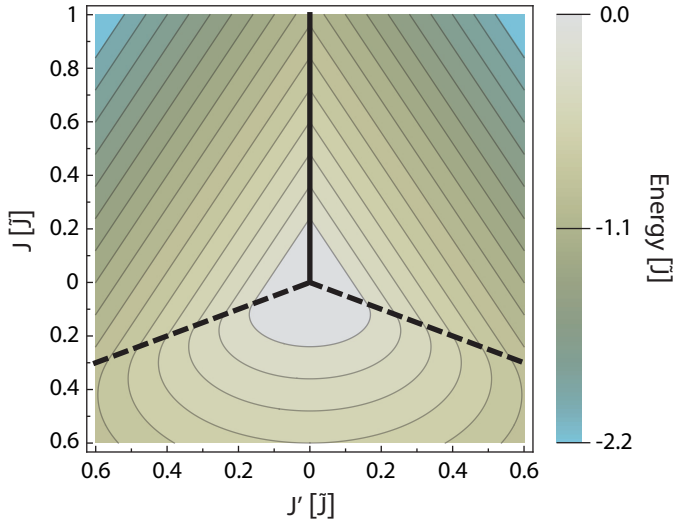

Figure 4.3: Ground state energy of the XY model as a function of the coupling parameters J and J'. The thick solid line represents a first order phase transition, while the dashed lines indicate second order phase transitions. At zero temperature three different phases can be accessed by tuning J and J'.

of the energy is encountered when going from ferromagnetic into spiral 2 region as well as from rhombic to spiral 1. In these cases the second derivative of $E_{\mathrm{XY}}^{\mathrm{gs}}$ shows a discontinuity, corresponding to a second order phase transition. This transition is marked by thick dashed lines in Fig. 4.3. The three phases of the system are respectively located in the ferromagnetic, rhombic and joined spiral region.

The geometrical frustration of the lattice is predominately important for spin configurations of the spiral phase. It leads to two-fold degenerate ground states, where two different spin-configurations minimize the energy of the system. This is equivalent to the presence of two minima in the first Brillouin zone of the dispersion relation (see Eq. (4.12)), which are not connected by reciprocal lattice vectors.

For the ferromagnetic and rhombic phase the system has fixed ground state quasimomenta and associated fixed spin configurations (see Eq. (4.12)). Whereas in the spiral phase the spin configurations smoothly evolve as a function of the coupling parameters J and J'. Different spin configurations and their experimental signatures will be discussed in the next section.

4.4 Spin Configurations and Signatures in the Reciprocal Space

A long-range ordered spin-configuration breaks the rotation symmetry of the XY model (see Eq. (4.4)). By recalling that the spins are emulated by the phase of bosons this is equivalent to the onset of Bose-Einstein condensation accompanied by a broken $U(1)$ symmetry. Therefore every long-range ordered vector-spin configuration is directly connected to a superfluid state at a specific quasimomentum. The respective spin-order can be inferred from the momentum distribution of the atoms measured after TOF. However, it is impossible to distinguish between spin-configurations that are connected by a global rotation transformation (see Eq. 4.4) as these states have the

same quasimomentum. In the following we will omit this ambiguity by only considering a single spin arrangement of each infinitely degenerate manifold.

A very important point for the realization of vector-spin configurations with long-range order is the dimensionality. The Mermin-Wagner-Hohenberg theorem [196, 197] states that continuous symmetries in a system with short-range interactions - for example nearest-neighbor interactions on a lattice - cannot be broken spontaneously at non-zero temperature in two or less dimensions. This means for a pure two-dimensional XY model no long-range order is expected at finite temperature. In our case we do observe long-range order due to the fact that the atoms are allowed to move along tubes perpendicular to our two-dimensional lattice. This renders our system three dimensional and the Mermin-Wagner-Hohenberg theorem does not apply.

In this section we describe characteristic spin configurations arising in different regions of the phase diagram and their respective momentum signatures (see Figs. (4.4) and (4.5)).

Ferromagnetic order (F)

In the ferromagnetic region of the phase diagram ($J' > -2J$ and $J' > 0$) the spins are aligned parallel to each other. This situation corresponds to a superfluid at zero quasimomentum.

Rhombic order (R)

In the rhombic region of the phase diagram ($J' < 2J$ and $J'<0$) the spins align antiparallel along the bonds characterized by the coupling parameter J' and parallel along the horizontal bonds determined by coupling parameter J. The corresponding superfluid state has a non-zero quasimomentum located at the two edges of the first Brillouin zone in the k_x direction.

1D chains (C)

The phase transition from the ferromagnetic to the rhombic region is of first order. The corresponding experimental signature is an abrupt change of the quasimomentum when traversing the phase boundary. As a consequence of the finite experimental fluctuations of the control parameter J', we observe a collection of ferromagnetic and rhombic peaks in the averaged pictures (see Fig. 4.5). The two spin configurations are degenerate at $J' = 0$. The momentum peaks are broadened along k_x, indicating a loss of coherence along the directions defined by the coupling parameter J'. This is a finite temperature effect.

Unlike the ferromagnetic or rhombic phase, the spiral phase is not characterized by a single spin configuration. First, the spin ordering is a continuous function of the ratio J/J'. Therefore, infinitely many different configurations exist in the spiral phase. Second, geometrical frustration leads to a non-collinear arrangement of the spins. This has an important consequence: Application of a mirror transformation (see Eq. (4.5)) on the spin-configuration leads to a new ordering, which cannot be obtained by a global rotation of all spins (see Eq. (4.4)). Therefore, each ground-state in the spiral phase is doubly degenerate and two possible ground state spin-configurations exist. As we will see later on, they can be distinguished in the experiment. For collinear spin-configurations the mirror transformation leads to states which can also be obtained from a rotation.

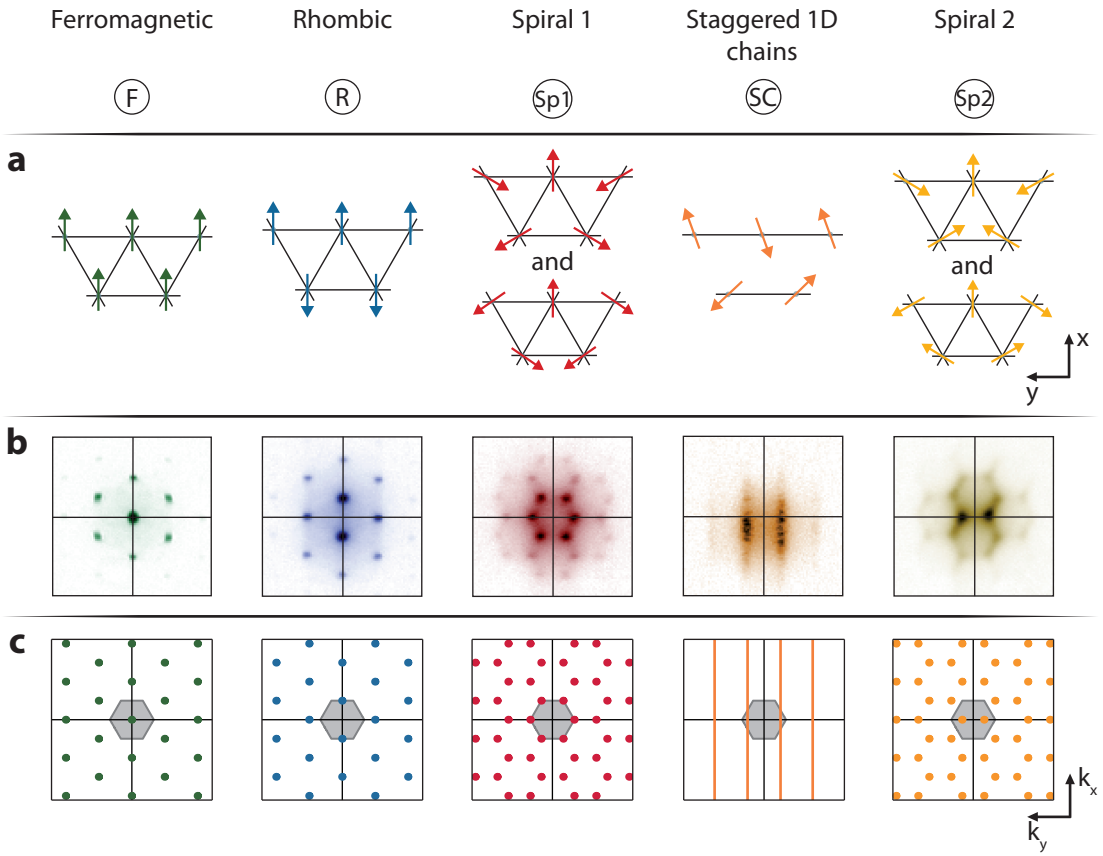

Figure 4.4: Spin configurations and their signatures in the reciprocal space. **a** Small subsets of the lattice showing five different spin configurations, that can be realized by tuning J and J', are shown. In the spiral phase two different spin configurations are ground states of the system. **b** The measured momentum distributions of the different long-range spin states show distinct peak structures. The images embody an average of multiple experimental realizations. For the degenerate spin configurations the momentum peak structures of both states are averaged, resulting in a combined momentum distribution shown in the corresponding pictures. **c** For comparison the theoretically expected positions of the minima in the dispersion relation (Eq. (4.13)) are shown. The grey shaded region in the center depicts the first Brillouin zone.

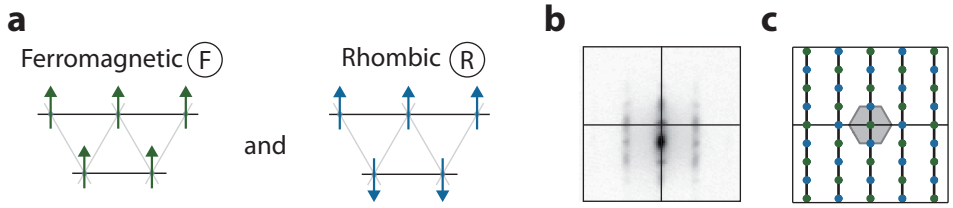

Figure 4.5: Behavior of the system close to the first order phase transition. **a** Two spin configurations arise in close vicinity to the phase boundary due to the limited experimental resolution and finite temperature. The grey bonds indicate the weak coupling of the spins along J'. **b** Averaged momentum distribution obtained for $J' \approx 0$. **c** The theoretically expected positions of the minima in the dispersion relation at exactly $J' = 0$ are indicated by vertical black lines. In addition, the minima for ferromagnetic (green circles) and rhombic region (blue circles) are shown.

Spiral 1 order (S1)

For the case of isotropic antiferromagnetic couplings $J = J' < 0$ the spins align in a 120° configuration. The combined momentum distribution of both ground state configurations features peaks at the six corners of the first Brillouin zone.

Staggered 1D chains (SC)

For small values of the coupling parameter $J' \approx 0$ and $J < 0$, thermal effects become important and lead to complete loss of lange order across the lattice. Correlations are only preserved along the J-bonds, leading to stripes along k_x in the momentum distribution. In contrast to the 1D chains for $(J > 0)$ there is no collection of different spin orderings which stems from the fact that the systems does not cross any phase boundary in this case.

Spiral 2 order (S2)

Frustrated spin configurations can also arise when only J is negative. For $J = -J' < 0$ the spins align in a mixed configuration: Along the negative J-bonds the angle between two neighboring spins is 120° while the angle difference along the positive J'-bonds amounts to 60°. The combined momentum distribution of both ground-states results in two momentum peaks located inside the first Brillouin zone.

4.5 Experimental Characterization of the Phase Diagram

The different quasimomentum signatures allow for a clear identification of the experimentally realized spin configurations. The independent control over the coupling parameters J and J' permits the experimental mapping of the phase diagram (Fig. 4.6). The Bessel function renormalization provides access to a region of the phase diagram, where J and $J' \geq -0.4$. The background colors in Fig. 4.6 indicate the theoretically expected spin configurations, according to Eqs. (4.11), (4.12). The colors match with those of Fig. 4.4. In the spiral phase a smooth change of the background color indicates the continuous change of the spin configuration as a function of the ratio J'/J. At zero temperature, the spin configurations do not depend on the radial distance to the origin of the phase diagram. For finite temperature, the long-range order of the spins is completely lost in close vicinity to the origin of the phase diagram. This is indicated by the grey shaded circle in the center of Fig. 4.6. For small absolute values of the coupling parameters finite temperature and especially non-equilibrium phenomena become important. The critical temperature approaches zero and timescales for adiabatic behavior diverge. We indicate measurements without a momentum peak structure with crosses. The measured momentum signatures, which correspond to the ferromagnetic phase are shown as circles in Fig. 4.6, while points belonging to the rhombic and spiral phase are indicated by squares and triangles, respectively.

Almost all relevant parts of the phase diagram could be mapped out and the measured data points are in very good agreement with the expected zero-temperature phase diagram. Deviations only arise close to the first order phase boundary between the ferromagnetic and rhombic phase. The data points with a combined circle and square symbol indicate measurements where, as discussed in section 4.4, rhombic and ferromagnetic spin order have been observed (see Fig. 4.5).

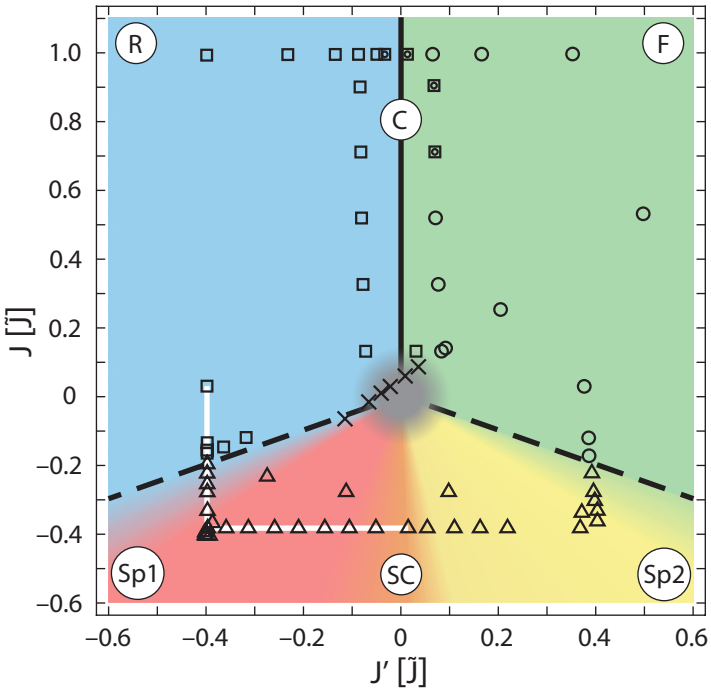

Figure 4.6: Experimental mapping of the phase diagram. Without the periodic driving of the lattice coupling parameters are fixed to $J = J' = 1$, corresponding to the ferromagnetic phase. Dashed lines indicate second order phase transitions while the solid line designates a first order phase transition. Circles, squares and triangles mark the measurements of the ferromagnetic phase, rhombic phase and spiral phase, respectively. Crosses indicate measurements without long-range coherence.

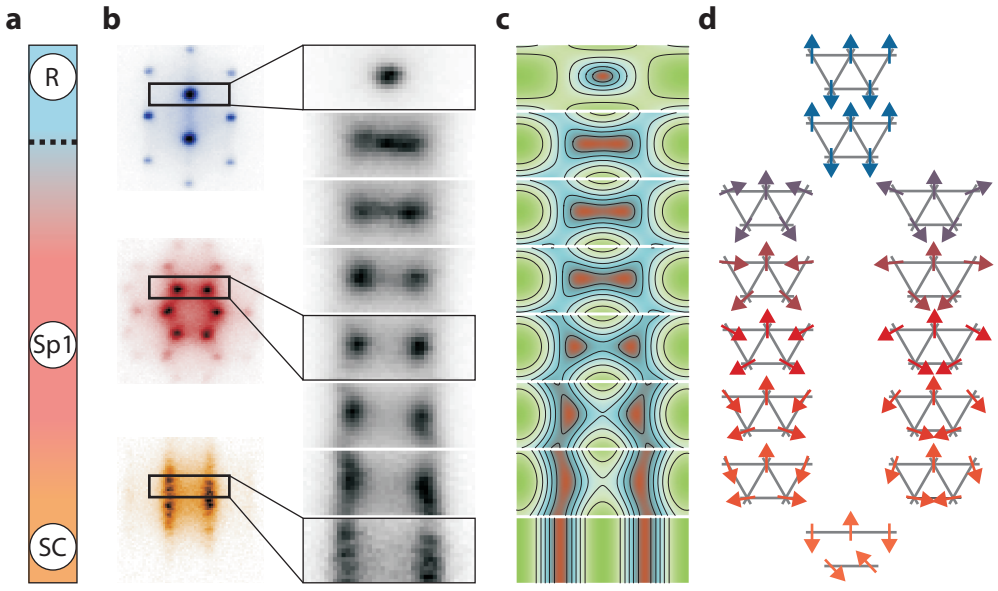

Figure 4.7: Measurement of the second order phase transition from rhombic to spiral phase. **a** The colorbar illustrates the trajectory along the white line in Fig. 4.6. **b** On the left, three examples of averaged momentum distribution are shown. Uncolored data corresponds to a magnified part of the momentum distributions. **c** The corresponding dispersion relations. Red regions correspond to the lowest energy. **d** Continues change of the spin configurations.

The phase transition from the rhombic into the spiral phase is of second order and is characterized by a continuous evolution of spin configurations in the phase diagram. We measure the spin ordering along the trajectory indicated by the white line in Fig. 4.6. A smooth evolution of the quasimomentum is observed while crossing the phase boundary located at $J'/J = 2$ (Fig. 4.7b). In the spiral phase, the single momentum peak from the rhombic phase splits into two peaks. These correspond to the two degenerate ground state spin-configurations. With decreasing ratio J'/J the distance between momentum peaks increases. At $J'/J = 1$ we recover the momentum peak structure of the 120°-spin-order. For the case of $J' = 0$, which is the last data point on the trajectory, we observe staggered 1D chains. The measured momentum distributions shown in Fig. 4.7b are averaged over several experimental realizations. The quasimomentum peaks agree very well with the position of the minima in the corresponding dispersion relation (Fig. 4.7c). The evolution of the spin configurations is indicated in Fig. 4.7d.

In conclusion, we have shown that we can access all spin configurations and phases in a well controlled way and thereby validated our simulator approach. A drawback not mentioned so far is the limited lifetime of the spiral phase, which is on the order of 10ms. This is well below the lifetime of a superfluid state in the unshaken lattice, which corresponds to several hundreds of milliseconds. It remains an open question wether this limitation is a technical problem or a fundamental issue.

4.6 Degenerate Spiral Phases

In this section, we focus on the degenerate ground states for the particular case of isotropic antiferromagnetic interactions ($J' = J = -0.4$). In Section 4.4 we discussed and presented the averaged momentum peak structure for the corresponding 120°-spin-order. The two possible ground state configurations are mirror images of each other (Fig 4.8a). Both states can be uniquely characterized by the chiral order parameter per plaquette [198]

$$\kappa = \mathrm{sgn}\left(\mathbf{S}_1 \times \mathbf{S}_2 + \mathbf{S}_2 \times \mathbf{S}_3 + \mathbf{S}_3 \times \mathbf{S}_1\right)_z , \tag{4.14}$$

where the three vector spins $\mathbf{S}_1, \mathbf{S}_2$ and $\mathbf{S}_3$ are positioned in counter-clockwise orientation around a single plaquette of the lattice and $\mathrm{sgn}(x)$ is the signum function. In the following we label the two ground states as chiral mode 1 and 2. In the chiral mode 1, κ is positive for downwards pointing triangular plaquettes and negative for upwards pointing ones. For the chiral mode 2 the value of the chiral order parameter is exactly inverted (Fig. 4.8a).

Experimentally, the two chiral modes can be distinguished by their momentum distributions. The momentum distribution of a single chiral mode consist of three peaks at corners of the first Brillouin zone. Momentum peaks of a single mode are connected to each other via reciprocal lattice vectors. The two different chiral modes occupy the complementary corners of the first Brillouin zone (Fig. 4.8b), resulting in averaged momentum distributions as shown in Fig. 4.4b. The relative occupancy of the chiral modes in a single experimental realization is quantified by the chiral contrast χ (see Fig. 4.8b). For positive values of χ, the chiral mode 1 is predominantly occupied, while the opposite holds for negative values. If χ is close to zero both modes are equally populated.

In consecutive experimental runs, performed under the same experimental conditions, the chiral contrast strongly fluctuates (Fig. 4.8c). Most of the time we observe

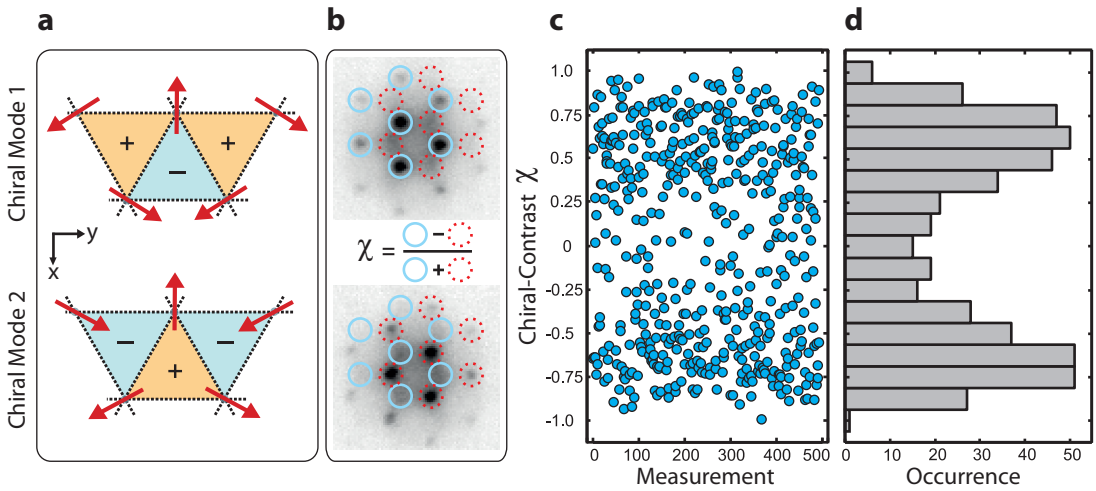

Figure 4.8: Spontaneous symmetry breaking of the spiral phase for isotropic antiferromagnetic coupling parameters ($J = J' = -0.4$). **a** Two energetically degenerate spin configurations exist in the spiral phase. They can be distinguished by their opposite chirality. The plus and minus signs describe the chiral order parameter for each plaquette. The respective spin ordering is depicted by the red arrows. **b** An unambiguous identification of the spin configurations is possible as the corresponding momentum peaks are located at different positions marked by the blue and red circles. The chiral contrast χ is determined by the number of atoms inside the blue versus the number atoms in the red circles. It is a measure for the occupancy of the two different ground state spin configurations in a single experimental realization. Values larger than zero indicate a dominant occupancy of the chiral mode 1, while negative values signify the contrary case. **c** The measured chiral contrast of nearly 500 consecutive experimental realizations. The chiral contrast is normalized to the maximum absolute value of the measurement series. **d** Histogram of the chiral contrast for the respective measurements of **c**. The binning width is 0.125.

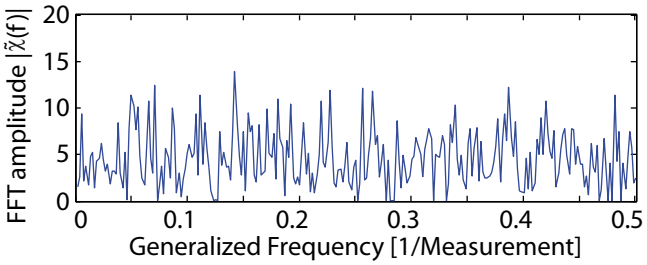

Figure 4.9: Fast fourier transform of the chiral measurement as shown in Fig. 4.8. Plotted is the absolute value of the Fast fourier transformed chirality measurement versus the generalized frequency in units of the inverse measurement.

that a single spin configuration dominates. Therefore, the $\mathbb{Z}_2$ symmetry (Eq. (4.5)) of the system is spontaneously broken (Fig. 4.8d). However, in few cases both modes are equally populated corresponding to an energetically excited state. Most likely this effect arises due to the formation of spatial domains with different chirality. The domain walls separating the different chiral modes can feature complicated structures including topological excitations [199]. Assuming the most simple domain wall, a straight line, we can estimate the energy cost for the simultaneous occupation of two chiral modes as

$$\Delta E_{\mathrm{DW}} \sim L_{\mathrm{DW}} |J| \bar{n}, \tag{4.15}$$

where L_{DW} is the length of the domain wall in units of lattice sites. In principle, the momentum distribution of the state allows for the identification of the size of these domains via the peak width. In our case the width of the peaks is dominated by the in-situ size of the atomic cloud (see Section 2.4.5) and we are not able to extract quantitative results.

To exclude experimental drifts as the origin for the symmetry breaking, we have analyzed the frequency components of the chiral contrast data with a Fast-Fourier transformation (Fig. 4.8c). The spectrum of the chiral contrast does not show clear features in the frequency spectrum, which is in full agreement with white noise (Fig. 4.9). Therefore, long-term drifts of the experimental apparatus can be excluded as the origin of the symmetry breaking. Nevertheless, any white noise technical fluctuations can not be excluded as the origin of the symmetry breaking.

Additional aspects of our system are revealed by recalling that the spin configurations are identified with superfluid states of bosons occupying Bloch functions at distinct quasimomenta. Within the spiral phase the two chiral modes feature staggered bosonic mass currents around the triangular plaquettes, thus spontaneously breaking time-reversal symmetry. In most cases, bosonic ground states are real-valued and do not break time-reversal symmetry as stated in Feynmans *no-node* theorem [200]. In this context we have realized an unconventional superfluid state [60, 62, 201] which goes beyond the *no-node* theorem.

The aforementioned simultaneous occupation of both chiral modes in a single experimental realization can also be explained by a coherent single particle superposition of the atoms in the two corresponding Bloch states with quasimomenta $\mathbf{q}_+$ and $\mathbf{q}_-$:

$$\begin{aligned} |\mathrm{Frg}\rangle &= (N!)^{-1/2} \left(c_{\mathbf{q}_+} B^+_{\mathbf{q}_+} + c_{\mathbf{q}_-} B^+_{\mathbf{q}_-} \right)^N |0\rangle \,, \\ &\approx \mathrm{e}^{-N/2} \prod_{i=0}^{M-1} \exp\left(\sqrt{\bar{n}} \left[c_{\mathbf{q}_+} \mathrm{e}^{\mathrm{i}\mathbf{q}_+\mathbf{R}_i} + c_{\mathbf{q}_-} \mathrm{e}^{\mathrm{i}\mathbf{q}_-\mathbf{R}_i} \right] \; a_i^+ \right) |0\rangle \,, \end{aligned} \tag{4.16}$$

with $B_{\mathbf{q}} = \frac{1}{\sqrt{M}} \sum_{i=0}^{M-1} \exp(-\mathrm{i}\mathbf{q}\mathbf{R}_i) \hat{a}_i$ as the destruction operator for a Bloch state with quasimomentum $\mathbf{q}$. In the second step the state was approximated by a coherent state [23], which is valid in the limit $\bar{n} = N, M \to \infty$ and $N/M =$ constant. Normalization of the state requires $|c_{\mathbf{q}_+}|^2 + |c_{\mathbf{q}_-}|^2 = 1$. Equation (4.16) describes a fragmented state [202, 203] which is typically energetically disfavored by repulsive interactions. This can be intuitively understood in the context of the real space density of such a state which is given by

$$\langle \mathrm{Frg} | \hat{n}_i | \mathrm{Frg} \rangle = \bar{n} \left(1 + 2 |c_{\mathbf{q}_+}| |c_{\mathbf{q}_-}| \cos([\mathbf{q}_+ - \mathbf{q}_-]\mathbf{R}_i + \theta_+ - \theta_-) \right), \tag{4.17}$$

with $\theta_\pm = \arg(c_\pm)$. In the fragmented state the density is periodically modulated with the wavevector $(\mathbf{q}_+ - \mathbf{q}_-)$. Such a density wave is accompanied by an increase of the interaction energy of the system. The interaction energy difference with respect to the occupation of a single Bloch state is

$$\Delta E_{\mathrm{Frg}} = E_{\mathrm{Frg}} - E_{\mathrm{B}} = \frac{2U}{M} N_+ N_-, \tag{4.18}$$

with the number of particles in one mode $N_\pm = N \cdot |c_{\mathbf{q}_\pm}|^2$. In our case the energy scale associated with this state is much larger than that of a domain wall (Eq. 4.15) as long as each Bloch state is occupied with a macroscopic fraction of atoms. We can therefore conclude that the simultaneous occupation of two chiral modes is more likely due to the presence of different domains.

4.7 Conclusion and Outlook

The results presented in this chapter demonstrate the first realisation of a tunable large-scale simulator for a frustrated classical XY model on a triangular lattice. The motional degrees of freedom and the local phases of spinless superfluid bosons are used to map the system onto a spin-model. The high degree of tunability and controllability allows for the observation of various spin-configurations, different types of phase transitions and spontaneous symmetry breaking induced by geometrical frustration.

So far, our experiments focused on the static properties of the system. In the future, an investigation of the dynamical behavior of the different phases might provide valuable inside into the field of non-equilibrium thermodynamics. Interesting questions in this direction are: How do the different spin-configuration relax into excited states for sudden quenches of the control parameters? What is the influence of a specific trajectory in the phase diagram? Is it possible to prepare long-lived metastable states, which are out-of-equilibrium?

Furthermore, the presented simulator approach can be extended into the hardcore bosonic limit of the Bose-Hubbard Hamiltonian, where the system can be mapped onto a quantum XY-model [204, 205]. In this case, the critical temperature for a quantum magnetic Néel order directly scales with the tunneling matrix elements J. This constitutes a major advantage compared to simulator approaches for quantum magnetism, which are based on superexchange couplings [92, 93, 206], where the critical temperature scales with J^2/U and is typically much lower. An interesting feature of the quantum XY-model on the frustrated triangular lattice is the predicted existence of spin-liquid quantum phases [69, 104, 207–210]. These exotic and complicated states are highly debated and it is very difficult to investigate them in solid state materials. Here, a quantum simulator might shed light on one of the most complicated problems of quantum magnetism.

Chapter 5

Tunable Gauge Potentials for Neutral Particles in Driven Lattices

Basic concepts of lattice gauge theory are discussed for the case of classical electrodynamics. Time-asymmetric lattice shaking is introduced as a method for the creation of complex valued tunneling matrix elements, mimicking the presence of a vector gauge potential for neutral particles in an optical lattice. As a proof-of-principle experiment, the emulation of a tunable gauge potential for ultracold bosons in a one-dimensional lattice is demonstrated. The dynamical response of the atoms to changes of the gauge potential is investigated. The last part of this chapter is devoted to the realization of gauge-independent staggered fluxes in a two-dimensional triangular lattice by means of time-asymmetric lattice shaking.

The Lorentz force, acting on charged particles in magnetic fields, is a key ingredient of condensed matter physics. It lacks direct presence in quantum gas experiments because the atoms are neutral. Over the last few years there have been increasing efforts to close this gap by engineering artificial gauge potentials [111].

In this chapter we introduce a novel approach for the creation of synthetic gauge potentials for neutral atoms confined in an optical lattice. The presented scheme is an extension of the periodic driving technique, that was introduced in the foregoing chapters. As an important feature, it is independent of the internal structure of the atoms[1]. A major advantage over the common Raman-laser based approaches is the tunability: The strength of the gauge potentials can be directly controlled by the driving amplitude. We experimentally demonstrate the feasibility of this method by measuring the momentum distributions of ultracold bosonic atoms subjected to a suitable periodic forcing. In particular, we reach the strong field limit were the flux strength is on the order of an elementary flux quantum. Finally, let us point out that the introduced scheme is equally applicable for fermionic atoms.

Parts of this chapter have been published in [212] and [213]. The experiments and the data analysis presented in this chapter were performed within the team of: J. Struck, M. Weinberg, C. Ölschläger and J. Simonet.

[1] In Ref. [211] a similar idea, for the creation of complex tunneling matrix elements, is discussed.

5.1 Electromagnetic Fields in a Tight-Binding Model: Peierls Substitution

The quantum mechanical behavior of a charged particle in the presence of a vector gauge potential is described by a modification of the kinetic part of the Hamiltonian according to

$$\frac{1}{2m}\hat{\mathbf{p}}^2 \rightarrow \frac{1}{2m}\left(\hat{\mathbf{p}} - q\mathbf{A}(\mathbf{r})\right)^2, \tag{5.1}$$

where q is the charge and $\mathbf{A}(\mathbf{r})$ the vector gauge potential. In electrodynamics the vector potential is defined in relation to the magnetic $\mathbf{B}(\mathbf{r},t)$ and electric field $\mathbf{E}(\mathbf{r},t)$,

$$\mathbf{B}(\mathbf{r},t) = \nabla \times \mathbf{A}(\mathbf{r},t), \tag{5.2}$$

$$\mathbf{E}(\mathbf{r},t) = -\frac{\partial}{\partial t}\mathbf{A}(\mathbf{r},t), \tag{5.3}$$

where in the second line the term connected to a scalar potential has been omitted. In the following the gauge potential will be treated as classical and external. This means that the quantum fluctuations of the fields are negligible (classical) and there is no back action of the atoms onto the fields (external) [71]. To very good approximation, the corresponding description of a charged particle in a tight-binding lattice, is captured by the Peierls substitution [142]: Real valued hopping parameters are replaced by complex valued elements

$$J_{ij} \rightarrow |J_{ij}|\mathrm{e}^{\theta_{ij}}, \tag{5.4}$$

where we have introduced the Peierls phase θ_{ij}, which is directly connected to the vector gauge potential

$$\theta_{ij} = \frac{q}{\hbar}\int_{\mathbf{R}_j}^{\mathbf{R}_i} d\mathbf{r}\mathbf{A}(\mathbf{r}). \tag{5.5}$$

The integral has to be evaluated along the straight path connecting site i and j. This translates into the Bose-Hubbard Hamiltonian by a modification of the kinetic part:

$$H = -\sum_{\langle ij\rangle}|J_{ij}|\mathrm{e}^{\theta_{ij}}\hat{a}_i^+\hat{a}_j + \frac{U}{2}\sum_i \hat{n}_i(\hat{n}_i - 1) + \sum_i \epsilon_i\hat{n}_i. \tag{5.6}$$

A phase θ_{ij} is picked up in a tunneling process from lattice site j to lattice site i. The Peierls phases introduce a directionality of the tunneling matrix elements (see Fig. 5.1a) and obey the relation

$$\theta_{ij} = -\theta_{ji}. \tag{5.7}$$

They are gauge dependent and the associated gauge transformation is given by a local $U(1)$ transformation of the creation and annihilation operators as

$$\hat{a}_j \rightarrow \hat{a}'_j = \hat{a}_j\mathrm{e}^{\mathrm{i}\gamma_j}, \tag{5.8}$$

$$\hat{a}_i^+ \rightarrow (\hat{a}'_i)^+ = \hat{a}_i^+\mathrm{e}^{-\mathrm{i}\gamma_i}, \tag{5.9}$$

resulting in new Peierls phases

$$\theta_{ij} \rightarrow \theta'_{ij} = \theta_{ij} + \gamma_i - \gamma_j. \tag{5.10}$$

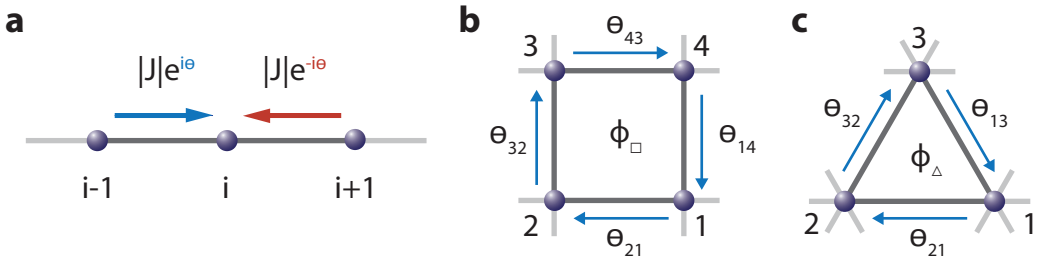

Figure 5.1: Complex tunneling matrix elements and gauge invariant fluxes. **a** Complex valued tunneling matrix elements on a one-dimensional lattice. Gauge invariant flux on a square **b** and triangular lattice **c**.

Such a transformation only leads to a – physically irrelevant – global shift of the dispersion relation. In the context of lattice gauge theory the complex phases characterize a $U(1)$ Abelian gauge potential [71].

A gauge invariant quantity is given by the sum of the Peierls phases around an elementary plaquette $\mathcal{P}$ of the lattice (see Figure 5.1b,c), which is equal to the magnetic flux through that plaquette

$$\Phi = \sum_{\mathcal{P}} \theta_{ij} = \frac{q}{\hbar} \oint_{\mathcal{P}} d\mathbf{r}\mathbf{A}(\mathbf{r}) = \frac{q}{\hbar} \int_{A_{\mathcal{P}}} d\mathbf{n}\,\mathbf{B}(\mathbf{r}), \tag{5.11}$$

where $\sum_{\mathcal{P}}$ stands for the sum over the bonds of an elementary plaquette of the lattice and $\mathbf{n}$ is the normal vector of the surface $A_{\mathcal{P}}$ enclosed by the bonds of the elementary plaquette. Figures 5.1b and c illustrate how this quantity is obtained on a square and triangular lattice. The flux is left invariant under the gauge transformations of Eqs. (5.8) and (5.9),

$$\Phi = \sum_{\mathcal{P}} \theta_{ij} = \sum_{\mathcal{P}} \theta'_{ij}, \tag{5.12}$$

and describes – physically relevant – deformations of the dispersion relation.

The Peierls substitution works up to the point where different bands of the lattice get significantly coupled by magnetic fields [143]. In solid state systems this practically never happens and the Peierls substitution is an excellent approximation. As a central concept of our gauge field emulation, we mimic the presence of $\mathbf{A}(\mathbf{r})$ by directly tailoring complex valued tunneling matrix elements. Or, in other words, we directly engineer the Hamiltonian (5.6) without the approximations involved in the Peierls substitution.

5.2 Complex Tunneling Elements via Lattice Shaking

In order to create artificial gauge fields for neutral atoms in optical lattices, complex tunneling matrix elements are required. Periodic forcing can lead to a renormalization of the tunneling such that the effective hopping parameters become complex valued. The imaginary part of the effective tunneling matrix elements (Eq. (3.52)) is given by

$$\mathrm{Im}(J_{ij}^{\mathrm{eff}}/J) = \langle \sin(W_{ij}(t)/\hbar) \rangle_T \,, \tag{5.13}$$

where we have defined $W_{ij} = W_i - W_j$. It can only be non-zero provided that the function $W_{ij}(t)$ breaks two fundamental symmetries[2]. First, the function needs to break inversion symmetry

$$W_{ij}(t-\tau) = -W_{ij}(-t-\tau), \tag{5.14}$$

with respect to all points τ in time. Second, a shift inversion symmetry

$$W_{ij}(t) = -W_{ij}(t-T/2) \tag{5.15}$$

has to be broken. Here, T is the period of the function. If the lattice spacing does not change over time ($\mathbf{R}_i(t) - \mathbf{R}_j(t) = \text{const.}$) – which is always fulfilled for the experiments presented in this thesis – the symmetry breaking conditions stated in Eqs. (5.14) and (5.15) can be directly applied to the time-dependent momentum shift $\Delta\mathbf{p}(t)$, as can be inferred from Eq. (3.50). The analogue conditions for the driving function $v_{ij} \equiv v_i - v_j$ in the Hamiltonian (3.48) are given by the breaking of time-reversal symmetry

$$v_{ij}(t-\tau) = v_{ij}(-t-\tau) \tag{5.16}$$

(see Eq. (D.12)) and again the breaking of a shift inversion symmetry

$$v_{ij}(t) = -v_{ij}(t-T/2). \tag{5.17}$$

For rachet-type lattice experiments in the classical [214], as well as in the quantum regime [215], the same symmetries need to be broken to create directed currents. In this spirit, the asymmetric lattice forcing can lead to directed currents. Hence, our system belongs to the class of dissipationless quantum ratchets [215, 216]. However, the reverse conclusion does not hold: In general, a quantum ratchet cannot be described in terms of a synthetic vector gauge potential. This is only possible in the high frequency driving limit, where the Hamiltonian can be replaced by an effective version.

In case the lattice spacing is constant, the symmetry breaking conditions 5.16 and 5.17 can be directly applied to the forcing function itself. However, it is possible to create lattices with time- and also spatially dependent spacing by the usage of, e.g. superlattice geometries. This extends the possibilities of engineering gauge fields via periodic lattice forcing tremendously (see, e.g. [217]).

Any time-asymmetric forcing function, breaking those two symmetries, consist of more than one Fourier component. Experimentally this is a drawback because it is more involved to find a parameter regime, where the shaking does not lead to resonant band excitations.

5.3 Tunable Peierls Phase in a 1D Optical Lattice

5.3.1 Sine-Pulse Forcing

As a proof of principle experiment, we demonstrate the realization of a tunable vector gauge potential in a one dimensional lattice. The bosonic atoms in the lattice are

[2] A detailed proof of the symmetry breaking conditions required for complex valued renormalized tunnel matrix elements is given in appendix D.

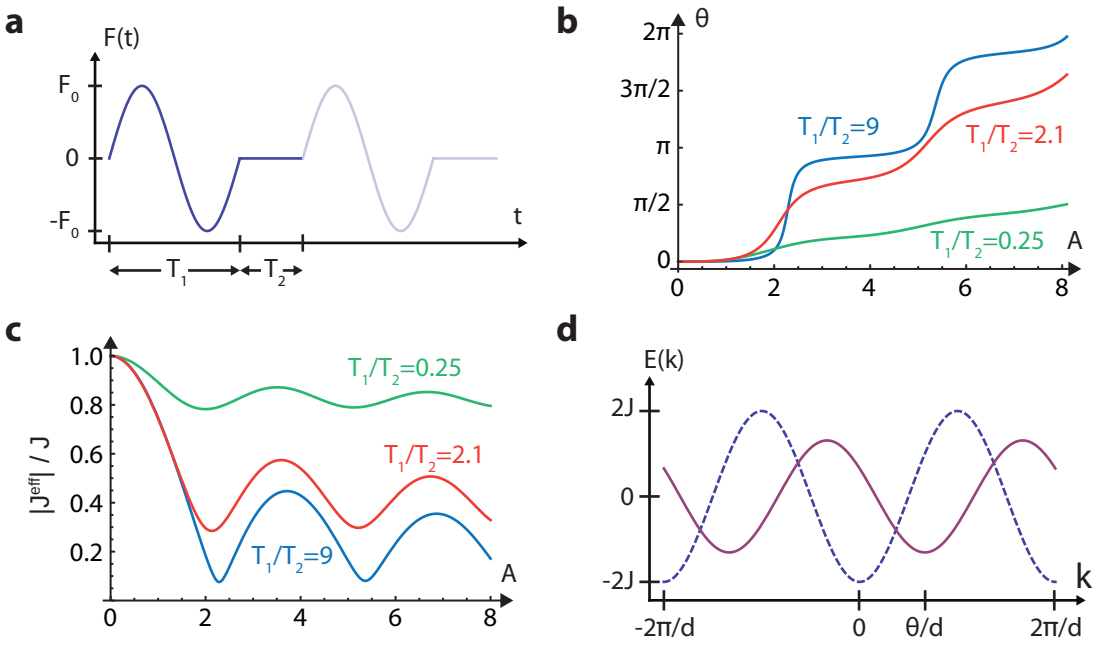

Figure 5.2: Asymmetric periodic driving of the lattice. **a** Forcing function comprised of trains of sinusoidal pulses, leading to complex valued tunneling matrix elements. **b** Phase and **c** absolute value of the tunneling matrix element for different ratios T_1/T_2 as a function of the forcing parameter A. **d** Modification of the tight binding dispersion relation due to the asymmetric driving. The dashed line indicates the dispersion relation of the undriven system, while the solid line shows the dispersion relation for the driven system.

subjected to an inertial force comprised of a train of sinusoidal pulses[3] (Fig. 5.2a),

$$F(t) = \begin{cases} F_0 \sin(\Omega_1 t) & \text{for } 0 \ < t \bmod T < T_1 \\ 0 & \text{for } T_1 < t \bmod T < T, \end{cases} \tag{5.18}$$

where T_1 ($\Omega_1 = 2\pi/T_1$) denotes the period (frequency) of the sine pulse, T_2 corresponds to rest time separating the sine pulses (Fig. 5.2a) and $T = T_1 + T_2$ is the period of the function. This forcing function clearly breaks the two symmetries 5.16 and 5.17 which is the prerequisite for the creation of complex hopping parameters. A calculation for the effective renormalized tunneling matrix elements (see appendix B.1) yields

$$J^{\text{eff}}_{i,i-1}/J = J^{\text{eff}}_{\rightarrow}/J = \frac{T_1}{T} \exp\left(-\mathrm{i}A\frac{T_2}{T}\right) J_0^{\text{B}}(A) + \frac{T_2}{T} \exp\left(\mathrm{i}A\frac{T_1}{T}\right), \tag{5.19}$$

$$J^{\text{eff}}_{i,i+1}/J = J^{\text{eff}}_{\leftarrow}/J = \left(J^{\text{eff}}_{\rightarrow}/J\right)^*, \tag{5.20}$$

where $J^{\text{eff}}_{\rightarrow}$ ($J^{\text{eff}}_{\leftarrow}$) describes the hopping process to the right (left) as shown in Fig. 5.1a by the blue (red) arrow. The variable A is the dimensionless forcing parameter. $J_0^{\text{B}}(A)$ denotes the zeroth order Bessel function of first kind. The Peierls phase is defined as

$$\theta = \arg(J^{\text{eff}}_{\rightarrow}), \tag{5.21}$$

[3]The corresponding frequency modulation of the laser beams, forming the running wave 1D lattice, can be found in appendix B.1.

giving rise to the following expression for the kinetic energy of the tight-binding lattice system:

$$H_{\mathrm{kin}} = -|J^{\mathrm{eff}}| \sum_i \left(\mathrm{e}^{\mathrm{i}\theta}\, \hat{a}_i^+ \hat{a}_{i-1} + \mathrm{e}^{-\mathrm{i}\theta}\, \hat{a}_i^+ \hat{a}_{i+1} \right) . \tag{5.22}$$

The ratio of the two periods T_1/T_2 strongly influences the renormalization behavior of the tunneling matrix element (Fig. 5.2a,b). For $T_2/T = 0$ the monochromatic driving of section 3.2 is recovered, which only leads to real valued tunneling elements. In the opposite limit of $T_1/T \to 0$, the absolute value of the tunneling $|J^{\mathrm{eff}}|$ only marginally depends on the forcing parameter, whereas the Peierls phase θ changes almost linearly with the forcing parameter. Nevertheless, in this regime, the phase is only slightly modified as a function of A. In principle, it is desirable to work in this limit. However, a strong forcing is required to reach significant values of the Peierls phase, which leads to heating of the atoms.

Therefore, we have chosen an intermediate value of $T_1/T_2 = 2.1$ (Fig. 5.2a,b) for the experiments presented in this section. In this case, the Peierls phase shows a pronounced nonlinear dependency on the forcing parameter A and the absolute value $|J^{\mathrm{eff}}|$ is also strongly modified by the renormalization.

The lattice depth for experiments presented in this chapter is $V_0 = 10 \pm 1 E_{\mathrm{rec}}$, corresponding to the tight-binding regime. This results in a bare tunneling element of $J = 7 \cdot 10^{-3} E_{\mathrm{rec}}$ and a band gap which is given by $E_{\mathrm{gap}} = 4.3 E_{\mathrm{rec}} = h \cdot 14.4$ kHz. Perpendicular to the lattice axis the atoms are only weakly confined by an optical dipole trap. This results in a periodic array of pancake-like density distributions[4]. We have chosen the period of the forcing as $T = 1$ms ($\Omega = 2\pi \cdot 1$kHz) in order to minimize the heating of the system.

Measurement of the Peierls Phase

A vector gauge potential introduces a shift of the dispersion relation

$$\epsilon(k) = -2|J^{\mathrm{eff}}| \cos(k d_{\mathrm{RW}} - \theta), \tag{5.23}$$

which is given by the Peierls phase θ. Here, k is the quasimomentum and $d_{\mathrm{RW}} = 486$nm the spacing of the lattice. The quasimomentum associated with the minimum of the dispersion relation is given by

$$k_{\mathrm{gs}} = \theta / d_{\mathrm{RW}}. \tag{5.24}$$

Starting with an undriven lattice, where the Peierls phase is zero, the atoms form a superfluid state at zero quasimomentum. Subsequently, we increase the forcing parameter according to a ramping function which is adapted to the nonlinear Peierls phase behavior (Fig. 5.2b). This ramp $A(t)$ is designed such that the nonlinearity of $\theta(A(t))$ is partially compensated. The total length of the ramp is adapted as well. For the maximum value of $A = 9$ the ramping time amounts to 120ms. After the final value of the forcing parameter has been reached, we wait for another 20ms to let the atoms relax to the new minimum of the dispersion relation. Afterwards, we suddenly switch of all confining potentials and record the momentum distribution of the atoms after TOF (Fig. 5.3a). The presence of sharp momentum peaks, up to a forcing parameter

[4] For more information on the density distribution, size of the lattice and interaction energy scales see Tab. C.1

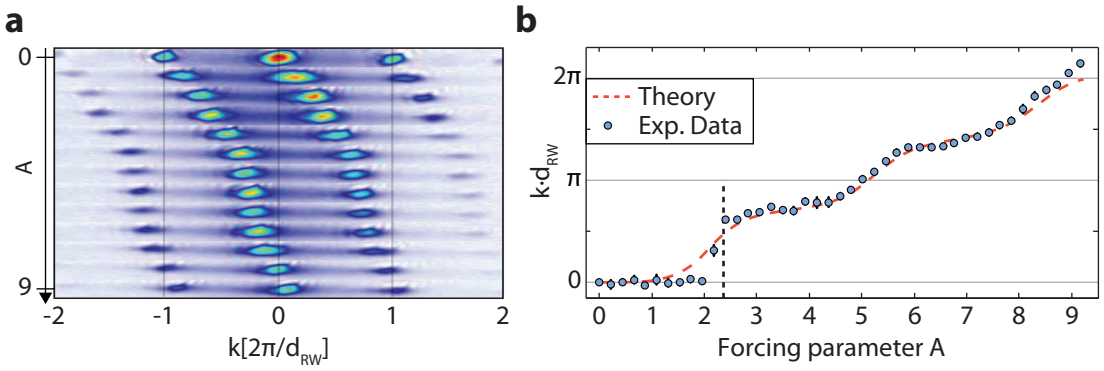

Figure 5.3: Momentum distribution under the influence of a tunable Peierls phase. **a** Momentum distribution of the one dimensional lattice recorded after TOF. The forcing parameter is successively increased from top to bottom, resulting in a shift of the quasimomentum to the right. **b** The data points correspond to the extracted quasimomenta of **a**, multiplied with the lattice spacing. The red dashed line indicates the ground state quasimomentum according to Eq. (5.24). The dashed vertical line marks the quasimomentum at which the onset of a dynamical instability is expected.

of $A = 9$, indicates that the driving does not lead to significant heating of the system and that the coherence across the lattice is preserved.

The corresponding quasimomentum of the Bloch-state can be determined according to the position of the momentum peaks in TOF. Figure 5.3b depicts the extracted quasimomentum versus the forcing parameter A. The agreement with the theoretical curve for the ground state quasimomentum given by Eq. (5.24) is very good. This shows, that via asymmetric periodic lattice shaking, complex tunneling elements can be engineered and that they can be tuned to any value $\theta \in [0, 2\pi[$. However, there is a systematic deviation between the measured quasimomentum and the theoretically expected ground state quasimomentum for small forcing parameters up to slightly above $A = 2$. The reason for this discrepancy is, that the atoms do not relax to the new quasimomentum ground state for small θ. We will postpone the explanation for this behavior to the end of this section, were we discuss the dynamical behavior of the system.

One important peculiarity about synthetic gauge potentials for ultracold atoms should be mentioned at this point: As the gauge potentials are directly engineered and not, e.g., created by a magnetic field, it is possible to choose between different specific gauges corresponding to the same gauge invariant quantities. Moreover, a specific gauge can be identified in TOF experiments. Indeed, all states are measured with respect to the momentum distribution in the laboratory frame (specific gauge). This can be understood as follows: If we perform a gauge transformation on an operator $\hat{O}$, e.g. given by Eqs. (5.8) and (5.9), then the states transform as

$$\hat{O} \to \hat{O}', \quad |\psi\rangle \to |\psi'\rangle\,. \tag{5.25}$$

The expectation values have to be invariant under this transformation:

$$\langle\psi'|\hat{O}'(\mathbf{k})|\psi'\rangle = \langle\psi|\hat{O}(\mathbf{k})|\psi\rangle\,. \tag{5.26}$$

In TOF measurements, a certain state in the lattice with a specific gauge is always measured with respect to laboratory momentum distribution. Hence, states belonging

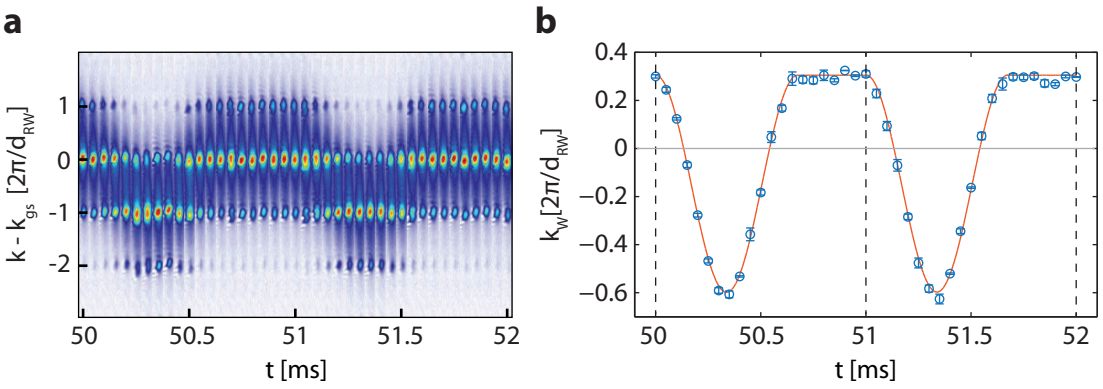

Figure 5.4: Time-resolved measurement of the driving cycle for $A = 2.8$. **a** The momentum distribution of the atoms, which is recorded over two driving cycles. The Wannier envelope clearly oscillates during the cycle, while the positions of the momentum peaks remain constant. **b** The data points correspond to the maxima of the Wannier envelope from **a**. The red line indicates the theoretically expected momentum shift of the atoms (Eq. (B.9)).

---

to different gauges have different momentum distributions, when measured in TOF:

$$\langle \psi' | \hat{n}_{\mathrm{lab}}(\mathbf{k}) | \psi' \rangle \neq \langle \psi | \hat{n}_{\mathrm{lab}}(\mathbf{k}) | \psi \rangle \,. \tag{5.27}$$

In this way, it is possible to distinguish between different gauges.

Driving Cycle Resolved Measurement of the Sine-Pulse Forcing

We performed time resolved measurements of the momentum distribution in order to exclude time-dependent shifts of the momentum peaks during a single driving cycle. Figure 5.4a clearly demonstrates that the positions of the momentum peaks remain fixed during a driving cycle. Hence, the measurement of the Peierls phase is independent of the specific timing with respect to the driving time-scale.

To further strengthen the agreement between theory and experiment, the time-resolved motion of the Wannier envelope, encoded in the momentum distribution, has been measured. According to Eq. (3.59) the center of the Wannier envelope k_W (fitted with a broad gaussian function) is directly connected to the time-dependent momentum shift of the atoms. The extracted position of the envelope is in excellent agreement with theoretical prediction of the respective momentum shift (Fig. 5.4b). This proves that the atoms accurately respond to the inertial forces, which are created by a suitable periodic acceleration of the lattice.

5.3.2 Dynamical Response to the Time-Dependent Peierls Phase

In the following, we analyze the dynamical response of the atoms to a time-dependent Peierls phase. A change of the Peierls phase imprints a force on the atoms and leads to oscillations of the atoms in the external harmonic confinement. These oscillations correspond to AC-currents in the lattice, which can decay via certain interaction induced instabilities. Thus, allowing the atoms to relax to the minimum of the dispersion relation.

Induced Dipole Oscillations

The oscillatory-behavior of the atoms can be qualitatively examined in a simplified, semi-classical single-particle model. A time-dependent change of the Peierls phase leads to a finite group velocity of the atoms, which were initially at rest. This can be described by a force of the form

$$F_\theta(t) = \hbar \frac{\mathrm{d}}{\mathrm{d}t} k_{\mathrm{gs}}(t) = \frac{\hbar}{d_{\mathrm{RW}}} \frac{\mathrm{d}}{\mathrm{d}t} \theta(t). \tag{5.28}$$

This is a semi-classical model describing the acceleration of the mean quasimomentum of the atoms. Note that this model is describing the effective, time-averaged behavior of the atoms: The fast periodic acceleration of the atoms due to the lattice driving has been already integrated out. Furthermore, interactions between the atoms are completely neglected. For simplicity we assume that the Peierls phase is linearly ramped up to the final value θ_0 over a time t_{R}, resulting in a time-dependent force given by

$$F_\theta(t) = \begin{cases} 0 & ;\ t < 0 \\ \hbar\theta_0 / \left(t_{\mathrm{R}} d_{\mathrm{RW}}\right) & ;\ 0 \leq t \leq t_{\mathrm{R}}, \\ 0 & ;\ t_{\mathrm{R}} < t, \end{cases} \tag{5.29}$$

where the starting point of the ramp has been assumed as $t = 0$ without loss of generality. The semi-classical equation of motion for a kicked particle, which is trapped in a lattice with an additional harmonic confinement, is given by

$$\frac{\mathrm{d}^2}{\mathrm{dt}^2} x(t) + {\omega_{\mathrm{eff}}}^2 x(t) = \frac{F_\theta(t)}{m_{\mathrm{eff}}(J,k)}, \tag{5.30}$$

where the quasimomentum k and position x are related by $\hbar k = m_{\mathrm{eff}} \dot{x}(t)$. Here,

$$m_{\mathrm{eff}}\left(|J^{\mathrm{eff}}|, k\right) = \hbar^2 \left(\frac{\mathrm{d}^2 \epsilon(k)}{\mathrm{dk}^2}\right)^{-1} \tag{5.31}$$

is the effective mass and

$$\omega_{\mathrm{eff}} = \omega \sqrt{\frac{m}{m_{\mathrm{eff}}}} \tag{5.32}$$

is the effective harmonic trapping frequency. The bare trapping frequency and mass are denoted by ω and m. Equation (5.30) describes a kicked non-linear pendulum, where the final oscillation frequency after the kick depends on the amplitude of the quasimomentum oscillations in the reciprocal space [76, 218, 219]. However, for small quasimomentum oscillations around the minimum k_{gs} of the dispersion relation, it is valid to simplify Eq. (5.30) by approximating the effective mass in lowest order as

$$m_{\mathrm{eff}}\left(|J^{\mathrm{eff}}|, k\right)\big|_{k=k_{\mathrm{gs}}} \approx \frac{\hbar^2}{2|J^{\mathrm{eff}}| d_{\mathrm{RW}}^2}. \tag{5.33}$$

In the following we neglect the time dependence of the tunneling matrix elements. In this approximation, Eq. (5.30) describes a kicked harmonic oscillator. For the initial conditions $x(t=0) = 0$ and $\dot{x}(t=0) = 0$, it has the solution

$$\begin{aligned} x(t) &= \frac{\hbar\theta_0}{d_{\mathrm{RW}}\, m_{\mathrm{eff}}\, \omega_{\mathrm{eff}}^2\, t_{\mathrm{R}}} \left(1 - \cos(\omega_{\mathrm{eff}}\, t)\right); \quad 0 < t < t_{\mathrm{R}} \\ x(t) &= \frac{\hbar\theta_0}{d_{\mathrm{RW}}\, m_{\mathrm{eff}}\, \omega_{\mathrm{eff}}} \frac{2\sin\left(\omega_{\mathrm{eff}} t_{\mathrm{R}}/2\right)}{\omega_{\mathrm{eff}} t_{\mathrm{R}}} \sin\left(\omega_{\mathrm{eff}}(t - t_{\mathrm{R}}/2)\right); \quad t_{\mathrm{R}} < t. \end{aligned} \tag{5.34}$$

This equation describes the oscillations induced by the change of the Peierls phase. The corresponding oscillations in the reciprocal space are given by

$$k(t) = \frac{\theta_0}{d_{\mathrm{RW}}\,\omega_{\mathrm{eff}}\,t_{\mathrm{R}}}\sin(\omega_{\mathrm{eff}}\,t); \quad 0 < t < t_{\mathrm{R}}$$
$$k(t) = \frac{\theta_0}{d_{\mathrm{RW}}}\frac{2\sin\left(\omega_{\mathrm{eff}}t_{\mathrm{R}}/2\right)}{\omega_{\mathrm{eff}}t_{\mathrm{R}}}\cos\left(\omega_{\mathrm{eff}}(t-t_{\mathrm{R}}/2)\right); \quad t_{\mathrm{R}} < t. \tag{5.35}$$

The amplitude of the oscillation after the kick ($t > t_{\mathrm{R}}$) is proportional to the induced Peierls phase and is linked to the ramping time via the term

$$\frac{2\sin\left(\omega_{\mathrm{eff}}t_{\mathrm{R}}/2\right)}{\omega_{\mathrm{eff}}t_{\mathrm{R}}} = \begin{cases} 1 & ;\ \omega_{\mathrm{eff}}t_{\mathrm{R}} \to 0 \\ 0 & ;\ \omega_{\mathrm{eff}}t_{\mathrm{R}} \to \infty \\ 0 & ;\ \omega_{\mathrm{eff}}t_{\mathrm{R}} = z\cdot 2\pi \quad z \in \mathbb{N}^*, \end{cases} \tag{5.36}$$

of Eqs. (5.34) and (5.35). The amplitude of the oscillation is small if the ramp time is long compared to the inverse of the effective trapping frequency. Furthermore, the amplitude perfectly vanishes for ramp times, which are a multiple of the effective trapping period ($2\pi/\omega_{\mathrm{eff}}$). For our experimental conditions, with $|J^{\mathrm{eff}}|/J \approx 1 \ldots 0.3$ the effective mass lies in the range of $m_{\mathrm{eff}}/m \approx 10 \ldots 35$. With a trapping frequency along the lattice axis of $\omega \approx 2\pi \cdot 20\mathrm{Hz}$, the effective frequency is within the range $\omega_{\mathrm{eff}} \approx (0.17 \ldots 0.31)\omega = 2\pi \cdot (3.1 \ldots 6.2)\mathrm{Hz}$. The resulting time scale for ramping of the Peierls phase without oscillations is therefore $t_{\mathrm{R}} \gg 1/\omega_{\mathrm{eff}} \approx 25 \ldots 50\mathrm{ms}$. Experimentally we are limited to ramp times on the order of a few hundreds of milliseconds, due to the finite lifetime of the system. In this regime oscillations are still present and have to be taken into account for the analysis of the dynamical behavior. Note that the solutions 5.34 and 5.35 are derived under the assumption of a constant absolute value of the tunneling matrix element and linear ramping of the Peierls phase. Both assumptions are not fulfilled in the experiments presented in this section. Nevertheless, the qualitative behavior should be described rather well with this model.

To create oscillations, we suddenly quench the Peierls phase to a value slightly below $\theta_0 = \pi/4$. The atoms experience a strong kick and are accelerated towards a Bloch state with finite group velocity (Fig. 5.5a). A superfluid current builds up and the cloud of atoms moves in real space. Due to the external harmonic confinement the atoms experience a restoring force towards the center of the trap. This results in oscillations of the center-of-mass position and quasimomentum as shown in Fig. 5.5b. The peak of the corresponding FFT spectrum (Fig. 5.5c) is located at 3.8Hz. This is in very good agreement with overall harmonic trapping frequency $\omega/(2\cdot\pi) \approx 20\mathrm{Hz}$ if we take into account an effective mass of $m_{\mathrm{eff}} = 35 \cdot m$, which is determined by $|J^{\mathrm{eff}}| = 0.3 \cdot J$ at a Peierls phase of $\pi/4$.

Relaxation to the Minimum of the Dispersion Relation

So far, the dynamical treatment of the atoms did not involve any kind of damping mechanism for the oscillations. Nevertheless, the system relaxes to the ground state with zero group velocity, which can only result from damping. The two mechanisms that lead to the dissipation of currents, i.e. the breakdown of superfluidity, are energetic (Landau) and dynamical (modulational) instabilities [23, 220]. In the lattice, both

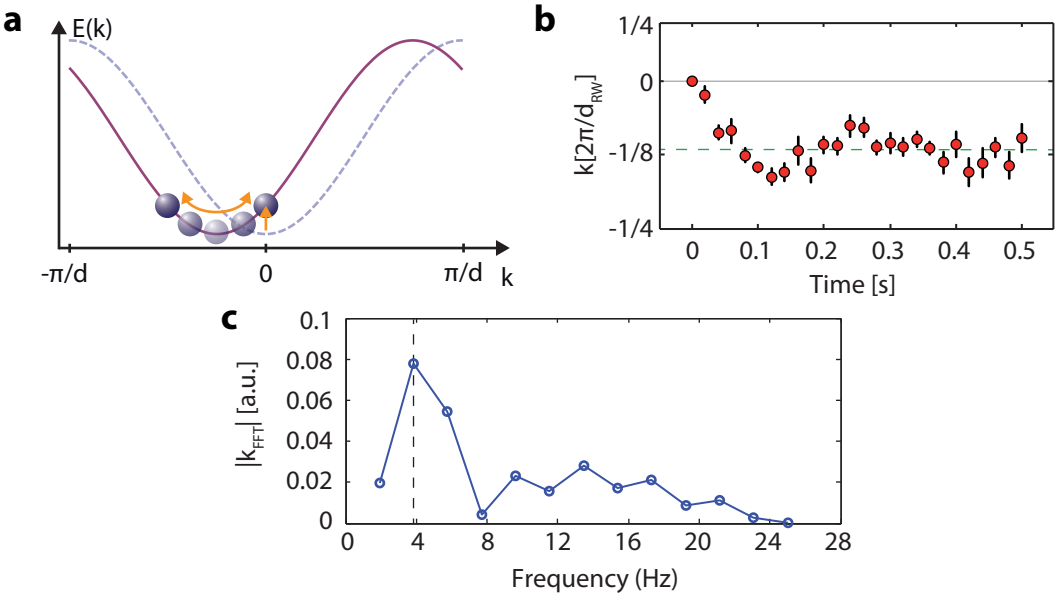

Figure 5.5: Sudden quench of the Peierls phase to 0.24π within a millisecond. **a** The quench results in an almost instantaneous promotion of the atoms into a Bloch state with non-zero group velocity. Due to the overall harmonic confinement the atoms perform oscillations in real and momentum space. **b** Extracted quasimomentum from TOF absorption images for times up to half a second. The atoms oscillate around the new quasimomentum ground state indicated by the dashed green line. **c** FFT spectrum of the quasimomentum measurement of **b**. The dashed vertical line marks the FFT peak at 3.8Hz.

mechanisms feature sharp onsets at respective critical quasimomenta. An energetic instability arises if the energy of the system can be lowered by creating phonons: The condensate is in a quasimomentum eigenstate that does not correspond to a minimum of the energy spectrum. Dynamical instabilities can be understood as small disturbances or fluctuations around the stationary solution of the system that grow exponentially in time. In this case, a part of the spectrum is complex valued. These two mechanisms have been extensively studied experimentally [81, 221–229] and theoretically [230–238] in the context of BECs in optical lattices.

In the tight-binding limit dynamical instabilities arise only for quasimomenta above the threshold [232, 235]

$$|k_{\mathrm{gs}}+k|d_{\mathrm{RW}} \geq \pi/2, \tag{5.37}$$

where k_{gs} is the ground state quasimomentum with zero group velocity. Intuitively, this can be understood by the sign inversion of the effective mass at this point: The mean field interactions become effectively attractive and lead to the dynamical instability of the condensate.

The onset of energetic instabilities typically occurs for smaller values of the quasimomentum than for dynamical instabilities. An analytical expression of the quasimomentum boundary of the Landau instabilities in the tight-binding limit is given in [235]. The region of the energetic instabilities decreases for increasing interaction strength. For the densities and interactions in the center of our lattice (see Tab. C.1) the region of energetic instability is vanishing. In combination with the fact that our system has no discernable thermal fraction before loading the atoms in the lattice, we conclude

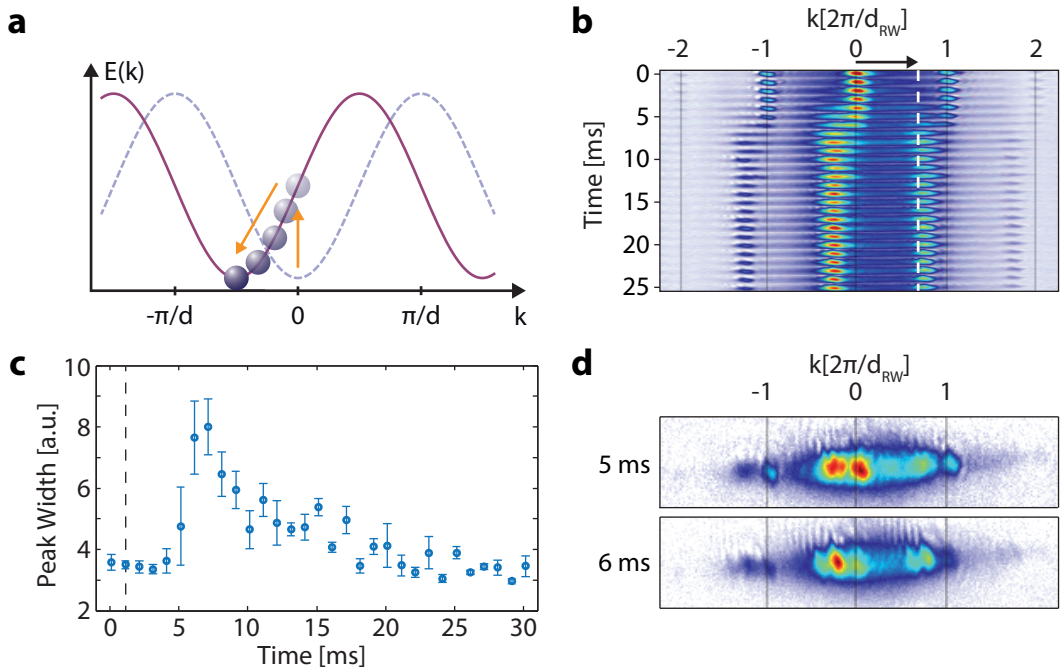

Figure 5.6: Sudden quench of the Peierls phase to 1.4π. **a** Almost instantaneous ramping of the Peierls phase accelerates the condensate towards a quasimomentum state with negative effective mass. **b** Evolution of the momentum distribution during the quench, measured in TOF. The white dashed line indicates the shift of the minima in the dispersion relation. The TOF images represent averages over 4 measurements. **c** Fitted gaussian width of the momentum peaks. The dashed line indicates the end of the ramp for the Peierls phase. **d** Single shot realizations of the momentum distribution in the vicinity of the dynamical instability.

that energetic instabilities should play no role in our experiment: Landau instability relies on the presence of a thermal component, while dynamical instability also occurs in the zero temperature limit [224, 228].

In order to investigate the dynamical instability, we have performed a second quench measurement. This time, the Peierls phase is increased from zero to a large value of 1.4π within one millisecond. Compared to the motion of the atoms in the harmonic trap, this quench is instantaneous and the atoms are accelerated towards $(k_{\mathrm{gs}}+k)d_{\mathrm{RW}} \approx 0.6\pi$ in the dispersion relation, where the effective mass becomes negative (Fig. 5.6a). It takes a few milliseconds until the condensate responds to this perturbation. The momentum peaks strongly broaden, indicating a loss of coherence (Fig. 5.6c) across the lattice. Nevertheless, the momentum peak structure is not completely lost during this process but features additional momentum peaks (Fig. 5.6d), which might hint on the exponential growth of collective modes in the BEC [81, 224, 236]. Shortly after the onset of the instability, the system recondenses close to k_{gs} (Fig. 5.6b). The recondensation process occurs on a very fast time scale of 10ms as can be inferred from the decrease of the momentum peak width in Fig. 5.6c. The weakly confined directions, perpendicular to the lattice axis, might serve as heat reservoir, where the entropy created by this non-adiabatic process can be stored. It is not clear, why the recondensation does not take place exactly at the quasimomentum ground state (see dashed line in Fig. 5.6b). One possible explanation is that the short time spent at the instability is not enough to completely damp out the dipole oscillations.

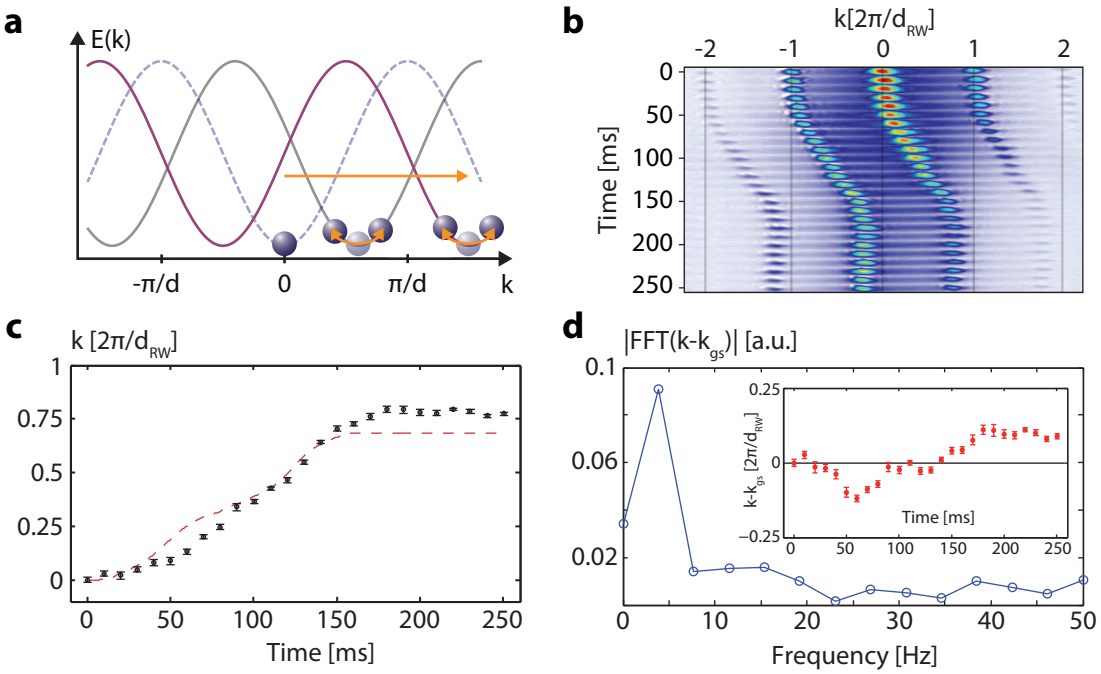

Figure 5.7: Dipole oscillations created by a slow increase of the Peierls phase. **a** Slow increase of the Peierls phase over a time of 160ms to the same value of the Peierls phase as in Fig. 5.6. The imprinted force on the condensate is to weak to accelerate the atoms into a dynamical instability. The quasimomentum oscillates around the changing ground state. **b** Evolution of the momentum distribution across the slow ramp, measured in TOF. **c** Extracted quasimomentum of **b** and theoretical position of the quasimomentum ground state (dashed red line) due to the finite Peierls phase. **d** FFT spectrum of the difference between the measured quasimomentum and the ground state of **c**. The inset shows the corresponding measurement in the time-domain.

In order to confirm that this kind of damping process only plays a role for oscillations with an amplitude larger or equal than $\pi/2$, we have performed the same measurement with a longer ramp duration for the Peierls phase. The ramp time now amounts to 160ms to reach a Peierls phase of 1.4π. In this case, the oscillations in the reciprocal space are expected to have an amplitude lower than required for a dynamical instability and should therefore show undamped oscillatory motion (5.7a). The time-resolved measurement of the momentum distribution of the atoms during and after the ramp is shown in Fig. 5.7. The momentum peaks are not broadened during the ramp of the Peierls phase (Fig. 5.7b), indicating that the coherence is preserved. By comparison of the measured quasimomentum with the actual position of k_{gs} throughout the ramping procedure one can clearly identify significant deviations. The difference between the quasimomentum of the atoms and the time- dependent ground state k_{gs} reveals an oscillatory motion (Fig. 5.7d). The frequency of the oscillation matches the one obtained from the measurements presented in Fig. 5.5.

Therefore, we can conclude that in our case the main damping mechanism for dipole oscillations of the condensate in the lattice is the onset of a dynamical instability [221, 230, 239] at a critical quasimomentum (Eq. (5.37)). Furthermore, the measured deviations reported in Fig. 5.3b can be explained by the lack of damping for small Peierls phases, where the atoms do not relax to the ground state but perform oscillations. The dashed vertical line in Fig. 5.3b indicates the expected onset of dynamical instability

according to Eq. 5.35 under the assumption that the ramping time t_{R} is short compared to the inverse of effective trapping frequency ω_{eff}.

5.4 Tunable Gauge Invariant Fluxes on a Triangular Lattice

The time-asymmetric lattice shaking, presented in the foregoing sections, can be extended to higher dimensional lattices. In this way, it is possible to create gauge-invariant fluxes. In general, simple global forcing, where atoms residing on different lattice sites experience the same force, can only lead to staggered flux patterns. This statement rests on a basic symmetry argument: Global forcing does not break the translational lattice symmetries. Therefore, the total gauge flux through a primitive cell must vanish, otherwise the periodicity of the lattice would change. Thus, a necessary – but not sufficient – condition for flux generation via global forcing is a lattice structure with a primitive cell containing more than one elementary plaquette. In this case, the flux through a single plaquette can be non-zero, even though the total flux through the primitive cell vanishes. This means that global shaking can be used to strongly deform the single particle dispersion relation, corresponding to a gauge-invariant staggered flux. However, it cannot lead to, e.g. periodicity changes and subband splitting [117]. In principle, these limitations can be overcome by the usage of more involved shaking schemes, e.g. oscillating superlattice potentials that lead to site dependent forces for the atoms [217].

In this section, we demonstrate the realization of tunable staggered gauge fluxes on a triangular optical lattice (Fig. 5.8), via time-asymmetric global lattice forcing. The primitive cell of the triangular lattice contains one upwards and one downwards pointing triangular plaquette. The sign of the flux changes between those two plaquette types, resulting in a zero total flux per primitive cell. A suitable lattice translation on a closed two-dimensional orbit (see appendix B.2) leads to the following inertial force acting on the atoms in the lattice frame

$$\mathbf{F}(t) = -F_{0,\mathrm{x}} \cos(\Omega t)\hat{\mathbf{e}}_{\mathrm{x}} - F_{0,\mathrm{y}} \left(\sin(\Omega t) + \delta \sin(2\Omega t)\right) \hat{\mathbf{e}}_{\mathrm{y}}. \tag{5.38}$$

This function is similar to the one used in the experiments of chapter 4 (Eq. (4.6)). However, it includes an additional higher harmonic term ($\delta \sin(2\Omega t)$). Therefore, it breaks the two symmetries given by Eqs. (5.16) and (5.17), provided the control parameter δ is non-zero.

The renormalization of the tunneling matrix elements and the corresponding integrals (Eqs. B.34 in appendix B.2) have been solved numerically. The forcing of Eq. (5.38) always leads to the same renormalization for the tunneling along the directions $2 \rightarrow 3$ and $3 \rightarrow 1$ (Fig. 5.8b), $J_{32}^{\mathrm{eff}} = J_{13}^{\mathrm{eff}}$. To simplify the notation we introduce the following nomenclature:

$$J'_{\mathrm{eff}} = J_{32}^{\mathrm{eff}} = J_{13}^{\mathrm{eff}}, \quad \theta' = \theta_{32} = \theta_{13}, \tag{5.39}$$

together with

$$J_{\mathrm{eff}} = J_{21}^{\mathrm{eff}}, \quad \theta = \theta_{21}. \tag{5.40}$$

The flux through the elementary plaquettes is given by

$$\Phi \equiv \Phi_{\triangle} = \theta_{21} + \theta_{32} + \theta_{13} = \theta + 2\theta' = -\Phi_{\triangledown}, \tag{5.41}$$

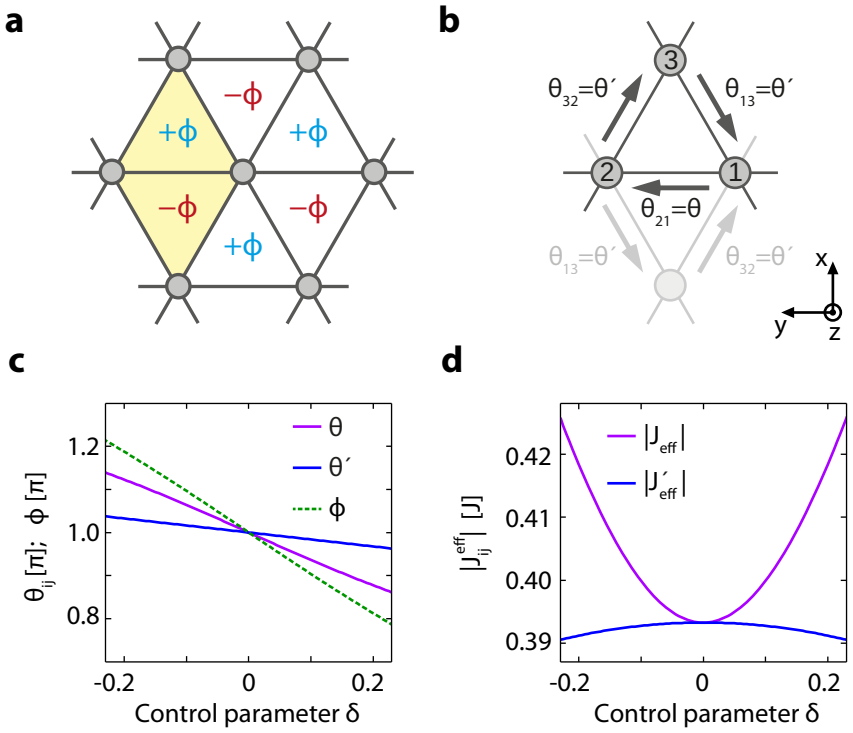

Figure 5.8: Gauge invariant staggered fluxes on a triangular lattice, created by asymmetric lattice shaking. **a** Staggered flux pattern realized by the periodic forcing as shown in Eq. (5.38). The primitive cell of the lattice is shaded in yellow. **b** Peierls phases on an elementary plaquette of the lattice. The transparent part of the figure corresponds to the rest of the primitive cell. **c** Flux strength and Peierls phases as a function of the control parameter δ, introduced in Eq. (5.38) **d** Absolute values of the tunneling matrix elements as a function of the control parameter δ. The dimensionless forcing parameters in **c** and **d** are $A = A' \approx 3.62$.

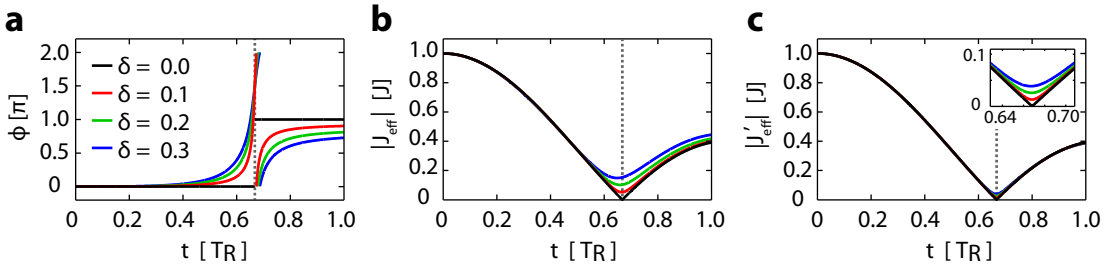

Figure 5.9: Evolution of the effective hopping parameters during the ramp. **a** Time-resolved behavior of the gauge flux strength and **b**, **c** the magnitudes of the tunneling along J_{eff} and J'_{eff} for four different values of the control parameter. The time t is given in units of the total ramp time T_{R}. A vertical dashed line marks the jump of the flux and the minima of J_{eff} and J'_{eff} for the case of $\delta = 0$. The inset of **c** is a magnification of the behavior around the minima of the curves.

where $\Phi_\triangle$ ($\Phi_\triangledown$) denotes the flux through the upwards (downwards) pointing triangular plaquettes. This quantity can be tuned via the control parameter δ (Fig. 5.8c).

We use the same dimensionless forcing parameters as defined in chapter 4 to quantify the driving strength. In the following, we focus on the case $A = A' = 3.616$ and small δ, where the magnitudes of the tunneling matrix elements $|J_{\text{eff}}|$ and $|J'_{\text{eff}}|$ only differ by a few percent (Fig. 5.8d).

In the tight-binding limit, the dispersion relation of the triangular lattice with complex hopping elements reads

$$\varepsilon(\mathbf{k}) = -2|J_{\text{eff}}| \left[\cos\left(\mathbf{k}\cdot\mathbf{d}_1 - \theta\right) + \cos\left(\mathbf{k}\cdot\mathbf{d}_2 - \theta'\right) + \cos\left(\mathbf{k}\cdot\mathbf{d}_3 - \theta'\right)\right], \tag{5.42}$$

where the $\mathbf{d}_i$ denote the lattice directions and are defined in Eq. (B.30). Under the assumption of separability, the dispersion relation in the z-direction has been omitted for clarity.

In the experiments presented in this section the atoms are only weakly confined along the z-directions. The density distribution of the atoms resembles an array of tubes. The lattice depth is $V_0 = 4.6 \pm 0.1 E_{\text{rec}}$, resulting in a bare single particle tunneling rate of $J = 4 \cdot 10^{-3} E_{\text{rec}}$ and a gap to the first excited band of $E_{\text{gap}} = (3.38 \pm 0.06) E_{\text{rec}} \approx h \cdot (11.3 \pm 0.2)\text{kHz}$. The shaking frequency has been chosen as $\Omega = 2\pi \cdot 2.791\text{kHz}$. Characteristic numbers for the system, e.g. interactions strength, occupied lattice sites, filling factors, etc., are summarized in Tab. C.3.

In this parameter regime the atoms form a superfluid state with well defined quasi-momentum. We initiate the experiments with an unshaken lattice, where the flux strength is zero. Subsequently, we linearly ramp up the amplitudes of the frequency modulation for the lattice beams over a ramp time of $T_{\text{R}} = 50\text{ms}$ (see Eqs. (B.26) and (B.27)). Hence, the flux strength is non-linearly increased (see Fig. 5.9a). After the final flux strength has been reached, lattice shaking is performed for a few more milliseconds at constant shaking amplitudes. Finally, the atoms are suddenly released from the lattice and their momentum distribution is recorded in a TOF measurement. While the gauge potential is ramped up the flux strongly varies at times between $t/T_{\text{R}} = 0.6$ and 0.7 (Fig. 5.9a). Furthermore, the magnitudes of the tunneling matrix elements become vanishingly small (Fig. 5.9b,c). The long time-scales, associated with the vanishing tunneling rate during the ramping procedure, lead to a non-adiabatic behavior of the system. Coherence across the lattice is lost during the ramp but the atoms start to recondense into the new minima of the dispersion relation, as soon as the magnitudes of the effective tunneling matrix elements start to increase again.

Figure 5.10a depicts the respective deformation of the dispersion relation (Eq. (5.42)) for different staggered fluxes. A flux strength of $\Phi = \pi$ results in an exactly inverted version of the dispersion relation for zero flux, with two degenerate minima in the first Brillouin zone. A non-zero value of the control parameter leads to flux deviations from $\Phi = \pi$. This lifts the degeneracy between the two minima, resulting in a global and a metastable minimum. The averaged momentum distribution of the atoms, released from the lattice, are shown in Fig. 5.10b[5]. We clearly observe a strong influence of the applied gauge flux onto the momentum distribution.

For the largest possible flux strength of $\Phi = \pi$, both minima are degenerate and on average equally populated. A reduced flux of $\Phi = \pi \pm 0.19\,\pi$, lifts the degeneracy

[5]The analysis of single shot measurements reveals strong fluctuations, which are presented and discussed in chapter 6.

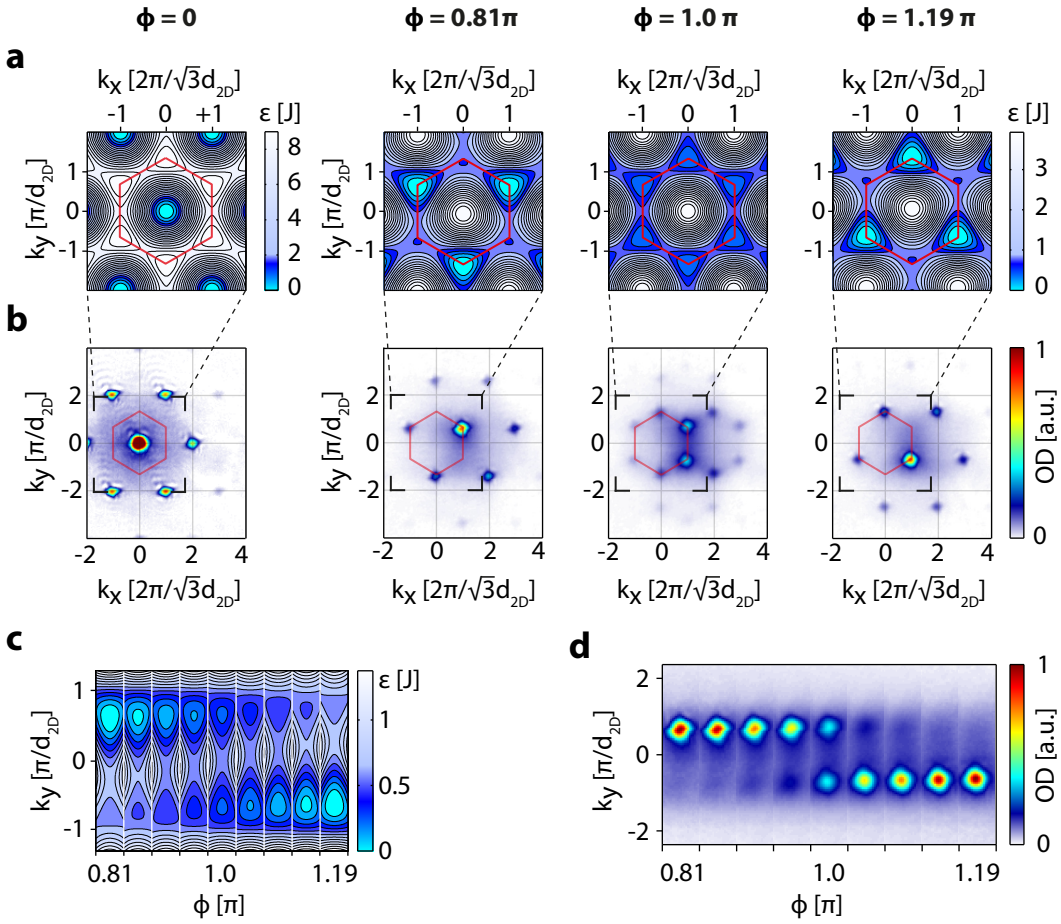

Figure 5.10: Influence of the staggered fluxes on the dispersion relation and momentum distribution. **a** Calculated tight-binding dispersion relations for different flux strength. Note the different colorbar for zero flux. The red solid line indicates the first Brillouin zone. **b** Momentum distribution of the atoms obtained in TOF measurements. The distributions are averages over many experimental realizations, thus corresponding to the expectation value. **c** Cut along the dispersion relation around $k_x = \pm 2\pi/\sqrt{3}d_{2D}$ for different values of the flux strength. **d** Corresponding averaged momentum distribution along $k_x = \pm 2\pi/\sqrt{3}d_{2D}$.

of the minima and the atoms mainly occupy the energetically lower lying minimum. Figures 5.10c and d demonstrate the tunability of the flux strength by focusing on the two minima in the first Brillouin zone. Due to the non-adiabaticity of the ramping process, the atoms do not necessarily condense into the ground state but also into the metastable minimum, provided the energy difference is not large. This behavior will be discussed in the next chapter. Therefore, the average population difference of the two minima can be continuously tuned as a function of the flux strength.

5.5 Conclusion and Outlook

In conclusion, we have successfully demonstrated the creation of complex valued tunneling matrix elements, by time-asymmetric lattice shaking. This mimics the effect of a vector gauge potential on a charged particle. The dynamical response of the quantum

gas to the non-adiabatic switching of the artificial gauge potentials has been investigated in depth. Thus, the onset of a dynamical instability was identified as the relevant process for current decay and relaxation towards the minimum of the dispersion relation. Furthermore, we have applied this method to the triangular lattice and realized tunable gauge invariant fluxes. The asymmetric lattice shaking offers a simple approach to the emulation of gauge fields for neutral atoms in optical lattices.

An alternative route for the creation of synthetic gauge fields is based on the Raman-coupling of internal states. This has been successfully demonstrated in a series of experiments [134–137]. Compared to these Raman-laser based approaches, the two major advantages of the time-asymmetric lattice driving are: First, lattice driving allows for the creation of fully tunable gauge potentials, which can be modified *in-situ*. Whereas, the gauge potentials created by Raman-lasers typically require a geometrical rearrangement of the beams, which cannot be performed *in-situ*. Second, the periodic lattice driving does not couple any internal states of the atoms. Therefore, the system is not subjected to a spontaneous scattering of photons, which generally leads to heating and reduced lifetime. However, time-asymmetric lattice driving leads to heating of the system as a consequence of excitations to higher bands (see chapter 3).

With the possibilities of a continuously tunable dispersion relation, the creation of period doubled states [236] via parametric amplification of Bloch-states [81] should be possible. This paves the way towards density modulated, supersolid phases in the triangular lattice, which posses two minima in a single Brillouin zone for a flux of π. A coherent superposition of the two Bloch-modes, corresponding to these minima, results in a density wave in real space.

Extension of the measurements into the strongly correlated regime might give access to an exotic intermediate phase in between the superfluid and Mott-insulating phases [240–242]. This phase, the chiral Mott-insulator, is characterized by a gapped excitation spectrum, vanishing long-range coherence but long-range order of chiral mass currents.

Chapter 6

Engineering Ising-XY Spin Models in a Triangular Lattice

A spin-model exhibiting a combined discrete $\mathbb{Z}_2$ (Ising) and continuous $U(1)$ symmetry is engineered in a triangular lattice. Full control over the $\mathbb{Z}_2$ symmetry is obtained by applying strong staggered gauge fluxes to the lattice. We define two distinct order parameters, the magnetization and the coherence, which are connected to the two symmetries of the system. The behavior of those order parameters is studied in dependence of the initial entropy and the gauge flux strength.

The fundamental concept of spontaneous symmetry breaking accompanying phase transitions plays a key role in statistical physics: Typically a low energy state looses symmetries contained in the underlying Hamiltonian, indicating that a phase boundary has been crossed. This is a purely statistical phenomenon driven by thermal or quantum fluctuations. The interplay between different classes of symmetries naturally raises the question of coupled ordered parameters and new universality classes [198, 243–247]. A paradigm for a system with combined discrete and continuous symmetries is the geometrically frustrated XY model on the triangular lattice, incorporating vector-spin related rotation symmetry and chiral inversion symmetry. At low temperatures the model shows a strong coupling behavior of the order parameters associated with vector-spin and chirality degrees of freedom [248]. In solid state physics it is difficult to resemble these types of models in a clean and controllable way. Until now, experimental studies have been mainly restricted to arrays of superconducting Josephson junctions [249–256].

In this chapter, we demonstrate the experimental realization of a model system with combined $U(1)$ and controllable $\mathbb{Z}_2$ (Ising) symmetry by applying tunable synthetic staggered gauge fluxes to atoms confined in a triangular lattice. We identify two distinct order parameters associated with long-range order of local on-site phases and staggered bosonic mass currents. A broken $U(1)$ symmetry or, in other words, long-range coherence is equivalent to Bose-Einstein condensation. The Ising symmetry, which is initially created in the system for maximum flux strength of π, can be broken on purpose by reducing the field strength. The system features substantial similarities to the classical Ising model in presence of a longitudinal magnetic field. A spontaneously broken $\mathbb{Z}_2$ symmetry can be interpreted as the analog of spontaneous magnetization occurring in an Ising ordered state.

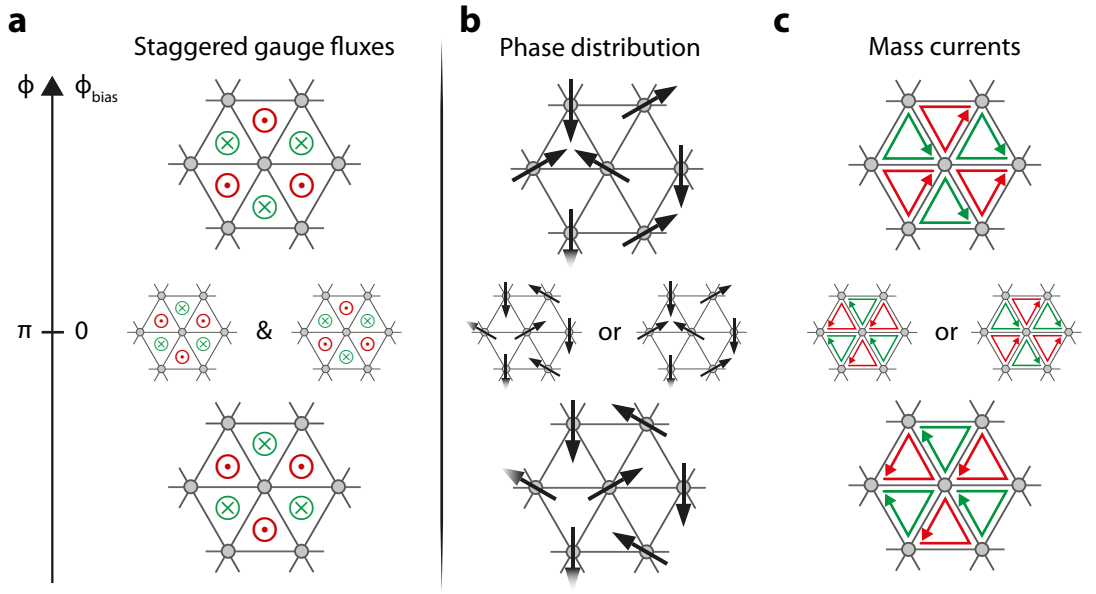

Figure 6.1: Illustration of the characteristic control parameter and the degrees of freedom of the system. **a** Control over the staggered flux strength allows to preserve ($\Phi_{\text{bias}} = 0$) or to break the $\mathbb{Z}_2$ symmetry ($\Phi_{\text{bias}} \neq 0$). **b** The Phase distribution of the on-site wavefunctions can be depicted as vector spins and **c** cyclotron like staggered mass currents. The red (green) arrows in **c** indicate mass currents flowing anticlockwise (clockwise) around the plaquettes.

The measurement of a suitable Ising order parameter reveals magnetization curves as a function of the staggered gauge flux strength and the temperature. A thermal phase transition from an ordered Ising (ferromagnetic) to an unordered (paramagnetic) state is observed. In addition, we are able to qualitatively observe changes of the $U(1)$ related order parameter or, in other words, of the coherence across the lattice, while breaking the $\mathbb{Z}_2$ symmetry on purpose. This indicates the strong coupling between both order parameters of the system.

Parts of this chapter have been published in [213]. The experiments and the data analysis presented in this chapter were performed within the team of: J. Struck, M. Weinberg, C. Ölschläger and J. Simonet.

6.1 Ising-XY Model

We experimentally realize a coupled $\mathbb{Z}_2 \times U(1)$, Ising-XY lattice model with ultracold bosons in a triangular lattice subjected to strong staggered gauge fluxes. Synthetic gauge fields are created by the method of periodic lattice driving as presented in section 5.4. The strength of the driving serves as an external control knob on the $\mathbb{Z}_2$ symmetry: Only in the limit of maximum flux ($\Phi = \pi$) per plaquette the symmetry is exactly preserved (Fig. 6.1a). In the single-particle dispersion relation this symmetry property is reflected in the presence of two degenerate minima in the first Brillouin zone (Fig. 5.10a).

Experimental parameters coincide with those of the measurements presented in section 5.4 (see also Tab. C.3). As in the preceding chapters, the atoms are only weakly confined along the direction perpendicular to the triangular lattice, giving rise to an

array of tubes. The system is described by the effective tight-binding Hamiltonian

$$H = -|J| \sum_{\langle ij \rangle} \mathrm{e}^{\mathrm{i}\theta_{ij}}\, \hat{a}_i^+ \hat{a}_j + U \sum_i \hat{n}_i(\hat{n}_i - 1), \tag{6.1}$$

where the spatial degrees of freedom along the tubes have been omitted for sake of clarity and under the assumption of phase stiffness along the tubes[1]. This means we assume that each tube (lattice site) can be described by a coherent state $\langle \hat{a}_i \rangle = \sqrt{n_i} \exp(\mathrm{i}\varphi_i)$, which is characterized by the phase φ_i. This reasoning is confirmed by classical Monte-Carlo simulations including the third spatial direction in a discretized form [257]. Nevertheless, it is important to keep in mind that the system is not two- but three-dimensional. The dimensionality has an important impact on the thermodynamic properties of the system. In addition, Eq. (6.1) assumes isotropic tunneling amplitudes

$$|J| \equiv |J_{\mathrm{eff}}| = |J'_{\mathrm{eff}}|\,, \tag{6.2}$$

which is fulfilled to good approximation for the periodic forcing of Eq. (5.38) with forcing parameters $A = A' \approx 3.62$, as can be seen in Fig. 5.8d. The flux per upwards pointing triangular plaquette is defined in Eq. (5.41) with the two independent Peierls phases θ and θ'. In the following we will use the better suited bias flux

$$\Phi_{\mathrm{bias}} \equiv \Phi - \pi = \theta + 2\theta' - \pi, \tag{6.3}$$

to describe the system under the influence of the staggered fields. The two symmetries $U(1)$ and $\mathbb{Z}_2$ are tied to the invariance of the Hamiltonian under the two transformations:

$$a_i \to \begin{cases} a_i\, \mathrm{e}^{\mathrm{i}\eta} & ;\ \text{Global rotation} \\ a_i^+ & ;\ \text{Local inversion.} \end{cases} \tag{6.4}$$

As can be easily seen, the Hamiltonian (6.1) is invariant under the global rotation transformation, thus implying a $U(1)$ symmetry. The second transformation leads to the following Hamiltonian:

$$\begin{aligned} H \to H' &= -|J| \sum_{\langle ij \rangle} \mathrm{e}^{\mathrm{i}\theta_{ij}}\, \hat{a}_j^+ \hat{a}_i + U \sum_i \hat{n}_i(\hat{n}_i - 1) \\ &= -|J| \sum_{\langle ij \rangle} \mathrm{e}^{-\mathrm{i}\theta_{ij}}\, \hat{a}_i^+ \hat{a}_j + U \sum_i \hat{n}_i(\hat{n}_i - 1). \end{aligned} \tag{6.5}$$

The transformation causes an inversion of the Peierls phases and therefore an inversion of the flux

$$\Phi \to \Phi' = -\theta - 2\theta', \tag{6.6}$$

meaning the energy spectrum changes, except for the cases $\Phi = 0$ or π. Hence, the Hamiltonian is only $\mathbb{Z}_2$ symmetric at a flux strength of zero or π.

For maximum staggered fluxes ($\Phi = \pi$) the equilibrium state of the system may spontaneously break the $\mathbb{Z}_2$ and/or the $U(1)$ symmetry as a consequence of phase transitions. We focus on a thermally driven phase transition but, in principle, similar

[1] The equivalent Hamiltonian – without gauge fields – including the spatial degrees of freedom in the third direction is given by Eq. (2.35).

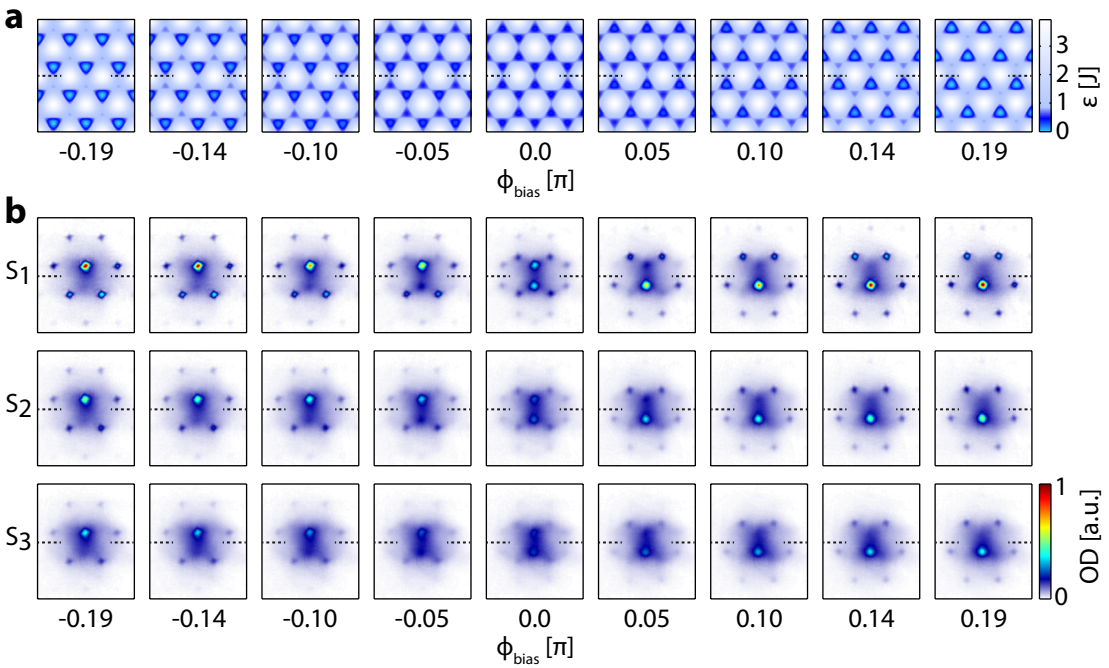

Figure 6.2: Measurement series of the momentum distribution. **a** Calculated tight-binding dispersion relation for different values of the bias flux Φ_{bias}. **b** Averaged momentum distributions for the corresponding values of the bias flux. The entropy was increased in descendent order of the rows ($S_1 < S_2 < S_3$).

spontaneous symmetry breaking effects can arise due to quantum phase transitions [240–242]. It is an interesting question, wether the $U(1)$ and $\mathbb{Z}_2$ symmetry are broken simultaneously or at distinct temperatures, corresponding to separated phase transitions. In the context of classical XY models on frustrated two-dimensional lattices this topic has been controversially debated over many decades [244–246, 258–264]. Recently, large-scale Monte-Carlo simulations were able to resolve two closely spaced but separated phase transitions in frustrated two dimensional lattice systems [265, 266].

In our case – of ultracold bosonic atoms in an optical lattice – the spontaneously broken $U(1)$ symmetry implies Bose-Einstein condensation. The local phases on each lattice site (Fig. 6.1b) show a long-range order, thus providing one of the two order parameters for the system. This parameter can be quantified by the first order correlation function in the infinite distance limit

$$\lim_{|\mathbf{R}_i-\mathbf{R}_j|\to\infty} \langle a_i^+ a_j \rangle = \text{const.} \cdot \mathrm{e}^{\mathrm{i}(\varphi_j-\varphi_i)} = \text{const.} \cdot \mathrm{e}^{\mathrm{i}\mathbf{q}(\mathbf{R}_j-\mathbf{R}_i)}. \tag{6.7}$$

Strong artificial gauge fluxes induce cyclotron-like mass currents around the plaquettes. Below a certain temperature, these mass currents develop a staggered long-range order with well defined chirality: All upwards pointing triangles feature mass currents with the same orientation and all downwards pointing triangles feature mass currents with the opposite orientation. Therefore, only two possible long-range ordered chiral configurations exist (see Fig. 6.1c). Both chiral configurations are energetically degenerate for $\Phi_{\text{bias}} = 0$. Thus, the emergence of a state with well defined chirality breaks the $\mathbb{Z}_2$ symmetry of the system. For non-zero bias flux one of the two possible chiral configurations is energetically preferred. If the magnitude of bias flux is smaller

than $\pi/2$, the first Brillouin zone exhibits two minima. However, for non-zero bias flux, the two minima are not degenerate and form a local (upper) and global (lower) minimum.

The second order parameter, related to the $\mathbb{Z}_2$ symmetry of the system, can be defined via the total staggered current of the lattice

$$\mathcal{J} = \sum_{s}^{M} \sum_{i=1}^{3} \left\langle \hat{j}_{\mathbf{d}_i s} \right\rangle , \tag{6.8}$$

with single bond currents $\langle \hat{j}_{\mathbf{d}_i s} \rangle$ flowing from lattice site s to the nearest-neighbor along the lattice direction $\mathbf{d}_i$ (see Eq. (B.30)). In the thermodynamic limit, a non-zero value of $\mathcal{J}$ signals the phase transition to a state with long-range ordered chiral mass currents and thus broken $\mathbb{Z}_2$ symmetry. As we will see in the next section, this can be identified with a non-symmetric occupation of quasimomentum states.

The total staggered current depends on the first order correlation function $\langle a_i^+ a_j \rangle$ as can be seen by the expression for the current along a single bond[2]:

$$\left\langle \hat{j}_{\mathbf{d}_i s} \right\rangle = -\frac{2|J|}{\hbar} \operatorname{Im} \left[\mathrm{e}^{\mathrm{i}\theta_i} \, \langle \hat{a}^+_{\mathbf{d}_i} \hat{a}_s \rangle \right] , \tag{6.9}$$

where $\hat{a}_{\mathbf{d}_i}$ is the annihilation operator at the lattice site described by the vector $\mathbf{R}_s + \mathbf{d}_i$ and θ_i is the Peierls phase corresponding to the tunneling process from site s to the nearest-neighbor in direction $\mathbf{d}_i$. Therefore, both order parameters are strongly linked.

To investigate the thermally driven phase transition, the initial entropy has been varied in three steps. Atoms were held for a different amount of time in the lattice before initiating the periodic lattice driving: The same sets of measurements have been performed for hold times of 0ms (S_1), 80ms (S_2) and 160ms (S_3). The entropy increases as a function of the hold time due to the technically induced heating of the atoms. Averaged momentum distributions for the three different measurement sets are shown in Fig. 6.2b together with the corresponding tight-binding dispersion relations (Fig. 6.2a).

It is possible to qualitatively extract information about both order parameters, related to the $U(1)$ and the $\mathbb{Z}_2$ symmetry, from the measured momentum distributions of the atoms. The width of the momentum peaks is related to the decay of the first order correlation function and the chiral order parameter is connected to the occupation of distinct parts of the Brillouin zone. In the next sections we will investigate the momentum distributions of single experimental realizations with respect to the introduced order parameters.

6.2 Measurement of the Magnetization

The total staggered flux of the lattice can be related to the momentum distribution of the atoms by the transformation of the current operator into the reciprocal space (see appendix E). For a lattice with tunneling directions $\mathbf{d}_i$ and corresponding Peierls phases θ_i along those directions, the current operator in reciprocal space is

$$\hat{j}_{\mathbf{d}_i s} = \frac{|J_i|}{\mathrm{i}\hbar M} \sum_{\mathbf{q},\mathbf{q}'} \hat{B}^+_{\mathbf{q}} \hat{B}_{\mathbf{q}'} \mathrm{e}^{\mathrm{i}(\mathbf{q}'-\mathbf{q})\mathbf{R}_s} \left(- \mathrm{e}^{\mathrm{i}(\theta_i - \mathbf{q}\mathbf{d}_i)} + \mathrm{e}^{-\mathrm{i}(\theta_i - \mathbf{q}'\mathbf{d}_i)} \right) , \tag{6.10}$$

[2]The expression for the current is derived in appendix E.

where M is the number of lattice sites and $\hat{B}_{\mathbf{q}} = \frac{1}{\sqrt{M}} \sum_i^M \hat{a}_i \exp(-\mathrm{i}\mathbf{q}\mathbf{R}_i)$ is the annihilation operator for a particle in the Bloch state with quasimomentum $\mathbf{q}$. Inserting Eq. (6.10) into Eq. (6.8) results in an expression for the total staggered flux (see appendix E)

$$\mathcal{J} = \frac{2|J|}{\hbar} \sum_{\mathbf{q}} \langle \tilde{n}_{\mathbf{q}} \rangle \, \mathcal{X}(\theta, \theta', \mathbf{q}), \tag{6.11}$$

which explicitly depends on the quasimomentum distribution $\langle \tilde{n}_{\mathbf{q}} \rangle = \langle \hat{B}_{\mathbf{q}}^{+} \hat{B}_{\mathbf{q}} \rangle$ of the atoms. The weighting function

$$\mathcal{X}(\theta, \theta', \mathbf{q}) = \sin(\mathbf{q}\mathbf{d}_1 - \theta) + \sin(\mathbf{q}\mathbf{d}_2 - \theta') + \sin(\mathbf{q}\mathbf{d}_3 - \theta'), \tag{6.12}$$

accounts for the specific gauges of the experiments (see Fig. 6.3a). This finally leads to gauge-independent results for $\mathcal{J}$ because the weighting function cancels gauge-dependent effects in the momentum distributions. The differences between the weighting functions for the distinct gauges, used in our experiments, are rather small (see Fig. 6.3a). In principle, we can use Eq. (6.11) to directly infer the total staggered mass current from the TOF absorption images. In case of $\Phi_{\mathrm{bias}} = 0$, a non-zero value of $\mathcal{J}$ requires a momentum distribution which violates inversion symmetry ($\langle \tilde{n}_{\mathbf{Q}+\mathbf{q}} \rangle \neq \langle \tilde{n}_{\mathbf{Q}-\mathbf{q}} \rangle$) with respect to the point $\mathbf{Q} = \left(\pi/\sqrt{3}\, d_{2\mathrm{D}}, \pi/d_{2\mathrm{D}}, 0\right)$. This reasoning does not hold for non-zero bias flux. In this case the weighting function $\mathcal{X}(\theta, \theta', \mathbf{q})$ of the total staggered current is nowhere point symmetric. Therefore, no symmetry constraints are imposed on the momentum distribution in order to acquire a finite total staggered mass current.

For the evaluation of the momentum distribution obtained in TOF, we have chosen a slightly different order parameter

$$\mathcal{M} = \sum_{\mathbf{k}} \langle \tilde{n}_{\mathbf{k}} \rangle \, \mathcal{X}(\theta, \theta', \mathbf{k}) \Big/ \sum_{\mathbf{k}} \langle \tilde{n}_{\mathbf{k}} \rangle \,, \tag{6.13}$$

which we call the magnetization. Here the summation over $\mathbf{k}$ indicates that all momentum components of the absorption images are considered and not only quasimomenta $\mathbf{q}$ which are restricted to a single Brillouin zone. The magnetization is closely related to the total staggered current per particle.

As the central point of this section, we investigate the thermal dependence of the magnetization. The measurement of the magnetization for the case of zero bias flux ($\Phi_{\mathrm{bias}} = 0$) reveals strong shot-to-shot fluctuations for low entropy (S_1). This results in a bimodal distribution in the corresponding histogram (see Fig. 6.3b). Most of the time, a non-zero magnetization is measured. Thus, the state of the system spontaneously breaks the $\mathbb{Z}_2$ symmetry of the Hamiltonian. In the classical Ising model this phenomenon is called spontaneous magnetization and signifies ferromagnetism. Increase of the entropy reduces the fluctuations until, for maximum entropy (S_1), the bimodal distribution has merged into a unimodal distribution which preserves the $\mathbb{Z}_2$ symmetry of the Hamiltonian. This corresponds to a thermally driven phase transition, similar to the ferromagnetic to paramagnetic transition in the Ising model.

Note that the experiment for low entropy corresponds to the same type of experiment as presented in section 4.6 with the degenerate spiral phases. The rather strong mean-field interactions between the atoms are responsible for the spontaneous magnetization in this system. Fragmented condensates are energetically disfavored as they are density waves in real space. Excitations resulting in zero net magnetization are probably related to domain formation as recently observed by Parker *et al.* [82].

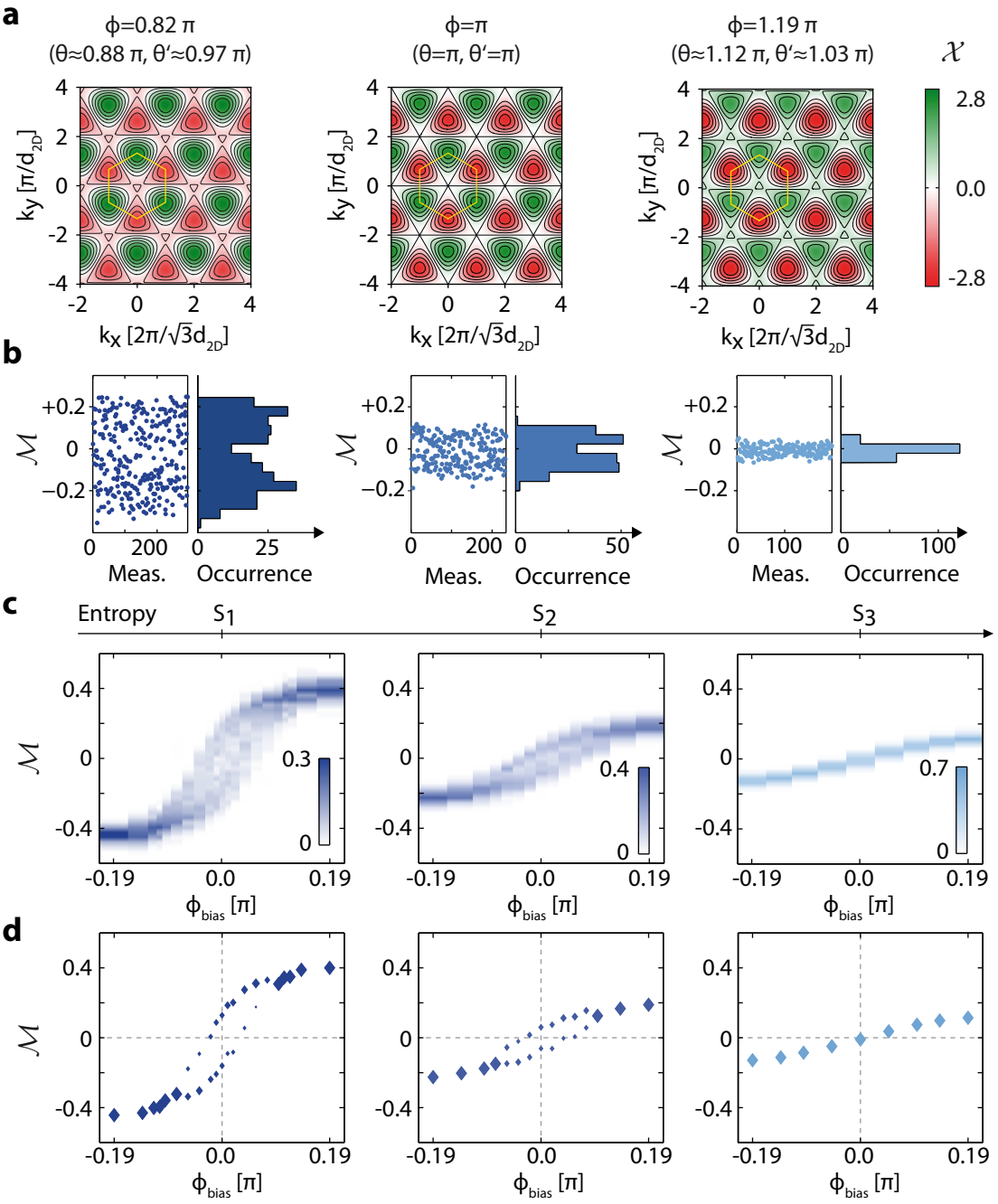

Figure 6.3: Measurement of the thermally driven phase transition. **a** The weighting function $\mathcal{X}(\theta, \theta', k)$ evaluated for three specific gauges of the experiments. **b** Consecutive measurements of the magnetisation $\mathcal{M}$ at zero bias flux (left) and the corresponding histograms of the statistical distribution (right) for three different entropies ($S_1 < S_2 < S_3$). **c** Collection of histograms for various different flux values and three different entropies. Each pixel column corresponds to a histogram for given bias flux Φ_{bias}. The histograms for $\Phi_{\text{bias}} = 0$ are shown in **b**. A single histogram consist of about 200 single measurements of $\mathcal{M}$. The histograms are normalized to the respective number of measurements that they contain. A colour code indicates the amplitudes of the histograms. **d** Maxima of Gaussian probability distributions fitted to the measured statistical distributions of $\mathcal{M}$. In case of bimodal distributions, where two maxima appear, the point sizes indicate the ratio of the amplitudes.

The tunability of the bias flux allows to lift the $\mathbb{Z}_2$ symmetry of the Hamiltonian on purpose. Hence, we can control which chiral order of the staggered mass currents is energetically favored. Opposite chiralities of the mass currents are reflected in an inversion of the sign of the magnetization. Therefore, the bias flux resembles the external longitudinal magnetic field in an Ising model. Figure 6.3c–d show the behavior of the magnetization as a function of the bias flux for the three different entropies S_1, S_2 and S_3. Subfigure 6.3c consists of a series of histograms for different bias fluxes, while subfigure 6.3d depicts the maxima of uni- or bimodal Gaussian probability distributions directly fitted to the set of measured magnetization values for a given flux (see Fig. 6.3b for the case of $\Phi_{\text{bias}} = 0$). The choice for the uni- or bimodal fit to the data is based on comparing the Schwarz-Bayes criterion [267] for both fits[3].

For large magnitudes of the bias fluxes we indeed magnetize the system in the energetically preferred chirality of the mass currents. In case of low enough entropy (S_1 and S_2) we observe two branches of magnetization for small bias fluxes. These two branches correspond to the occupation of the global- or local minimum of the dispersion relation, resulting in opposite chiralities of the mass currents. The occupation of a metastable state is a clear sign for non-equilibrium thermodynamics and arises from the non-adiabatic preparation of the final Ising state. Meanwhile increasing the gauge flux from initially zero to the final value around π, the magnitudes of the tunneling matrix elements become very small (Fig. 5.9b,c). This has the consequence that the dispersion relation becomes almost flat. Therefore, the timescales for adiabatic behavior of the system diverge. In this sense, the ramping procedure has to be understood as a non-adiabatic quench to the final state, even though the ramp time is not very fast (50ms). As a result, occupation of the local minimum occurs with a finite probability and the interactions tend to stabilize the atoms in this state, rendering it metastable.

The flux-dependent measurements of the magnetization (Fig. 6.3c,d) bear strong resemblance with the well-known hysteresis curves from the classical Ising model below the Curie temperature. Nevertheless, in our case, the two branches of the magnetization arise as a consequence of the non-adiabatic preparation of the final state. They do not occur due to the ramping of the magnetic flux from positive to negative values and vice versa.

The emergence of a metastable state, with a magnetization opposite to the bias flux, can be understood as a non-equilibrium signature for the ferromagnetic phase. Indeed, in the paramagnetic phase (S_3) we only observe a single branch of the magnetization.

6.3 Long-Range Order of the Phase Distribution

While the magnetization (Eq. (6.12)) is a measure for the long-range order of the chiral mass currents, the width of the momentum peaks is a measure for the decay of correlations between the vector spins over distance (see Fig. 6.1b). True long-range order is accompanied by the occupation of a single quasimomentum state and a broken $U(1)$ symmetry. Note the broken $U(1)$ symmetry is equivalent to the onset of BEC. Therefore, an increase in the width of the momentum peaks signals a decrease of the phase coherence. In other words: a faster decay of the first order correlation function.

From Fig. 6.2 we can infer that an increase of the entropy leads to the broadening of the momentum peaks, while an increase in the magnitude of the bias flux has the

[3]For more information on this analysis see the supplementary material of Ref. [213].

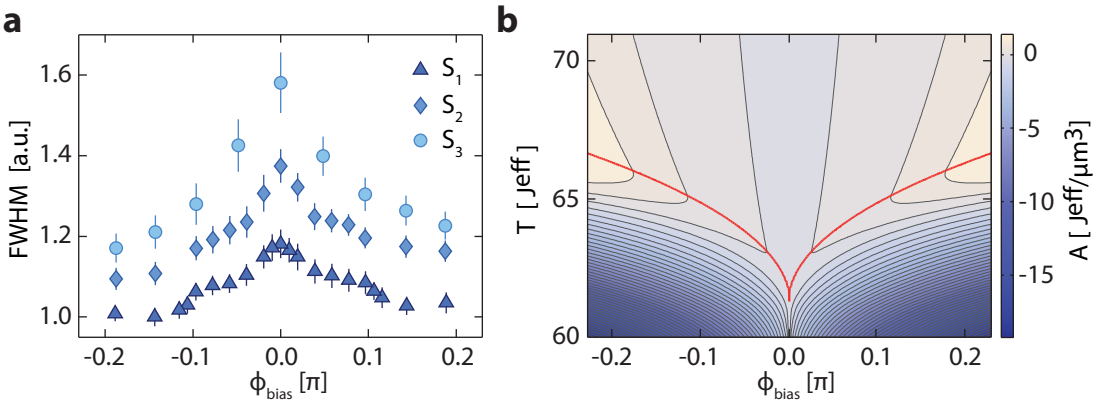

Figure 6.4: Momentum peak width and free energy of the system. **a** FWHM of the momentum peaks, determined with a Gaussian fit. The three measurement sets for different entropies are extracted from the same data as the magnetization $\mathcal{M}$ in Fig. 6.3. Decrease in long-range coherence is accompanied by a broadening of the peaks. **b** Free energy per volume A/V of the system obtained in a weak-coupling approximation [213, 257]. The red line marks a non-analytical behavior of the free energy, indicating the phase boundary between a thermal Bose gas and a condensate. Subfigure **b** was provided with kind permission of L. Mathey.

opposite effect. The full width at half maximum (FWHM) of the momentum peaks is extracted from the TOF absorption images by applying Gaussian fits to the peaks. Figure 6.4a depicts the extracted FWHM from the same set of measurements as shown in Figs. 6.2 and 6.3. As expected, we observe a strong dependence of the peak width on the entropy in the system: For increasing entropy the coherence decreases. This order of the coherence is maintained throughout all measurements, which explicitly confirms that $S_1 < S_2 < S_3$ is fulfilled for every flux value (see Fig. 6.4a). Furthermore, the peak width and thus the coherence strongly dependent on the bias flux. For all entropy measurements, we observe the same characteristic increase of the peak width towards zero bias flux. In this case the lattice is kinetically fully frustrated. This can be intuitively explained via the corresponding change of the single particle dispersion relation under the influence of staggered fluxes: The curvature of the minima decreases as a consequence of decreasing the magnitude of the bias flux. This leads to an increase in the density of states, thus to a lower critical temperature for BEC.

Note, however, that the extracted peak width does not reflect the true width of the momentum peaks but the convoluted width with the in-situ trap size of our atomic cloud. We are not imaging the atoms in the far field regime [176]. This, and the finite experimental resolution, prevents direct extraction of the condensate fraction and coherence length. Thus, we cannot exactly determine the presence or absence of a BEC close to the phase transition. With these experimental limitations it is difficult to deduce wether the phase transitions associated with the spontaneously broken $U(1)$ and $\mathbb{Z}_2$ symmetries occur simultaneously or at distinct temperatures.

The free energy of the system can be evaluated in a weak-coupling approach [213, 257, 268], where the interactions are considered as a first-order correction and the dispersion relation is expanded in second order around the two minima in the first Brillouin zone. A non-analytical behavior of the free energy signals the phase transition to a condensate. Figure 6.4b shows a pronounced cusp in the critical temperature which is perfectly consistent with the observed decrease in the long-range coherence for zero

bias flux (Fig. 6.4a).

6.4 Conclusion and Outlook

In conclusion, we have engineered a model featuring Ising-type $\mathbb{Z}_2$ and phase $U(1)$ symmetry by generating strong staggered gauge fluxes on a triangular lattice. A thermal phase transition from a state with long-range ordered chiral mass currents, spontaneously breaking the $\mathbb{Z}_2$ symmetry, to an unordered state has been observed. Furthermore, as a non-equilibrium signature for this transition, the occupation of metastable states with chiral currents opposite to the staggered fluxes has been measured. An analysis of the width of the momentum peaks revealed a strong influence of the gauge fluxes on the coherence length. This can be understood as a strong interplay between the associated discrete and continuous degrees of freedom.

In future experiments the exact coupling between the two types of phase transitions could be investigated in depth. There are strong indications that both transitions, which are of second order if they are isolated, merge into a single phase transition of first order [257]. This behavior is in contrast to two-dimensional XY systems, which have been realized with arrays of superconducting Josephson junctions [249–256]. In these systems, as the temperature is lowered, first the transition to a state with spontaneously broken $\mathbb{Z}_2$ symmetry is expected and then a Berezinsky-Kosterlitz-Thouless transition. In this sense we have realized a model system, which might constitute a playground to study novel kinds of coupled phase transitions.

Chapter 7

Towards Spin-Orbit Coupling in Driven Lattices

We discuss a scheme for the realization of a spin-orbit coupled tight-binding lattice system. The atoms are subjected to a spin-dependent periodic forcing, which is realized by an oscillating magnetic field gradient. This results in a spin selective renormalization of the tunneling matrix elements. In consequence, the dispersion relations for two spin states with inverse magnetic moments are shifted in opposite directions. Additional radio frequency coupling between the internal spin states of the atoms leads to a hybridization of the two spin bands. This resembles the effect of spin-orbit coupling.

The phenomenon of spin-orbit coupling generally describes an interplay between the spin state of a particle and its motional degrees of freedom. This effect naturally arises in the framework of relativistic quantum mechanics described by the Dirac equation. A spinful particle moving through an electric field experiences a magnetic field in the co-moving reference frame. The resulting interaction between the spin and the magnetic field depends on the amplitude of the field and thus on the velocity of the particle, leading to the coupling of motion and spin. A paradigm for the relevance of this coupling is the fine structure splitting encountered in atomic physics, where the spin of an electron – orbiting around the charged nucleus – is linked to its angular momentum. In solid state materials, spin-orbit coupling can result in exotic phases and phenomena, such as topological insulators [118, 269] or the spin Hall effect [141, 270–273].

The experimental realization of synthetic spin-orbit interactions with equal Rashba [274] and Dresselhaus [275] contributions for quantum degenerate bosons [139, 276] and fermions [277, 278] has raised considerable interest over the last years ([140] and references therein). Very recently, spin Hall phenomena have been observed with ultracold bosons [279]. All of these experiments rely on the use of Raman-laser schemes. In this chapter we introduce a novel method for the generation of artificial spin-orbit coupling via oscillating field gradients in a one-dimensional tight binding lattice[1].

[1] During the final preparation of this chapter we became aware of related approaches for the creation of spin-orbit coupling [280, 281].

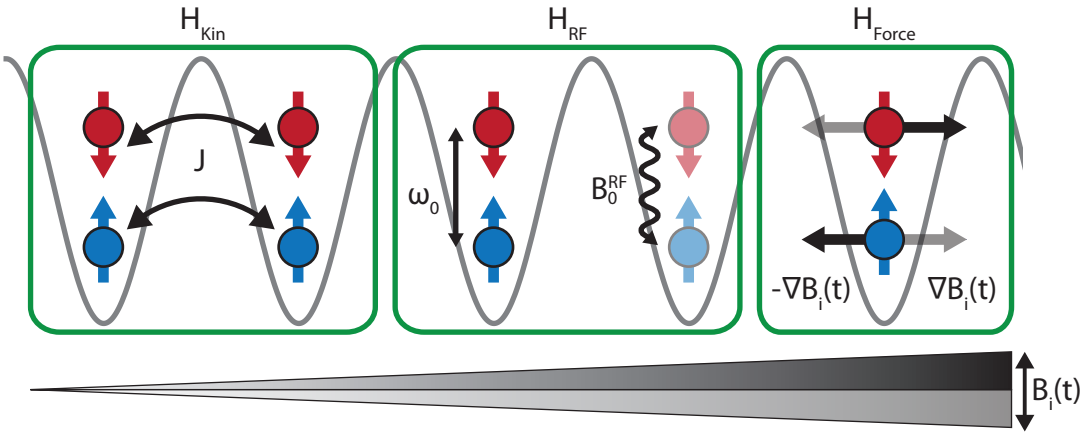

Figure 7.1: Schematic illustration of the relevant processes, which are captured in the two-component Hamiltonian (7.1).

7.1 Spin-Dependent Lattice Driving

We consider atoms with two internal spin states, confined in a one-dimensional lattice. The spin states are characterized by magnetic moments with same magnitude but opposite sign. An external, inhomogeneous, time-dependent magnetic field ($B_i(t) = B_i(t+T)$) periodically drives the atoms. The sign of the force is exactly inverted for both spin states. In addition, both internal spin states of the atoms are coupled via radio frequency fields.

The Hamiltonian of the system, neglecting the interactions and the harmonic confinement, can be separated into three parts (see Fig. 7.1):

$$H = H_{\mathrm{Kin}} + H_{\mathrm{RF}} + H_{\mathrm{Force}}. \tag{7.1}$$

First, H_{Kin} describes the next-neighbor tunneling processes, which are spin-independent and do not couple the spin states:

$$H_{\mathrm{Kin}} = -J \sum_i \left(\hat{a}_i^{\uparrow +} \hat{a}_{i-1}^{\uparrow} + \hat{a}_{i-1}^{\uparrow +} \hat{a}_i^{\uparrow} + \hat{a}_i^{\downarrow +} \hat{a}_{i-1}^{\downarrow} + \hat{a}_{i-1}^{\downarrow +} \hat{a}_i^{\downarrow} \right), \tag{7.2}$$

where $\hat{a}_i^{\uparrow(\downarrow)}$ is the annihilation operator for a spin-up (-down) particle on lattice site i. Second, H_{RF} describes a constant energy splitting $\hbar\omega_0$ of the spin states (e.g. due to a homogenous, time-independent magnetic field) and the coupling of both states by a radio wave:

$$H_{\mathrm{RF}} = \frac{\hbar\omega_0}{2} \sum_i \left(\hat{n}_i^{\uparrow} - \hat{n}_i^{\downarrow} \right) - B_0^{\mathrm{RF}} \cos(\omega_{\mathrm{RF}} t + \xi) \left[\mu_{\uparrow\downarrow} \sum_i \hat{a}_i^{\uparrow +} \hat{a}_i^{\downarrow} + \mu_{\uparrow\downarrow}^{*} \sum_i \hat{a}_i^{\downarrow +} \hat{a}_i^{\uparrow} \right], \tag{7.3}$$

where $\hat{n}_i^{\uparrow(\downarrow)} = \hat{a}_i^{\uparrow(\downarrow)+} \hat{a}_i^{\uparrow(\downarrow)}$ is the local number operator for spin-up (-down) atoms. The radio wave is characterized by the angular frequency ω_{RF}, the amplitude B_0^{RF} and some arbitrary phase ξ. The magnetic dipole matrix element between the spin-up and -down state is denoted by $\mu_{\uparrow\downarrow}$. The third term H_{Force} describes the spin-dependent driving of the atoms by the oscillating magnetic field:

$$H_{\mathrm{Force}} = \sum_i v_i(t) \left(\hat{n}_i^{\uparrow} - \hat{n}_i^{\downarrow} \right). \tag{7.4}$$

Here, $v_i(t) \equiv v_i^{\uparrow}(t) = -v_i^{\downarrow}(t) = -\mu B_i(t)$ describes the energy shift due to the magnetic field. The resulting force is proportional to gradient of the magnetic field and acts in opposite directions for spin-up and -down states.

The Hamiltonian (7.1) can be simplified by transforming into the co-rotating reference frame of the radio wave. This can be achieved with the unitary operator

$$U(t) = \exp\left(-\frac{\mathrm{i}}{2}\left[\omega_{\mathrm{RF}} t + \xi - \arg(\mu_{\uparrow\downarrow})\right] \sum_i (\hat{n}_i^{\uparrow} - \hat{n}_i^{\downarrow})\right), \tag{7.5}$$

which transforms the Hamiltonian (7.1) into H', according to

$$H' = U^{+} H U - \mathrm{i}\hbar\, U^{+}\left(\partial_t U\right). \tag{7.6}$$

Subsequently, we apply the rotating wave approximation, which discards the counter-rotating terms with $\omega_0 + \omega_{\mathrm{RF}}$, resulting in the Hamiltonian

$$\begin{aligned} H' \approx & -J \sum_i \left(\hat{a}_i^{\uparrow^+} \hat{a}_{i-1}^{\uparrow} + \hat{a}_{i-1}^{\uparrow^+} \hat{a}_i^{\uparrow} + \hat{a}_i^{\downarrow^+} \hat{a}_{i-1}^{\downarrow} + \hat{a}_{i-1}^{\downarrow^+} \hat{a}_i^{\downarrow}\right) + \frac{\hbar\Delta}{2} \sum_i \left(\hat{n}_i^{\uparrow} - \hat{n}_i^{\downarrow}\right) \\ & - \frac{\hbar\Omega_{\mathrm{RF}}}{2} \sum_i \left(\hat{a}_i^{\uparrow^+} \hat{a}_i^{\downarrow} + \hat{a}_i^{\downarrow^+} \hat{a}_i^{\uparrow}\right) + \sum_i v_i(t) \left(\hat{n}_i^{\uparrow} - \hat{n}_i^{\downarrow}\right). \end{aligned} \tag{7.7}$$

Here, $\Delta = \omega_0 - \omega_{\mathrm{RF}}$ is the detuning and $\Omega_{\mathrm{RF}} = |\mu_{\uparrow\downarrow}| B_0^{\mathrm{RF}} / 2\hbar$ the Rabi frequency.

7.2 Effective Spin-Orbit Coupled Hamiltonian

In this section, we introduce the effective time-averaged Hamiltonian. The basic theory behind this approach is detailed in chapter 3. Therefore, we will only sketch the most important steps. The effective Hamiltonian H_{eff} can be obtained from the time-periodic Hamiltonian H' by the relation

$$H_{\mathrm{eff}} = \left\langle U_Q^{+}(t) \left(H' - \mathrm{i}\hbar \frac{\partial}{\partial t}\right) U_Q(t) \right\rangle_T \tag{7.8}$$

(see Eq. (3.39)), with the unitary operator $U_Q(t) = \exp(-\mathrm{i}Q(t))$ and the notation $\langle \cdots \rangle_T = \frac{1}{T}\int_0^T \cdots \mathrm{d}t$ for the time-average. In order to cancel the driving term H_{Force}, which is the main purpose of this procedure, the time-periodic hermitian operator Q is chosen as

$$Q = \frac{1}{\hbar} \sum_i W_i(t) \left(\hat{n}_i^{\uparrow} - \hat{n}_i^{\downarrow}\right). \tag{7.9}$$

Here, $W_i(t)$ is defined by (see also Eq. (3.50)),

$$W_i(t) = \int_{t_0}^{t} \mathrm{d}t' v_i(t') - \left\langle \int_{t_0}^{t} \mathrm{d}t' v_i(t') \right\rangle_T. \tag{7.10}$$

The resulting expression for the effective Hamiltonian (7.8) is given by

$$\begin{aligned} H_{\mathrm{eff}} = & -J \sum_i \left(f\, \hat{a}_i^{\uparrow^+} \hat{a}_{i-1}^{\uparrow} + f^*\, \hat{a}_{i-1}^{\uparrow^+} \hat{a}_i^{\uparrow} + f^*\, \hat{a}_i^{\downarrow^+} \hat{a}_{i-1}^{\downarrow} + f\, \hat{a}_{i-1}^{\downarrow^+} \hat{a}_i^{\downarrow}\right) \\ & + \frac{\hbar\Delta}{2} \sum_i \left(\hat{n}_i^{\uparrow} - \hat{n}_i^{\downarrow}\right) - \frac{\hbar\Omega_{\mathrm{RF}}}{2} \sum_i \left(g_i\, \hat{a}_i^{\uparrow^+} \hat{a}_i^{\downarrow} + g_i^*\, \hat{a}_i^{\downarrow^+} \hat{a}_i^{\uparrow}\right). \end{aligned} \tag{7.11}$$

Here, the function

$$f \equiv \langle \exp\left(\mathrm{i}\left[W_i(t) - W_{i-1}(t)\right]/\hbar\right)\rangle_T\,, \tag{7.12}$$

describes the spin-dependent renormalization of the tunneling matrix elements, whereas

$$g_i \equiv \langle \exp\left(\mathrm{i}\,2W_i(t)/\hbar\right)\rangle_T\,, \tag{7.13}$$

describes the renormalization of the Rabi frequency, which in general depends on the lattice site index.

According to Eq. (7.11), the tunneling term of the two spin-components only differs in the sign of $\arg(f)$. A complex valued f leads to a shift of the two bare dispersion relations for the spin-up and -down components in opposite directions. This is analogous to the shift of a dispersion relation as a consequence of a finite Peierls phase (see chapter 5). The Rabi coupling between the two spin states leads to a hybridization of the two bare dispersion relations, resulting in two separated bands.

It is convenient to introduce a spinor notation with the two-component annihilation and creation vectors:

$$\psi_i = (a_i^{\uparrow}, a_i^{\downarrow})^{\mathrm{T}}, \quad \hat{\psi}_i^{+} = (a_i^{\uparrow +}, a_i^{\downarrow +}). \tag{7.14}$$

With this, the Hamiltonian (7.11) can be recast in the following form:

$$\begin{aligned} H_{\mathrm{eff}} = &- J \sum_i \left(\psi_i^{+} \begin{pmatrix} f & 0 \\ 0 & f^* \end{pmatrix} \psi_{i-1} + \psi_{i-1}^{+} \begin{pmatrix} f^* & 0 \\ 0 & f \end{pmatrix} \psi_i \right) + \frac{\hbar\Delta}{2} \sum_i \psi_i^{+} \begin{pmatrix} 1 & 0 \\ 0 & -1 \end{pmatrix} \psi_i \\ &- \frac{\hbar\Omega_{\mathrm{RF}}}{2} \sum_i \psi_i^{+} \begin{pmatrix} 0 & g_i \\ g_i^* & 0 \end{pmatrix} \psi_i\,. \end{aligned} \tag{7.15}$$

Furthermore, it proves advantageous to rewrite the Hamiltonian in terms of the Pauli matrices $\hat{\sigma}_{x,y,z}$ and the identity matrix $\mathbb{1}$:

$$\begin{aligned} H_{\mathrm{eff}} = &- J \sum_i \left(\hat{\psi}_i^{+} \left[\frac{f - f^*}{2}\,\hat{\sigma}_z + \frac{f + f^*}{2}\,\mathbb{1} \right] \hat{\psi}_{i-1} + \psi_{i-1}^{+} \left[\frac{f^* - f}{2}\,\hat{\sigma}_z + \frac{f + f^*}{2}\,\mathbb{1} \right] \psi_i \right) \\ &+ \frac{\hbar\Delta}{2} \sum_i \psi_i^{+}\,\hat{\sigma}_z\,\psi_i - \frac{\hbar\Omega_{\mathrm{RF}}}{2} \sum_i \psi_i^{+} \left[\frac{g_i + g_i^*}{2}\,\hat{\sigma}_x + \mathrm{i}\,\frac{g_i - g_i^*}{2}\,\hat{\sigma}_y \right] \psi_i. \end{aligned} \tag{7.16}$$

If we decompose the complex numbers f and g_i into magnitude and phase $f{=}|f|\exp(\mathrm{i}\theta)$, $g_i{=}|g_i|\exp(\mathrm{i}\chi_i)$, we can write down the simplified version of the effective Hamiltonian

$$\begin{aligned} H_{\mathrm{eff}} = &- |J^{\mathrm{eff}}| \sum_i \left(\psi_i^{+}\,\mathrm{e}^{\mathrm{i}\theta\hat{\sigma}_z}\,\psi_{i-1} + \psi_{i-1}^{+}\,\mathrm{e}^{-\mathrm{i}\theta\hat{\sigma}_z}\,\psi_i \right) \\ &+ \frac{\hbar\Delta}{2} \sum_i \hat{\psi}_i^{+}\,\hat{\sigma}_z\,\hat{\psi}_i - \frac{\hbar\Omega_{\mathrm{RF}}}{2} \sum_i |g_i| \psi_i^{+} \left[\cos(\chi_i)\,\hat{\sigma}_x - \sin(\chi_i)\,\hat{\sigma}_y \right] \psi_i, \end{aligned} \tag{7.17}$$

Here, we have defined the magnitude of the renormalized tunneling matrix element as $|J^{\mathrm{eff}}| = J \cdot |f|$. Examination of the effective Hamiltonian (7.17) reveals a spin-dependent tunneling without mixing of the components.

For strong radio frequency coupling of the internal spin states it is reasonable to work with dressed states that diagonalize the radio frequency term of Eq. (7.17). The Hamiltonian can be transformed into the dressed spin state basis by subsequent application of the unitary transformations $T_i = \exp(\mathrm{i}\chi_i\hat{\sigma}_z/2)$ and $G = \exp(\mathrm{i}\pi\hat{\sigma}_y/4)$. The

first transformation T_i corresponds to a local rotation in spin space around the z-axis followed by the global spin rotation G around the y-axis. These transformations finally lead to the expression

$$H_{\text{eff}} = -|J^{\text{eff}}| \sum_i \left(\psi_i'^{+} \, \mathrm{e}^{-\mathrm{i}(\theta+[\chi_{i-1}-\chi_i]/2)\hat{\sigma}_x} \, \psi'_{i-1} + \psi'^{+}_{i-1} \, \mathrm{e}^{\mathrm{i}(\theta+[\chi_{i-1}-\chi_i]/2)\hat{\sigma}_x} \, \psi'_i \right) + \frac{\hbar\Delta}{2} \sum_i \psi_i'^{+} \, \hat{\sigma}_x \, \psi'_i + \frac{\hbar\Omega_{\text{RF}}}{2} \sum_i |g_i| \psi_i'^{+} \, \hat{\sigma}_z \, \psi'_i, \tag{7.18}$$

where the dressed spinors $\psi_i'^{+} = \psi_i^{+} T_i G$ and $\psi'_i = G T_i^{+} \psi_i$ have been introduced. Tunneling processes in the dressed spin state basis are not diagonal and lead to mixing of both components. The Hamiltonian (7.18) resembles the tight-binding lattice version of a spin-orbit coupled system with equal Rashba and Dresselhaus contributions. The strength of the spin-orbit coupling is described by the parameter

$$\alpha = \theta + [\chi_{i-1} - \chi_i]/2. \tag{7.19}$$

In general, the lattice site dependence of the radio frequency coupling term lifts the translational symmetry of the Hamiltonian and prevents the description in terms of a band structure. However, for certain driving functions, the site dependence can be neglected. This will be discussed in the following section based on the example of sine pulse forcing.

7.3 Sinusoidally Pulsed Magnetic Field Gradient

Sine pulse forcing has already been considered in section 5.3 (see also appendix B.1) and we can reuse most of the results. Here, the forcing is realized by a time dependent magnetic field

$$B_i(t) = B_0 \, i \begin{cases} \sin(\Omega_1 t) & \text{for } 0 \ < t \bmod T < T_1; \ (1) \\ 0 & \text{for } T_1 < t \bmod T < T \ ; \ (2). \end{cases} \tag{7.20}$$

According to Eqs. (7.10) and (B.9) one obtains

$$W_i(t) = \hbar \, K \, i \begin{cases} \cos(\Omega_1 t) - T_2/T & (1) \\ T_1/T & (2), \end{cases} \tag{7.21}$$

with the dimensionless forcing parameter

$$K = \frac{\mu_{\text{B}} m_F g_F B_0}{\hbar \Omega_1}. \tag{7.22}$$

In this calculation, K is defined via the quantum number m_F and Landé factor g_F of the spin-up state[2]. For the parameters f (Eq. 7.12) and g_i (Eq. 7.13) we can readily use the results of section 5.3 (see Eq. (5.19)):

$$f = \frac{T_1}{T} \exp\left(-\mathrm{i}K\frac{T_2}{T}\right) J_0^{\text{B}}(K) + \frac{T_2}{T} \exp\left(\mathrm{i}K\frac{T_1}{T}\right), \tag{7.23}$$

$$g_i = \frac{T_1}{T} \exp\left(-\mathrm{i}2Ki\frac{T_2}{T}\right) J_0^{\text{B}}(2Ki) + \frac{T_2}{T} \exp\left(\mathrm{i}2Ki\frac{T_1}{T}\right). \tag{7.24}$$

[2]This convention only plays a role concerning the sign of K.

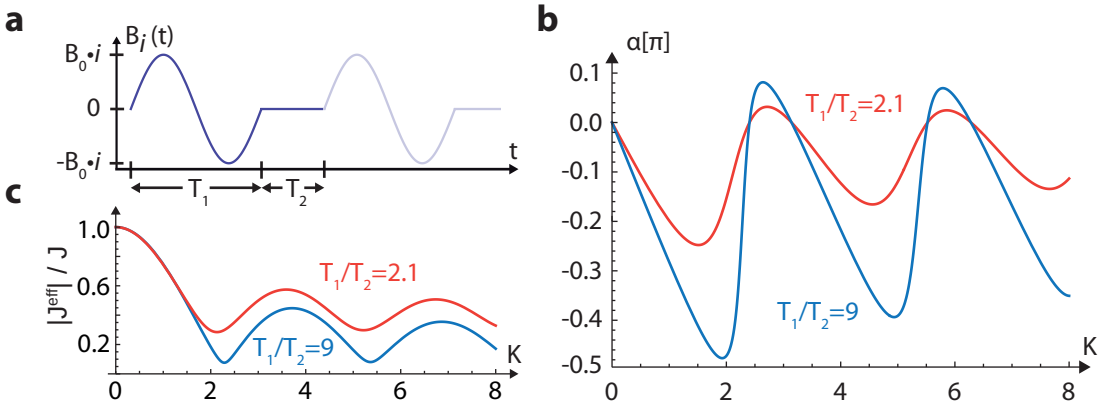

Figure 7.2: Spin-dependent driving of the atoms with sine-pulses. **a** The amplitude of the magnetic field gradient is modulated with trains of sinusoidal pulses. **b** The resulting spin-orbit coupling strength. **c** The magnitude of the renormalized tunneling matrix elements. In **b** and **c** the colored lines correspond to different ratios T_1/T_2 of the pulse to hold time.

The lattice site with index $i = 0$ is defined as the site where the magnetic field vanishes (see Eq. (7.20)). If we assume that the zero-crossing of the magnetic field gradient is far away from the atoms ($2Ki \gg 0$), Eq. (7.24) can be approximated by

$$g_i \approx \frac{T_2}{T} \exp\left(\mathrm{i}2Ki\frac{T_1}{T}\right). \tag{7.25}$$

In this case, the magnitude of g_i is site independent

$$|g_i| \approx \frac{T_2}{T} \equiv |g| \tag{7.26}$$

and the argument is given by

$$\chi_i \approx 2Ki\frac{T_1}{T}. \tag{7.27}$$

Figure 7.2 displays the resulting spin-orbit coupling strength (Eq. (7.19)) as a function of the forcing parameter.

7.4 Spinful Dispersion Relation

The dispersion relation of the spin-orbit coupled system can be determined by transforming the dressed state spinors into reciprocal space via the relation

$$\psi_i' = \frac{1}{\sqrt{M}} \sum_q \phi_q' \mathrm{e}^{\mathrm{i}\,q\,d\,i}, \tag{7.28}$$

where M is the number of lattice sites and the reciprocal spinor is

$$\phi_q' = \left(\hat{B}_q^{\uparrow\prime}, \hat{B}_q^{\downarrow\prime}\right)^{\mathrm{T}}. \tag{7.29}$$

Here $\hat{B}_q^{\uparrow\prime}$ is the annihilation operator for the dressed spin-up particle in the Bloch state with quasimomentum q. Expansion of the spinors in Bloch states (Eq. (7.28)) transforms Eq. (7.17) into

$$H_{\mathrm{eff}} = \sum_q \phi_q'^{+} \mathfrak{H}'(q)\, \phi_q', \tag{7.30}$$

with

$$\mathfrak{H}'(q) = -2|J^{\text{eff}}|\left(\cos(\alpha)\cos(qd)\,\mathbb{1} - \sin(\alpha)\sin(qd)\,\hat{\sigma}_{\text{x}}\right) + \frac{\hbar\Delta}{2}\hat{\sigma}_{\text{x}} + \frac{\hbar\Omega_{\text{RF}}^{\text{Eff}}}{2}\hat{\sigma}_{\text{z}}\,, \tag{7.31}$$

where the effective renormalized Rabi frequency has been defined as $\Omega_{\text{RF}}^{\text{Eff}} = \Omega_{\text{RF}}|g|$. The quasimomentum dependent eigenvalues of the 2×2 matrix $\mathfrak{H}'$ represent the two lowest spinful bands of the spin-orbit coupled tight-binding lattice.

Diagonalization of $\mathfrak{H}'$ is straightforward and the resulting dispersion relations for different values of the spin-orbit coupling strength α, detuning Δ and effective Rabi frequency $\Omega_{\text{RF}}^{\text{eff}}$ are shown in Fig. 7.3. An increase of $\Omega_{\text{RF}}^{\text{eff}}$ leads to a larger splitting of the two bands, while the bandwidth decreases (Fig. 7.3a). The strength of the spin-orbit coupling strongly impacts on the separation of the minima (maxima) of the lowest (upper) band (Fig. 7.3b). A finite value of the detuning Δ lifts the degeneracy of those minima (Fig. 7.3c). For $\alpha = 0$ – corresponding to the case of no spin-orbit coupling – only one minimum is present within the first Brillouin zone of each band.

So far, we have not evaluated the driving frequency constraints imposed by the description of the system with the effective Hamiltonian (7.11). The validity of the effective Hamiltonian approach relies on small coupling terms between the different Floquet bands (see Eq. (3.40)) compared to the energy scale of the shaking frequency. For the Hamiltonian (7.11), the coupling between the Floquet bands arises due to the kinetic part and the radio frequency terms, which scale with the Rabi frequency. This results in the additional condition

$$\Omega_{\text{RF}} \ll \Omega, \tag{7.32}$$

besides those given in Eqs. (3.56) and (3.57). The energy scale of the Rabi frequency is on the order of the tunneling rate (see Fig. 7.3). Thus, the constraint given by Eq. (7.32) is typically fulfilled, if the driving frequency is large compared to the tunneling matrix elements.

7.5 Conclusion and Outlook

To conclude, we proposed a method based on spin-dependent shaking and radio frequency fields that can be used to engineer spin-orbit coupling for neutral atoms in an optical lattice. In this scheme the coupling strength is tunable.

The presented scheme could be realized in the case of ^{87}Rb with the two hyperfine states $|\uparrow\rangle \equiv |F = 1, m_F = -1\rangle$ and $|\downarrow\rangle \equiv |F = 2, m_F = -1\rangle$ of the $5^2S_{1/2}$ ground state. The required magnetic field gradient for a forcing parameter K would be

$$\frac{B_0}{d} = K\frac{\hbar\Omega_1}{d\mu_{\text{B}}m_F g_F} \approx K \cdot 21\frac{\text{G}}{\text{cm}}, \tag{7.33}$$

where we have assumed the frequency $\Omega_1 = 2\pi \cdot 1.48\text{kHz}$, which is the same as in section 5.3 and $g_{F=1,2} = \mp 1/2$. The lattice spacing d has been set to 0.5μm.

In particular, it is interesting to study the impact of interactions on such a system as the dressed spin states are not eigenstates of the on-site interactions. This leads to a complicated mixing behavior of the spin components [139]. In principle, this method can be extended to higher dimensional lattice geometries.

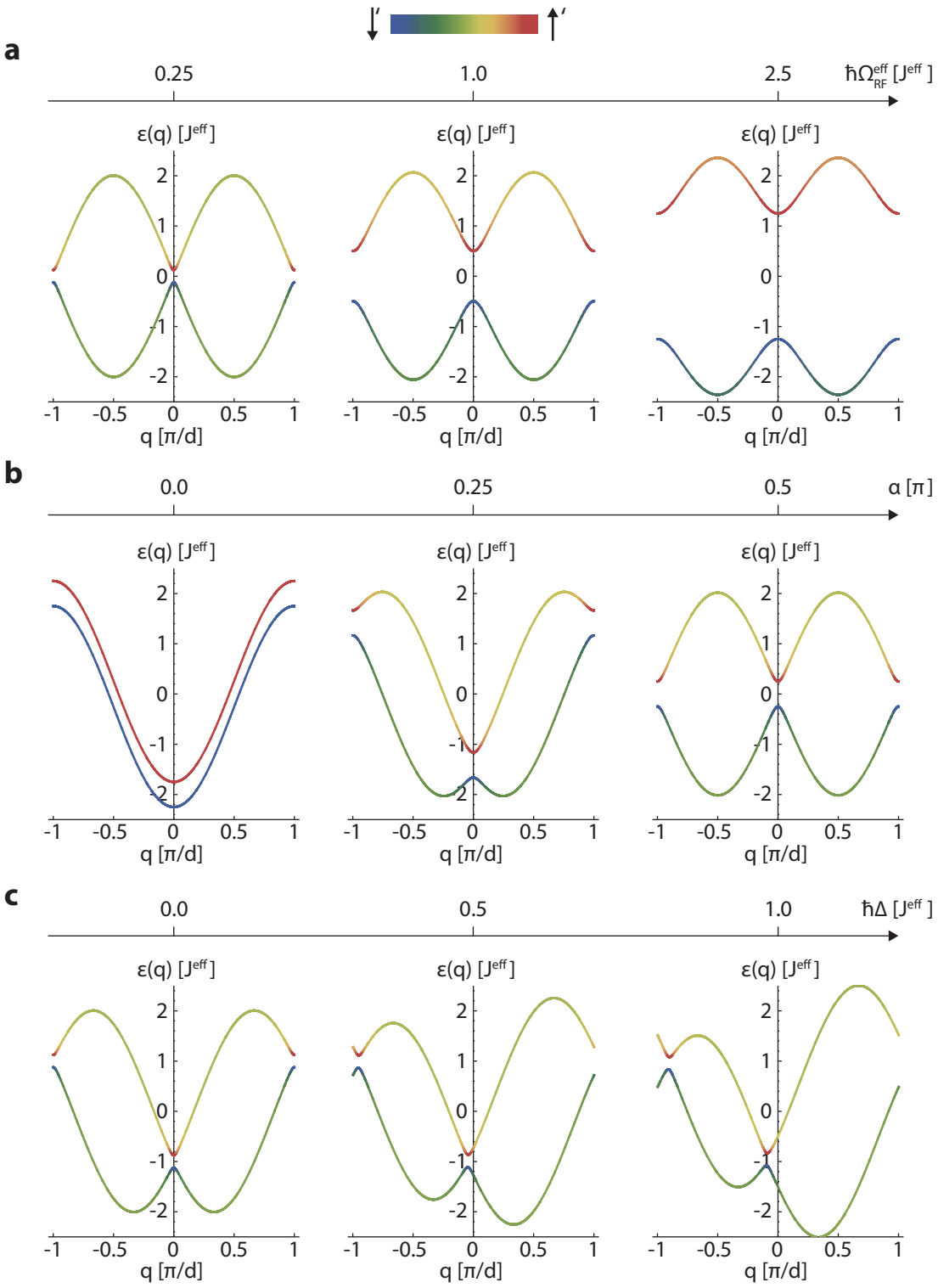

Figure 7.3: Dispersion relations of the spin-orbit coupled system. The colorcode indicates the respective admixture of dressed spin states. **a** Influence of the Rabi frequency on the dispersion relation for fixed $\alpha = \pi/2$ and $\hbar\Delta = 0$. **b** Influence of the spin-orbit coupling strength α on the dispersion relation for fixed $\hbar\Omega_{\mathrm{RF}}^{\mathrm{eff}} = 0.5|J^{\mathrm{eff}}|$ and $\hbar\Delta = 0$. **c** Influence of the detuning Δ on the dispersion relation for fixed $\alpha = \pi/3$ and $\hbar\Omega_{\mathrm{RF}}^{\mathrm{eff}} = 0.5|J^{\mathrm{eff}}|$.

Appendix A

Measured Three Beam Lattice Geometry

This section of the appendix summarizes the results of Ref. [155] for the actual experimentally realized three beam lattice which exhibits deviations from the perfect 120° configuration. The real beam arrangement was determined according to the measured momentum distribution of a coherent superfluid state in the lattice featuring well defined momentum peaks. All results were obtained under the assumption that the lattice has only deviations within the xy-plane but that the beams are not pointing outside of the plane in the z-direction. This assumption is justified *a posteriori*, as the corrected lattice constants lead to a very good agreement between experiment and theory concerning the shaking experiments in the running wave 1D lattice. The measured angles between the lattice beams are shown in table A.1. The resulting lattice constants of the three beam lattice are shown in table A.2. The inferred lattice constants deviate up to one percent from the value 553nm, expected for the perfect 120° geometry. For the running wave 1D lattice the resulting lattice spacing amounts to 486.3 ± 0.5nm.

Lattice beams	$\measuredangle$
$\mathbf{k}_1$, $\mathbf{k}_2$	$120.4° \pm 0.4°$
$\mathbf{k}_2$, $\mathbf{k}_3$	$117.1° \pm 0.2°$
$\mathbf{k}_1$, $\mathbf{k}_3$	$122.4° \pm 0.4°$

Table A.1: Measured angles between the lattice beams of the three beam lattice.

Lattice constants
$\lvert\mathbf{a}_1\rvert = 560.6 \pm 1.0$nm
$\lvert\mathbf{a}_2\rvert = 545.9 \pm 0.8$nm
$\lvert\mathbf{a}_1 + \mathbf{a}_2\rvert = 554.3 \pm 1.0$nm

Table A.2: Corrected lattice constants for the measured lattice geometry.

Appendix B

Inertial Forces and Tunneling Matrix Renormalization

In this appendix we derive the frequency modulation functions for the lattice laser beams, needed in order to create specific inertial forces for the atoms in the co-moving reference frame of the lattice.

B.1 Running Wave 1D Lattice

The lattice potential of the running wave 1D lattice is given by

$$V_{\mathrm{RW}}(x, \phi_2(t)) = -\frac{V_0}{2}\left[1 + \cos(bx - \phi_2(t))\right] \tag{B.1}$$

(see also Eq. (2.21)), where b is defined in Eq. (2.22). The laser beam characterized by the wavevector $\mathbf{k}_2$ (see Fig. 2.6) is frequency modulated in the following way

$$\omega_2(t) = \omega_{\mathrm{L}} + \delta\omega_2(t) = 2\pi\left(\nu_{\mathrm{L}} + \delta\nu_2(t)\right), \tag{B.2}$$

resulting in a time-dependent phase

$$\phi_2(t) = -\int_{-\infty}^{t} \mathrm{d}\tau \delta\omega_2(\tau), \tag{B.3}$$

while for the other beam, working at constant frequency ω_L, the phase $\phi_2(t)$ is set to zero. A finite phase ϕ_2 leads to a shift of the whole lattice potential according to

$$V_{\mathrm{RW}}(x, \phi_2(t)) = V_{\mathrm{RW}}(x - R_0(t), 0), \tag{B.4}$$

resulting in the direct relation

$$\phi_2(t) = bR_0(t), \tag{B.5}$$

where $R_0(t)$ is the trajectory of a lattice well. The lattice modulation

$$\delta\nu_2(t) = -\frac{\dot{\phi_2}(t)}{2\pi} = \frac{\Delta p(t)}{m d_{\mathrm{RW}}}, \tag{B.6}$$

results in a momentum shift Δp (Eq. (3.7)) and thus in an inertial force (see section 3.1)

$$F(t) = -m\ddot{R}_0(t) = -m\ddot{\phi}_2(t)/b \tag{B.7}$$

in the co-moving lattice frame.

The sinusoidal pulse forcing function reads

$$F(t) = \begin{cases} F_0 \sin(\Omega_1 t) & \text{for } 0 \ < t \bmod T < T_1; \ (1) \\ 0 & \text{for } T_1 < t \bmod T < T \ ; \ (2). \end{cases} \tag{B.8}$$

This results in a momentum shift of the atoms given by

$$\Delta p(t) = -\frac{F_0}{\Omega_1} \begin{cases} \cos(\Omega_1 t) - T_2/T & (1) \\ T_1/T & (2). \end{cases} \tag{B.9}$$

The required frequency modulation for this forcing function is therefore given by the expression

$$\delta\nu_2(t) = -\nu_0 \begin{cases} \cos(\Omega_1 t) - T_2/T & (1) \\ T_1/T & (2), \end{cases} \tag{B.10}$$

with the amplitude $\nu_0 = F_0/(\Omega_1 m d_{\mathrm{RW}})$. The monochromatic forcing function is obtained for the case $T_1 = T \rightarrow \Omega_1 = \Omega$. The corresponding frequency modulation is given by

$$\delta\nu_2(t) = -\nu_0 \cos(\Omega_1 t). \tag{B.11}$$

With Eq. (3.50) we derive the expression

$$W_{i,i\mp1}(t) \equiv W_i(t) - W_{i\mp1}(t) = \mp d_{\mathrm{RW}} \Delta p(t), \tag{B.12}$$

where the convention $R_i - R_{i\mp1} = \pm d_{\mathrm{RW}}$ has been used. By inserting this expression into Eq. (3.52), the tunneling matrix renormalization is obtained as

$$J^{\mathrm{eff}}_{i,i-1}/J = J^{\mathrm{eff}}_{\rightarrow}/J = \frac{T_1}{T} \exp\left(-\mathrm{i}A\frac{T_2}{T}\right) J_0^{\mathrm{B}}(A) + \frac{T_2}{T} \exp\left(\mathrm{i}A\frac{T_1}{T}\right) \tag{B.13}$$

$$J^{\mathrm{eff}}_{i,i+1}/J = J^{\mathrm{eff}}_{\leftarrow}/J = \left(J^{\mathrm{eff}}_{\rightarrow}/J\right)^* \tag{B.14}$$

with the dimensionless forcing parameter being defined as

$$A = \frac{d_{\mathrm{RW}} F_0}{\hbar \Omega_1} = \frac{m d_{\mathrm{RW}}^2 \nu_0}{\hbar}, \tag{B.15}$$

and $J^{\mathrm{eff}}_{\rightarrow}$ ($J^{\mathrm{eff}}_{\leftarrow}$) describing a hopping process into positive (negative) direction. For the case of $T_1 = T$ the pure Bessel function renormalization is recovered.

B.2 Triangular Lattice

For the triangular lattice potential given by (see Eq. (2.15)),

$$V_{\triangle}(\mathbf{r}) = -V_0 \left[\frac{3}{4} + \frac{1}{2}(\cos[(\mathbf{b}_1 - \mathbf{b}_2)\mathbf{r} - \phi_2] + \cos[\mathbf{b}_1\mathbf{r} - \phi_3] + \cos[\mathbf{b}_2\mathbf{r} + \phi_2 - \phi_3])\right], \tag{B.16}$$

two beams are modulated while the remaining one works at constant frequency,

$$\begin{aligned}\omega_1(t) &= \omega_\mathrm{L} = 2\pi\nu_\mathrm{L},\\ \omega_{2/3}(t) &= \omega_\mathrm{L} + \delta\omega_{2/3}(t) = 2\pi\left(\nu_\mathrm{L} + \delta\nu_{2/3}(t)\right).\end{aligned} \tag{B.17}$$

The frequency modulation leads to time-dependent phases for the beams 2 and 3 given by

$$\phi_{2/3}(t) = -\int_{-\infty}^{t} \mathrm{d}\tau\delta\omega_{2/3}(\tau), \tag{B.18}$$

expressing the phases in terms of a lattice shift given by the trajectory $\mathbf{R}_0(t)$ and $V_\triangle(\mathbf{r},\phi_2(t),\phi_3(t)) = V_\triangle(\mathbf{r}-\mathbf{R}_0(t),0,0)$ leads to

$$\phi_2(t) = (\mathbf{b}_1-\mathbf{b}_2)\mathbf{R}_0(t) = \frac{b}{2}\left(-R_{0,\mathrm{x}}(t) + \sqrt{3}R_{0,\mathrm{y}}(t)\right), \tag{B.19}$$

$$\phi_3(t) = \mathbf{b}_1\mathbf{R}_0(t) = \frac{b}{2}\left(R_{0,\mathrm{x}}(t) + \sqrt{3}R_{0,\mathrm{y}}(t)\right), \tag{B.20}$$

with the l-th component of the trajectory vector $R_{0,l}(t)$. The creation of an inertial force $\mathbf{F}(t) = -m\ddot{\mathbf{R}}_0(t)$ requires a modulation of the two beams, given by

$$\delta\nu_2(t) = -\frac{\dot{\phi}_2(t)}{2\pi} = \frac{1}{md_\mathrm{2D}\sqrt{3}}\left(-\Delta p_\mathrm{x}(t) + \sqrt{3}\ \Delta p_\mathrm{y}(t)\right), \tag{B.21}$$

$$\delta\nu_3(t) = -\frac{\dot{\phi}_3(t)}{2\pi} = \frac{1}{md_\mathrm{2D}\sqrt{3}}\left(\Delta p_\mathrm{x}(t) + \sqrt{3}\ \Delta p_\mathrm{y}(t)\right), \tag{B.22}$$

where $\Delta p_l(t)$ is the l-th component of the momentum shift vector.

The two dimensional forcing function

$$\mathbf{F}(t) = -F_{0,\mathrm{x}}\cos(\Omega t)\hat{\mathbf{e}}_\mathrm{x} - F_{0,\mathrm{y}}\left(\sin(\Omega t) + \delta\sin(2\Omega t)\right)\hat{\mathbf{e}}_\mathrm{y}, \tag{B.23}$$

is connected to a momentum shift given by (see Eq. (3.7))

$$\Delta p_\mathrm{x}(t) = -\frac{F_{0,\mathrm{x}}}{\Omega}\sin(\Omega t), \tag{B.24}$$

$$\Delta p_\mathrm{y}(t) = +\frac{F_{0,\mathrm{y}}}{\Omega}\left(\cos(\Omega t) + \frac{\delta}{2}\cos(2\Omega t)\right). \tag{B.25}$$

Using Eqs. (B.21) and (B.22), the functions for the frequency modulation of the lattice beams are readily obtained

$$\delta\nu_2(t) = +\nu_{0,\mathrm{x}}\sin(\Omega t) + \nu_{0,\mathrm{y}}\left(\cos(\Omega t) + \frac{\delta}{2}\cos(2\Omega t)\right), \tag{B.26}$$

$$\delta\nu_3(t) = -\nu_{0,\mathrm{x}}\sin(\Omega t) + \nu_{0,\mathrm{y}}\left(\cos(\Omega t) + \frac{\delta}{2}\cos(2\Omega t)\right), \tag{B.27}$$

with the amplitudes $\nu_{0,\mathrm{x}} = F_{0,\mathrm{x}}/(md_\mathrm{2D}\Omega\sqrt{3})$ and $\nu_{0,\mathrm{y}} = F_{0,\mathrm{y}}/(md_\mathrm{2D}\Omega)$. With Eq. (3.50) we derive the expression

$$W_{ij}(t) \equiv W_i(t) - W_j(t) = -\Delta\mathbf{p}(t)\cdot\mathbf{d}_{ij}, \tag{B.28}$$

and obtain

$$W_{21}(t) = -\frac{F_{0,\mathrm{y}} d_{2\mathrm{D}}}{\Omega}\left(\cos(\Omega t) + \frac{\delta}{2}\cos(2\Omega t)\right),$$
$$W_{32/13}(t) = \frac{d_{2\mathrm{D}}}{2\Omega}\left(\pm\sqrt{3}F_{0,\mathrm{x}}\sin(\Omega t) + F_{0,\mathrm{y}}\left[\cos(\Omega t) + \frac{\delta}{2}\cos(2\Omega t)\right]\right), \tag{B.29}$$

with the lattice directions being defined as:

$$\mathbf{d}_{21} = d_{2\mathrm{D}}\begin{pmatrix}0\\1\\0\end{pmatrix} \equiv \mathbf{d}_1, \quad \mathbf{d}_{32} = \frac{d_{2\mathrm{D}}}{2}\begin{pmatrix}\sqrt{3}\\-1\\0\end{pmatrix} \equiv \mathbf{d}_2, \quad \mathbf{d}_{13} = \frac{d_{2\mathrm{D}}}{2}\begin{pmatrix}-\sqrt{3}\\-1\\0\end{pmatrix} \equiv \mathbf{d}_3. \tag{B.30}$$

These vectors form an elementary triangular plaquette in clockwise orientation. The resulting expressions for the effective tunneling matrix elements (Eq. (3.52))

$$J_{21}^{\mathrm{eff}}/J = \frac{1}{2\pi}\int_0^{2\pi}\mathrm{d}\beta\exp\left(-\frac{\mathrm{i}d_{2\mathrm{D}}^2 m}{\hbar}\nu_{0,\mathrm{y}}\left[\cos(\beta) + \delta\cos(2\beta)/2\right]\right),$$
$$J_{32/13}^{\mathrm{eff}}/J = \frac{1}{2\pi}\int_0^{2\pi}\mathrm{d}\beta\exp\left(\frac{\mathrm{i}d_{2\mathrm{D}}^2 m}{2\hbar}\left[\pm 3\nu_{0,\mathrm{x}}\sin(\beta) + \nu_{0,\mathrm{y}}\left[\cos(\beta) + \delta\cos(2\beta)/2\right]\right]\right), \tag{B.31}$$

can be evaluated numerically. Here, the unrenormalized tunneling matrix element is denoted by J. It is straightforward to proof that $J_{32}^{\mathrm{eff}} = J_{13}^{\mathrm{eff}}$:

$$\begin{aligned} J_{32}^{\mathrm{eff}}/J &= \frac{1}{2\pi}\int_{-2\pi}^{0}\mathrm{d}\beta'\exp\left(\frac{\mathrm{i}d_{2\mathrm{D}}^2 m}{2\hbar}\left[-3\nu_{0,\mathrm{x}}\sin(\beta') + \nu_{0,\mathrm{y}}\left[\cos(\beta') + \delta\cos(2\beta')/2\right]\right]\right) \\ &= \frac{1}{2\pi}\int_0^{2\pi}\mathrm{d}\tilde{\beta}\exp\left(\frac{\mathrm{i}d_{2\mathrm{D}}^2 m}{2\hbar}\left[-3\nu_{0,\mathrm{x}}\sin(\tilde{\beta}) + \nu_{0,\mathrm{y}}\left[\cos(\tilde{\beta}) + \delta\cos(2\tilde{\beta})/2\right]\right]\right) \\ &= J_{13}^{\mathrm{eff}}/J, \end{aligned} \tag{B.32}$$

with the substitutions $\beta' = -\beta$ and $\tilde{\beta} = \beta' + 2\pi$. Introducing the dimensionless forcing parameters

$$A = \frac{d_{2\mathrm{D}}F_{0,\mathrm{y}}}{\hbar\Omega} = \frac{m d_{2\mathrm{D}}^2\nu_{0,\mathrm{y}}}{\hbar},$$
$$A' = \frac{d_{2\mathrm{D}}}{2\hbar\Omega}\sqrt{3F_{0,\mathrm{x}}^2 + F_{0,\mathrm{y}}^2} = \frac{m d_{2\mathrm{D}}^2}{2\hbar}\sqrt{9\nu_{0,\mathrm{x}}^2 + \nu_{0,\mathrm{y}}^2}, \tag{B.33}$$

Eqs. (B.31) can be recast into

$$J_{21}^{\mathrm{eff}}/J = \frac{1}{2\pi}\int_0^{2\pi}\mathrm{d}\beta\exp\left(-\mathrm{i}A\left[\cos(\beta) + \delta\cos(2\beta)/2\right]\right),$$
$$J_{32}^{\mathrm{eff}}/J = \frac{1}{2\pi}\int_0^{2\pi}\mathrm{d}\beta\exp\left(\mathrm{i}A'\left[\cos(\beta-\alpha) + \delta\cos(\alpha)\cos(2\beta)/2\right]\right), \tag{B.34}$$

with $A'\sin(\alpha) \equiv 3\nu_{0,\mathrm{x}} m d_{2\mathrm{D}}^2/(2\hbar)$ and $A'\cos(\alpha) \equiv \nu_{0,\mathrm{y}} m d_{2\mathrm{D}}^2/(2\hbar)$ and the angle α is given by

$$\tan(\alpha) = \sqrt{3}\,\frac{F_{0,\mathrm{x}}}{F_{0,\mathrm{y}}} = 3\,\frac{\nu_{0,\mathrm{x}}}{\nu_{0,\mathrm{y}}}. \tag{B.35}$$

For the special case of time-reversal symmetry preserving elliptical forcing ($\delta = 0$) one obtains

$$J_{21}^{\mathrm{eff}}/J = \frac{1}{2\pi}\int_0^{2\pi} \mathrm{d}\beta \exp\left(-\mathrm{i}A\cos(\beta)\right) = J_0^{\mathrm{B}}(A),$$
$$J_{32}^{\mathrm{eff}}/J = \frac{1}{2\pi}\int_0^{2\pi} \mathrm{d}\beta \exp\left(\mathrm{i}A'\cos(\beta-\alpha)\right) = J_0^{\mathrm{B}}(A'), \tag{B.36}$$

with the zeroth order Bessel function of first kind $J_0^{\mathrm{B}}(x)$.

Appendix C

System Parameters for Non-3D Optical Lattices

In this appendix, basic expressions for the relevant quantities and parameters in the non-3D lattice potentials are derived. By replacing the operators in Eq. (2.35) with c-numbers (Eq. (2.38)) and minimizing with respect to $\chi_i^*(\mathbf{r}_\perp)$ in the grand canonical ensemble one arrives at the stationary Gross-Pitaevskii equation

$$\left\{\tilde{g}|\chi_i(\mathbf{r}_\perp)|^2 n_i + V_{\mathrm{Harm}}(\mathbf{R}_i) + V_{\mathrm{Harm}}(\mathbf{r}_\perp) - \mu\right\}\chi_i(\mathbf{r}_\perp) = 0, \tag{C.1}$$

where μ is the chemical potential and the kinetic energy has been neglected (Thomas-Fermi approximation). The renormalized interaction parameter is defined as $\tilde{g} = g\int \mathrm{d}r_\parallel |w_i(\mathbf{r}_\parallel)|^4$ with the three dimensional interaction parameter $g = 4\pi\hbar^2 a_s/m$. For ^{87}Rb atoms in the ground-state $|F=1, m_F=-1\rangle$ the scattering length is $a_s = (100.4 \pm 0.1)a_0$ [282]. The resulting Thomas-Fermi profile of the interaction broadened wavefunction is given by [283, 284]

$$|\chi_i(\mathbf{r}_\perp)|^2 = \frac{\mu - (V_{\mathrm{Harm}}(\mathbf{R}_i) + V_{\mathrm{Harm}}(\mathbf{r}_\perp))}{\tilde{g} n_i}. \tag{C.2}$$

Within a continuum approximation $\sum_i n_i \to A_{\mathrm{UC}}^{-1}\int \mathrm{d}r_\parallel N(\mathbf{r}_\parallel)$ with $\mathbf{R}_i \to \mathbf{r}_\parallel$ the chemical potential can be calculated analytically, yielding the result

$$\mu = \left(\frac{15\tilde{g}A_{\mathrm{UC}}}{\pi 16\sqrt{2}}\,\omega_x\,\omega_y\,\omega_z\,m^{3/2}\,N\right)^{2/5}, \tag{C.3}$$

where A_{UC} is the size of the unit cell of the lattice and $N = \sum_i n_i$ the total particle number.

C.1 One-Dimensional Lattice

In the one-dimensional running wave lattice the atoms are periodically confined along the axis $\mathbf{r}_\parallel = (x, 0, 0)$ and weakly confined along $\mathbf{r}_\perp = (0, y, z)$, resulting in layers of pancake-like density distributions. Furthermore, $A_{\mathrm{UC}} = d_{\mathrm{RW}}$ and $\tilde{g} = g\int \mathrm{d}x|w_i(x)|^4$. The elliptical Thomas-Fermi boundary of the perpendicular density profile (see Eq. (C.2)) is given by the semi-axes

$$y_{i,\mathrm{TF}} = \left(\frac{2\mu - m\omega_x^2\mathbf{R}_i^2}{m\omega_y^2}\right)^{1/2}, \quad z_{i,\mathrm{TF}} = \left(\frac{2\mu - m\omega_x^2\mathbf{R}_i^2}{m\omega_z^2}\right)^{1/2}. \tag{C.4}$$

The number of atoms per layer is

$$n_i = \frac{\pi}{4\tilde{g}\omega_y\omega_z m}(2\mu - m\omega_x^2\mathbf{R}_i^2) \tag{C.5}$$

and the overall energy scale of a single layer is obtained via

$$U_i = \tilde{g}\int_{TF} \mathrm{d}y\mathrm{d}z|\chi_i(y,z)|^4 = \frac{4\tilde{g}\omega_y\omega_z m^2}{\pi\left(2\mu - m\omega_x^2\mathbf{R}_i^2\right)}. \tag{C.6}$$

N	4.0×10^5
N_{Sites}	70
n_{max}	$1.1\cdot10^4$
N/N_{Sites}	$5.7\cdot10^3$
$N_>$	35
$U_{\mathrm{weighted}} = \sum_i(U_i\,n_i)/(N)$	$1\cdot10^{-4}E_{\mathrm{rec}}$
$A_{\mathrm{TF}} = \sum_i(\pi\,y_{i,\mathrm{TF}}\,z_{i,\mathrm{TF}}\,n_i)/N$	$450\mu\mathrm{m}^2$
$\rho_{2\mathrm{D}} = \sum_i\left[n_i^2/(\pi\,y_{i,\mathrm{TF}}\,z_{i,\mathrm{TF}})\right]/N$	$56\,\mu\mathrm{m}^{-2}$
$\tilde{g}\rho_{2\mathrm{D}}/J$	86

Table C.1: Calculated system parameters for experiments presented in section 5.3. The table shows the number of occupied sites N_{Sites}, maximum tube occupancy n_{max}, mean layer occupancy N/N_{Sites}, number of sites with occupancy larger than the mean layer occupancy $N_>$, occupation weighted interaction parameter U_{weighted}, occupation weighted 2D area of the atomic layers A_{TF} and occupation weighted 2D-Density $\rho_{2\mathrm{D}}$. The corresponding lattice depth is $10E_{\mathrm{rec}}$, overall harmonic trapping frequencies are $\omega \approx 2\pi\cdot(20,20,50)\mathrm{Hz}$ and $\tilde{g}/g = 4.6\mu\mathrm{m}^{-1}$.

C.2 Two-Dimensional Triangular Lattice

For the triangular lattice without additional periodic confinement along the z-direction the system consist of a periodic array of elongated tubes. The lattice axes are defined as $\mathbf{r}_\parallel = (x,y,0)$ and the weakly confined axis is along $\mathbf{r}_\perp = (0,0,z)$. Furthermore, the unit cell of the triangular lattice is $A_{\mathrm{UC}} = \sqrt{3/4}\;d_{2D}^2$ and the renormalized interaction parameter is $\tilde{g} = g\int \mathrm{d}x\mathrm{d}y|w_i(x,y)|^4$. The result for the Thomas-Fermi boundary of the tubes yields

$$x_{\mathrm{TF}} = \left(\frac{2\mu - m(\omega_x^2R_{i,x}^2 + \omega_y^2R_{i,y}^2)}{m\omega_z^2}\right)^{1/2}, \tag{C.7}$$

where $R_{i,x}, R_{i,y}$ are the x,y components of the lattice vector of site i. The length of the tubes is $2x_{\mathrm{TF}}$ and the number of particles in a single tube is

$$n_i = \frac{2m\omega_z^2x_{\mathrm{TF}}^3}{3\tilde{g}}. \tag{C.8}$$

The overall interaction parameter of a single tube is obtained via

$$U_i = \tilde{g}\int_{TF} \mathrm{d}x|\chi_i(x)|^4 = \frac{3\tilde{g}}{5x_{\mathrm{TF}}}. \tag{C.9}$$

N	1.0×10^5
N_{Sites}	931
n_{max}	267
N/N_{Sites}	107
$N_{>}$	433
$U_{\mathrm{weighted}} = \sum_i (U_i\, n_i)/(N)$	$4 \cdot 10^{-3} E_{\mathrm{rec}}$
$l_{\mathrm{Tube}} = \sum_i (2\, x_{i,\mathrm{TF}}\, n_i)/N$	15μm
$\rho_{1\mathrm{D}} = \sum_i \left[n_i^2/(2\, x_{i,\mathrm{TF}})\right]/N$	$11\,\mu\mathrm{m}^{-1}$

Table C.2: Calculated system parameters for experiments presented in chapter 4. The table shows the number of occupied sites N_{Sites}, maximum tube occupancy n_{max}, mean tube occupancy N/N_{Sites}, number of sites with occupancy larger than the mean tube occupancy $N_{>}$, occupation weighted interaction parameter U_{weighted}, occupation weighted length of the tubes l_{Tube} and occupation weighted 1D-Density $\rho_{1\mathrm{D}}$. The corresponding lattice depth is $5.6 E_{\mathrm{rec}}$. The overall harmonic trapping frequencies are approximately equal $\omega \approx 2\pi \cdot 100$Hz and $\tilde{g}/g = 19.3\mu\mathrm{m}^{-2}$.

N	1.5×10^5	2.5×10^5
N_{Sites}	2157	2629
n_{max}	174	237
N/N_{Sites}	70	95
$N_{>}$	985	1201
$U_{\mathrm{weighted}} = \sum_i (U_i\, n_i)/(N)$	$2 \cdot 10^{-3} E_{\mathrm{rec}}$	$2 \cdot 10^{-3} E_{\mathrm{rec}}$
$l_{\mathrm{Tube}} = \sum_i (2\, x_{i,\mathrm{TF}}\, n_i)/N$	$23\,\mu$m	$25\,\mu$m
$\rho_{1\mathrm{D}} = \sum_i \left[n_i^2/(2\, x_{i,\mathrm{TF}})\right]/N$	$5\mu\mathrm{m}^{-1}$	$6\,\mu\mathrm{m}^{-1}$

Table C.3: Calculated system parameters for experiments presented in section 5.4 and chapter 6. The table shows the number of occupied sites N_{Sites}, maximum tube occupancy n_{max}, mean tube occupancy N/N_{Sites}, number of sites with occupancy larger than the mean tube occupancy $N_{>}$, occupation weighted interaction parameter U_{weighted}, occupation weighted length of the tubes l_{Tube} and occupation weighted 1D-Density $\rho_{1\mathrm{D}}$. The corresponding lattice depth is $4.6 E_{\mathrm{rec}}$, overall harmonic trapping frequencies are $\omega = 2\pi \cdot (31, 53, 40)$Hz and $\tilde{g}/g = 17.3\mu\mathrm{m}^{-2}$.

Appendix D

Symmetry Constraints for Complex Tunneling Matrix Elements

Here, we prove the statement of section 5.2, claiming that the imaginary part of the renormalized tunneling matrix elements can only be non-zero provided the symmetries (5.14), (5.15) and equivalently (5.16), (5.17) are broken.

D.1 Constraints for the Function $W_{ij}(t)$

We start with the proof for (5.14) by writing down the imaginary part of Eq. (3.52),

$$\mathrm{Im}(J_{ij}^{\mathrm{eff}}/J) = \langle \sin(W_{ij}(t)/\hbar)\rangle_T \tag{D.1}$$

$$= \frac{1}{T}\int_{\tau}^{T+\tau} \mathrm{d}t' \, \sin(W_{ij}(t'-\tau)/\hbar) \; ; \quad t' = t+\tau, \tag{D.2}$$

with $W_{ij}(t) \equiv W_i(t) - W_j(t)$. If this function fulfills the inversion symmetry $W_{ij}(t'-\tau) = -W_{ij}(-t'-\tau)$ (see Eq. (5.14)), we obtain

$$\mathrm{Im}(J_{ij}^{\mathrm{eff}}/J) = -\frac{1}{T}\int_{\tau}^{T+\tau} \mathrm{d}t' \, \sin(W_{ij}(-t'-\tau)/\hbar) \tag{D.3}$$

$$= \frac{1}{T}\int_{T}^{0} \mathrm{d}\tilde{t} \, \sin(\underbrace{W_{ij}(\tilde{t}-2\tau-T)}_{=W_{ij}(\tilde{t}-2\tau)}/\hbar) \quad \text{with} \quad \tilde{t} = -t'+T+\tau \tag{D.4}$$

$$= -\langle \sin(W_{ij}(t-2\tau)/\hbar)\rangle_T \tag{D.5}$$

$$= -\langle \sin(W_{ij}(t)/\hbar)\rangle_T \, , \tag{D.6}$$

where in the last step we have used the relation

$$\langle \sin(W_{ij}(t-t_0)/\hbar)\rangle_T = \langle \sin(W_{ij}(t)/\hbar)\rangle_T \, . \tag{D.7}$$

This holds for arbitrary times t_0, provided $W_{ij}(t)$ is time-periodic ($W_{ij}(t+T) = W_{ij}(t)$). Comparing the lines (D.1) and (D.6) one can immediately deduce that the imaginary

part vanishes. That the imaginary part of the tunneling matrix elements always vanishes for fulfilled symmetry (5.15) can be proven as follows:

$$\begin{aligned}
\mathrm{Im}(J_{ij}^{\mathrm{eff}}/J) =& \langle \sin(W_{ij}(t)/\hbar)\rangle_T && \text{(D.8)}\\
=& \frac{1}{T}\int_0^{T/2} \mathrm{d}t\, \sin(W_{ij}(t)/\hbar) + \frac{1}{T}\int_{T/2}^{T} \mathrm{d}t\, \sin(W_{ij}(t)/\hbar) && \text{(D.9)}\\
=& \frac{1}{T}\int_0^{T/2} \mathrm{d}t\, \sin(W_{ij}(t)/\hbar)\\
&+ \frac{1}{T}\int_0^{T/2} \mathrm{d}t'\, \sin(\underbrace{W_{ij}(t'+T/2)}_{=W_{ij}(t'-T/2)}/\hbar)\ ; \quad t' = t - T/2. && \text{(D.10)}
\end{aligned}$$

Insertion of symmetry (5.15) ($W_{ij}(t') = -W_{ij}(t'-T/2)$) results in

$$\mathrm{Im}(J_{ij}^{\mathrm{eff}}/J) = \frac{1}{T}\int_0^{T/2} \mathrm{d}t\, \sin(W_{ij}(t)/\hbar) - \int_0^{T/2} \mathrm{d}t'\, \sin(W_{ij}(t')/\hbar) = 0 \qquad \text{(D.11)}$$

If either Eq. (5.14) or (5.15) are fulfilled, the imaginary part of J_{ij}^{eff} has to vanish.

D.2 Constraints for the Driving Function $v_{ij}(t)$

Now we prove that the symmetry constraints (5.16) and (5.17) of $v_{ij}(t)$ are equivalent to those of $W_{ij}(t)$. The starting point for this proof is a generalized form of Eq. (3.7), which is given by

$$W_{ij}(t) = \int_{t_0}^{t} \mathrm{d}t' v_{ij}(t') - \left\langle \int_{t_0}^{t} \mathrm{d}t' v_{ij}(t') \right\rangle_T . \qquad \text{(D.12)}$$

The equation is applicable as long as the time-average of v_{ij} vanishes ($\langle v_{ij}\rangle_T = 0$) and it is independent of t_0 (see Eq. (3.7)). With Eq. (D.12) at hand, a relation between the symmetry condition for W_{ij} and v_{ij} can be established:

$$\begin{aligned}
W_{ij}(t-\tau) =& \int_{t_0}^{t-\tau} \mathrm{d}t' v_{ij}(t') - \left\langle \int_{t_0}^{t-\tau} \mathrm{d}t' v_{ij}(t') \right\rangle_T && \text{(D.13)}\\
=& \int_{t_0+\tau}^{t} \mathrm{d}t'' v_{ij}(t''-\tau) - \left\langle \int_{t_0+\tau}^{t} \mathrm{d}t'' v_{ij}(t''-\tau) \right\rangle_T ; \quad t'' = t' + \tau. && \text{(D.14)}
\end{aligned}$$

Assuming that time-reversal symmetry holds (5.16) ($v_{ij}(t''-\tau) = v_{ij}(-t''-\tau)$), line (D.14) can be recast into

$$\begin{aligned}
W_{ij}(t-\tau) =& \int_{t_0+\tau}^{t} \mathrm{d}t'' v_{ij}(-t''-\tau) - \left\langle \int_{t_0+\tau}^{t} \mathrm{d}t'' v_{ij}(-t''-\tau) \right\rangle_T && \text{(D.15)}\\
=& -\int_{-t_0-2\tau}^{-t-\tau} \mathrm{d}\tilde{t}\, v_{ij}\left(\tilde{t}\right) + \left\langle \int_{-t_0-2\tau}^{-t-\tau} \mathrm{d}\tilde{t}\, v_{ij}\left(\tilde{t}\right) \right\rangle_T ; \quad \tilde{t} = -t''-\tau && \text{(D.16)}\\
=& -W_{ij}(-t-\tau). && \text{(D.17)}
\end{aligned}$$

This proves the equivalence of the symmetries (5.14) and (5.16). Both are either broken or fulfilled simultaneously.

We are left with the proof of the equivalence of (5.15) and (5.17). Insertion of the shift antisymmetry $v_{ij}(t'') = -v_{ij}(t'' - T/2)$ (Eq .(5.17)) into Eq. D.12 results in

$$W_{ij}(t) = -\int_{t_0-T/2}^{t-T/2} \mathrm{d}t'' v_{ij}(t'') + \left\langle \int_{t_0-T/2}^{t-T/2} \mathrm{d}t'' v_{ij}(t'') \right\rangle_T \tag{D.18}$$

$$= -W_{ij}(-t - T/2). \tag{D.19}$$

This proves the equivalence of the symmetry constraints (5.15) and (5.17). For the derivation of Eqs. D.17 and D.19 we have used the invariance of W_{ij} under changes of the lower bounds of the integrals.

Appendix E

Staggered Currents on the Frustrated Triangular Lattice

The current operator on the lattice is defined via the continuity equation

$$\frac{\mathrm{d}}{\mathrm{d}t}\langle\hat{n}_s\rangle + \sum_{\langle i\rangle_s}\langle\hat{j}_{is}\rangle = 0, \tag{E.1}$$

where $\hat{j}_{is}$ is the current operator and $\langle i\rangle_s$ denotes all bonds connected to lattice site s. The expectation value of the current is positive for currents flowing from lattice site s to i. The time derivative of $\langle\hat{n}_s\rangle$ can be obtained with the Ehrenfest theorem

$$\begin{aligned}\frac{\mathrm{d}}{\mathrm{d}t}\langle\hat{n}_s\rangle &= \frac{\mathrm{i}}{\hbar}\langle[H,\hat{n}_s]\rangle + \left\langle\frac{\partial\hat{n}_s}{\partial t}\right\rangle \\ &= \frac{\mathrm{i}}{\hbar}\langle[H_{\mathrm{kin}},\hat{n}_s]\rangle \\ &= \frac{\mathrm{i}}{\hbar}\sum_{\langle i\rangle_s}|J_{is}|\left(-\mathrm{e}^{\mathrm{i}\theta_{is}}\ \langle\hat{a}_i^+\hat{a}_s\rangle + \mathrm{e}^{-\mathrm{i}\theta_{is}}\ \langle\hat{a}_s^+\hat{a}_i\rangle\right),\end{aligned} \tag{E.2}$$

provided H is a tight-binding Hamiltonian of the kind

$$H = H_{\mathrm{kin}} + H_{\mathrm{onsite}} = -\sum_{\langle ij\rangle}|J_{ij}|\mathrm{e}^{\mathrm{i}\theta_{ij}}\ \hat{a}_i^+\hat{a}_j + H_{\mathrm{onsite}}, \tag{E.3}$$

where H_{onsite} only depends on on-site number operators $\hat{n}_i = \hat{a}_i^+\hat{a}_i$. Comparison of Eqs. (E.1) and (E.2) yields the expression

$$\hat{j}_{is} = \frac{|J_{is}|}{\mathrm{i}\hbar}\left(-\mathrm{e}^{\mathrm{i}\theta_{is}}\ \hat{a}_i^+\hat{a}_s + \mathrm{e}^{-\mathrm{i}\theta_{is}}\ \hat{a}_s^+\hat{a}_i\right), \tag{E.4}$$

for the current operator. The expectation value of this observable can be recast into

$$\langle\hat{j}_{is}\rangle = -\frac{2|J_{is}|}{\hbar}\,\mathrm{Im}\left[\mathrm{e}^{\mathrm{i}\theta_{is}}\ \langle\hat{a}_i^+\hat{a}_s\rangle\right]. \tag{E.5}$$

For later derivations, we need to express the current operator in terms of quasi-momenta. The transformation of the local creation and annihilation operators into reciprocal space is given by

$$\hat{a}_i\ = \frac{1}{\sqrt{M}}\sum_{\mathbf{q}}\hat{B}_{\mathbf{q}}\,\mathrm{e}^{\mathrm{i}\mathbf{q}\mathbf{R}_i}, \quad \hat{a}_i^+ = \frac{1}{\sqrt{M}}\sum_{\mathbf{q}}\hat{B}_{\mathbf{q}}^+\mathrm{e}^{-\mathrm{i}\mathbf{q}\mathbf{R}_i}, \tag{E.6}$$

where M is the number of lattice sites and $\hat{B}_{\mathbf{q}}$ ($\hat{B}^+_{\mathbf{q}}$) is the annihilation (creation) operator for a particle in the Bloch state with quasimomentum q. The current operator in the reciprocal space is then

$$\hat{j}_{is} = \frac{|J_{is}|}{\mathrm{i}\hbar M} \sum_{\mathbf{q},\mathbf{q}'} \hat{B}^+_{\mathbf{q}} \hat{B}_{\mathbf{q}'} \left(- \mathrm{e}^{\mathrm{i}(\theta_{is} + \mathbf{q}'\mathbf{R}_s - \mathbf{q}\mathbf{R}_i)} + \mathrm{e}^{\mathrm{i}(-\theta_{is} + \mathbf{q}'\mathbf{R}_i - \mathbf{q}\mathbf{R}_s)} \right). \tag{E.7}$$

If the Peierls phases θ_{is} and the magnitude of the tunneling elements $|J_{is}|$ only depend on the lattice directions $\mathbf{d}_i$, we can introduce a simplified notation for the current operator

$$\hat{j}_{\mathbf{d}_i s} = \frac{|J_i|}{\mathrm{i}\hbar M} \sum_{\mathbf{q},\mathbf{q}'} \hat{B}^+_{\mathbf{q}} \hat{B}_{\mathbf{q}'} \mathrm{e}^{\mathrm{i}(\mathbf{q}'-\mathbf{q})\mathbf{R}_s} \left(- \mathrm{e}^{\mathrm{i}(\theta_i - \mathbf{q}\mathbf{d}_i)} + \mathrm{e}^{-\mathrm{i}(\theta_i - \mathbf{q}'\mathbf{d}_i)} \right), \tag{E.8}$$

where θ_i denotes the Peierls phase and $|J_i|$ the absolute value of the tunneling along the direction $\mathbf{d}_i$.

The total staggered current $\mathcal{J}$ on the triangular lattice is obtained by summing all currents along suitable directions. The lattice directions have to be chosen such that upwards pointing elementary triangular plaquettes are formed in a clockwise orientation. This necessarily results in a counter-clockwise orientation for downwards pointing triangles (see (B.30)). For simplicity, we assume that the magnitude of the tunneling is isotropic $|J_i| \equiv |J|$, but the obtained results can be generalized straightforwardly to anisotropic tunneling amplitudes. The total staggered current of the lattice can be linked to the quasimomentum distribution of the atoms:

$$\begin{aligned}
\mathcal{J} &= \sum_{s}^{M} \sum_{i=1}^{3} \left\langle \hat{j}_{\mathbf{d}_i s} \right\rangle \\
&= \frac{|J|}{\mathrm{i}\hbar M} \sum_{s}^{M} \sum_{i=1}^{3} \sum_{\mathbf{q},\mathbf{q}'} \left\langle \hat{B}^+_{\mathbf{q}} \hat{B}_{\mathbf{q}'} \right\rangle \mathrm{e}^{\mathrm{i}(\mathbf{q}'-\mathbf{q})\mathbf{R}_s} \left(- \mathrm{e}^{\mathrm{i}(\theta_i - \mathbf{q}\mathbf{d}_i)} + \mathrm{e}^{-\mathrm{i}(\theta_i - \mathbf{q}'\mathbf{d}_i)} \right) \\
&= \frac{|J|}{\mathrm{i}\hbar} \sum_{i=1}^{3} \sum_{\mathbf{q},\mathbf{q}'} \left\langle \hat{B}^+_{\mathbf{q}} \hat{B}_{\mathbf{q}'} \right\rangle \delta_{\mathbf{q}'\mathbf{q}} \left(- \mathrm{e}^{\mathrm{i}(\theta_i - \mathbf{q}\mathbf{d}_i)} + \mathrm{e}^{-\mathrm{i}(\theta_i - \mathbf{q}'\mathbf{d}_i)} \right) \\
&= \frac{2|J|}{\hbar} \sum_{i=1}^{3} \sum_{\mathbf{q}} \left\langle \hat{B}^+_{\mathbf{q}} \hat{B}_{\mathbf{q}} \right\rangle \sin(\mathbf{q}\mathbf{d}_i - \theta_i) \\
&= \frac{2|J|}{\hbar} \sum_{\mathbf{q}} \langle \tilde{n}_{\mathbf{q}} \rangle \, \mathcal{X}(\theta, \theta', \mathbf{q}),
\end{aligned} \tag{E.9}$$

with the number operator $\tilde{n}_{\mathbf{q}}$ for quasimomentum $\mathbf{q}$ and the gauge dependent quasimomentum weighting function

$$\begin{aligned}
\mathcal{X}(\theta, \theta', \mathbf{q}) &= \sum_{i=1}^{3} \sin(\mathbf{q}\mathbf{d}_i - \theta_i) \\
&= \sin(\mathbf{q}\mathbf{d}_1 - \theta) + \sin(\mathbf{q}\mathbf{d}_2 - \theta') + \sin(\mathbf{q}\mathbf{d}_3 - \theta'),
\end{aligned} \tag{E.10}$$

with lattice directions being defined in Eq. (B.30).

Bibliography

[1] S. Chu, L. Hollberg, J. Bjorkholm, A. Cable and A. Ashkin: "Three-dimensional viscous confinement and cooling of atoms by resonance radiation pressure", Phys. Rev. Lett. **55**, 48–51 (1985).

[2] E. Raab, M. Prentiss, A. Cable, S. Chu and D. Pritchard: "Trapping of Neutral Sodium Atoms with Radiation Pressure", Phys. Rev. Lett. **59**, 2631–2634 (1987).

[3] P. Lett, R. Watts, C. Westbrook, W. Phillips, P. Gould and H. Metcalf: "Observation of Atoms Laser Cooled below the Doppler Limit", Phys. Rev. Lett. **61**, 169–172 (1988).

[4] J. Dalibard and C. Cohen-Tannoudji: "Laser cooling below the Doppler limit by polarization gradients: simple theoretical models", Journal of the Optical Society of America B **6**, 2023–2045 (1989).

[5] H. J. Metcalf and P. van der Straten: *Laser Cooling and Trapping*, Springer New York.

[6] S. Chu: "Nobel Lecture: The manipulation of neutral particles", Reviews of Modern Physics **70**, 685–706 (1998).

[7] C. N. Cohen-Tannoudji: "Nobel Lecture: Manipulating atoms with photons", Reviews of Modern Physics **70**, 707–719 (1998).

[8] W. D. Phillips: "Nobel Lecture: Laser cooling and trapping of neutral atoms", Reviews of Modern Physics **70**, 721–741 (1998).

[9] M. H. Anderson, J. R. Ensher, M. R. Matthews, C. E. Wieman and E. A. Cornell: "Observation of Bose-Einstein Condensation in a Dilute Atomic Vapor", Science **269**, 198–201 (1995).

[10] K. Davis, M. Mewes, M. Andrews, N. van Druten, D. Durfee, D. Kurn and W. Ketterle: "Bose-Einstein Condensation in a Gas of Sodium Atoms", Phys. Rev. Lett. **75**, 3969–3973 (1995).

[11] C. Bradley, C. Sackett, J. Tollett and R. Hulet: "Evidence of Bose-Einstein Condensation in an Atomic Gas with Attractive Interactions", Phys. Rev. Lett. **75**, 1687–1690 (1995).

[12] D. Jin, J. Ensher, M. Matthews, C. Wieman and E. Cornell: "Collective Excitations of a Bose-Einstein Condensate in a Dilute Gas", Phys. Rev. Lett. **77**, 420–423 (1996).

[13] M. O. Mewes, M. Andrews, N. van Druten, D. Kurn, D. Durfee, C. Townsend and W. Ketterle: "Collective Excitations of a Bose-Einstein Condensate in a Magnetic Trap", Phys. Rev. Lett. **77**, 988–991 (1996).

[14] M. O. Mewes, M. R. Andrews, D. M. Kurn, D. S. Durfee, C. G. Townsend and W. Ketterle: "Output Coupler for Bose-Einstein Condensed Atoms", Phys. Rev. Lett. **78**, 582–585 (1997).

[15] M. R. Andrews, C. G. Townsend, H. J. Miesner, D. S. Durfee, D. M. Kurn and W. Ketterle: "Observation of Interference Between Two Bose Condensates", Science **275**, 637–641 (1997).

[16] M. Matthews, B. Anderson, P. Haljan, D. Hall, C. Wieman and E. Cornell: "Vortices in a Bose-Einstein Condensate", Phys. Rev. Lett. **83**, 2498–2501 (1999).

[17] E. A. Cornell and C. E. Wieman: "Nobel Lecture: Bose-Einstein condensation in a dilute gas, the first 70 years and some recent experiments", Reviews of Modern Physics **74**, 875–893 (2002).

[18] W. Ketterle, D. S. Durfee and D. M. Stamper-Kurn: "Making, probing and understanding Bose-Einstein condensates.", Bose-Einstein condensation in atomic gases: Proceedings of the International School of Physics "Enrico Fermi", Course CXL pages 67–176 (1999).

[19] B. DeMarco and D. S. Jin: "Onset of Fermi Degeneracy in a Trapped Atomic Gas", Science **285**, 1703–1706.

[20] H. Feshbach: "Unified theory of nuclear reactions", Annals of Physics **5**, 357–390 (1958).

[21] S. Inouye, M. Andrews, J. Stenger, H. Miesner, D. Stamper-Kurn, W. Ketterle and D. Miesner: "Observation of Feshbach resonances in a Bose-Einstein condensate", Nature **392**, 151–154 (1998).

[22] W. Ketterle and M. W. Zwierlein: "Making, probing and understanding ultracold Fermi gases", Rivista del Nuovo Cimento **31**, 247–422 (2008).

[23] I. Bloch, J. Dalibard and W. Zwerger: "Many-body physics with ultracold gases", Reviews of Modern Physics **80**, 885–964 (2008).

[24] T. Lahaye, T. Koch, B. Fröhlich, M. Fattori, J. Metz, A. Griesmaier, S. Giovanazzi and T. Pfau: "Strong dipolar effects in a quantum ferrofluid", Nature **448**, 672–675 (2007).

[25] M. A. Baranov: "Theoretical progress in many-body physics with ultracold dipolar gases", Physics Reports **464**, 71–111 (2008).

[26] T. Lahaye, C. Menotti, L. Santos, M. Lewenstein and T. Pfau: "The physics of dipolar bosonic quantum gases", Reports on Progress in Physics **72**, 126401 (2009).

[27] K. K. Ni, S. Ospelkaus, D. Wang, G. Quéméner, B. Neyenhuis, M. H. de Miranda, J. L. Bohn, J. Ye and D. S. Jin: "Dipolar collisions of polar molecules in the quantum regime", Nature **464**, 1324–1328 (2010).

[28] P. Schauß, M. Cheneau, M. Endres, T. Fukuhara, S. Hild, A. Omran, T. Pohl, C. Gross, S. Kuhr and I. Bloch: "Observation of spatially ordered structures in a two-dimensional Rydberg gas", Nature **491**, 87–91 (2012).

[29] S. Ospelkaus, K. K. Ni, D. Wang, M. H. de Miranda, B. Neyenhuis, G. Quemener, P. S. Julienne, J. L. Bohn, D. S. Jin and J. Ye: "Quantum-State Controlled Chemical Reactions of Ultracold Potassium-Rubidium Molecules", Science **327**, 853–857 (2010).

[30] Y. il Shin: "Determination of the equation of state of a polarized Fermi gas at unitarity", Physical Review A **77**, 041603 (2008).

[31] T.-L. Ho and Q. Zhou: "Obtaining the phase diagram and thermodynamic quantities of bulk systems from the densities of trapped gases", Nature Physics **6**, 131–134 (2009).

[32] S. Nascimbène, N. Navon, K. J. Jiang, F. Chevy and C. Salomon: "Exploring the thermodynamics of a universal Fermi gas", Nature **463**, 1057–1060 (2010).

[33] S. Nascimbène, N. Navon, F. Chevy and C. Salomon: "The equation of state of ultracold Bose and Fermi gases: a few examples", New J. Phys. **12**, 103026 (2010).

[34] N. Navon, S. Piatecki, K. Günter, B. Rem, T. C. Nguyen, F. Chevy, W. Krauth and C. Salomon: "Dynamics and Thermodynamics of the Low-Temperature Strongly Interacting Bose Gas", Phys. Rev. Lett. **107**, 135301 (2011).

[35] K. van Houcke, F. Werner, E. Kozik, N. Prokof'ev, B. Svistunov, M. J. Ku, A. T. Sommer, L. W. Cheuk, A. Schirotzek and M. W. Zwierlein: "Feynman diagrams versus Fermi-gas Feynmanemulator", Nature Physics **8**, 366–370 (2012).

[36] C. Westbrook, R. Watts, C. Tanner, S. Rolston, W. Phillips, P. Lett and P. Gould: "Localization of atoms in a three-dimensional standing wave", Phys. Rev. Lett. **65**, 33–36 (1990).

[37] G. Grynberg, B. Lounis, P. Verkerk, J. Y. Courtois and C. Salomon: "Quantized motion of cold cesium atoms in two- and three-dimensional optical potentials", Phys. Rev. Lett. **70**, 2249–2252 (1993).

[38] A. Hemmerich and T. Hänsch: "Two-dimensional atomic crystal bound by light", Phys. Rev. Lett. **70**, 410–413 (1993).

[39] A. Kastberg, W. Phillips, S. Rolston, R. Spreeuw and P. Jessen: "Adiabatic Cooling of Cesium to 700 nK in an Optical Lattice", Phys. Rev. Lett. **74**, 1542–1545 (1995).

[40] M. Greiner, O. Mandel, T. Esslinger, T. Hänsch and I. Bloch: "Quantum phase transition from a superfluid to a Mott insulator in a gas of ultracold atoms", Nature **415**, 39–44 (2002).

[41] D. Jaksch, C. Bruder, J. Cirac, C. Gardiner and P. Zoller: "Cold Bosonic Atoms in Optical Lattices", Phys. Rev. Lett. **81**, 3108–3111 (1998).

[42] M. P. Fisher, G. Grinstein and D. S. Fisher: "Boson localization and the superfluid-insulator transition", Physical Review B **40**, 546–570 (1989).

[43] D. Jaksch, H. J. Briegel, J. I. Cirac, C. W. Gardiner and P. Zoller: "Entanglement of Atoms via Cold Controlled Collisions", Phys. Rev. Lett. **82**, 1975–1978 (1999).

[44] H. J. Briegel and R. Raussendorf: "Persistent Entanglement in Arrays of Interacting Particles", Phys. Rev. Lett. **86**, 910–913 (2001).

[45] O. Mandel, M. Greiner, A. Widera, T. Rom, T. Hänsch and I. Bloch: "Controlled collisions for multi-particle entanglement of optically trapped atoms", Nature **425**, 937–940 (2003).

[46] T. Stöferle, H. Moritz, C. Schori, M. Köhl and T. Esslinger: "Transition from a Strongly Interacting 1D Superfluid to a Mott Insulator", Phys. Rev. Lett. **92**, 130403 (2004).

[47] M. Köhl, H. Moritz, T. Stöferle, C. Schori and T. Esslinger: "Superfluid to Mott insulator transition in one, two, and three dimensions", Journal of Low Temperature Physics **138**, 635–644 (2005).

[48] I. Spielman, W. Phillips and J. von Porto: "Mott-Insulator Transition in a Two-Dimensional Atomic Bose Gas", Phys. Rev. Lett. **98**, 080404 (2007).

[49] I. Spielman, W. Phillips and J. von Porto: "Condensate Fraction in a 2D Bose Gas Measured across the Mott-Insulator Transition", Phys. Rev. Lett. **100**, 120402 (2008).

[50] F. Gerbier, A. Widera, S. Fölling, O. Mandel, T. Gericke and I. Bloch: "Interference pattern and visibility of a Mott insulator", Physical Review A **72**, 053606 (2005).

[51] F. Gerbier, A. Widera, S. Fölling, O. Mandel, T. Gericke and I. Bloch: "Phase Coherence of an Atomic Mott Insulator", Phys. Rev. Lett. **95**, 050404 (2005).

[52] P. Sengupta, M. Rigol, G. Batrouni, P. Denteneer and R. Scalettar: "Phase Coherence, Visibility, and the Superfluid–Mott-Insulator Transition on One-Dimensional Optical Lattices", Phys. Rev. Lett. **95**, 220402 (2005).

[53] M. Köhl, H. Moritz, T. Stöferle, K. Günter and T. Esslinger: "Fermionic Atoms in a Three Dimensional Optical Lattice: Observing Fermi Surfaces, Dynamics, and Interactions", Phys. Rev. Lett. **94**, 080403 (2005).

[54] T. Rom, T. Best, D. van Oosten, U. Schneider, S. Fölling, B. Paredes and I. Bloch: "Free fermion antibunching in a degenerate atomic Fermi gas released from an optical lattice", Nature **444**, 733–736 (2006).

[55] R. Jördens, N. Strohmaier, K. Günter, H. Moritz and T. Esslinger: "A Mott insulator of fermionic atoms in an optical lattice", Nature **455**, 204–207 (2008).

[56] U. Schneider, L. Hackermüller, S. Will, T. Best, I. Bloch, T. Costi, R. Helmes, D. Rasch and A. Rosch: "Metallic and Insulating Phases of Repulsively Interacting Fermions in a 3D Optical Lattice", Science **322**, 1520–1525 (2008).

[57] W. Bakr, J. Gillen, A. Peng, S. Fölling and M. Greiner: "A quantum gas microscope for detecting single atoms in a Hubbard-regime optical lattice", Nature **462**, 74–77 (2009).

[58] J. Sherson, C. Weitenberg, M. Endres, M. Cheneau, I. Bloch and S. Kuhr: "Single-atom-resolved fluorescence imaging of an atomic Mott insulator", Nature **467**, 68–72 (2010).

[59] C. Weitenberg, M. Endres, J. Sherson, M. Cheneau, P. Schauß, T. Fukuhara, I. Bloch and S. Kuhr: "Single-spin addressing in an atomic Mott insulator", Nature **471**, 319–324 (2011).

[60] G. Wirth, M. Ölschläger and A. Hemmerich: "Evidence for orbital superfluidity in the P-band of a bipartite optical square lattice", Nature Physics **7**, 147–153 (2011).

[61] P. Soltan-Panahi, D.-S. Lühmann, J. Struck, P. Windpassinger and K. Sengstock: "Quantum phase transition to unconventional multi-orbital superfluidity in optical lattices", Nature Physics **8**, 71–75 (2011).

[62] M. Ölschläger, G. Wirth and A. Hemmerich: "Unconventional Superfluid Order in the F Band of a Bipartite Optical Square Lattice", Phys. Rev. Lett. **106**, 15302 (2011).

[63] P. Soltan-Panahi: "Multi-Component Quantum Gases in Hexagonal Lattices", Ph.D. thesis, Department Physik der Universität Hamburg (2010).

[64] L. Tarruell, D. Greif, T. Uehlinger, G. Jotzu and T. Esslinger: "Creating, moving and merging Dirac points with a Fermi gas in a tunable honeycomb lattice", Nature **483**, 302–305 (2012).

[65] C. Becker, P. Soltan-Panahi, J. Kronjäger, S. Dörscher, K. Bongs and K. Sengstock: "Ultracold quantum gases in triangular optical lattices", New J. Phys. **12**, 065025 (2010).

[66] G.-B. Jo, J. Guzman, C. K. Thomas, P. Hosur, A. Vishwanath and D. M. Stamper-Kurn: "Ultracold Atoms in a Tunable Optical Kagome Lattice", Phys. Rev. Lett. **108**, 045305 (2012).

[67] L. H. Haddad and L. D. Carr: "The nonlinear Dirac equation in Bose–Einstein condensates: Foundation and symmetries", Physica D: Nonlinear Phenomena **238**, 1413–1421 (2009).

[68] L. H. Haddad and L. D. Carr: "Relativistic linear stability equations for the nonlinear Dirac equation in Bose-Einstein condensates", Europhysics Letters **94**, 56002 (2011).

[69] L. Balents: "Spin liquids in frustrated magnets", Nature **464**, 199–208 (2010).

[70] A. Eckardt, P. Hauke, P. Soltan-Panahi, C. Becker, K. Sengstock and M. Lewenstein: "Frustrated quantum antiferromagnetism with ultracold bosons in a triangular lattice", Europhysics Letters **89**, 10010 (2010).

[71] M. Lewenstein, A. Sanpera and V. Ahufinger: *Ultracold Atoms in Optical Lattices*, Oxford University Press (2012).

[72] I. Bloch, J. Dalibard and S. Nascimbène: "Quantum simulations with ultracold quantum gases", Nature Physics **8**, 267–276 (2012).

[73] C. Schori, T. Stöferle, H. Moritz, M. Köhl and T. Esslinger: "Excitations of a Superfluid in a Three-Dimensional Optical Lattice", Phys. Rev. Lett. **93**, 240402 (2004).

[74] J. Heinze, S. Götze, J. S. Krauser, B. Hundt, N. Fläschner, D. S. Lühmann, C. Becker and K. Sengstock: "Multiband Spectroscopy of Ultracold Fermions: Observation of Reduced Tunneling in Attractive Bose-Fermi Mixtures", Phys. Rev. Lett. **107**, 135303 (2011).

[75] J. F. Sherson, S. J. Park, P. L. Pedersen, N. Winter, M. Gajdacz, S. Mai and J. Arlt: "The pump–probe coupling of matter wave packets to remote lattice states", New J. Phys. **14**, 083013 (2012).

[76] J. Heinze, J. S. Krauser, N. Fläschner, B. Hundt, S. Götze, A. P. Itin, L. Mathey, K. Sengstock and C. Becker: "Intrinsic Photoconductivity of Ultracold Fermions in Optical Lattices", Phys. Rev. Lett. **110**, 085302 (2013).

[77] W. Bakr, P. Preiss, M. Tai, R. Ma, J. Simon and M. Greiner: "Orbital excitation blockade and algorithmic cooling in quantum gases", Nature **480**, 500–503 (2011).

[78] R. Ma, M. Tai, P. Preiss, W. Bakr, J. Simon and M. Greiner: "Photon-Assisted Tunneling in a Biased Strongly Correlated Bose Gas", Phys. Rev. Lett. **107**, 095301 (2011).

[79] D. Greif, L. Tarruell, T. Uehlinger, R. Jördens and T. Esslinger: "Probing Nearest-Neighbor Correlations of Ultracold Fermions in an Optical Lattice", Phys. Rev. Lett. **106**, 145302 (2011).

[80] J. Denschlag, J. Simsarian, H. Häffner, C. McKenzie, A. Browaeys, D. Cho, K. Helmerson, S. Rolston and W. Phillips: "A Bose-Einstein condensate in an optical lattice", Journal of Physics B: Atomic, Molecular and Optical Physics **35**, 3095–3110 (2002).

[81] N. Gemelke, E. Sarajlic, Y. Bidel, S. Hong and S. Chu: "Parametric Amplification of Matter Waves in Periodically Translated Optical Lattices", Phys. Rev. Lett. **95**, 170404 (2005).

[82] C. V. Parker, L.-C. Ha and C. Chin: "Direct observation of effective ferromagnetic domains of cold atoms in a shaken optical lattice", Nature Physics advance online publication, doi:10.1038/nphys2789, 1–6 (2013).

[83] A. Eckardt, C. Weiss and M. Holthaus: "Superfluid-Insulator Transition in a Periodically Driven Optical Lattice", Phys. Rev. Lett. **95**, 260404 (2005).

[84] H. Lignier, C. Sias, D. Ciampini, Y. Singh, A. Zenesini, O. Morsch and E. Arimondo: "Dynamical Control of Matter-Wave Tunneling in Periodic Potentials", Phys. Rev. Lett. **99**, 220403 (2007).

[85] A. Zenesini, H. Lignier, D. Ciampini, O. Morsch and E. Arimondo: "Coherent Control of Dressed Matter Waves", Phys. Rev. Lett. **102**, 100403 (2009).

[86] D. Dunlap and V. Kenkre: "Dynamic localization of a charged particle moving under the influence of an electric field", Physical Review B **34**, 3625–3633 (1986).

[87] F. Großmann, P. Jung, T. Dittrich and P. Hänggi: "Tunneling in a periodically driven bistable system", Zeitschrift für Physik B Condensed Matter **84**, 315–325 (1991).

[88] F. Großmann and P. Hänggi: "Localization in a Driven Two-Level Dynamics", Europhysics Letters **18**, 571–576 (1992).

[89] M. Holthaus: "Collapse of minibands in far-infrared irradiated superlattices", Phys. Rev. Lett. **69**, 351–354 (1992).

[90] X.-G. Zhao: "The suppression of a Bloch band in a driving laser field", Journal of Physics: Condensed Matter **6**, 2751–2756 (1994).

[91] K. Madison, M. Fischer, R. Diener, Q. Niu and M. Raizen: "Dynamical Bloch Band Suppression in an Optical Lattice", Phys. Rev. Lett. **81**, 5093–5096 (1998).

[92] M. Lewenstein, A. Sanpera, V. Ahufinger, B. Damski, A. Sen(De) and S. Ujjwal: "Ultracold atomic gases in optical lattices: mimicking condensed matter physics and beyond", Advances in Physics **56**, 243–379 (2007).

[93] S. Trotzky, P. Cheinet, S. Fölling, M. Feld, U. Schnorrberger, A. Rey, A. Polkovnikov, E. Demler, M. Lukin and I. Bloch: "Time-Resolved Observation and Control of Superexchange Interactions with Ultracold Atoms in Optical Lattices", Science **319**, 295–299 (2008).

[94] Y.-A. Chen, S. Nascimbène, M. Aidelsburger, M. Atala, S. Trotzky and I. Bloch: "Controlling Correlated Tunneling and Superexchange Interactions with ac-Driven Optical Lattices", Phys. Rev. Lett. **107**, 210405 (2011).

[95] T. Fukuhara, A. Kantian, M. Endres, M. Cheneau, P. Schauß, S. Hild, D. Bellem, U. Schollwöck, T. Giamarchi, C. Gross, I. Bloch and S. Kuhr: "Quantum dynamics of a mobile spin impurity", Nature Physics **9**, 235–241 (2013).

[96] J. Simon, W. Bakr, R. Ma, M. Tai, P. Preiss and M. Greiner: "Quantum simulation of antiferromagnetic spin chains in an optical lattice", Nature **472**, 307–312 (2011).

[97] J. Meineke, J.-P. Brantut, D. Stadler, T. Müller, H. Moritz and T. Esslinger: "Interferometric measurement of local spin fluctuations in a quantum gas", Nature Physics **8**, 455–459 (2012).

[98] D. Greif, T. Uehlinger, G. Jotzu, L. Tarruell and T. Esslinger: "Short-Range Quantum Magnetism of Ultracold Fermions in an Optical Lattice", Science **340**, 1307–1310 (2013).

[99] E. Stoner: "Atomic moments in ferromagnetic metals and alloys with non-ferromagnetic elements", Philosophical Magazine Series 7 **15**, 1018–1034 (1933).

[100] G. B. Jo, Y. R. Lee, J. H. Choi, C. A. Christensen, T. H. Kim, J. H. Thywissen, D. E. Pritchard and W. Ketterle: "Itinerant Ferromagnetism in a Fermi Gas of Ultracold Atoms", Science **325**, 1521–1524 (2009).

[101] D. Pekker, M. Babadi, R. Sensarma, N. Zinner, L. Pollet, M. W. Zwierlein and E. Demler: "Competition between Pairing and Ferromagnetic Instabilities in Ultracold Fermi Gases near Feshbach Resonances", Phys. Rev. Lett. **106**, 050402 (2011).

[102] C. Sanner, E. J. Su, W. Huang, A. Keshet, J. Gillen and W. Ketterle: "Correlations and Pair Formation in a Repulsively Interacting Fermi Gas", Phys. Rev. Lett. **108**, 240404 (2012).

[103] G. Wannier: "Antiferromagnetism. The Triangular Ising Net", Physical Review **79**, 357–364 (1950).

[104] S. Sachdev: "Quantum magnetism and criticality", Nature Physics **4**, 173–185 (2008).

[105] L. Pauling: "The Structure and Entropy of Ice and of Other Crystals with Some Randomness of Atomic Arrangement", Journal of the American Chemical Society **57**, 2680–2684 (1935).

[106] A. Ramirez, A. Hayashi, R. Cava, R. Siddharthan, B. Shastry and B. Siddharthan: "Zero-point entropy in 'spin ice' ", Nature **399**, 333–335 (1999).

[107] R. Moessner and A. P. Ramirez: "Geometrical Frustration", Physics Today **59**, 24 (2006).

[108] C. Castelnovo, R. Moessner and S. L. Sondhi: "Magnetic monopoles in spin ice", Nature **451**, 42–45 (2008).

[109] D. J. Morris, D. A. Tennant, S. A. Grigera, B. Klemke, C. Castelnovo, R. Moessner, C. Czternasty, M. Meissner, K. C. Rule, J. U. Hoffmann, K. Kiefer, S. Gerischer, D. Slobinsky and R. S. Perry: "Dirac Strings and Magnetic Monopoles in the Spin Ice Dy2Ti2O7", Science **326**, 411–414 (2009).

[110] T. Fennell, P. P. Deen, A. R. Wildes, K. Schmalzl, D. Prabhakaran, A. T. Boothroyd, R. J. Aldus, D. F. McMorrow and S. T. Bramwell: "Magnetic Coulomb Phase in the Spin Ice Ho2Ti2O7", Science **326**, 415–417 (2009).

[111] J. Dalibard, F. Gerbier, G. Juzeliūnas and P. Öhberg: "Colloquium: Artificial gauge potentials for neutral atoms", Reviews of Modern Physics **83**, 1523–1543 (2011).

[112] K. Klitzing, G. Dorda and M. Pepper: "New Method for High-Accuracy Determination of the Fine-Structure Constant Based on Quantized Hall Resistance", Phys. Rev. Lett. **45**, 494–497 (1980).

[113] R. Laughlin: "Quantized Hall conductivity in two dimensions", Physical Review B **23**, 5632–5633 (1981).

[114] D. C. Tsui, H. L. Stormer and A. C. Gossard: "Two-Dimensional Magnetotransport in the Extreme Quantum Limit", Phys. Rev. Lett. **48**, 1559–1562 (1982).

[115] R. B. Laughlin: "Anomalous Quantum Hall Effect: An Incompressible Quantum Fluid with Fractionally Charged Excitations", Phys. Rev. Lett. **50**, 1395–1398 (1983).

[116] P. G. Harper: "Single Band Motion of Conduction Electrons in a Uniform Magnetic Field", Proceedings of the Physical Society. Section A **68**, 874–878 (1955).

[117] D. Hofstadter: "Energy levels and wave functions of Bloch electrons in rational and irrational magnetic fields", Physical Review B **14**, 2239–2249 (1976).

[118] M. Z. Hasan and C. L. Kane: "Colloquium: Topological insulators", Reviews of Modern Physics **82**, 3045–3067 (2010).

[119] J. E. Moore: "The birth of topological insulators", Nature **464**, 194–198 (2010).

[120] K. Madison, F. Chevy, W. Wohlleben and J. Dalibard: "Vortex Formation in a Stirred Bose-Einstein Condensate", Phys. Rev. Lett. **84**, 806–809 (2000).

[121] J. R. Abo-Shaeer, C. Raman, J. M. Vogels and W. Ketterle: "Observation of Vortex Lattices in Bose-Einstein Condensates", Science **292**, 476–479 (2001).

[122] V. Schweikhard, I. Coddington, P. Engels, V. Mogendorff and E. Cornell: "Rapidly Rotating Bose-Einstein Condensates in and near the Lowest Landau Level", Phys. Rev. Lett. **92**, 040404 (2004).

[123] V. Bretin, S. Stock, Y. Seurin and J. Dalibard: "Fast Rotation of a Bose-Einstein Condensate", Phys. Rev. Lett. **92**, 050403 (2004).

[124] N. Gemelke, E. Sarajlic and S. Chu: "Rotating Few-body Atomic Systems in the Fractional Quantum Hall Regime", arXiv 1007.2677, 1–22 (2010).

[125] N. R. Cooper: "Rapidly rotating atomic gases", Advances in Physics **57**, 539–616 (2008).

[126] A. Fetter: "Rotating trapped Bose-Einstein condensates", Reviews of Modern Physics **81**, 647–691 (2009).

[127] D. Jaksch and P. Zoller: "Creation of effective magnetic fields in optical lattices: the Hofstadter butterfly for cold neutral atoms", New J. Phys. **5**, 56 (2003).

[128] E. Mueller: "Artificial electromagnetism for neutral atoms: Escher staircase and Laughlin liquids", Physical Review A **70**, 041603 (2004).

[129] I. Spielman: "Raman processes and effective gauge potentials", Physical Review A **79**, 063613 (2009).

[130] F. Gerbier and J. Dalibard: "Gauge fields for ultracold atoms in optical superlattices", New J. Phys. **12**, 033007 (2010).

[131] N. R. Cooper: "Optical Flux Lattices for Ultracold Atomic Gases", Phys. Rev. Lett. **106**, 175301 (2011).

[132] A. R. Kolovsky: "Creating artificial magnetic fields for cold atoms by photon-assisted tunneling", Europhysics Letters **93**, 20003 (2011).

[133] C. E. Creffield and F. Sols: "Comment on "Creating artificial magnetic fields for cold atoms by photon-assisted tunneling" by Kolovsky A. R.", Europhysics Letters **101**, 40001 (2013).

[134] Y. J. Lin, R. Compton, A. Perry, W. Phillips, J. von Porto and I. Spielman: "Bose-Einstein Condensate in a Uniform Light-Induced Vector Potential", Phys. Rev. Lett. **102**, 130401 (2009).

[135] Y. J. Lin, R. Compton, K. Jiménez-García, J. von Porto and I. Spielman: "Synthetic magnetic fields for ultracold neutral atoms", Nature **462**, 628–632 (2009).

[136] Y. J. Lin, R. Compton, K. Jiménez-García, W. Phillips, J. von Porto and I. Spielman: "A synthetic electric force acting on neutral atoms", Nature Physics **7**, 531–534 (2011).

[137] M. Aidelsburger, M. Atala, S. Nascimbène, S. Trotzky, Y. A. Chen and I. Bloch: "Experimental Realization of Strong Effective Magnetic Fields in an Optical Lattice", Phys. Rev. Lett. **107**, 255301 (2011).

[138] K. Jiménez-García, L. LeBlanc, R. Williams, M. Beeler, A. Perry and I. Spielman: "Peierls Substitution in an Engineered Lattice Potential", Phys. Rev. Lett. **108**, 225303 (2012).

[139] Y. J. Lin, K. Jiménez-García and I. Spielman: "Spin-orbit-coupled Bose-Einstein condensates", Nature **471**, 83–86 (2011).

[140] V. Galitski and I. B. Spielman: "Spin–orbit coupling in quantum gases", Nature **494**, 49–54 (2013).

[141] M. I. D'Yakonov and I. V. Perel': "Possibility of Orienting Electron Spins with Current", Journal of Experimental and Theoretical Physics Letters **13**, 467–469 (1971).

[142] R. Peierls: "Zur Theorie des Diamagnetismus von Leitungselektronen", Zeitschrift für Physik **80**, 763–791 (1933).

[143] J. Luttinger: "The Effect of a Magnetic Field on Electrons in a Periodic Potential", Physical Review **84**, 814–817 (1951).

[144] C. R. Dean, L. Wang, P. Maher, C. Forsythe, F. Ghahari, Y. Gao, J. Katoch, M. Ishigami, P. Moon, M. Koshino, T. Taniguchi, K. Watanabe, K. L. Shepard, J. Hone and P. Kim: "Hofstadter's butterfly and the fractal quantum Hall effect in moiré superlattices", Nature **497**, 598–602 (2013).

[145] L. A. Ponomarenko, R. V. Gorbachev, G. L. Yu, D. C. Elias, R. Jalil, A. A. Patel, A. Mishchenko, A. S. Mayorov, C. R. Woods, J. R. Wallbank, M. Mucha-Kruczynski, B. A. Piot, M. Potemski, I. V. Grigorieva, K. S. Novoselov, F. Guinea, I. V. Fal'ko and A. K. Geim: "Cloning of Dirac fermions in graphene superlattices", Nature **497**, 594–597 (2013).

[146] B. Hunt, J. D. Sanchez-Yamagishi, A. F. Young, M. Yankowitz, B. J. LeRoy, K. Watanabe, T. Taniguchi, P. Moon, M. Koshino, P. Jarillo-Herrero and R. C. Ashoori: "Massive Dirac Fermions and Hofstadter Butterfly in a van der Waals Heterostructure", Science **340**, 1427–1430 (2013).

[147] M. Erhard: "Experimente mit mehrkomponentigen Bose-Einstein-Kondensaten", Ph.D. thesis, Department Physik der Universität Hamburg (2004).

[148] H. Schmaljohann: "Spindynamik in Bose-Einstein Kondensaten", Ph.D. thesis, Department Physik der Universität Hamburg (2004).

[149] J. Kronjäger: "Coherent Dynamics of Spinor Bose-Einstein Condensates", Ph.D. thesis, Department Physik der Universität Hamburg (2007).

[150] C. Becker: "Multi component Bose-Einstein Condensates", Ph.D. thesis, Department Physik der Universität Hamburg (2009).

[151] M. Kottke: "Magnetfallen und Signaturen der Eindimensionalität für Bose-Einstein-Kondensate", Ph.D. thesis, Fachbereich Physik der Universität Hannover (2004).

[152] C. Cohen-Tannoudji, J. Dupont-Roc and G. Grynberg: *Atom-Photon Interactions*, Wiley-VCH Verlag GmbH (2004).

[153] R. Grimm, M. Weidemüller and Y. B. Ovchinnikov: "Optical Dipole Traps for Neutral Atoms", Advances In Atomic, Molecular, and Optical Physics **42**, 95–170 (2000).

[154] D. A. Steck: "Rubidium 87 D Line Data", http://steck.us/alkalidata .

[155] C. Ölschläger: "Quantensimulation von frustriertem Magnetismus in einem optischen Dreiecksgitter", Master's thesis, Department Physik der Universität Hamburg (2011).

[156] P. B. Blakie and C. Clark: "Wannier states and Bose Hubbard parameters for 2D optical lattices", Journal of Physics B: Atomic, Molecular, and Optical Physics **37**, 1391–1404 (2004).

[157] P. Soltan-Panahi, J. Struck, P. Hauke, A. Bick, W. Plenkers, G. Meineke, C. Becker, P. Windpassinger, M. Lewenstein and K. Sengstock: "Multi-component quantum gases in spin-dependent hexagonal lattices", Nature Physics **7**, 434–440 (2011).

[158] C. Kittel: *Introduction to Solid State Physics*, Wiley (2004).

[159] N. W. Ashcroft and N. D. Mermin: *Solid state physics*, Brooks Cole (1976).

[160] G. Wannier: "The Structure of Electronic Excitation Levels in Insulating Crystals", Physical Review **52**, 191–197 (1937).

[161] W. Kohn: "Analytic Properties of Bloch Waves and Wannier Functions", Physical Review **115**, 809–821 (1959).

[162] M. L. Goldberger and K. M. Watson: *Collision Theory*, Dover Publications (2004).

[163] H. Gersch and G. Knollman: "Quantum Cell Model for Bosons", Physical Review **129**, 959–967 (1963).

[164] C. Chin, R. Grimm, P. Julienne and E. Tiesinga: "Feshbach resonances in ultracold gases", Reviews of Modern Physics **82**, 1225–1286 (2010).

[165] J. Li, Y. Yu, A. M. Dudarev and Q. Niu: "Interaction broadening of Wannier functions and Mott transitions in atomic BEC", New J. Phys. **8**, 154 (2006).

[166] G. K. Campbell, J. Mun, M. Boyd, P. Medley, A. E. Leanhardt, L. G. Marcassa, D. E. Pritchard and W. Ketterle: "Imaging the Mott Insulator Shells by Using Atomic Clock Shifts", Science **313**, 649–652 (2006).

[167] P. R. Johnson, E. Tiesinga, J. V. Porto and C. J. Williams: "Effective three-body interactions of neutral bosons in optical lattices", New J. Phys. **11**, 093022 (2009).

[168] S. Will, T. Best, U. Schneider, L. Hackermüller, D.-S. Lühmann and I. Bloch: "Time-resolved observation of coherent multi-body interactions in quantum phase revivals", Nature **465**, 197–201 (2010).

[169] D.-S. Lühmann, O. Jürgensen and K. Sengstock: "Multi-orbital and density-induced tunneling of bosons in optical lattices", New J. Phys. **14**, 033021 (2012).

[170] D. Jaksch and P. Zoller: "The cold atom Hubbard toolbox", Annals of Physics **315**, 52–79 (2005).

[171] A. Leggett: "Superfluidity", Reviews of Modern Physics **71**, S318–S323 (1999).

[172] R. Diener, Q. Zhou, H. Zhai and T.-L. Ho: "Criterion for Bosonic Superfluidity in an Optical Lattice", Phys. Rev. Lett. **98**, 180404 (2007).

[173] V. Kashurnikov, N. Prokof'ev and B. Svistunov: "Revealing the superfluid–Mott-insulator transition in an optical lattice", Physical Review A **66**, 031601 (2002).

[174] Y. Kato, Q. Zhou, N. Kawashima and N. Trivedi: "Sharp peaks in the momentum distribution of bosons in optical lattices in the normalstate", Nature Physics **4**, 617–621 (2008).

[175] F. Gerbier, S. Foelling, A. Widera and I. Bloch: "Visibility of a Bose-condensed gas released from an optical lattice at finite temperatures", arXiv cond-mat/0701420, 1–5 (2007).

[176] F. Gerbier, S. Trotzky, S. Fölling, U. Schnorrberger, J. Thompson, A. Widera, I. Bloch, L. Pollet, M. Troyer, B. Capogrosso-Sansone, N. von Prokof'Ev and B. von Svistunov: "Expansion of a Quantum Gas Released from an Optical Lattice", Phys. Rev. Lett. **101**, 155303 (2008).

[177] E. Toth and P. B. Blakie: "Thermally induced coherence in a Mott insulator of bosonic atoms", Physical Review A **83**, 021601 (2011).

[178] S. Trotzky, L. Pollet, F. Gerbier, U. Schnorrberger, I. Bloch, N. von Prokof'ev, B. Svistunov and M. Troyer: "Suppression of the critical temperature for superfluidity near the Mott transition", Nature Physics **6**, 998–1004 (2011).

[179] A. Eckardt and M. Holthaus: "AC-induced superfluidity", Europhysics Letters **80**, 50004 (2007).

[180] A. Hemmerich: "Effective time-independent description of optical lattices with periodic driving", Physical Review A **81**, 063626 (2010).

[181] E. Arimondo, D. Ciampini, A. Eckardt, M. Holthaus and O. Morsch: "Kilohertz-Driven Bose-Einstein Condensates in Optical Lattices", Advances in Atomic, Molecular, and Optical Physics **61**, 515–547 (2012).

[182] C. Sias, H. Lignier, Y. Singh, A. Zenesini, D. Ciampini, O. Morsch and E. Arimondo: "Observation of Photon-Assisted Tunneling in Optical Lattices", Phys. Rev. Lett. **100**, 040404 (2008).

[183] A. Eckardt: "Zum Mott-Übergang im Bose-Hubbard Modell: Kritische Parameter und kohärente Kontrolle", Ph.D. thesis, Fakultät für Mathematik und Naturwissenschaften der Carl von Ossietzky Universität Oldenburg (2007).

[184] W. Houston: "Acceleration of Electrons in a Crystal Lattice", Physical Review **57**, 184–186 (1940).

[185] A. Eckardt, M. Holthaus, H. Lignier, A. Zenesini, D. Ciampini, O. Morsch and E. Arimondo: "Exploring dynamic localization with a Bose-Einstein condensate", Physical Review A **79**, 013611 (2009).

[186] T. O. Levante, M. Baldus, B. H. Meier and R. R. Ernst: "Formalized quantum mechanical Floquet theory and its application to sample spinning in nuclear magnetic resonance", Molecular Physics **86**, 1195–1212 (1995).

[187] M. Grifoni and P. Hänggi: "Driven quantum tunneling", Physics Reports **304**, 229–354 (1998).

[188] G. Floquet: "Sur les équations différentielles linéaires à coefficients périodiques", Annales scientifiques de l'École Normale Supérieure, Sér. 2 **12**, 47–88.

[189] J. Shirley: "Solution of the Schrödinger Equation with a Hamiltonian Periodic in Time", Physical Review **138**, 979–987 (1965).

[190] H. Sambe: "Steady States and Quasienergies of a Quantum-Mechanical System in an Oscillating Field", Physical Review A **7**, 2203–2213 (1973).

[191] A. G. Fainshtein, N. L. Manakov and L. P. Rapoport: "Some general properties of quasi-energetic spectra of quantum systems in classical monochromatic fields", Journal of Physics B: Atomic and Molecular Physics **11**, 2561–2577 (1978).

[192] A. Eckardt and M. Holthaus: "Avoided-Level-Crossing Spectroscopy with Dressed Matter Waves", Phys. Rev. Lett. **101**, 245302 (2008).

[193] D. Poletti and C. Kollath: "Slow quench dynamics of periodically driven quantum gases", Physical Review A **84**, 013615 (2011).

[194] E. Kierig, U. Schnorrberger, A. Schietinger, J. Tomkovic and M. Oberthaler: "Single-Particle Tunneling in Strongly Driven Double-Well Potentials", Phys. Rev. Lett. **100**, 190405 (2008).

[195] J. Struck, C. Ölschläger, R. L. L. Targat, P. Soltan-Panahi, A. Eckardt, M. Lewenstein, P. Windpassinger, K. Sengstock and R. L. L. Targat: "Quantum Simulation of Frustrated Classical Magnetism in Triangular Optical Lattices", Science **333**, 996–999 (2011).

[196] N. Mermin and H. Wagner: "Absence of Ferromagnetism or Antiferromagnetism in One- or Two-Dimensional Isotropic Heisenberg Models", Phys. Rev. Lett. **17**, 1133–1136 (1966).

[197] P. C. Hohenberg: "Existence of Long-Range Order in One and Two Dimensions", Physical Review **158**, 383–386 (1967).

[198] H. T. Diep: *Frustrated Spin Systems*, World Scientific Publishing Co. (2005).

[199] S. Korshunov: "Phase transitions in two-dimensional systems with continuous degeneracy", Physics Uspekhi **49**, 225–262 (2006).

[200] R. P. Feynman: *Statistical Mechanics: A Set Of Lectures*, Westview Press (1998).

[201] C. Wu: "UNCONVENTIONAL BOSE–EINSTEIN CONDENSATIONS BEYOND THE "NO-NODE" THEOREM", Modern Physics Letters B **23**, 1–24 (2009).

[202] P. Noziéres: *Bose–Einstein Condensation: Some Comments on Bose–Einstein Condensation*, pages 15–30, Cambridge University Press (1995).

[203] A. J. Leggett: *Quantum Liquids*, Oxford University Press (2006).

[204] T. Holstein and H. Primakoff: "Field Dependence of the Intrinsic Domain Magnetization of a Ferromagnet", Physical Review **58**, 1098–1113 (1940).

[205] W. Nolting and A. Ramakanth: *Quantum Theory of Magnetism*, Springer Berlin Heidelberg.

[206] L. M. Duan, E. Demler and M. Lukin: "Controlling Spin Exchange Interactions of Ultracold Atoms in Optical Lattices", Phys. Rev. Lett. **91**, 090402 (2003).

[207] R. Schmied, T. Roscilde, V. Murg, D. Porras and J. I. Cirac: "Quantum phases of trapped ions in an optical lattice", New J. Phys. **10**, 045017 (2008).

[208] P. Hauke, T. Roscilde, V. Murg, J. Cirac and R. Schmied: "Modified spin-wave theory with ordering vector optimization: frustrated bosons on the spatially anisotropic triangular lattice", New J. Phys. **12**, 053036 (2010).

[209] P. Hauke, T. Roscilde, V. Murg, J. Cirac and R. Schmied: "Modified spin-wave theory with ordering vector optimization: spatially anisotropic triangular lattice and model with Heisenberg interactions", New J. Phys. **13**, 075017 (2011).

[210] P. Hauke: "Quantum disorder in the spatially completely anisotropic triangular lattice", Physical Review B **87**, 014415 (2013).

[211] K. Sacha, K. Targoska and J. Zakrzewski: "Frustration and time-reversal symmetry breaking for Fermi and Bose-Fermi systems", Physical Review A **85**, 053613 (2012).

[212] J. Struck, C. Ölschläger, M. Weinberg, P. Hauke, J. Simonet, A. Eckardt, M. Lewenstein, K. Sengstock and P. Windpassinger: "Tunable Gauge Potential for Neutral and Spinless Particles in Driven Optical Lattices", Phys. Rev. Lett. **108**, 225304 (2012).

[213] J. Struck, M. Weinberg, C. Ölschläger, P. Windpassinger, J. Simonet, K. Sengstock, R. Höppner, P. Hauke, A. Eckardt, M. Lewenstein and L. Mathey: "Engineering Ising-XY spin-models in a triangular lattice using tunable artificial gauge fields", Nature Physics **9**, 738–743 (2013).

[214] S. Flach, O. Yevtushenko and Y. Zolotaryuk: "Directed Current due to Broken Time-Space Symmetry", Phys. Rev. Lett. **84**, 2358–2361 (2000).

[215] S. Denisov, L. Morales-Molina, S. Flach and P. Hänggi: "Periodically driven quantum ratchets: Symmetries and resonances", Physical Review A **75**, 063424 (2007).

[216] T. Salger, S. Kling, T. Hecking, C. Geckeler, L. Morales-Molina and M. Weitz: "Directed Transport of Atoms in a Hamiltonian Quantum Ratchet", Science **326**, 1241–1243 (2009).

[217] P. Hauke, O. Tieleman, A. Celi, C. Ölschläger, J. Simonet, J. Struck, M. Weinberg, P. Windpassinger, K. Sengstock, M. Lewenstein and A. Eckardt: "Non-Abelian Gauge Fields and Topological Insulators in Shaken Optical Lattices", Phys. Rev. Lett. **109**, 145301 (2012).

[218] A. R. Kolovsky and H. J. Korsch: "Bloch Oscillations of Cold Atoms in Optical Lattices", International Journal of Modern Physics B **18**, 1235–1260 (2004).

[219] L. Pezzè, L. Pitaevskii, A. Smerzi, S. Stringari, G. Modugno, E. Mirandes, F. Ferlaino, H. Ott, G. Roati and M. Inguscio: "Insulating Behavior of a Trapped Ideal Fermi Gas", Phys. Rev. Lett. **93**, 120401 (2004).

[220] O. Morsch and M. Oberthaler: "Dynamics of Bose-Einstein condensates in optical lattices", Reviews of Modern Physics **78**, 179–215 (2006).

[221] S. Burger, F. Cataliotti, C. Fort, F. Minardi, M. Inguscio, M. Chiofalo and M. Tosi: "Superfluid and Dissipative Dynamics of a Bose-Einstein Condensate in a Periodic Optical Potential", Phys. Rev. Lett. **86**, 4447–4450 (2001).

[222] F. S. Cataliotti, L. Fallani, F. Ferlaino, C. Fort, P. Maddaloni and M. Inguscio: "Dynamics of a trapped BoseEinstein condensate in the presence of a one-dimensional optical lattice", Journal of Optics B: Quantum and Semiclassical Optics **5**, S17–S22 (2003).

[223] F. S. Cataliotti, L. Fallani, F. Ferlaino, C. Fort, P. Maddaloni and M. Inguscio: "Superfluid current disruption in a chain of weakly coupled Bose–Einstein condensates", New J. Phys. **5**, 71–71 (2003).

[224] L. Fallani, L. Sarlo, J. Lye, M. Modugno, R. Saers, C. Fort and M. Inguscio: "Observation of Dynamical Instability for a Bose-Einstein Condensate in a Moving 1D Optical Lattice", Phys. Rev. Lett. **93**, 140406 (2004).

[225] M. Cristiani, O. Morsch, N. Malossi, M. Jona-Lasinio, M. Anderlini, E. Courtade and E. Arimondo: "Instabilities of a Bose-Einstein condensate in a periodic potential: an experimental investigation", Optics Express **12**, 4 (2004).

[226] L. de Sarlo, L. Fallani, J. Lye, M. Modugno, R. Saers, C. Fort and M. Inguscio: "Unstable regimes for a Bose-Einstein condensate in an optical lattice", Physical Review A **72**, 013603 (2005).

[227] C. Fertig, K. O'Hara, J. Huckans, S. Rolston, W. Phillips and J. Porto: "Strongly Inhibited Transport of a Degenerate 1D Bose Gas in a Lattice", Phys. Rev. Lett. **94**, 120403 (2005).

[228] K. Iigaya, S. Konabe, I. Danshita and T. Nikuni: "Landau damping: Instability mechanism of superfluid Bose gases moving in optical lattices", Physical Review A **74**, 053611 (2006).

[229] J. Mun, P. Medley, G. Campbell, L. Marcassa, D. Pritchard and W. Ketterle: "Phase Diagram for a Bose-Einstein Condensate Moving in an Optical Lattice", Phys. Rev. Lett. **99**, 150604 (2007).

[230] B. Wu and Q. Niu: "Landau and dynamical instabilities of the superflow of Bose-Einstein condensates in optical lattices", Physical Review A **64**, 061603 (2001).

[231] V. Konotop and M. Salerno: "Modulational instability in Bose-Einstein condensates in optical lattices", Physical Review A **65**, 021602 (2002).

[232] A. Smerzi, A. Trombettoni, P. Kevrekidis and A. Bishop: "Dynamical Superfluid-Insulator Transition in a Chain of Weakly Coupled Bose-Einstein Condensates", Phys. Rev. Lett. **89**, 170402 (2002).

[233] C. Menotti, A. Smerzi and A. Trombettoni: "Superfluid dynamics of a Bose–Einstein condensate in a periodic potential", New J. Phys. **5**, 112–112 (2003).

[234] M. Machholm, C. Pethick and H. Smith: "Band structure, elementary excitations, and stability of a Bose-Einstein condensate in a periodic potential", Physical Review A **67**, 053613 (2003).

[235] B. Wu and Q. Niu: "Superfluidity of Bose–Einstein condensate in an optical lattice: Landau–Zener tunnelling and dynamical instability", New J. Phys. **5**, 104 (2003).

[236] M. Machholm, A. Nicolin, C. Pethick and H. Smith: "Spatial period doubling in Bose-Einstein condensates in an optical lattice", Physical Review A **69**, 043604 (2004).

[237] Y. Zheng, M. Kostrun and J. Javanainen: "Low-Acceleration Instability of a Bose-Einstein Condensate in an Optical Lattice", Phys. Rev. Lett. **93**, 230401 (2004).

[238] A. Polkovnikov, E. Altman, E. Demler, B. Halperin and M. Lukin: "Decay of superfluid currents in a moving system of strongly interacting bosons", Physical Review A **71**, 063613 (2005).

[239] S. Burger, F. Cataliotti, C. Fort, F. Minardi, M. Inguscio, M. Chiofalo and M. Tosi: "Burger et al. Reply:", Phys. Rev. Lett. **89**, 088902 (2002).

[240] A. Dhar, M. Maji, T. Mishra, R. V. Pai, S. Mukerjee and A. Paramekanti: "Bose-Hubbard model in a strong effective magnetic field: Emergence of a chiral Mott insulator ground state", Physical Review A **85**, 041602 (2012).

[241] S. Greschner, L. Santos and T. Vekua: "Ultracold bosons in zig-zag optical lattices", Physical Review A **87**, 033609 (2013).

[242] A. Dhar, T. Mishra, M. Maji, R. Pai, S. Mukerjee and A. Paramekanti: "Chiral Mott insulator with staggered loop currents in the fully frustrated Bose-Hubbard model", Physical Review B **87**, 174501 (2013).

[243] J. Villain: "Spin glass with non-random interactions", Journal of Physics C: Solid State Physics **10**, 1717–1734 (1977).

[244] S. Teitel and C. Jayaprakash: "Phase transtions in frustrated two-dimensional XY models", Physical Review B **27**, 598–601 (1983).

[245] M. Yosefin and E. Domany: "Phase transitions in fully frustrated spin systems", Physical Review B **32**, 1778–1795 (1985).

[246] M. Choi and S. Doniach: "Phase transitions in uniformly frustrated XY models", Physical Review B **31**, 4516–4526 (1985).

[247] S. Sachdev: *Quantum Phase Transitions*, Cambridge University Press (2011).

[248] M. Hasenbusch, A. Pelissetto and E. Vicari: "Multicritical behaviour in the fully frustrated model and related systems", Journal of Statistical Mechanics: Theory and Experiment **2005**, P12002–P12002 (2005).

[249] S. Teitel and C. Jayaprakash: "Josephson-Junction Arrays in Transverse Magnetic Fields", Phys. Rev. Lett. **51**, 1999–2002 (1983).

[250] R. Webb, R. Voss, G. Grinstein and P. Horn: "Magnetic Field Behavior of a Josephson-Junction Array: Two-Dimensional Flux Transport on a Periodic Substrate", Phys. Rev. Lett. **51**, 690–693 (1983).

[251] W. Shih and D. Stroud: "Superconducting arrays in a magnetic field: Effects of lattice structure and a possible double transition", Physical Review B **30**, 6774–6777 (1984).

[252] B. Pannetier, J. Chaussy, R. Rammal and J. Villegier: "Experimental Fine Tuning of Frustration: Two-Dimensional Superconducting Network in a Magnetic Field", Phys. Rev. Lett. **53**, 1845–1848 (1984).

[253] B. Wees, H. Zant and J. Mooij: "Phase transitions of Josephson-tunnel-junction arrays at zero and full frustration", Physical Review B **35**, 7291–7294 (1987).

[254] X. Ling, H. Lezec, M. Higgins, J. Tsai, J. Fujita, H. Numata, Y. Nakamura, Y. Ochiai, C. Tang, P. Chaikin and S. Bhattacharya: "Nature of Phase Transitions of Superconducting Wire Networks in a Magnetic Field", Phys. Rev. Lett. **76**, 2989–2992 (1996).

[255] P. Martinoli and C. Leemann: "Two Dimensional Josephson Junction Arrays", Journal of Low Temperature Physics **118**, 699–731 (2000).

[256] J. Affolter, M. Tesei, H. Pastoriza, C. Leemann and P. Martinoli: "Observation of Ising-like critical fluctuations in frustrated Josephson junction arrays with modulated coupling energies", Physica C: Superconductivity **369**, 313–316 (2002).

[257] R. Höppner and L. Mathey: In preparation .

[258] S. Miyashita and H. Shiba: "Nature of the Phase Transition of the Two-Dimensional Antiferromagnetic Plane Rotator Model on the Triangular Lattice", Journal of the Physics Society Japan **53**, 1145–1154 (1984).

[259] D. Lee, J. Joannopoulos, J. Negele and D. Landau: "Symmetry analysis and Monte Carlo study of a frustrated antiferromagnetic planar (XY) model in two dimensions", Physical Review B **33**, 450–475 (1986).

[260] E. Granato and J. Kosterlitz: "Critical behavior of coupled XY models", Physical Review B **33**, 4767–4776 (1986).

[261] S. Korshunov and G. Uimin: "Phase transitions in two-dimensional uniformly frustratedXY models. I. Antiferromagnetic model on a triangular lattice", Journal of Statistical Physics **43**, 1–16 (1986).

[262] P. Olsson: "Two Phase Transitions in the Fully Frustrated XY Model", Phys. Rev. Lett. **75**, 2758–2761 (1995).

[263] G. S. Jeon, S. Y. Park and M. Y. Choi: "Double transitions in the fully frustrated XY model", Physical Review B **55**, 14088–14091 (1997).

[264] E. Boubcheur and H. Diep: "Critical behavior of the two-dimensional fully frustrated XY model", Physical Review B **58**, 5163–5165 (1998).

[265] S. Okumura, H. Yoshino and H. Kawamura: "Spin-chirality decoupling and critical properties of a two-dimensional fully frustrated XY model", Physical Review B **83**, 094429 (2011).

[266] T. Obuchi and H. Kawamura: "Spin and Chiral Orderings of the Antiferromagnetic XY Model on the Triangular Lattice and Their Critical Properties", Journal of the Physical Society of Japan **81**, 054003 (2012).

[267] G. Schwarz: "Estimating the Dimension of a Model", The Annals of Statistics **6**, 461–464 (1978).

[268] K. Huang, C. Yang and J. Luttinger: "Imperfect Bose Gas with Hard-Sphere Interaction", Physical Review **105**, 776–784 (1957).

[269] D. Hsieh, D. Qian, L. Wray, Y. Xia, Y. S. Hor, R. J. Cava and M. Z. Hasan: "A topological Dirac insulator in a quantum spin Hall phase", Nature **452**, 970–974 (2008).

[270] M. I. D'Yakonov and I. V. Perel': "Current-induced spin orientation of electrons in semiconductors", Physics Letters A **35**, 459–460 (1971).

[271] J. Hirsch: "Spin Hall Effect", Phys. Rev. Lett. **83**, 1834–1837 (1999).

[272] Y. K. Kato, R. C. Myers, A. C. Gossard and D. D. Awschalom: "Observation of the Spin Hall Effect in Semiconductors", Science **306**, 1910–1913 (2004).

[273] J. Wunderlich, B. Kaestner, J. Sinova and T. Jungwirth: "Experimental Observation of the Spin-Hall Effect in a Two-Dimensional Spin-Orbit Coupled Semiconductor System", Phys. Rev. Lett. **94**, 047204 (2005).

[274] Y. A. Bychkov and E. I. Rashba: "Oscillatory effects and the magnetic susceptibility of carriers in inversion layers", Journal of Physics C: Solid State Physics **17**, 6039–6045 (1984).

[275] G. Dresselhaus: "Spin-Orbit Coupling Effects in Zinc Blende Structures", Physical Review **100**, 580–586 (1955).

[276] J.-Y. Zhang, S.-C. Ji, Z. Chen, L. Zhang, du Zhi-Dong, B. Yan, G.-S. Pan, B. Zhao, Y.-J. Deng, H. Zhai, S. Chen and J.-W. Pan: "Collective Dipole Oscillations of a Spin-Orbit Coupled Bose-Einstein Condensate", Phys. Rev. Lett. **109**, 115301 (2012).

[277] L. W. Cheuk, A. T. Sommer, Z. Hadzibabic, T. Yefsah, W. S. Bakr and M. W. Zwierlein: "Spin-Injection Spectroscopy of a Spin-Orbit Coupled Fermi Gas", Phys. Rev. Lett. **109**, 095302 (2012).

[278] P. Wang, Z.-Q. Yu, Z. Fu, J. Miao, L. Huang, S. Chai, H. Zhai and J. Zhang: "Spin-Orbit Coupled Degenerate Fermi Gases", Phys. Rev. Lett. **109**, 095301 (2012).

[279] M. C. Beeler, R. A. Williams, K. Jiménez-García, L. J. LeBlanc, A. R. Perry and I. B. Spielman: "The spin Hall effect in a quantum gas", Nature **498**, 201–204 (2013).

[280] B. M. Anderson, I. B. Spielman and G. Juzeliūnas: "Magnetically Generated Spin-Orbit Coupling for Ultracold Atoms", Physical Review Letters **111**, 125301 (2013).

[281] Z.-F. Xu, L. You and M. Ueda: "Atomic spin-orbit coupling synthesized with magnetic-field-gradient pulses", Physical Review A **87**, 063634 (2013).

[282] E. G. van Kempen, S. J. Kokkelmans, D. J. Heinzen and B. J. Verhaar: "Interisotope Determination of Ultracold Rubidium Interactions from Three High-Precision Experiments", Phys. Rev. Lett. **88**, 093201 (2002).

[283] P. Pedri, L. Pitaevskii and S. Stringari: "Expansion of a Coherent Array of Bose-Einstein Condensates", Phys. Rev. Lett. **87**, 220401 (2001).

[284] L. P. Pitaevskii and S. Stringari: *Bose-Einstein Condensation*, Clarendon Press (2003).

Danksagung

Die Durchführung dieser Doktorarbeit wäre ohne die tatkräftige Unterstützung und Hilfe vieler Menschen deutlich schwieriger verlaufen oder sogar unmöglich gewesen. Damit sind insbesondere die Mitarbeiter der Arbeitsgruppe „Quantengase und Spektroskopie“ gemeint, die mit ihrem Fachwissen, ihrer Hilfsbereitschaft und Freundlichkeit für eine fruchtbare und angenehme Arbeitsatmosphäre gesorgt haben. Im Folgenden möchte ich einigen von ihnen namentlich danken.

An erster Stelle muss ich meinem Doktorvater Prof. Klaus Sengstock danken. Er hat nicht nur die ausgezeichneten Rahmenbedingungen für diese Arbeit geschaffen, vielmehr hat er mich, durch seine hervorragende Betreuung im Studium, erst dazu gebracht in das Forschungsfeld der ultrakalten Quantengase einzusteigen.
Explizit danken möchte ich allen Kollegen mit denen mich zahlreiche gemeinsame Stunden, Tage, Monate oder Jahre am Spinor-Projekt verbinden: Christoph Becker, Andreas Bick, Dirk-Sören Lühmann, Georg Meineke, Christoph Ölschläger, Wiebke Plenkers, Juliette Simonet, Parvis Soltan-Panahi, Christina Staarmann, Rodolphe Le Targat, Malte Weinberg und Patrick Windpassinger.

Besonderer Dank gebührt meinen Mitdoktoranden, zu denen ich ein stets angenehmes und freundschaftliches Verhältnis hatte:
Parvis, „meinem“ Seniordoktoranden, der mich schon als HiWi und anschließend als Diplomand an das Experiment herangeführt hat. Seine Begeisterung fürs Experiment und auch die Theorie haben sich in zahllosen Diskussionen auf mich übertragen und dabei essentiell für meine Motivation gesorgt.
Christoph Ölschläger, den ich schon als Diplomand betreuen durfte und der sich schnell zum vollwertigen Laborpartner entwickelte, als ich dringend Unterstützung brauchte. Die Arbeit mit ihm hat unglaublich viel Spaß gebracht und verlief darüber hinaus extrem erfolgreich.
Dies gilt ebenso für Malte, der es einem leicht gemacht hat mit ihm zusammenzuarbeiten aufgrund seiner unkomplizierten und humorvollen Art. Darüber hinaus ist Malte mit dem Anfertigen meines Doktorhutes etwas gelungen, woran Parvis in ganzer Linie gescheitert ist, nämlich in überzeugender Weise darzulegen warum Mikrocontroller genial sind. Außerdem muss ich mich für das bereitwillige anfertigen zahlreicher Plots und Bilder, sogar des Titelbildes dieser Arbeit, bei ihm bedanken.

Unseren beiden französischen Postdocs Juliette und Rodolphe danke ich für ihre exzellente Arbeit, das beispielhafte Engagement und die hervorragenden Kochkünste. Ohne Rodolphes Hilfe beim Flicken der Magnetfalle und dem Reinigen von Optiken mit Kalkflecken hätte sich meine Promotionsdauer sicherlich signifikant verlängert.
Patrick danke ich für seine ruhige aber bestimmte Vorgehensweise, wenn es darum ging, uns anzutreiben und zu motivieren. Darüber hinaus hat er wesentlich dazu beigetragen, dass es uns im Labor an nichts mangelte. Ich wünsche ihm alles Gute und viel Erfolg mit seiner eigenen Arbeitsgruppe in Mainz.
Prof. Andreas Hemmerich danke ich für die Übernahme und sehr schnelle Bearbeitung meines Zweitgutachtens.
Für das gewissenhafte Korrekturlesen meiner Doktorarbeit und für zusätzliche Anmerkungen zum Text danke ich Christoph, Juliette und Malte.

Bei André Eckardt, Philipp Hauke, Maciej Lewenstein, Robert Höppner und Ludwig Mathey bedanke ich mich für die erfolgreichen und effektiven Kollaborationen. Darüber hinaus standen mir André, Dirk und Ludwig häufig mit Rat und Antwort in Theoriefragen zur Seite.
Dem technischen Personal und dem Verwaltungspersonal bin ich für den reibungslosen Ablauf verschiedenster Dinge am Institut dankbar. Dabei möchte ich insbesondere Reinhard Mielck hervorheben, der sich in aufopferungsvoller Weise um alles von der Haustechnik bis zum Wickeln von Magnetfeldspulen kümmert. Ellen Gloy, Janina Dahms und Nadja Wardenburg danke ich dafür, dass sie das Aufkommen von bürokratischen Aufgaben für die Doktoranden auf einem Minimum halten.

Zum Schluss danke ich meinen Eltern für die Unterstützung und den starken Rückhalt während des Studiums, der Promotion und auch jetzt noch.